Surface-Atmosphere coupling over the central Arctic Ocean

by

Cathryn Ellen Birch

Submitted in accordance with the requirements for the
degree of Doctor of Philosophy

University of Leeds
School of Earth and Environment
October 2009

The candidate confirms that the work submitted is her own, except where work which has formed part of jointly-authored publications has been included. The contribution of the candidate and the other authors to this work has been explicitly indicated overleaf. The candidate confirms that appropriate credit has been given within the thesis where reference has been made to the work of others.

Declaration of Authorship

The publication *Birch et al. (2009), The performance of a global and mesoscale model over the central Arctic ocean during late summer, Journal of Geophysical Research, 114, D13104, doi:10.1029/2008JD10790,* presented in Appendix One was jointly-authored with Ian Brooks, Michael Tjernström, Sean Milton, Paul Earnshaw, Stefan Söderberg and Ola Persson. This work forms the majority of Chapter 4. The text of the publication was written solely by the candidate. The analysis of the data sets was also performed by the candidate, with guidance from the coauthors. The entire AOE 2001 observational data set and the back trajectories shown in Figure 11 of the publication were provided by Michael Tjernström (efforts from individuals during the AOE 2001 campaign to acquire the measurements are outlined in the Acknowledgements). All data was provided ready processed and quality controlled, apart from the turbulence data from the meteorological mast, which was processed by the candidate. Data from the Met Office Unified Model was provided by Paul Earnshaw, who also participated actively in discussions of the results. Stefan Söderberg provided data from the COAMPS run and advice on the model formulation during the analysis stage. Details of the Met Office Unified Model formulation and parameterisations were provided by Sean Milton and details of COAMPS by Michael Tjernström. Michael Tjernström, Sean Milton and most significantly, Ian Brooks provided suggestions and advice during both the data analysis and writing stage of the publication. Ola Persson was an anonymous reviewer of the paper who later surrendered his anonymity to become the final coauthor. He provided invaluable advice and suggestions during the review process. Where data from or work by people other than the candidate are used in other chapters of the thesis, credit has been given in the Acknowledgements.

Acknowledgements

First and foremost, I would like to thank my supervisor, Ian Brooks for the significant amount of time and effort he has put into supporting me throughout this project and for making the research and field work an enjoyable experience. Thanks also goes to my research support group; Andrew Ross and Alan Blyth. I am grateful to Michael Tjernström for his advice and support throughout the project and especially for providing me with the AOE 2001 observations and guidance for my publication. I would also like to thank Ola Persson for his advice and suggestions during the peer review of the paper.

Funding for this research has come from the Natural Environmental Research Council (studentship and grant number NE/E010008/1) and via a CASE award from the U.K. Met Office, and I am grateful to them for making this project possible. I would like to thank my co-supervisor, Sean Milton for his support and helpful discussions throughout the project and Paul Earnshaw for providing the Met Office Unified Model data sets and input into the analysis. Thanks also goes to Jeff Ridley for providing the climate model data and to him and Adrian Lock for their helpful discussions. I am also grateful to Stefan Söderberg for providing the data sets from COAMPS and for providing help and advice during the analysis and to Ola Persson and Edgar Andreas for sharing the SHEBA bulk turbulent flux algorithm with me.

AOE 2001 was a multinational expedition. Logistics were funded by the Swedish Secretariat for Polar Research and partly by the Knut and Alice Wallenberg Foundation. I am grateful to the AOE 2001 participants for sharing their data with me. The S-band radar was operated by Scott Abbott and thanks go to Allen White for providing the data from it. The ISFF data sets were provided by John Militzer and Steve Oncley and the albedo measurements by Bertil Larsson and Maria Lundin.

The Arctic Summer Cloud Ocean Study (ASCOS) was made possible by funding from the Knut and Alice Wallenberg Foundation and the DAMOCLES European Union 6th Framework Program Integrated Research Project. The Swedish Polar Research Secretariat (SPRS) provided access to the icebreaker Oden and logistical support. I am grateful to the Chief Scientists Caroline Leck and Michael Tjernström for the planning and coordination of ASCOS, to the SPRS logistical staff and to Oden's Captain Mattias Peterson and his crew. ASCOS is an IPY project under the AICIA-IPY umbrella and an endorsed SOLAS project. The meteorological measurements were made as part of a team consisting of myself, Ian Brooks, Thorsten Mauritsen, Joseph Sedlar and Michael Tjernström. I would specifically like to thank Matthew Shupe for providing the remote sensing data products, Joseph Sedlar for providing the radiation data, Ian Brooks for providing the tethersonde measurements, Thorsten Mauritsen for providing the turbulence data from

the C-SAT sonic anemometers and the mean profile measurements, Michael Tjernström for providing the radiosonde observations and Andreas Held for providing the raw data from the open lead flux tripod, the flux footprint data sets and sharing his ideas for the analysis.

On a more personal note, I would like to thank my family and friends for their support throughout the project.

Abstract

Recent and future changes to Arctic climate have the potential to impact the region's wildlife, vegetation and the local indigenous communities. In addition, changes in the Arctic impact lower latitudes through the modification of weather patterns and ocean circulation. There is a need to accurately represent the Arctic region on various timescales to predict future climate changes and to produce improved seasonal and sub-seasonal mid-latitude weather forecasts. Both climate and numerical weather prediction models currently perform poorly over the Arctic region, especially in their representation of cloud occurrence, cloud radiative and microphysical properties and the surface turbulent fluxes.

The Arctic Ocean Experiment (AOE) 2001 and the Arctic Summer Cloud-Ocean Study (ASCOS) 2008 took place in the central Arctic Ocean during the late summer/early freeze-up period. The aim of both campaigns was to improve the understanding of processes relating to the formation and persistence of low-level Arctic clouds. This study uses data from both campaigns to gain an insight into surface exchange, the structure of the lower atmosphere and cloud formation and then uses this knowledge to evaluate the performance of the Met Office Unified Model (MetUM) over the central Arctic region.

The air temperature away from the surface, pressure and wind speed fields are generally well reproduced by the model, suggesting it captures the large-scale circulation with good accuracy. A significant problem is however, found in the model's temperature-dependent albedo parameterisation scheme. Due to an underestimation of the model ice surface albedo, too much radiation is absorbed at the surface, which causes the surface temperature to be too high. This causes a feedback of errors that locks the albedo at its minimum value of 0.5 and the surface temperature at 0 °C for most of the observation period. The model also significantly overestimates the magnitude of the surface turbulent fluxes. This is shown to be due to the use of a value for the roughness length for momentum, z_0 that is too large and the application of Monin-Obukhov similarity theory under the observed conditions. The measurements show that the boundary layer was almost always less than 200 m deep; this means that the constant flux layer was always less than 20 m deep and often extended to only a few metres above the surface. Spectral analysis of the turbulence measurements shows that turbulent properties differ between the upper (30.60 and 15.40 m) and lower measurement levels and that the observed boundary-layer depths are a likely explanation for this. The third main error involves the model's representation of the low-level layer of stratus cloud. The modelled clouds are too thin and too low in the model, which was at least partly due to the overestimation of boundary-layer depth and inaccuracies in the structure of the lower atmosphere. A number of sensitivity tests involving the surface albedo, roughness length for momentum

and vertical grid resolution are performed to refine these conclusions and investigate possible solutions. Several recommendations for improvements to the MetUM and for further research are also presented.

Contents

List of Figures

List of Tables

Abbreviations

AOE	Arctic Ocean Experiment
AMIP	Atmospheric Intercomparison Project
ARCMIP	Arctic Regional Climate Model Intercomparison Project
ASCOS	Arctic Summer Cloud-Ocean Study
BASE	Beaufort and Arctic Storms Experiment
CCN	Cloud Condensation Nuclei
CLASP	Compact Lightweight Aerosol Spectrometer Probe
COAMPS	Coupled Ocean/Atmosphere Mesoscale Prediction System
ECMWF	European Centre for Medium-Range Weather Forecasts
ERA-40	ECMWF 40 year reanalysis
FIRE	First ISCCP Regional Experiment
GPS	Global Positioning System
HadGEM1	Hadley Centre Global Environmental Model, Version 1
IAOE	International Arctic Ocean Expedition
IPCC	Intergovernmental Panel on Climate Change
ISCCP	International Satellite Cloud Climatology Project
ISFF	Integrated Surface Flux Facility
IWC	Ice water concentration
IWP	Ice water path
LWC	Liquid water concentration
LWP	Liquid water path
MAERI	Marine Atmosphere Emitted Radiance Interferometer
MetUM	Met Office Unified Model
M-PACE	Mixed-Phase Arctic Cloud Experiment
NCAR	National Center for Atmospheric Research
NCEP	National Centers for Environmental Prediction
NOAA	National Oceanic and Atmospheric Administration
NWP	Numerical Weather Prediction
SCM	Single Column Model

SHEBA	Surface Heat Budget of the Arctic Ocean
SODAR	SOnic Detection And Ranging
SSM/I	Special Sensor Microwave Imager
UTC	Coordinated Universal Time
WRF	Weather Research and Forecasting

Parameters

C_{DN10}	Neutral drag coefficient at 10 m
C_{Dr}	Drag coefficient at reference height r
C_{Er}	Transfer coefficient for latent heat at reference height r
C_{Hr}	Transfer coefficient for sensible heat at reference height r
c_p	Specific heat of air
E	Latent heat flux
e	Partial pressure of water
e_{srw}	Saturation vapour pressure with respect to water
e_{sri}	Saturation vapour pressure with respect to ice
f	Frequency
f_m	Reduced frequency
f_n	Normalised frequency
G	Surface conductive heat flux
g	Gravitational acceleration
H	Sensible heat flux
K	Kolmogorov constant
K_h	Eddy diffusivity for heat
K_m	Eddy diffusivity for momentum
L	Obukhov length scale
LW_{dn}	Downwards longwave radiation flux
LW_{net}	Net longwave radiation flux
LW_{up}	Upwards longwave radiation flux
L_v	Latent heat of vapourisation of water
m_{dair}	Mass of dry air
m_w	Mass of water vapour
P	Effective wind speed to represent gustiness
p	Air pressure
q	Specific humidity
q_*	Humidity scaling parameter

R	Gas constant
R_*	Roughness Reynolds number
RH	Relative humidity
Ri_b	Bulk Richardson number
Ri_f	Flux Richardson number
Ri_g	Gradient Richardson number
r	Water vapour mixing ratio
r_L	Liquid water mixing ratio
r_s	Saturation mixing ratio
S_x	Spectral or cospectral energy density
SW_{dn}	Downwards shortwave radiation flux
SW_{net}	Net shortwave radiation flux
SW_{up}	Upwards shortwave radiation flux
T	Air temperature
T_{ice}	Ice surface temperature
T_s	Surface temperature
T_{sonic}	Sonic temperature
T_v	Virtual air temperature
T_*	Temperature scaling parameter
U	Mean wind speed
u, v, w	Wind velocity components
u_*	Friction velocity
w_*	Deardorff's convective velocity scale
z	Height above surface
z_i	Depth of convective boundary layer
z_0	Roughness length for momentum
z_t	Roughness length for temperature
z_q	Roughness length for humidity
β_g	Constant for convection
ϵ	Rate of energy dissipation
ϵ_s	Surface emissivity
ζ	Stability parameter
η	Kolmogorov length scale
κ	von Karman constant
ρ	Air density
ρ_{dair}	Density of dry air
ρ_v	Density of water vapour
σ	Stefan Boltzmann constant

σ_x	Standard deviation
τ	Momentum flux
ν	Viscosity
θ	Potential temperature
θ_v	Virtual potential temperature
θ_*	Potential temperature scaling parameter
ϕ_ϵ	Dimensionless turbulent dissipation rate
φ_h	Universal stability function for temperature
φ_m	Universal stability function for momentum
φ_q	Universal stability function for humidity

Chapter 1

Introduction

Evidence is mounting that climate in the Arctic is changing, and at a rate faster than the global average. Many recent studies conclude that temperatures are rising and that this is accompanied by a decrease in both sea ice thickness and extent. These changes were emphasised by the record minimum sea ice extent in September 2007. A modified climate in the Arctic will impact the region's wildlife, vegetation and local indigenous communities. Arctic climate also impacts lower latitudes through the modification of weather patterns and ocean circulation. Seasonal and sub-seasonal forecasts for mid-latitudes in the Northern Hemisphere are currently limited by the poor representation of Arctic ice and atmospheric processes in models.

It is vital to accurately predict changes in Arctic climate to provide decision support for policy makers. Results from climate model ensemble predictions currently produce the most confident predictions of the future; however, there are large differences between individual model predictions, especially related to the magnitude and spatial patterns of the warming and to the extent and timing of the reduction in sea ice. These uncertainties are at least in part due to the lack in understanding of many of the unique processes that occur in the Arctic region. This is especially true in the harsh environment of the central Arctic, where it is difficult to make the extensive in-situ observations necessary to develop Arctic specific model parameterisations.

During the summer months a near-persistent layer of low level cloud exists over the sea ice in the central Arctic Ocean, which differs from the marine stratocumulus that occurs at lower latitudes in a number of ways. Since cloud is the single most important factor influencing the region's surface energy budget, it is vital to understand the formation and persistence of this cloud in order to develop parameterisations to accurately represent it. The Arctic Ocean Experiment (AOE) 2001 and the Arctic Summer Cloud-Ocean Study (ASCOS) were two Swedish-led field campaigns to the central Arctic Ocean, whose main

aim was to make measurements to help understand the formation and persistence of these clouds. One specific aim was to increase our knowledge of the vertical structure of the lower atmosphere and its turbulent properties in order to investigate the transport of aerosols, heat and moisture into the cloud layer from either the surface or via entrainment at cloud top.

Due to this poor understanding of the important processes, both regional and global models perform poorly over the central Arctic region, especially during the summer months. There are problems with simulated cloud occurrence, extent and microphysical properties, which are related to errors in the representation of the surface turbulent fluxes. Recent evidence has shown that these fluxes, especially the latent heat flux, are also not represented accurately in models. Since the existence of sea ice depends significantly on heat exchange between the surface and the atmosphere, it is vital to improve the representation of these small scale processes to accurately predict future atmospheric and sea ice changes.

This project aims to use observations from both the AOE 2001 and ASCOS campaigns to gain an insight into surface exchange, the structure of the lower atmosphere and cloud formation in the central Arctic Ocean during the late summer/early freeze-up periods. This knowledge can then be used to improve model simulations of the region on both weather forecasting and climate timescales, with a specific focus on the Met Office Unified Model. The global numerical weather prediction (NWP) version rather than the climate version of the model is used because the observations are available for periods of only a few weeks and therefore, it is easier to ascribe errors at the scale of individual weather systems. The assimilation of regular observations into the operational NWP version reduces errors in the synoptic flow, allowing systems to be resolved more accurately. Simulations using the climate version of the model are run unconstrained by observations and therefore, cannot reproduce the individual weather systems observed during the field campaigns. This method is justified since the climate version shares many of its physical parameterisations with the global NWP version of the model.

Chapter 2 provides an overview of the aspects of boundary-layer meteorology that are essential to this study and a review of literature published on Arctic climate change, previous observations of the surface energy budget, clouds and vertical atmospheric structure in the Arctic and details of previous model evaluations over the region. Chapter 3 gives details of the model parameterisations and an explanation of the model data sets used in the analysis. It also introduces the AOE 2001 and ASCOS field campaigns, describes the observations that are available from them and describes the methods used for the processing and quality control of the turbulence measurements made during ASCOS. Chapter 4 presents an evaluation of the MetUM and a mesoscale model, COAMPS over the central

Arctic region using the AOE 2001 data set. The aim of this is to provide a broad overview of model performance and identify key sources of error that require further investigation. The ASCOS observations are then used in a more detailed analysis of some of the parameterisations within the Met Office Unified Model. Chapter 5 uses the ASCOS turbulence measurements to test assumptions made in the model bulk surface flux parameterisation scheme. This includes the validity of Monin-Obukhov similarity theory and the representation of surface roughness. Chapter 6 provides a general evaluation of the MetUM using the ASCOS observations and an investigation into the relationship between the vertical structure of the lower atmosphere and cloud formation. This is followed by sensitivity tests performed with the MetUM to explore possible model improvements and a brief comparison between both sets of observations with the climate version of the MetUM. This comparison is conducted with the aim of determining whether the same biases found in the NWP version of the MetUM also exist in the climate version of the model. Finally, a summary of the results and recommendations for model improvements and future work are presented in Chapter 7.

Chapter 2

Literature Review

2.1 Boundary-layer meteorology

2.1.1 Structure of the lower atmosphere

The atmosphere can be divided into 4 main layers; the troposphere, stratosphere, mesosphere and thermosphere (Figure 2.1). The troposphere extends from the surface up to approximately 12 km and temperature generally decreases with altitude due to adiabatic expansion. Compared to other regions of the atmosphere, the air is relatively well-mixed by weather systems that cause both horizontal and vertical motion. Above the troposphere lies the stratosphere, extending up to approximately 50 km. In this layer air temperature increases with height due to increased absorption of solar radiation by ozone.

The focus of this study is within the troposphere and more specifically the region of air closest to the surface, the atmospheric boundary layer. As the name suggests it forms the boundary between the Earth's surface and the 'free atmosphere'. The air within the boundary layer is generally well-mixed by turbulence created by convective motions and surface friction. Stull (1988) defines the boundary layer as the region of the troposphere "that is directly influenced by the presence of the Earth's surface and responds to surface forcing with a timescale of about an hour or less". Figure 2.2 shows a typical fair weather daytime vertical potential temperature profile. In the troposphere potential temperature increases with height (i.e. it is statically stable) however, mixing near the surface causes the potential temperature to be uniform with height. This 'mixed-layer' is capped by a sharp increase in temperature called a temperature inversion (Stull, 2000).

Typical daytime boundary-layer profiles of several atmospheric parameters are shown in Figure 2.3. The virtual potential temperature profile shows an unstable surface layer

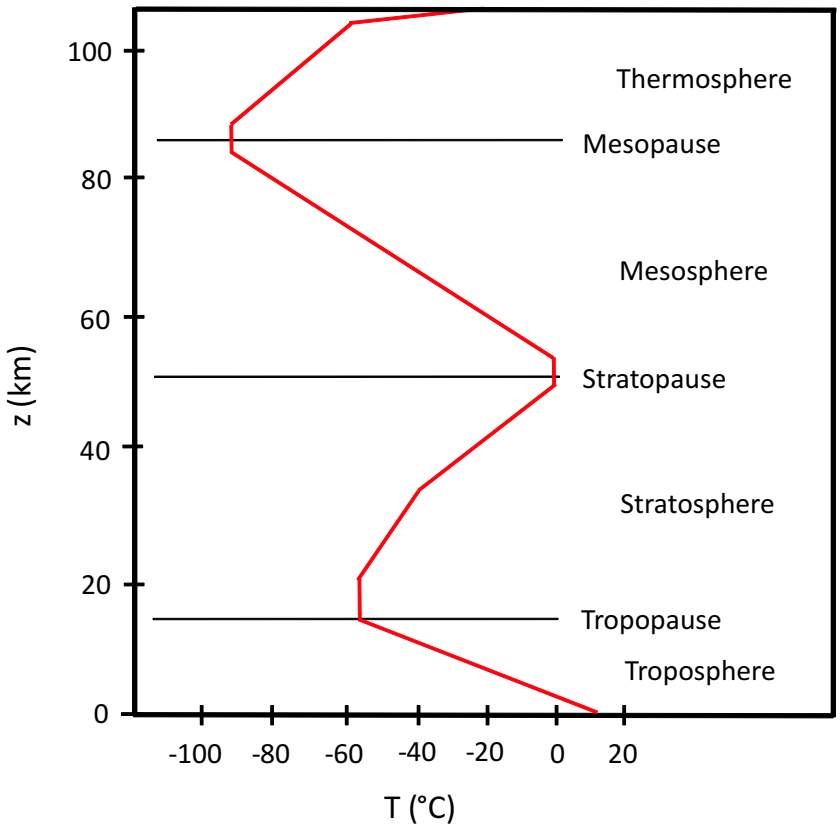

Figure 2.1: Vertical structure of the atmosphere (reproduced from Stull (2000) p.13)

due to strong heating at the surface. Wind speed increases sharply with height due to the decreasing effect of frictional forces with increasing distance from the surface. Water vapour concentration usually also decreases with height in the surface layer because the main source of water is evaporation at the surface. In the mixed layer all four variables are constant with height due to turbulent mixing. The temperature inversion at the top of the mixed layer caps the boundary layer and this restricts significant mixing to below this level. Here the wind speed often changes rapidly with height, which produces wind shear and turbulent mixing that cause air to be drawn into the boundary layer from above but little, if any boundary-layer air is mixed upwards into the free troposphere. The main mechanism by which boundary-layer air is mixed upwards into the free-troposphere is deep convection, rather than entrainment.

Figure 2.4 shows typical turbulent flux profiles in the convective mixed layer and the stable boundary layer. In the daytime convective boundary layer the fluxes are larger, tend to increase or decrease linearly with height in the mixed layer and decrease rapidly to zero at the top of the boundary layer. The surface layer is defined as the region where fluxes vary by less than 10% in magnitude from their surface value, which is approximately 10 % of boundary layer depth (Stull, 1988). Under daytime convective conditions the surface layer is typically between 20 and 200 m deep. At night, the strong

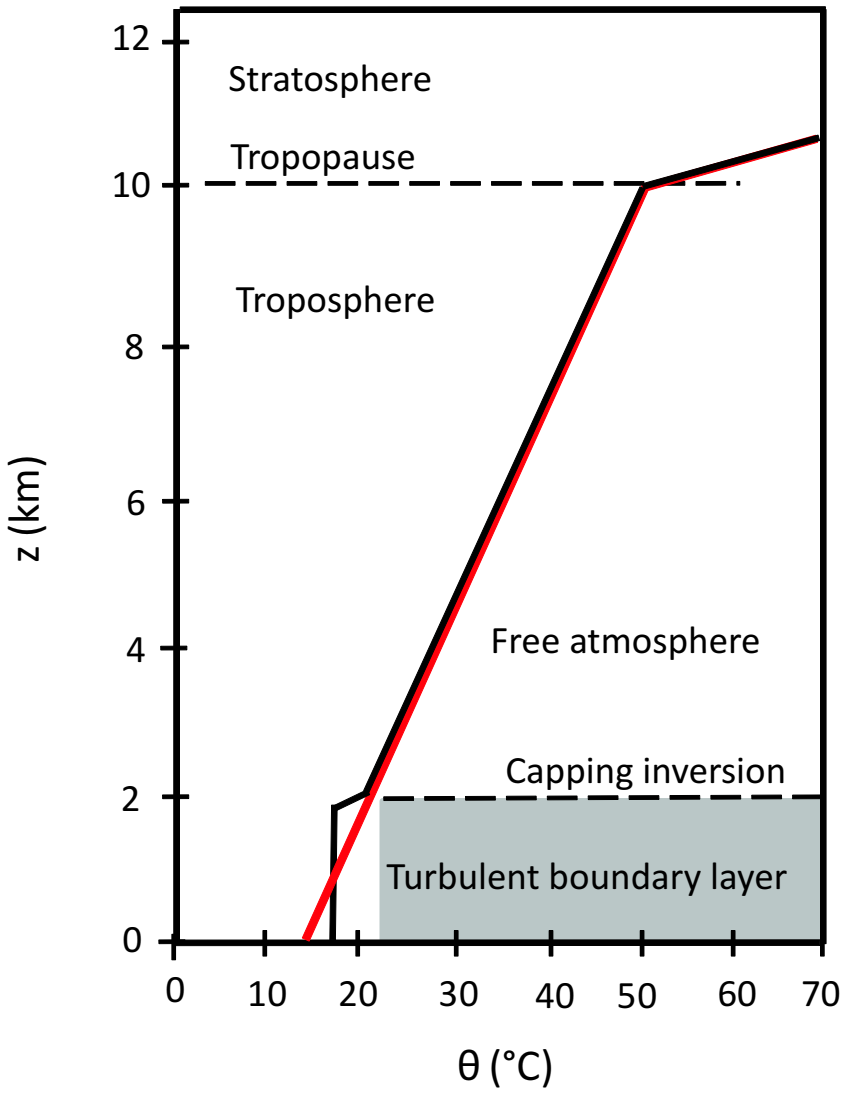

Figure 2.2: Typical vertical structure of a fair weather boundary layer (reproduced from Stull (2000) p.67). The red line is the potential temperature profile in air with a standard atmospheric lapse rate and the black line is the actual potential temperature profile.

stability of the boundary layer caused by surface cooling prevents strong turbulence and the boundary-layer depth is of the order of 10's of metres. The fluxes that do occur are mainly in the surface layer, which is often only a few metres deep.

2.1.2 Stability

When an air parcel rises, it expands due to the decreasing environmental pressure and cools. This rate of cooling with height in the atmosphere is called the dry adiabatic lapse rate. If the air becomes saturated water will condense out, latent heat is released and the parcel will cool more slowly at the saturated adiabatic lapse rate. In order to determine atmospheric stability, a vertical temperature profile is required. If the air temperature

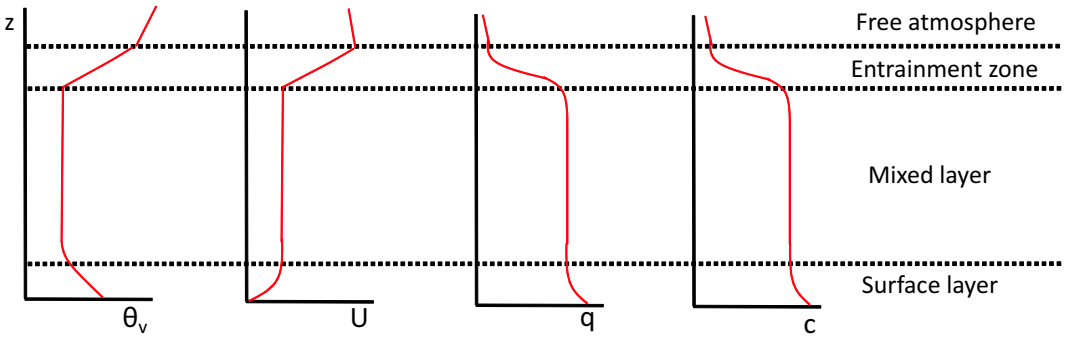

Figure 2.3: Typical daytime boundary-layer profiles of virtual potential temperature, wind speed, specific humidity and pollutant concentration (reproduced from Stull (1988) p.13).

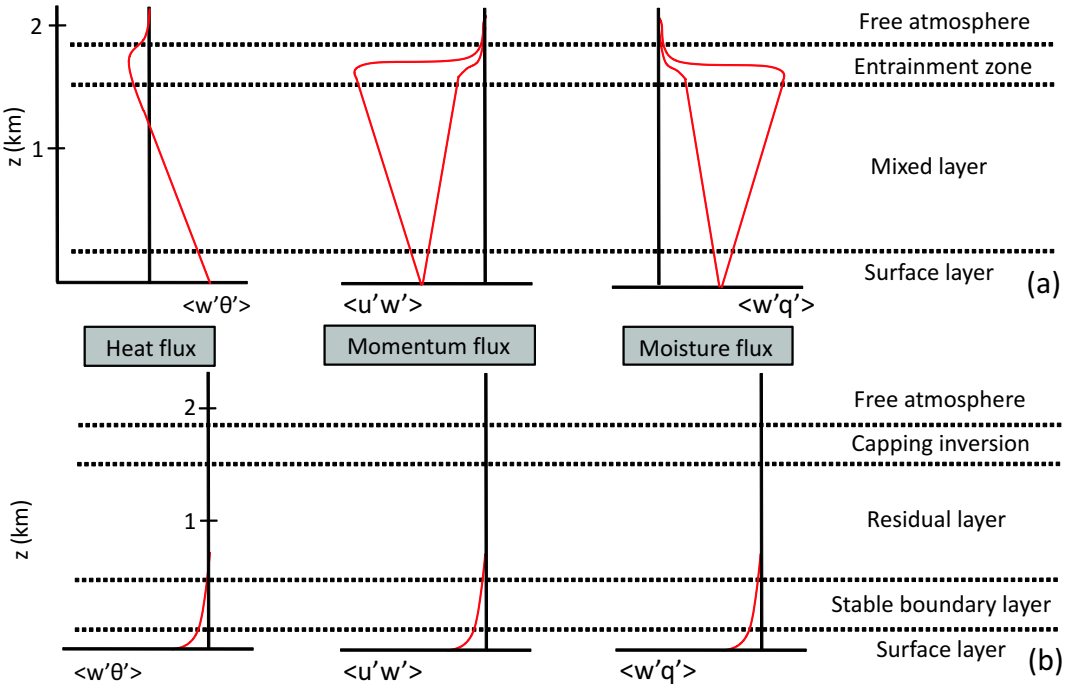

Figure 2.4: Idealised turbulent flux profiles for the (a) convective mixed layer and the (b) stable boundary layer (reproduced from Stull (1988) p.56). Positive (negative) numbers are upward (downward) fluxes.

decreases with height more slowly than the saturated adiabatic lapse rate the air is stable (Figure 2.5). If the air temperature decreases with height more quickly than the dry adiabatic rate the air is unstable and if the environmental lapse rate is between the dry and saturated adiabatic lapse rates the air is conditionally unstable. An alternative indicator of atmospheric stability is potential temperature, θ (or virtual potential temperature, θ_v for moist air) because it allows a more straightforward comparison of temperatures at different heights. If θ increases with height the atmosphere is stable, if it decreases it is unstable and if it is constant with height it is defined as neutral.

Another useful indicator of stability is the Richardson number; this is the ratio of buoyant

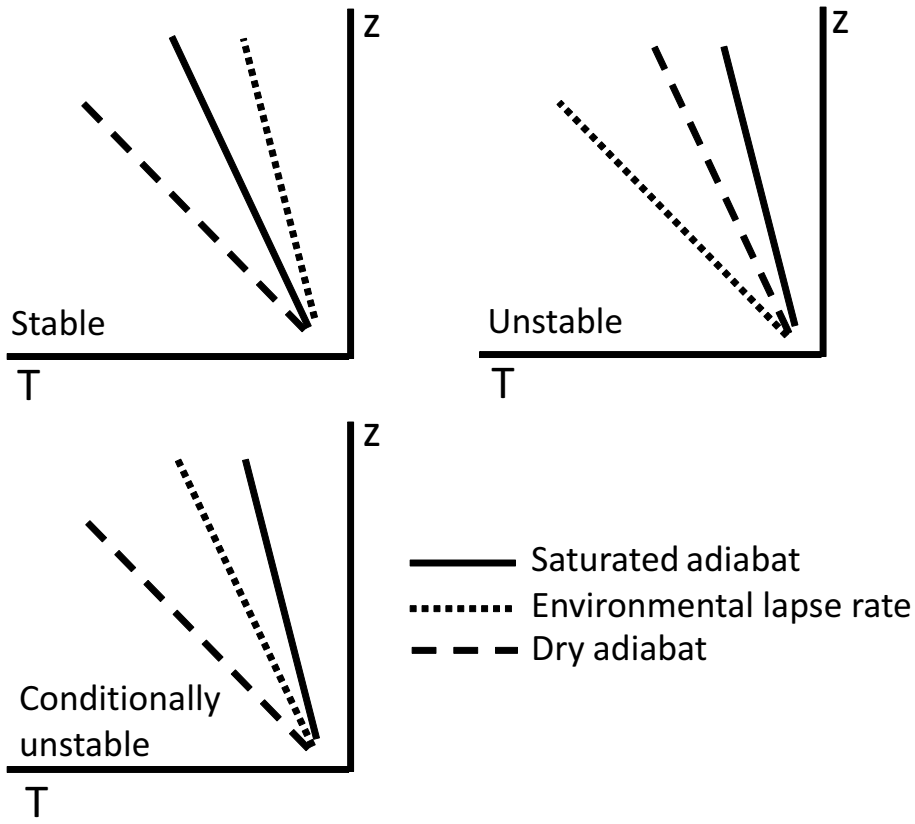

Figure 2.5: Stable and unstable atmospheric profiles (reproduced from Stimac (2003)).

and shear forcing terms and several variants exist. The flux Richardson number is derived from the buoyant and mechanical turbulent production terms of the turbulent kinetic energy equation (Stull (1988)):

$$Ri_f = \frac{\left(\frac{g}{T_v}\right)\overline{w'\theta'_v}}{\overline{u'w'}\left(\frac{\partial \overline{U}}{\partial z}\right) + \overline{v'w'}\left(\frac{\partial \overline{V}}{\partial z}\right)} \tag{2.1}$$

where z is height above the surface and g is gravitational acceleration. The numerator represents the buoyant suppression of turbulence and the denominator the shear production of turbulence. The problem with this form of the Richardson number is that measurements of the turbulent fluctuations are required, which means its value can only be computed for turbulent flow (Stull, 1988). An alternative and the most commonly used form is the gradient Richardson number:

$$Ri_g = \frac{\frac{g}{T_v}\frac{\partial \theta_v}{\partial z}}{\left(\frac{\partial U}{\partial z}\right)^2 + \left(\frac{\partial V}{\partial z}\right)^2} \tag{2.2}$$

There are two important thresholds between turbulent and laminar flow; R_c marks the onset of turbulence and R_t marks the termination of turbulence (Stull, 1988):

- Laminar flow becomes turbulent when $Ri_g < R_c$ (air becomes more unstable)
- Turbulent flow becomes laminar when $Ri_g > R_t$ (air becomes more stable)
- It has been found by experiment $R_c = 0.21$ to 0.25 and $R_t = 1.0$.

A third useful form is the bulk Richardson number, which approximates Ri_g by estimating local gradients using finite differences across layers (Glickman, 2000):

$$Ri_B = \frac{\left(\frac{g}{T_v}\right) \Delta\theta_v \Delta z}{(\Delta U)^2 + (\Delta V)^2} \tag{2.3}$$

2.1.3 Marine stratocumulus

Figure 2.6 illustrates processes that occur in a mid-latitude stratocumulus topped marine boundary layer. Clouds form when stable stratification and large-scale subsidence in the free troposphere override a moist, well-mixed boundary layer (Stevens *et al.*, 2007). The subsidence causes a temperature inversion, which traps water vapour that has evaporated from the surface in the boundary layer and forms clouds. The cloud top cools due to longwave emission, producing the lowest temperatures in the boundary layer. This enhances mixing in the boundary layer and evaporation from the surface, allowing the clouds to persist.

At mid-latitudes a distinct diurnal cycle has been observed in marine stratocumulus (Holtslag & Duynkerke, 1998; Duynkerke & Coauthors, 2004; Tjernström & Rune, 2003). The clouds are thickest at night and during the early morning. As the sun rises, solar radiation heats the cloud layer more than it is cooled by longwave emission. This destabilises the cloud layer and reduces turbulent mixing, which often decouples it from the air below, cutting off the cloud's supply of water from the surface. This and the fact that warmer, drier air is entrained from above causes the cloud to thin and possibly break up. The cloud minimum is therefore during the afternoon. Strong nighttime radiative cooling at cloud top causes the daily maximum in turbulent mixing and thus a well-mixed boundary layer. Drizzle is also most frequent during late night and early morning when the cloud is thickest and contains the highest water vapour concentrations (Comstock *et al.*, 2005).

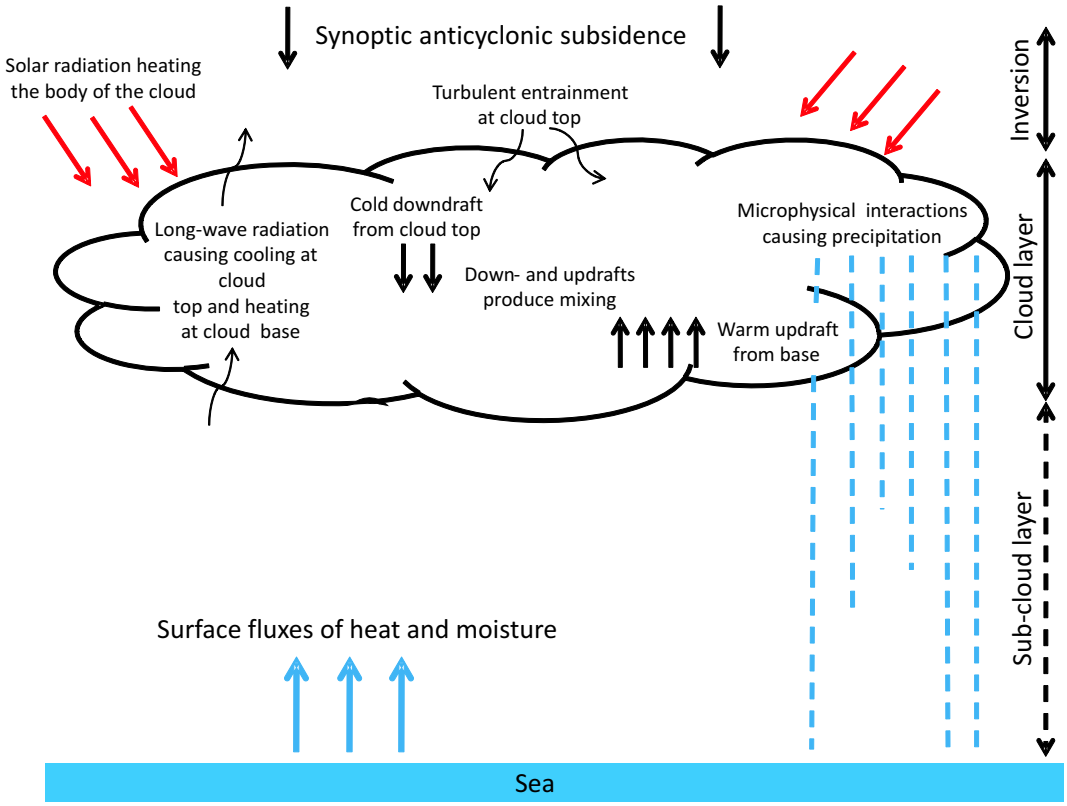

Figure 2.6: Processes within a mid-latitude marine stratocumulus cloud (reproduced from Holtslag & Duynkerke (1998) p.206).

2.1.4 Atmospheric variables

2.1.4.1 Humidity

The mixing ratio, r is the ratio of the mass of water vapour, m_w in a volume of air to the mass of the dry air, m_{dair} in the volume (Rogers & Yau, 1994):

$$r = \frac{m_w}{m_{dair}} = \frac{\rho_v}{\rho_{dair}} \tag{2.4}$$

where ρ_v and ρ_{dair} are the densities of vapour and dry air respectively. They are derived from the equation of state through:

$$\begin{aligned} \rho_v &= e/R_v T \\ \rho_{dair} &= (p-e)/R' T \end{aligned} \tag{2.5}$$

where $R'/R_v = 0.622$, p is the total air pressure, e is the partial pressure of water (vapour pressure) and T is the air temperature. An equation for the mixing ratio can be derived using Equations 2.4 and 2.5:

$$r = \frac{0.622e}{p-e} \tag{2.6}$$

The specific humidity, q is used widely in atmospheric science; it is the ratio of the mass of water vapour in a volume of air to the total mass of the volume:

$$q = \frac{m_w}{m_{dair} + m_w} = \frac{r}{1+r} \tag{2.7}$$

In many applications where the absolute humidity, ρ_v is small, q can be approximated by r.

The relative humidity, RH is defined as the ratio of the water vapour mixing ratio to the saturation mixing ratio, r_s:

$$RH = \frac{100r}{r_s} \tag{2.8}$$

r_s can be approximated using Equation 2.6 and an empirical formula to derive the saturation vapour pressure with respect to water, e_{sw} such as that by Bolton (1980):

$$e_{srw}(T) \approx 6.112 \exp\left(\frac{17.67T}{T+243.5}\right) \tag{2.9}$$

where T is in degrees Celsius and e_{srw} in millibars. The saturation vapour pressure with respect to ice, e_{sri} can be approximated from e_{srw} using Rogers & Yau (1994):

$$\frac{e_{srw}}{e_{sri}} \approx \left(\frac{273}{T}\right)^{2.66} \tag{2.10}$$

where T is in Kelvin.

2.1.4.2 Temperature

The potential temperature, θ of a parcel of dry air at some altitude in the atmosphere is the temperature that the parcel would acquire if it were brought adiabatically to 1000 mb:

$$\theta = T\left(\frac{p_0}{p}\right)^{\frac{R}{c_p}} \tag{2.11}$$

where T is the temperature of the air parcel, p is the pressure of the air parcel and $p_0 = 1000$ mb, R is the gas constant for dry air (287 J kg^{-1} K^{-1}) and c_p is the specific heat of air, at constant pressure and 273 K (1005.7 ± 2.5 J kg^{-1} K^{-1} for dry air).

The virtual temperature, T_v of an air parcel is the temperature that dry air would have if its pressure and density were equal to those of a sample of moist air (Glickman, 2000):

$$T_v = T(1 + 0.61r - r_L) \tag{2.12}$$

where r_L is the mixing ratio of liquid water in the air parcel.

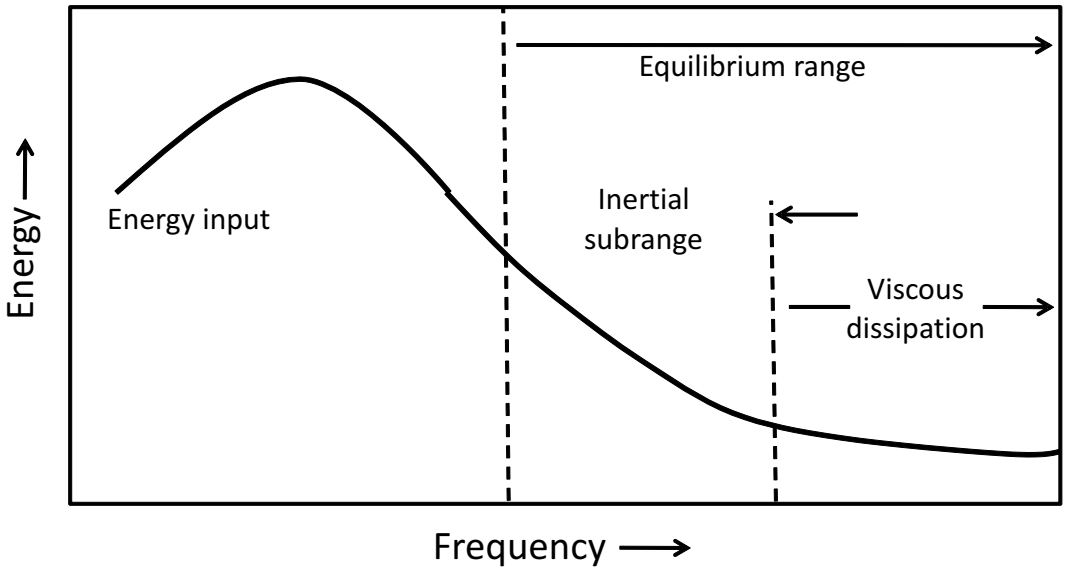

Figure 2.7: Energy spectrum of turbulence (reproduced from Garratt (1992), p17)

The virtual potential temperature, θ_v is similar to T_v and can be approximated in a similar way:

$$\theta_v = \theta(1 + 0.61r - r_L) \tag{2.13}$$

2.1.5 Turbulent fluxes

Turbulence is composed of eddies of different sizes, which are illustrated in the turbulent energy spectrum (Figure 2.7). Energy is input at the lowest frequencies via buoyant or shear processes. These eddies are unstable and eventually break up to form smaller eddies. Kinetic energy is transfered to increasingly smaller scales, in what is known as the energy cascade, until the scales become small enough for the kinetic energy to be dissipated as internal (heat) energy (Kaimal & Finnigan, 1994).

Kolmogorov (1941) developed a theory of turbulence based on the energy cascade process. He hypothesised that there is a sector of frequencies within the energy spectrum that forms the 'equilibrium range', where the direct influence of the largest eddies is lost and the eddies become isotropic. Within this sector is the inertial subrange, where frequencies are much smaller than those at which energy is input but are also much larger than the frequency scales of dissipation. In this subrange kinetic energy is not removed but is simply transfered to smaller and smaller scales until the onset of dissipation. Kolmogorov (1941) also suggested that the scale of eddies at which viscous dissipation begins can be determined by the fluid's viscosity, υ and the rate of energy dissipation, ϵ:

$$\eta = \left(\frac{\upsilon^3}{\epsilon}\right)^{1/4} \tag{2.14}$$

where η is known as the Kolmogorov length scale. Close to the surface in the atmosphere, $\upsilon = 1.5\text{x}10^{-5}$ m^2s^{-1}, $\epsilon \approx 0.01$ m^2s^{-3}, and therefore $\eta \approx 1$ mm (Garratt, 1992).

Kaimal & Finnigan (1994) show that the vertical fluxes of momentum and sensible and latent heat are almost entirely due to turbulent mixing, so can be defined using the vertical wind velocity, w. Firstly the instantaneous deviations of these quantities from the mean are computed:

$$x' = x - \overline{x} \tag{2.15}$$

where x is the measured quantity, $\overline{x}$ is the mean over a specified time and x' is the instantaneous turbulent component. Reynolds averaging allows the vertical flux of the variable x ($\overline{wx}$) to be approximated by $\overline{w'x'}$. For the quantities x and w, $x = \overline{x} + x'$ and $w = \overline{w} + w'$:

$$\begin{aligned} \overline{wx} &= \overline{(\overline{w} + w')(\overline{x} + x')} \\ &= \overline{\overline{w}.\overline{x}} + \overline{\overline{w}x'} + \overline{w'\overline{x}} + \overline{w'x'} \end{aligned} \tag{2.16}$$

Close to the surface it is assumed $\overline{w} = 0$ because there can be no flow through the surface, therefore $\overline{\overline{w}.\overline{x}} = 0$ and $\overline{\overline{w}x'} = 0$. $\overline{x'} = 0$ because the sum of the positive deviations from the mean must equal the sum of the negative deviations from the mean (Stull, 1988):

$$\overline{w}\overline{x'} = \overline{w}.0 = 0 \tag{2.17}$$

Applying this to Equation 2.16 gives:

$$\begin{aligned} \overline{wx} &= 0 + 0 + 0 + \overline{w'x'} \\ &= \overline{w'x'} \end{aligned} \tag{2.18}$$

The turbulent fluxes can be estimated from the covariances, $\overline{w'x'}$ as:

$$\tau = -\rho\overline{u'w'} \tag{2.19}$$

$$H = \rho c_p \overline{w'\theta'} \tag{2.20}$$

$$E = \rho L_v \overline{w'q'} \tag{2.21}$$

$$\tag{2.22}$$

where τ is the momentum flux, H the sensible heat flux, E the latent heat flux, ρ is air density, c_p is the specific heat of air and L_v is the latent heat of vaporisation of water.

One of the largest sources of uncertainty associated with this flux measurement technique is the sampling error. This error arises because flux measurements are highly variable by nature (Dyer & Bradley, 1982) and a small number of large eddies can dominate the flux

during a sample period (Shaw *et al.*, 1983). Typical sampling errors in flux estimates have been estimated at 12 to 31 %, depending on the variable of interest (sensible heat, CO_2 etc.) (Finkelstein & Sims, 2001). Large sampling periods increase the number of individual samples and therefore, may reduce the sampling error; but longer sample times lead to other problems, which are discussed below in more detail.

The chosen time averaging period is also important because if too long it may encompass mesoscale motions, which are not related to the local fields, causing scatter in the flux estimates (Voronovich & Kiely, 2007). If however, the averaging period is too short not all of the turbulent scales are captured, leading to an underestimation of the flux. Differentiating between these scales of motion can be especially difficult in the stable boundary layer, where turbulent fluxes are small and thus are easily affected by mesoscale motions (Mahrt & Vickers, 2006). A way of finding the optimum averaging time is by taking Fourier spectra or cospectra of the turbulence data, which illustrates the amount of kinetic energy (or eddy flux) associated with each scale of motion (Kaimal & Finnigan, 1994). Figure 2.8a shows an example of spectral energy density for $w'w'$ at each frequency scale from Arctic Ocean Experiment (AOE) 2001 observations. Kolmogorov (1941) found that in well behaved turbulence spectral energy density decreases with increasing frequency with a gradient of $-5/3$ in the the inertial subrange, which is illustrated by the red line in Figure 2.8a. Figure 2.8b shows power spectral energy density weighted by frequency, which illustrates the contribution of each frequency to the total energy. In this case the frequency of turbulent eddy with the highest contribution is at $f \approx 0.3$ s^{-1}.

Well behaved turbulence can produce a spectral gap in the frequency-weighted spectral energy density plot. This gap exists between frequencies that contribute to the energy through turbulence and frequencies that contribute through mesoscale motions. This can assist in determining the optimum averaging period. Attempts have been made to create algorithms to locate the spectral gap in order to indicate the best time averaging period, although this is challenging (Vickers & Mahrt, 2003). More recently, van den Kroonenberg & Bange (2007) were successful in using both multi-resolutional decomposition and wavelet transformations to separate the signal into different frequencies and then detected the spectral gap using an algorithm which looked for one of the following conditions; an accumulative flux that changes by less than 1 % with an increase in timescale or when the spectrum crosses zero.

Figure 2.8c shows the running integral of the spectral energy density in Figure 2.8a from high to low frequencies. This is commonly referred to as an ogive curve. For well behaved turbulence that is homogeneous and stationary this curve should approach a constant value at low frequencies, showing the point at which all the contributions to the covariances have been captured (Friehe *et al.*, 1991). This value represents the magnitude

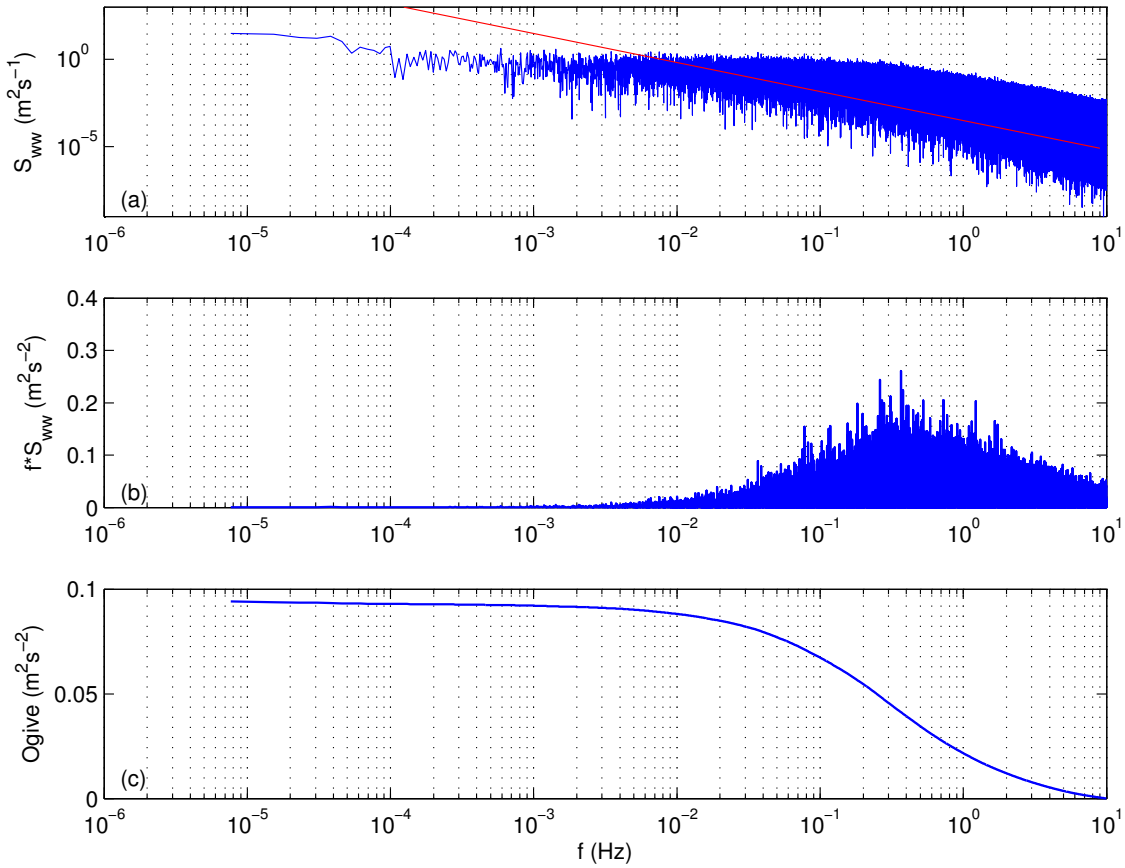

Figure 2.8: (a) Power spectral density, (b) frequency-weighted spectral energy density and (c) ogive function for $w'w'$, calculated from 24 hours of Arctic Ocean Experiment 2001 data collected on 15th August 2001. The red line in the upper panel has a gradient of $-5/3$.

of the flux. The ideal length of time averaging period is illustrated in Figure 2.8c; it is where the gradient of the curve becomes zero, since it is at this frequency that turbulent eddies cease to add to the total amount of energy in the system (Voronovich & Kiely, 2007). The curve in Figure 2.8c begins to level off at $\sim$2x10^{-3} Hz. This represents time scales of approximately 8 minutes, which is the minimum averaging period that should be used. An averaging period much longer than this (of the order hours) should not be used because only mesoscale motions add to the ogive curve at such low frequencies and would contaminate the flux calculation. A sensible choice would be 15 minutes since this is certain to capture all the turbulent frequencies, without being contaminated with mesoscale variation.

2.1.6 Similarity theory

Turbulent processes in the boundary layer are too complex to model explicitly in large-scale models therefore, a simplified method of representation is required. This is usually

in the form of parameterisations, which are observationally derived representations of complex processes using a few easily determined parameters. Most global circulation model surface flux parameterisation schemes are based on similarity theory and the flux-profile relationships.

Similarity theory is a method for finding universal relationships between variables that are made dimensionless using appropriate scaling factors (Glickman, 2000). The identity of a small number of parameters that dominate boundary-layer structure and dynamics are determined and then field or laboratory experiments are used to investigate how these variables are related to each other and how they can be assembled into dimensionless groups (Holtslag & Duynkerke, 1998).

Equations can then be fitted to the experimental data to describe the relationship between these dimensionless groups (Stull, 1988). The most widely used example is Monin-Obukhov similarity theory (Monin & Obukhov, 1954), which describes the behaviour of turbulence as a function of the Monin-Obukhov key parameters. It is only valid in the surface layer, where fluxes vary by less than 10% of their surface value allowing the charactersation of the surface layer fluxes to be simplified using the assumption that they are equal to the value of the fluxes at the surface (Stull, 1988). Monin-Obukhov similarity theory has been used extensively and has been shown to be valid for a large set of conditions.

According to the theory there are four relevant scaling parameters in the atmospheric boundary layer:

- height, z
- aerodynamic roughness length scale, z_0. Rough surfaces such as forests and urban areas have larger values ($z_0 \simeq 2$ m) than smoother surfaces such a snow covered fields ($z_0 \simeq 0.005$ m) (Stull, 2000). These lengths are not equal to the physical height of the roughness elements at the surface but they are directly related to it.
- friction velocity, u_*. Wind speed in the surface layer increases with height due to friction at the surface, producing wind shear and thus turbulence. The scaling parameter used to represent this is the friction velocity, u_*:

$$u_* = (\tau/\rho)^{1/2} = [(\overline{w'u'})^2 + (\overline{w'v'})^2]^{1/4} \tag{2.23}$$

- sensible heat flux, H (or temperature scale, θ_*). Horizontal variations in the surface heat flux produce vertical air motion and thus variations in air density, which causes turbulence via buoyant production (Holtslag & Duynkerke, 1998). The scaling

parameter θ_* is used to represent this:

$$\theta_* = -\overline{w'\theta'}/u_* \tag{2.24}$$

In addition to the four scaling parameters an analogous equation to 2.24 for the concentration of any quantity is:

$$x_* = -\overline{w'x'}/u_* \tag{2.25}$$

The Obukhov length scale (Obukhov, 1946) is applied on the assumption that a small number of parameters can describe the turbulent properties of the surface layer:

$$L = -\frac{u_*^3\theta_v}{\kappa g(\overline{w'\theta'_v})_0} \tag{2.26}$$

where κ is the von Kármán constant, which is commonly assumed to be 0.4 and $(\overline{w'\theta'_v})_0$ is the temperature flux at the surface. L is a ratio between the momentum and buoyancy fluxes and can be interpreted as the height above the surface where buoyant turbulence production equals shear production (Holtslag & Duynkerke, 1998). Equation 2.24 approximates $\overline{w'\theta'}$ with $-u_*\theta_*$, thus giving:

$$L \approx -\frac{u_*^2\theta_v}{\kappa g\theta_*} \tag{2.27}$$

This, along with the final scaling parameter, z is used to compute the stability parameter, ζ:

$$\zeta = z/L \tag{2.28}$$

In neutral stratification $\zeta \equiv 0$, in stable stratification $\zeta > 0$ and in unstable conditions $\zeta < 0$. The greater the magnitude of ζ the more (un)stable the atmosphere is.

2.1.6.1 The flux-profile relationships

In the neutral surface layer the wind speed generally increases logarithmically with height due to frictional drag at the surface (Figure 2.9). If the atmosphere is stably stratified the wind profile is more linear due to lower wind speeds near the surface but a more rapid increase with height above this. In an unstable atmosphere however, winds near the surface are stronger but the gradient is smaller. Dimensional analysis can be performed for the neutral case on observational data similar to that in Figure 2.9. In addition to z and U, it is assumed that the relevant variables are a measure of turbulence intensity, u_* and of the surface roughness, z_0 (Stull, 1988). These variables are used to fit a function

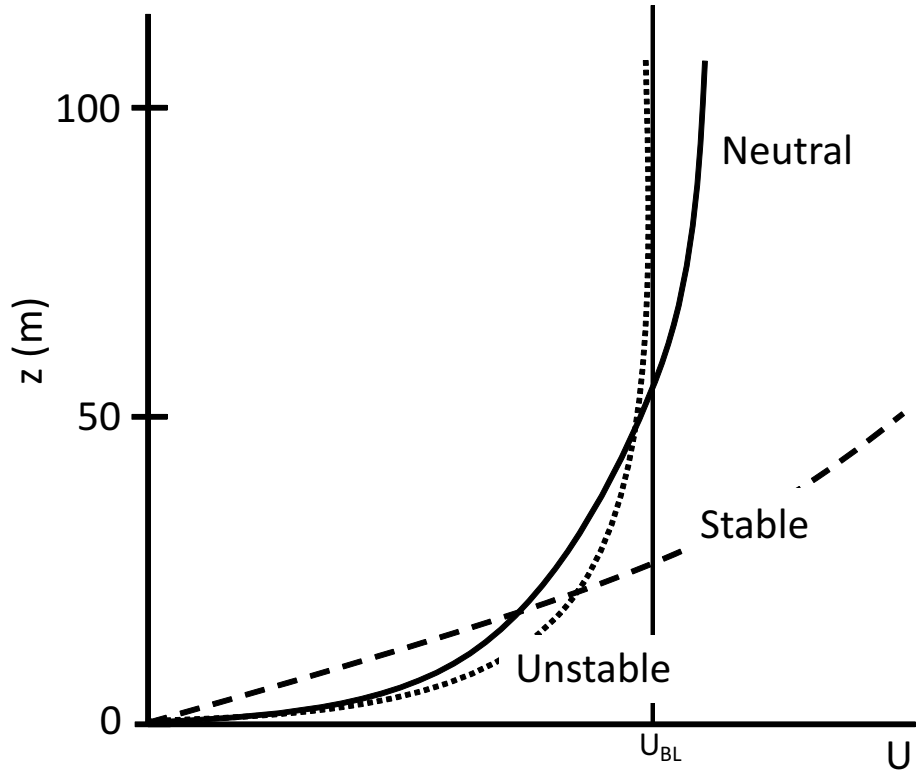

Figure 2.9: Wind speed profiles in stable, neutral and unstable surface layers. U_{BL} is the average boundary-layer wind speed (adapted from Stull (2000) p.77).

to field observations; the result of this analysis is the 'log wind' profile:

$$U = \frac{u_*}{\kappa} ln\left(\frac{z}{z_0}\right) \tag{2.29}$$

This relationship describes how wind speed is related to height in the neutral surface layer. The flux-profile relationships (Monin & Obukhov, 1954) describe how the wind speed profile varies in stabilities other than neutral and how other variables such as temperature and humidity vary with height:

$$\frac{dU}{dz} = \frac{u_*}{\kappa z}\varphi_m(\zeta) \tag{2.30}$$

$$\frac{d\theta}{dz} = \frac{\theta_*}{\kappa z}\varphi_h(\zeta) \tag{2.31}$$

In addition to this, the less widely used equivalent for the humidity gradient is (Large & Pond, 1982):

$$\frac{dq}{dz} = \frac{q_*}{\kappa z}\varphi_q(\zeta) \tag{2.32}$$

$\varphi_m(\zeta)$, $\varphi_h(\zeta)$ and $\varphi_q(\zeta)$ are the non-dimensional universal stability functions. The exact form of these functions is not predicted by similarity theory and must be determined

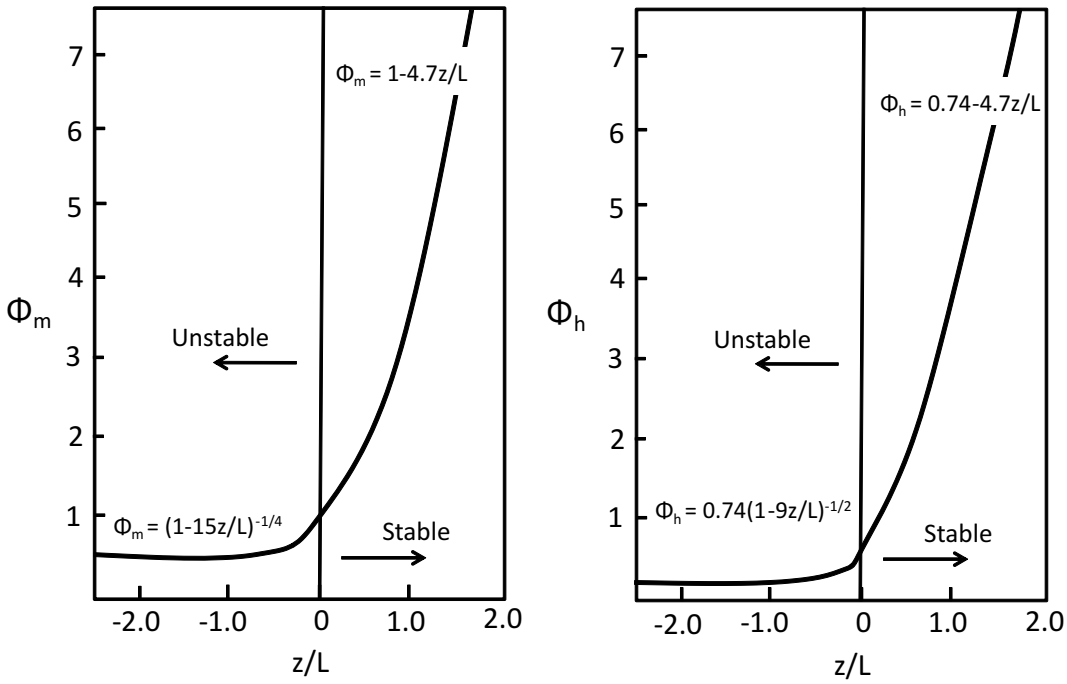

Figure 2.10: φ_m and φ_h from observations at a range of stabilities (reproduced from Stull (1988), p.384; observations from Businger *et al.* (1971))

by measurement (Grachev *et al.*, 2007). Businger *et al.* (1971) and Dyer (1974) used observations to independently estimate the forms of the stability functions, subsequently called the Businger-Dyer relations. They calculated φ_m, φ_h and z/L using Equations 2.26, 2.30 and 2.31 and then fitted functions to the data (Figure 2.10):

$$\left.\begin{aligned} \varphi_m &= 1 + \frac{4.7z}{L} \\ \varphi_h &= \frac{K_m}{K_h} + \frac{4.7z}{L} \end{aligned}\right\} \qquad z/L > 0 \tag{2.33}$$

$$\left.\begin{aligned} \varphi_m &= 1 \\ \varphi_h &= \frac{K_m}{K_h} \end{aligned}\right\} \qquad z/L = 0 \tag{2.34}$$

$$\left.\begin{aligned} \varphi_m &= \left(1 - \frac{15z}{L}\right)^{-\frac{1}{4}} \\ \varphi_h &= \frac{K_m}{K_h}\left(1 - \frac{9z}{L}\right)^{-\frac{1}{4}} \end{aligned}\right\} \qquad z/L < 0 \tag{2.35}$$

where K_m/K_h is the ratio of eddy diffusivities for heat and momentum, which was found to be 0.74 in neutral conditions (Stull, 1988).

The Businger-Dyer relations are only one of the many suggested forms of the functions.

Yaglom (1977) present a comprehensive list of suggested forms which are based on extensive and reliable observational data. There is still no consensus as to which is the true form of these functions because every new set of field measurements produces a slightly different result. Part of this uncertainty is probably due to instrumental error but the other reason is that strictly, Monin-Obukhov similarity theory only holds for idealised conditions that in reality are never fully satisfied (Yaglom, 1977). It assumes horizontally homogeneous, flat terrain, which even at the most ideal sites is never completely obtained, leading to biased results. For the theory to be valid the atmosphere must depend on the local scaling parameters and not on the history of the upstream flow or large-scale atmospheric motion (Arya & Sundararajan, 1976). It also assumes there is a surface layer and that the fluxes are constant within it. Grachev *et al.* (2005) showed that these conditions do not always occur, especially under strong static stability, which is discussed in the following section. Examples where Monin-Obukhov similarity theory may fail are:

- a rapidly developing boundary-layer episode such as the morning transition period. In this situation the surface layer is changing and thus does not depend solely on the local parameters (Arya & Sundararajan, 1976).
- convective conditions with light winds and horizontally heterogeneous strong daytime heating over land that generates turbulence. This transports momentum and thus alters wind shear and the vertical wind profiles (Holtslag & Duynkerke, 1998).

2.1.6.2 Flux-profile relationships in the stable boundary layer

Applying similarity theory to the stable boundary layer is particularly challenging because measurements are difficult due to the weak and intermittent nature of the turbulence. The surface layer may contain processes such as gravity waves, inertial oscillations and density currents, which change the vertical wind gradients and continually modify turbulent structure (Mahrt, 2007). Until recently only two stable boundary-layer regimes were defined; the very stable and the weakly stable boundary layers (Mahrt, 1998).

Grachev *et al.* (2005) used data from the Surface Heat Budget of the Arctic Ocean (SHEBA) Experiment (see Section 2.3.1) to classify the stable boundary layer into 4 scaling regimes. The first is the weakly stable regime ($0 < \zeta < 0.1$), where τ and H are approximately constant with height and the surface layer is governed by traditional Monin-Obukhov similarity theory. The next regime is the transition regime ($\zeta > 0.1$), in which the constant-flux layer breaks down but turbulence is still continuous and thus similarity theory remains adequate. The very stable boundary layer is split it into two regimes, the turbulent Ekman layer and the intermittently turbulent Ekman layer. In

the turbulent Ekman layer ($Ri_B < Ri_c$) the turbulent fluxes are small and no longer constant with height therefore, similarity theory ceases to be valid. Grachev *et al.* (2005) showed from observations in the very stable regimes that the flow becomes sensitive to the Earth's rotation because turbulent mixing ceases to cancel out changes in wind direction with height caused by the Coriolis force. In the intermittently turbulent Ekman layer ($Ri_B > Ri_c$) turbulence collapses, fluxes vanish and the Coriolis force has a large effect, producing observable Ekman spirals.

The Businger-Dyer relations are still the most widely and routinely used forms of the stability functions in the unstable case but other alternatives for stronger stability have been suggested, such as those by Holtslag & De Bruin (1988) and Beljaars & Holtslag (1991). Under stable conditions field experiments have shown that both φ_m and φ_h increase more slowly with increasing stability than predicted by the Businger-Dyer relationships (Howell & Sun, 1999). It has been suggested that the simple linear form of φ_m and φ_h (Equation 2.33) is only valid in moderate stabilities ($0 < z/L < 1$) and can only be used to blend between the neutral and very stable case (Businger *et al.*, 1971; Dyer, 1974).

Under very stable conditions ($z/L >> 0$), $4.7z/L$ in Equation 2.33 becomes large compared with K_m/K_h. Equating this with Equation 2.31 gives:

$$\varphi_h = \frac{\kappa z d\theta/dz}{\theta_*} = \frac{4.7z}{L} \tag{2.36}$$

Eliminating z then gives:

$$\frac{\kappa d\theta/dz}{\theta_*} = \frac{4.7}{L} \tag{2.37}$$

This produces a relationship between the heat flux and the potential temperature gradient that is independent of z; termed 'z-less' stratification (Wyngaard & Coté, 1972; Hicks, 1976; Nieuwstadt, 1984). This occurs when turbulence is constrained by a lack of buoyancy in the very stable atmosphere, causing vertical motion to cease so turbulence does not communicate with the surface and becomes independent of height, such that $\varphi_m \propto \varphi_h \propto \zeta$ (Monin & Yaglom, 1971; Mahrt, 1998).

2.1.7 Surface flux parameterisation schemes

It is necessary for numerical models to predict the turbulent surface fluxes (τ, H and E) in order to represent surface-atmosphere interactions (Andreas *et al.*, 2005). This is achieved through bulk flux algorithms, which generally employ Monin-Obukhov similarity theory to determine the fluxes from the difference in the bulk variables between the surface and first atmospheric layer. Most of the parameterisation schemes in both regional and global

scale models are based loosely on a scheme by Louis (1979):

$$\tau = \rho u_*^2 = \rho_r C_{Dr} U_r^2 \tag{2.38}$$

$$H = \rho_r c_p u_* \theta_* = \rho_r c_p C_{Hr} U_r (T_s - \theta_r) \tag{2.39}$$

$$E = \rho_r L_v u_* q_* = \rho_r L_v C_{Er} U_r (q_s - q_r) \tag{2.40}$$

where U_r, θ_r and Q_r are the values of wind speed, potential temperature and specific humidity at reference height r. T_s is the surface temperature and q_s the surface specific humidity, which is assumed to be the saturation humidity with respect to ice at T_s over ice surfaces (Andreas *et al.*, 2005). C_{Dr} is the drag coefficient and C_{Hr} and C_{Er} the transfer coefficients at height r. They are a function of the roughness of the surface and atmospheric stability:

$$C_{Dr} = \frac{\kappa^2}{[ln\left(\frac{z}{z_0}\right) - \varphi_m(z/L)]^2} \tag{2.41}$$

$$C_{Hr} = \frac{\kappa^2}{[ln\left(\frac{z}{z_0}\right) - \varphi_m(z/L)][ln\left(\frac{z}{z_t}\right) - \varphi_h(z/L)]} \tag{2.42}$$

$$C_{Er} = \frac{\kappa^2}{[ln\left(\frac{z}{z_0}\right) - \varphi_m(z/L)][ln\left(\frac{z}{z_q}\right) - \varphi_h(z/L)]} \tag{2.43}$$

where z_0, z_t and z_q are the aerodynamic roughness lengths of momentum, heat and humidity respectively.

Many studies have attempted to define these values for different categories of surface types. Andreas *et al.* (2005) used data from an ice station in the Weddell Sea to investigate the roughness lengths over snow-covered sea ice. They found their data did not support the common assumptions in models that $z_t = z_q = z_0$ and that they are constant values over a particular surface type. In fact, they found that the roughness lengths vary with u_* and as the roughness of the surface increases, z_0 increases but z_t and z_q decrease. Accurately determining and using these roughness lengths in model parameterisations remains a challenge for boundary-layer meteorologists.

2.2 Arctic climate

2.2.1 Recent trends

Recent evidence has shown that temperatures in the Arctic are rising at almost twice the rate of the global average (Solomon *et al.*, 2007) and that this increase is accompanied by a decrease in both sea ice thickness and extent (Parkinson *et al.*, 1999; Nghiem *et al.*, 2007; Comiso *et al.*, 2008; Parkinson & Cavalieri, 2008). This trend is predicted to continue and probably increase in the future (Holland *et al.*, 2006) and is partly due to processes such as the ice-albedo feedback (Curry *et al.*, 1996). Processes that occur in the Arctic are linked to both global ocean and atmospheric circulation (Graversen, 2006) and thus changes to the climate system over the central Arctic Ocean are expected to have a major impact elsewhere. There is mounting evidence that sea ice extent influences weather patterns in the Northern Hemisphere (Deser *et al.*, 2007; Alexander *et al.*, 2004; Bhatt *et al.*, 2008) by processes such as the warming and destabilisation of the lower troposphere and increased cloudiness (Francis *et al.*, 2009). Honda *et al.* (2009) linked low August sea ice extents to cold anomalies over Eurasia during the following winter and Chapman & Walsh (2007) suggest that a decrease in sea level pressure over the Bering Strait could cause a northward shift in the Pacific storm track, impacting the nearby coastal areas.

Effects on marine primary production have been observed by Arrigo *et al.* (2008), who show that over recent years primary production in the Arctic Ocean has increased due to a decreased August sea ice minimum and a longer phytoplankton growing season. Loss of sea ice has also been linked to increased warming of the land masses in the Western Arctic (Lawrence *et al.*, 2008). This is likely to cause permafrost degradation (Jorgenson *et al.*, 2006) and changes have already been observed in the tree line extent, growing season of vegetation and ranges of migratory birds (Hinzman, 2005).

2.2.2 2007 record sea ice minimum

Arctic sea ice reached a record low in September 2007, when the extent was reduced to 24% less than the previous record low in 2005 and 37% less than the climatological average (Comiso *et al.*, 2008). It is evident from Figure 2.11 that most of the ice loss was from the Pacific side of the basin.

The cause of the record minimum was not immediately clear. Schweiger *et al.* (2008) and Kay *et al.* (2008) suggested it could be explained by anomalously high pressure over the Beaufort Sea and an associated decrease in cloud cover that caused an increase in the

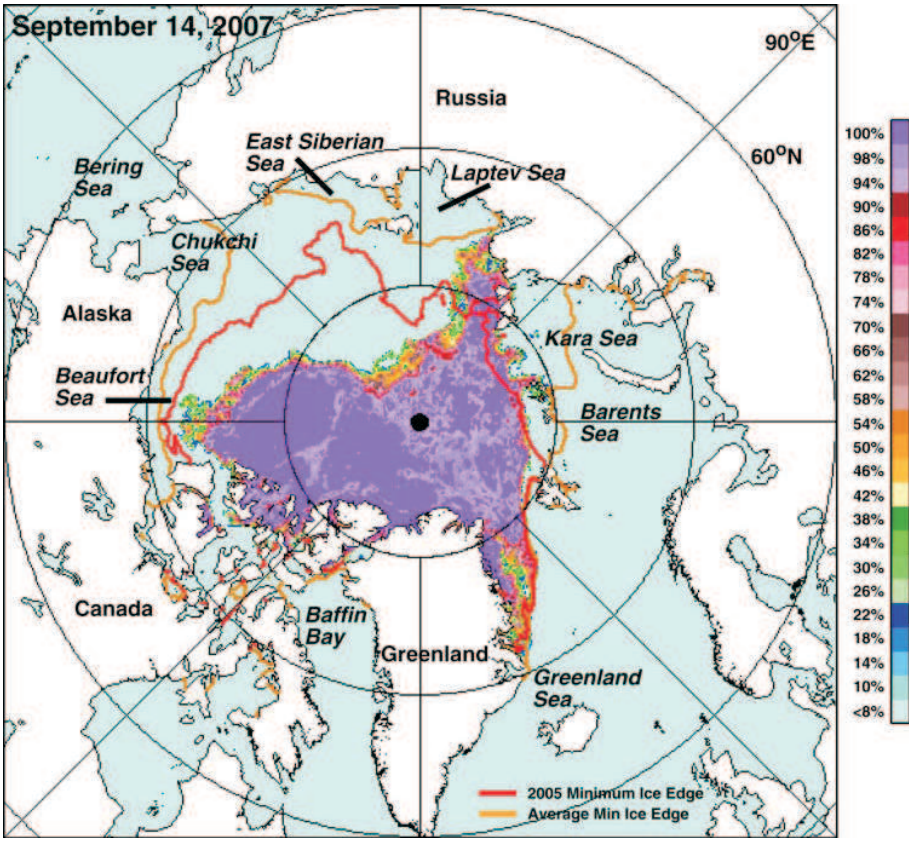

Figure 2.11: Sea ice concentration from the Advanced Microwave Scanning Radiometer for the Earth Observing System (AMSR-E) over the Arctic on 14 September 2007 (taken from Comiso *et al.* (2008)). The gold line represents the average sea ice extent for this date over the period 1979-2006 and the red line represents the previous record low ice extent in 2005.

downwards shortwave surface radiation flux. Having said that, despite the cloud cover being two standard deviations lower than the 1980-2007 average, it was not anomalous in the 62 year record (Kay *et al.*, 2008). Unusually high surface air (Comiso *et al.*, 2008) and ocean temperatures (Steele *et al.*, 2008) were also recorded but it is not clear if these caused the reduced sea ice or were a response of it. A second theory is that the persistent high pressure over the Beaufort Sea caused anomalous southerly winds during the summer of 2007, which blew from East Siberia towards the Pacific (Maslanik *et al.*, 2007). This produced the largest rate of ice mass advection from the Pacific to Atlantic sectors between 2003-2007 and pushed ice out of the central Arctic, into the Greenland Sea (Zhang *et al.*, 2008; Kwok, 2008).

Lindsay *et al.* (2009) report that even though the 2007 sea ice extent was anomalous, the total loss of ice mass was not compared to the last 20 years. Gradual preconditioning of the climate for such a rapid decrease could be due to the gradual decline of thick, perennial ice (Nghiem *et al.*, 2007; Maslanik *et al.*, 2007), wind induced changes to ice distribution (Rigor & Wallace, 2004), increased heat transfer from lower latitudes via

the ocean (Shimada *et al.*, 2006) or the atmosphere (Serreze *et al.*, 2007) and a greater absorption of shortwave radiation at the surface due to decreased sea ice fraction and thus surface albedo (Perovich *et al.*, 2007). Due to complicated feedback mechanisms in the Arctic climate system it is not clear what the relative importance of the suggested ice loss mechanisms were for the 2007 record minimum. It is most likely that this preconditioning of the ice over a number of decades left the ice vulnerable (Holland *et al.*, 2006; Deser & Teng, 2008) and this, coupled with the anomalous atmospheric conditions of 2007 (that were still within the bounds of normal natural variability) caused the record ice minimum of 2007. What is more concerning is that only perennial sea ice is thick enough to survive the warm summer months and thus several years of colder than average temperatures are required for the ice to completely recover to conditions observed in the early 1980's (Comiso *et al.*, 2008). Considering current future predictions of Arctic climate, this seems increasingly unlikely.

2.2.3 Future climate

Results from the Intergovernmental Panel on Climate Change (IPCC) Atmosphere-Ocean General Circulation Model (AOGCM) ensemble simulations suggest an increase in Arctic annual mean air temperature of 5 °C by the end of the 21st century; this is the largest magnitude of warming predicted for any region on the planet (Solomon *et al.*, 2007). Similar trends were found by Holland & Bitz (2003), who used 15 coupled Atmosphere Ocean General Circulation Models to examine the amplification of warming over the pole. Most of the models suggested warming between two and three times the global mean. Projections from the Community Climate System model suggest that abrupt changes in the Arctic environment are likely in the 21st century due to the ice-albedo feedback and heat transportation from further south, possibly leading to ice-free summers by the end of the century (Holland *et al.*, 2006); although largely depleted summer ice extents are expected within 40 years (Chapman & Walsh, 2007; Smeets & van den Broeke, 2008; Wang *et al.*, 2009).

Multi-model representation of sea ice extent between 1981-2000 agrees well with observations but even for these present day simulations there are large differences between each model (Arzel *et al.*, 2006). Some models show more advanced warming in the near future, whereas others do not display such extreme ice thinning and retreat until closer to the end of the 21st century (Serreze & Francis, 2006). All models within an ensemble predict ice free summers and significant temperature increases at some point in the future, even if there is no consensus as to the timing and spatial pattern of these changes. Since these

ensembles are currently our best indicator of the future it is vital to improve our knowledge and model simulations of the region in order to produce more reliable predictions of the timing of future changes.

2.3 Conditions in the central Arctic during the summer melt and early freeze-up period

2.3.1 Recent field observations

There have been a number of recent field campaigns to the Arctic that have focused, at least in part, on cloud structure and the boundary layer. The Beaufort and Arctic Storms Experiment (BASE) (Curry *et al.*, 1997) measured surface, cloud and boundary-layer properties in the Arctic via aircraft flights during Autumn 1994 in the Southern Beaufort Sea. The First ISCCP (International Satellite Cloud Climatology Project) Regional Experiment (FIRE) took place between April and July 1998, off the North coast of Alaska (Curry *et al.*, 2000). It studied Arctic cloud systems in spring and summer, with an aim of understanding how clouds affect atmospheric radiation exchange and how the surface influences boundary-layer clouds. The Surface Heat Budget of the Arctic Ocean experiment (SHEBA) (Uttal *et al.*, 2002) acquired comprehensive observations on drifting ice between 74 and 81°N over an entire year between October 1997 and October 1998. This campaign provided the first set of measurements from a wide range of disciplines ever obtained over an entire annual cycle in the central Arctic Ocean.

There have been three field campaigns to the central Arctic in a series of Swedish-led expeditions: International Arctic Ocean Expedition (IAOE) 1991 (Leck *et al.*, 1996), Arctic Ocean Experiment (AOE) 1996 (Leck *et al.*, 2001) and AOE 2001 (Tjernström *et al.*, 2004a). The primary objective of the 1991 campaign was to test the hypothesis that marine biogenically produced dimethyl sulphide (DMS) can modify cloud condensation nuclei and thus cloud properties. AOE-96 took place in the central Arctic Ocean during July to September with the main aim of improving knowledge of the indirect effect of aerosols on regional climate through the study of aerosol sources, formation and growth processes. AOE 2001 was the third project in the series, in which more emphasis was placed on summer boundary-layer structure and the surface energy budget. The Arctic Summer Cloud-Ocean Study (ASCOS) took place in August and September 2008 and encompassed marine biology, atmospheric chemistry and aerosol, oceanography and meteorology measurements with the aim of understanding the formation and persistence of Arctic summertime clouds. The two most recent experiments, AOE 2001 and ASCOS are discussed in detail in Chapter 3.

2.3.2 Structure of the lower atmosphere

The central Arctic Ocean is a unique environment, with a surface consisting of sea ice and open leads and which experiences near constant daylight during the summer months and darkness during winter. The summer boundary layer is sometimes weakly stable (Persson *et al.*, 2002b) but often well-mixed through its upper part and cloud layer, with a shallow stable surface layer (Tjernström *et al.*, 2004a). Near-surface temperatures are relatively constant, between -1.7 and 0 °C, due in large part to latent heat processes that act as a buffer against energy entering or leaving the surface. The near-surface humidity is high and always near ice saturation due to sublimation of ice at the surface and the high emission rate of water vapour from open leads compared with the low rate of removal by the ice surface (Andreas & Hicks, 2002). The lower atmosphere is therefore most often cloudy, with a stratus cloud base commonly at around 100 m (Tjernström *et al.*, 2004a). Strong capping inversions sometimes occur due to the advection of warm and relatively humid air aloft. Contrary to behaviour at lower latitudes, it is possible that this also contributes to the high near-surface humidity and to cloud development and persistence in the boundary layer because entrainment will act as a source of boundary-layer moisture (Pinto, 1998). Multiple cloud layers with a temperature inversion associated with each of them, are also common (Intrieri *et al.*, 2002; Tjernström *et al.*, 2004a). Cloud top is often found within the inversion, rather than below it, which is in contrast to low latitude marine stratocumulus, where cloud top sits at the base of the inversion (Tjernström, 2005; Sedlar & Tjernström, 2009).

2.3.3 Clouds

Studies have shown that in spring and autumn, Arctic clouds generally consist of both ice and water (Curry *et al.*, 1990, 1997; Gultepe *et al.*, 2000; Shupe *et al.*, 2006). During the Mixed-Phase Arctic Cloud Experiment (M-PACE) in October 2004 Verlinde *et al.* (2007) observed liquid water in clouds at temperatures as low as -30 °C and that the microphysical properties of an air mass can change significantly with small changes in synoptic flow. In the summer months however, liquid-only clouds dominate, although mixed-phase clouds are present some of the time (Herman & Curry, 1984; Sedlar & Tjernström, 2009).

Although the central Arctic Ocean experiences near constant daylight during the summer months, Tjernström (2007) found a statistically significant diurnal cycle in many parameters during the summer season. A weak diurnal temperature variation associated with the relative humidity cycle was found, along with an obvious peak in the sensible heat flux around noon due to the maximum in solar radiation. The diurnal cycle in cloud

is in strong contrast to that found in marine stratocumulus at lower latitudes, described in Section 2.1.3. At lower latitudes turbulent mixing is at a maximum during the day and drizzle is most frequent during late night and early morning (Holtslag & Duynkerke, 1998; Duynkerke & Coauthors, 2004; Tjernström & Rune, 2003). Although the sun is constantly above the horizon in the Arctic during mid-summer, Tjernström (2005) suggests from AOE 2001 observations that radiation is not strong enough to evaporate cloud during the afternoon. This means Arctic cloud may behave like a nighttime cloud at lower latitudes, with peaks in cloud fraction during the early morning and just before noon and drizzle most common in the afternoon. Tjernström (2007) found that in the morning the cloud layer is constant and well-mixed by cloud-top cooling but the air below this is decoupled from the cloud layer and mixing does not reach the surface.

There is very limited understanding of the processes that control the formation and persistence of low-level Arctic clouds. There are two main hypotheses for the formation of these types of clouds. The first suggests that the clouds have a good local source of moisture and aerosol, either from open leads (Curry *et al.*, 2000) or by entrainment into the boundary layer from the free troposphere, where the air is at least as moist as it is in boundary layer (Tsay & Jayaweera, 1984). The second suggested mechanism for cloud formation is by advection, due to spatial differences in boundary-layer conditions and frontal activity. Wang & Wang (2004) compared a cloudy and clear Arctic boundary-layer case using BASE data and found several cloud layers were present in the cloudy case that were not horizontally homogeneous, suggesting local cloud formation in air with horizontally homogeneous vertical temperature profiles. They suggest cloud formation can be caused by only small changes in air mass properties because the lower atmosphere is near saturated even during clear periods. Curry & Herman (1985b) also suggest that cloud in the Arctic is caused by low-level advection of moisture and cooling due to radiation and boundary-layer turbulence. Low clouds could be sensitive to frontal systems (Curry & Herman, 1985a; Nilsson & Bigg, 1996), which form as warm, moist air from the more southerly ocean is advected over the colder ice surface and cools to form clouds.

2.3.4 Radiation

It is important to understand the radiative properties of Arctic clouds because they are the single most important factor influencing the surface energy budget (Curry *et al.*, 1996). The effects Arctic clouds have on radiation are complex and are different to those at lower latitudes. This is due to the lack of downwelling shortwave radiation in winter, the presence of strong inversions, low air temperatures and low concentrations of aerosol and water vapour (Curry *et al.*, 1996; Verlinde *et al.*, 2007). In addition, the albedo of

the ice surface is high and similar to the cloud top albedo, minimising the effect cloud has on the total amount of shortwave radiation that is reflected back to space.

Shupe & Intrieri (2004) used SHEBA observations to determine what properties of Arctic clouds control the surface radiation budget. They show that low-level stratiform liquid and mixed phase clouds are the most important for surface radiation, whereas cirrus and diamond dust play only a small part. Longwave cloud forcing was dependent on cloud temperature, height, emissivity and liquid water path (LWP). Clouds warmed more by longwave radiation with increasing LWP, up to LWP approximately 20-50 gm^{-2}, where the cloud begins to behave as a black body and thus the absolute amount of water in the cloud becomes of less importance. Clouds cool the surface increasingly more effectively in the shortwave as the surface albedo and solar zenith angle decrease. There is general agreement that stratiform clouds over the central Arctic Ocean have an overall warming effect on the surface, except for a few weeks in midsummer, when the amount of incoming shortwave radiation is at a maximum, the surface albedo is at its lowest and shortwave cloud cooling outweighs the longwave cloud warming (Shupe & Intrieri, 2004; Curry & Ebert, 1992; Intrieri *et al.*, 2002; Nilsson *et al.*, 2001). This is in contrast to marine stratocumulus clouds over lower latitudes, which have an overall cooling effect (Harrison *et al.*, 1990).

Predictions of how cloud radiative forcing may change in the future are complicated because it is uncertain how the clouds themselves might change. Beesley *et al.* (2000) suggest that if the amount of low level cloud increases an overall cooling effect would be observed, whereas if the amount of high cloud increases there would be an overall warming effect because high clouds absorb more radiation than they reflect. Intrieri *et al.* (2002) compared clear-sky and cloudy days using a model and SHEBA data and found the overall difference in radiative forcing between clear and cloudy skies is much greater in summer than winter. This means that any cloud property or coverage changes in the future will have the most effect on the radiation budget during the summer months.

2.4 Models and parameterisations

Due to the sub-grid scale of many physical processes in the Arctic, they cannot be explicitly simulated in models and parameterisations are required to simplify the relationships between important variables. Data sets to quantify these relations are generally acquired through analysis of observations however, very few data sets are available for the central Arctic region because data acquisition is so difficult. No airports are in close enough proximity to allow comprehensive measurements from aircraft; surface measurements are difficult because there is no land mass on which to place instruments, winters are long,

dark and cold and satellite measurements are problematic because the differences between the temperature and albedo of the ice surface and the clouds are small (Curry *et al.*, 1996). In addition, a gap in satellite data exists directly over the north pole because polar orbiting satellites often take a slightly off-polar track. The general lack of knowledge and data from the region has limited the development of Arctic specific parameterisations and consequently most are based on data from lower latitudes (Curry *et al.*, 1996). Since the central Arctic ocean is such a unique environment, these parameterisations are not necessarily valid at such high latitudes.

2.4.1 Basic meteorological fields

Several evaluations of model performance over the central Arctic Ocean show that although the surface pressure and wind fields are generally reasonably well represented, near-surface air temperature is problematic. The IPCC Fourth Assessment Report (AR4) global model simulations reproduce the annual mean and seasonal cycle in air temperatures over the Arctic Ocean reasonably well, although the interannual variability and decadal trend varies significantly and the work suggests that the simulation of sea ice is an important factor (Liu *et al.*, 2008). Walsh *et al.* (2002) also assessed simulations of the present day Arctic climate from a number of coupled and uncoupled atmospheric models with gridded observational data from various sources and some near-surface air temperature and pressure data from the National Centers for Environmental Prediction (NCEP) reanalyses. They also found large across-model scatter in the coupled models due to the variance in sea ice coverage. The uncoupled models were warmer in winter because they did not simulate the formation of thin ice over leads, causing upwards heat fluxes from the open water to be too high. Large differences between observed and modelled 2 m air temperature were also found in the European Centre for Medium-Range Weather Forecasts (ECMWF) forecast model using observations from SHEBA during November and December even though the synoptic scale dynamics were accurate because the model was initialised with radiosonde observations from the SHEBA site (Beesley *et al.*, 2000). The study suggests these errors are again due to the interaction of the atmosphere with the ice surface. Sea ice in the model at that time is treated as a snow free isothermal slab and the large heat capacity of this ice has the potential to dampen temperature changes much more than in reality.

Reanalysis products are used extensively in Arctic research to diagnose climate trends, to develop models and to initialise and constrain model simulations. Makshtas *et al.* (2007) used observational data from the Soviet 'North Pole' drifting stations to evaluate the National Center for Atmospheric Research/National Centers for Environmental Prediction (NCAR/NCEP) reanalysis data. They found that the surface level pressure

is good and the wind is satisfactory but air temperature is underestimated by the model in autumn and overestimated in spring and summer. The specific humidity and cloud cover also show large errors, especially in summer. It is likely that some of the errors produced by regional and global climate models that are forced by the reanalysis data are an artifact of the reanalysis data, rather than the climate model that is forced by them. Unfortunately the source of these errors is often hard to identify and it is therefore important to acquire good quality, reliable observations over the Arctic to reduce the emphasis on reanalysis data.

2.4.2 Surface turbulent fluxes

Tjernström *et al.* (2005) used data from the SHEBA campaign to evaluate 6 regional climate models in the Arctic Regional Climate Model Intercomparison Project (ARCMIP). They found that the turbulent momentum flux was mostly quite reliable but the sensible and latent heat fluxes showed no significant correlation to the observations, and that the variability between and within each model was very large compared to the variability in the observations. Although the magnitudes of the fluxes themselves are relatively small and thus the model errors are small in an absolute sense, the surface net heat flux is of a similar magnitude to the turbulent flux errors and so even these small errors are significant. The models showed particular bias in the sensible heat flux under stable conditions and the latent heat fluxes, unlike the sensible heat fluxes were significantly overestimated by all the models. The authors were unable to deduce an explanation for this.

Brunke *et al.* (2006) evaluated bulk aerodynamic algorithms from 4 models using observations from the SHEBA campaign. All four schemes are based on that proposed by Louis (1979), using mean wind speed and vertical differences in temperature or humidity to compute the surface fluxes (see Section 2.1.7). The main difference between the schemes is in the method used to compute the turbulent exchange coefficients, which are functions of various roughness lengths and representations of stability. Although monthly averages of wind stress, sensible and latent heat were found to be mostly within one standard deviation of the mean observation, their magnitudes were generally too high. During the summer months the magnitude of modelled latent heat fluxes are much higher than those observed, in agreement with the findings of Tjernström *et al.* (2005) and although the bias in the sensible heat flux is smaller, it is still not satisfactory. The different fluxes show different accuracies over different stability regimes. Modelled sensible heat and wind stress were found to be more accurate in unstable and weakly stable regimes and the least accurate in stable regimes.

2.4.3 Clouds and radiation

To accurately simulate the surface radiation budget, careful representation of cloud radiative properties is crucial. Having said that, correct cloud radiative properties only produce accurate surface radiation fluxes when cloud occurrence is well represented. Chen *et al.* (1995) found that models studied during the Atmospheric Intercomparison Project (AMIP) produced significantly different total cloud fraction over the Arctic Ocean during all months of the year. Curry *et al.* (2000), Beesley *et al.* (2000) and Walsh *et al.* (2002) report that the most significant cause of model surface radiation flux errors is the misrepresentation of cloud occurrence. Walsh *et al.* (2009) also show using observations from Barrow, Alaska that in four reanalysis models the primary reason for the errors in summertime surface radiation fluxes is the underestimation of cloud fraction, rather than biases caused by the cloud microphysics.

A study by Tjernström *et al.* (2008) showed that a number of regional scale models produced clouds that were too low and physically too thin and that the occurrence of low cloud water paths was overestimated, causing the downward longwave radiation flux to be too low in summer. The downward shortwave flux was also underestimated in both clear and cloudy conditions. In cloudy conditions the attenuation of solar radiation is too large for a given cloud water path and the authors speculate that this could be due to an overestimation of cloud optical thickness for a given cloud water path due to the low aerosol concentrations that occur in the Arctic compared to lower latitudes (Bigg, 1996; Jiang & Cotton, 2000). In clear conditions the reason could be similar, that the clear sky aerosol attenuation rate is overestimated because it is based on data from lower latitudes.

2.4.4 Cloud microphysics

A range of microphysics schemes with various degrees of complexity are used in weather and climate models. The least complex parameterisations incorporate a single-moment scheme with temperature dependent partitioning, in which a single variable for the mass of cloud condensate is diagnosed and a temperature function is used to partition the ice and liquid cloud water ratio. More sophisticated schemes predict both liquid and ice masses and the number concentrations of cloud particles, which allows cloud and aerosol processes to be coupled within the model.

It is important for climate models to accurately represent the relative amounts of liquid and frozen water in clouds because cloud phase is closely tied to cloud radiative properties (Sun & Shine, 1994; Pinto, 1998; Gayet *et al.*, 2002), cloud lifetime and precipitation

(Jiang & Cotton, 2000). Liquid water clouds emit more downwelling longwave radiation because they are optically thicker than ice clouds (Prenni *et al.*, 2007) and therefore, errors in the phase partitioning of cloud water in climate models can have a large impact on 21st century Arctic climate predictions (Gorodetskaya *et al.*, 2008).

Microphysical processes in Arctic clouds are not well understood due to a lack of in-situ observations (Vavrus, 2004) and parameterisations are rarely Arctic specific. The phase of water in a cloud depends largely on what aerosol is available to act as cloud condensation nuclei. The concentrations of ice nuclei in the Arctic atmosphere are much lower than those at lower latitudes (Bigg, 1996; Jiang & Cotton, 2000) and the aerosol concentrations are highest aloft due to long range transport and lower level scavenging by boundary-layer clouds (Curry *et al.*, 2000). It has been shown through modelling studies that Arctic clouds are very sensitive to the number of ice nuclei available to the cloud (Morrison *et al.*, 2005; Jiang & Cotton, 2000) and its parameterisation in the Arctic is a particular problem in regional and global climate models (Prenni *et al.*, 2007).

Klein *et al.* (2009) and Morrison *et al.* (2009) evaluated simulations of single and multi-layered clouds from a variety of highly constrained single column and cloud-resolving models using case studies from M-PACE. They found that as the sophistication of the microphysics schemes increased, agreement between the modelled and observed liquid and ice water paths was generally better. In the single cloud case, IWP was well represented but LWP was underestimated by a factor of three, which is in agreement with the findings of Curry *et al.* (2000), Inoue *et al.* (2006) and Sandvik *et al.* (2007). In contrast, simulations of the multi-layered case overestimated LWP by a small amount and significantly underestimated the IWP. Findings from this model evaluation and from studies by Pinto (1998), Harrington & Olssin (2001), Morrison & Pinto (2006) and Prenni *et al.* (2007) suggest that interactions between the ice and liquid microphysics are likely to be responsible for these differences. It is possible that cloud parameterisations over-predict ice nuclei concentrations and thus ice crystal concentrations, leading to rapid depletion of the liquid water in mixed-phase clouds.

2.4.5 Surface albedo

Good representation of the surface albedo is necessary to accurately represent the surface radiation budget. General circulation models are generally unsuccessful in representing the annual albedo cycle and in summer the albedo tends to be overestimated (Curry *et al.*, 2001; Koltzow, 2007). There are two main types of sea ice surface albedo parameterisations; the first is based on the temperature of the surface and the second is a prognostic scheme with a decay factor for ageing snow, where the albedo is reset to

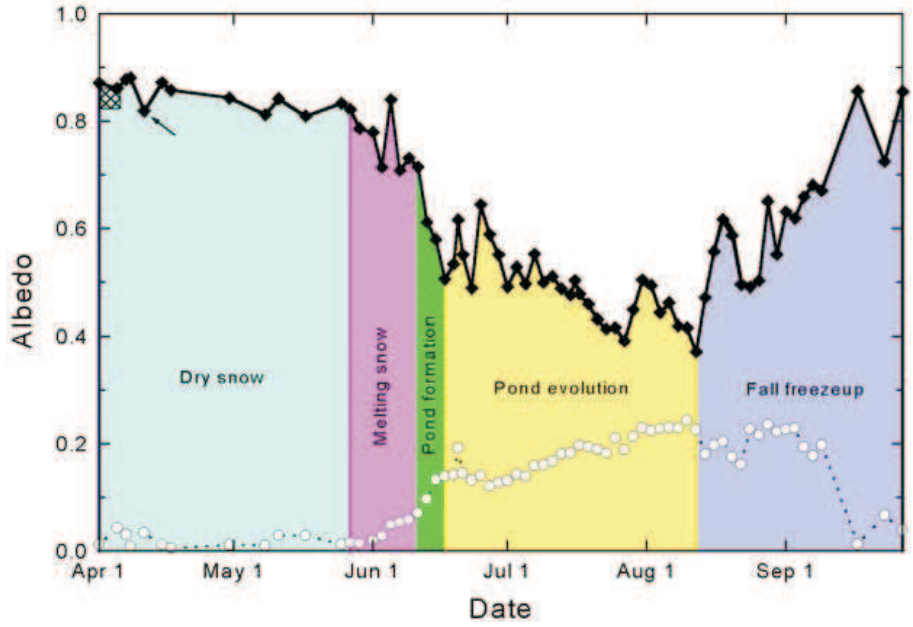

Figure 2.12: Time series of albedo measurements made during SHEBA in 1998 at approximately 74°N (taken from Perovich *et al.* (2002a)). The black diamonds are albedo averages along a 200 m transect of the ice floe and the open circles are the standard deviation of the albedo measurements along each transect.

a higher value with new snowfall (Pedersen *et al.*, 2009). The temperature dependent scheme in the UK Met Office Unified Model was found by Pedersen & Winther (2005) and Curry *et al.* (2001) to be very unrealistic. It significantly underestimates the albedo in winter and during the melt period it decreases the value of the albedo too early and too fast. Prognostic schemes were found to perform better if the thresholds are tuned to give reasonable results, although this is not suitable for climate models that need to simulate ice-albedo feedbacks.

The most comprehensive set of surface albedo measurements in the central Arctic Ocean were made by Perovich *et al.* (2002a,b) during the SHEBA campaign at approximately 74°N. They found that in May the surface was covered in cold, dry snow and had an areal averaged albedo of approximately 0.8. This decreased by the end of July to a minimum of 0.65 for ice surfaces, 0.066 for open leads and 0.1 for melt ponds, where the aerially averaged value was 0.4. The study highlighted 5 phases in the albedo life cycle that are critical to model surface albedo; the dry snow period, melting snow period, pond formation, pond evolution and fall freeze-up (Figure 2.12). Although the annual observations are site specific, they speculate that the form of the annual cycle is similar over all Arctic pack ice and only the timing and amplitude of the cycle varies by location and year.

This data was used by Bromwich *et al.* (2009) to formulate a new albedo parameterisation for the recently developed Polar Weather Research and Forecasting (Polar WRF) model.

Instead of predicting surface albedo through surface temperature, amount of snowfall or surface conditions it computes a value as a function of latitude and time of year. The dry snow albedo (September to May) is set to 0.82 and this decreases linearly over 35 days to 0.5 at the onset of the melt period, which is determined from Special Sensor Microwave Imager (SSM/I) brightness temperatures. The date of the start of the melt period gets later with increasing latitude. The albedo remains at 0.65 during the first part of August and on 12th August it increases linearly over 18 days, back to 0.82. This scheme inevitably parameterises surface conditions well for a specific location during the SHEBA year but it is known that the multi-year ice was relatively thin and the melt season 25 % longer than is typical (Curry *et al.*, 2001). More observations are needed to assertain how representative this parameterisation is of the entire Arctic Ocean.

Other new schemes, developed by Pedersen *et al.* (2009) and Koltzow (2007) consider bare ice and snow covered ice separately as well as including a pond fraction. They demonstrate that these new schemes are more successful in capturing the annual cycle, the spring and freeze-up transition periods are better represented and summer values of albedo are more accurate than if a temperature dependent scheme is used.

Chapter 3

Observations and models

3.1 Arctic Ocean Experiment 2001

The Arctic Ocean Experiment (AOE) 2001 (Tjernström *et al.*, 2004a) took place in a region of drifting pack ice between 88 and 89°N, 2nd to 21st August 2001, on the Swedish icebreaker Oden. An 18 m meteorological mast was positioned on a large floe in the pack ice (1.5 x 3 km), approximately 300 m from the ship and 500 m from the nearest open leads. The micro-meteorological data set includes mean-profile measurements of wind speed at 5 levels (1.7, 3.4, 7.1, 12.9 and 17.3 m), humidity and air temperature at 2 levels (3.6 and 14.5 m) and wind direction at one level (18 m). High frequency measurements of the turbulent wind components and temperature were made using Gill sonic anemometers at heights of 4.7 and 15.4 m and of water vapour using Krypton hygrometers at heights of 3.6 and 14.5 m.

Longwave and shortwave upwelling and downwelling radiation fluxes were measured at two sites during the field campaign. The first set of observations were made using Eppley pyranometers and pyrgeometers, which were situated on the ice near the meteorological mast and made measurements for the duration of the field campaign. A second set of shortwave radiation measurements, using Kipp & Zonen CM11 pyranometers were made periodically over an undisturbed snow surface on the pack ice half way between the ship and the meteorological mast. All radiation measurements presented here, apart from the albedo observations and the upwelling shortwave radiation flux (discussed below) were made using the first set of sensors.

The sensor measuring upwelling shortwave radiation from the first set of instruments did not work for the entire campaign so a polynomial function was fitted to a time series of surface albedo derived from the second set of shortwave radiation measurements

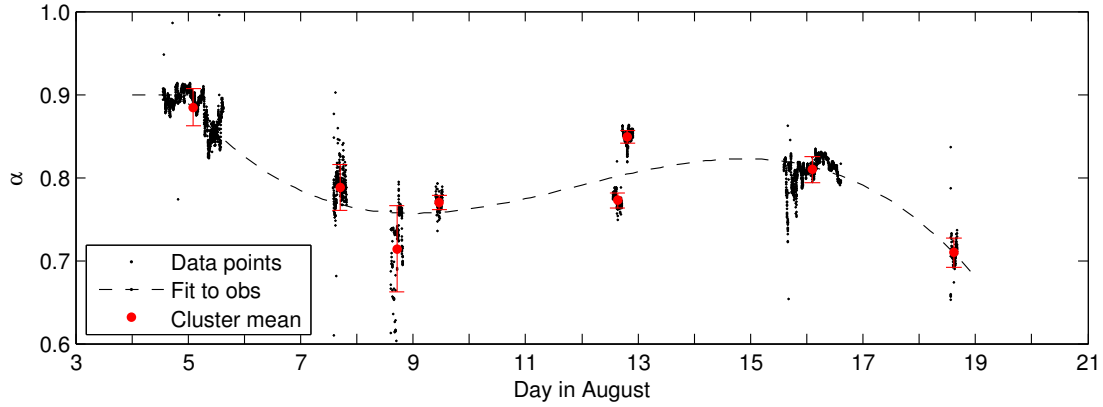

Figure 3.1: One minute averaged measurements of surface albedo made over an undisturbed snow surface during AOE 2001. The measurements were made using the second set of up and downward facing pyranometers and a polynomial function is fitted to the time series. The mean of each cluster of data points and an error bar ±1 standard deviation about each mean is also shown.

(Figure 3.1). The upwelling shortwave radiation flux was then computed from this and the continuous downwelling shortwave radiation flux observations from the first set of instruments. Such an estimate is a potential source of error in the value of the observed upwelling shortwave radiation flux, SW_{up} and also in the net shortwave radiation, SW_{net} and net radiation, Rad_{net} fluxes. This is discussed further in Section 4.5.

The turbulence data sets from the meteorological mast are limited due to instrument problems during the field campaign. The turbulent winds were the least affected but the sonic temperature measurements suffered from contamination most likely caused by water droplets formed by condensation on the transducer heads. Water vapour measurements also suffered from condensation on the optical hygrometers. Rigorous checks were made to ensure data were used only from periods where there is high confidence it is uncontaminated. Firstly, a visual check of the time series was made and obvious periods of instrument failure and any erroneous, single outlying points were removed. Corrections for cross-wind contamination of the sonic temperature were made following Schotanus *et al.* (1983) and oxygen corrections to the water vapour measurements following van Dijk *et al.* (2003). Eddy covariance fluxes of sensible heat, H, latent heat, E and the friction velocity, u_* were then estimated with a 30 minute averaging period. Measurements that were made when the instruments were downwind of the mast were removed from the data set. A flux footprint model (Horst & Weil, 1992) was used to determine that over 90 % of the total flux is representative of a region of the ice surface that is less than 300 m from the mast. This suggests that the ship and open leads should have a very limited impact on the flux data set and it should therefore represent a surface covered almost entirely by pack ice.

Additional measurements included surface pressure and 6 hourly radiosonde measurements of water vapour, pressure, temperature, and wind velocity up to 12 km. Three Integrated Surface Flux Facility (ISFF) stations were deployed on the ice, which made additional turbulence measurements at 3 m and air temperature, wind speed, humidity and pressure measurements at 2 m. Two of these (ISFF 1 and ISFF 2) were located on separate ice floes to the main ice camp, approximately 7 and 9 km from the ship, forming a rough triangle with the ship. ISFF 3 was located 1.5 km from the ice camp, near an open lead. The measurements made by the CSI ultrasonic anemometers and Krypton hygrometers suffered far less from the problems experienced by those on the main meteorological mast. The turbulent fluxes were computed in the same way as described above. There was an array of remote sensing instruments making continuous measurements, including a sodar to measure wind speed, direction and boundary-layer structure, a ceilometer to measure cloud base and an S-band Doppler radar to observe clouds and precipitation (see Tjernström *et al.* (2004b) for further details).

3.2 ASCOS Field Campaign

The Arctic Summer Cloud Ocean Study (ASCOS) took place on the Swedish icebreaker Oden (Figure 3.2) during August and September 2008. The ship departed the island of Svalbard on 2nd August and sailed north (Figure 3.3) until a suitable ice floe was located at 87°N and 2°W on 12th August. The floe was approximately 4 x 8 km and surrounded by a mixture of open leads and other ice floes of various sizes (Figure 3.4). The ship was moored to the ice and instrumentation deployed in the vicinity of the ship and at an open lead site that was 3 km away, on the opposite side of the floe. The ship remained with this floe until 1st September, allowing measurements to be made at the ice station between 13th August and 1st September. During this period the floe drifted a significant distance and rotated relative to true north. Instruments on the ice were therefore not constantly aligned in a particular direction, although their relative positions remained the same. The orientation of the ice floe relative to true north was derived using Global Positioning System (GPS) measurements that were made at two fixed points on the floe. This information and a measure of the relative orientation of each instrument at a single point in time were used to rotate the horizontal components of wind velocity, u and v into a geophysical reference frame.

Figure 3.2: The Swedish icebreaker Oden at the ice station during ASCOS (Photo by Sarah Norris).

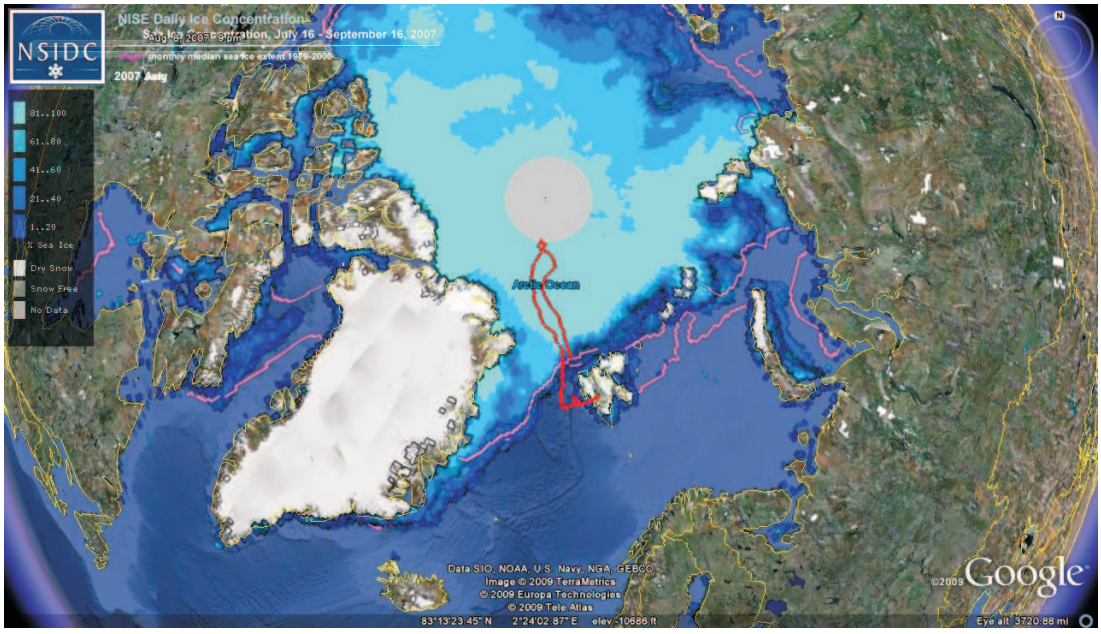

Figure 3.3: Route through the pack ice during ASCOS. The light blue shades show the August 2007 ice extent, the pink line is the August median sea ice extent for 1979-2000 and the red line is the route taken by Oden (by Sarah Norris using Google Earth).

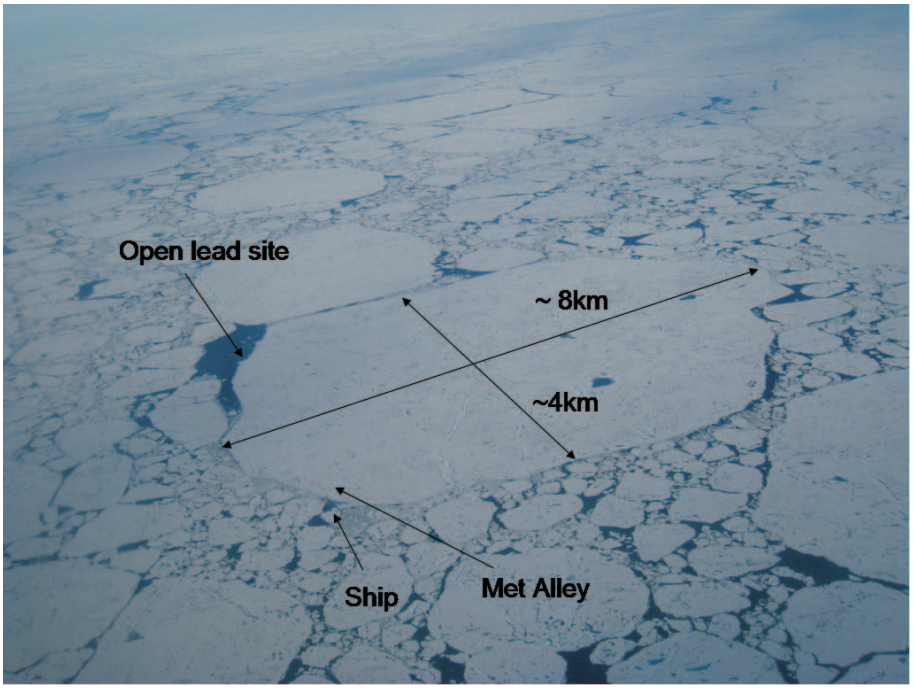

Figure 3.4: Ice floe used for the ice camp during ASCOS. The relative locations of the ship, Met Alley and the open lead site are shown (Photo by Staffan Sjögren).

3.2.1 Atmospheric measurements

The majority of the micro-meteorological instrumentation was installed in a more or less linear arrangement on the ice, running away from the ship. Referred to as 'Met Alley', the arrangement was designed to minimise the sector in which measurements might be contaminated by flow over the ship, other instruments, or the masts. It was situated as far from the ship as possible within the constraints imposed by the need to run power cables from the ship to the measurement site. Figures 3.5 and 3.6 show the approximate layout of the area. The ship was moored to the ice in one of two positions to optimise on board aerosol sampling. The 15 and 30 m masts supported the sonic anemometers, Licor open path analyzers, and the mean temperature and humidity profile measurements. The radiometers were positioned away from the mast sites to avoid contamination of the measured surface and the tether balloon was placed in an area that was a safe distance away from the ship, masts and other equipment.

3.2.1.1 Meteorological masts

The 15 m mast was approximately 400 m from the ship and supported aspirated temperature sensors at 0.20, 1.02, 1.79, 5.32, and 8.36 m, and relative humidity sensors at 3.19 and 14.92 m (Figure 3.7). Compact Lightweight Aerosol Spectrometer Probe (CLASP) instruments (Hill *et al.*, 2008)) were also situated at 2.45 and 14.66 m on the 15 m mast,

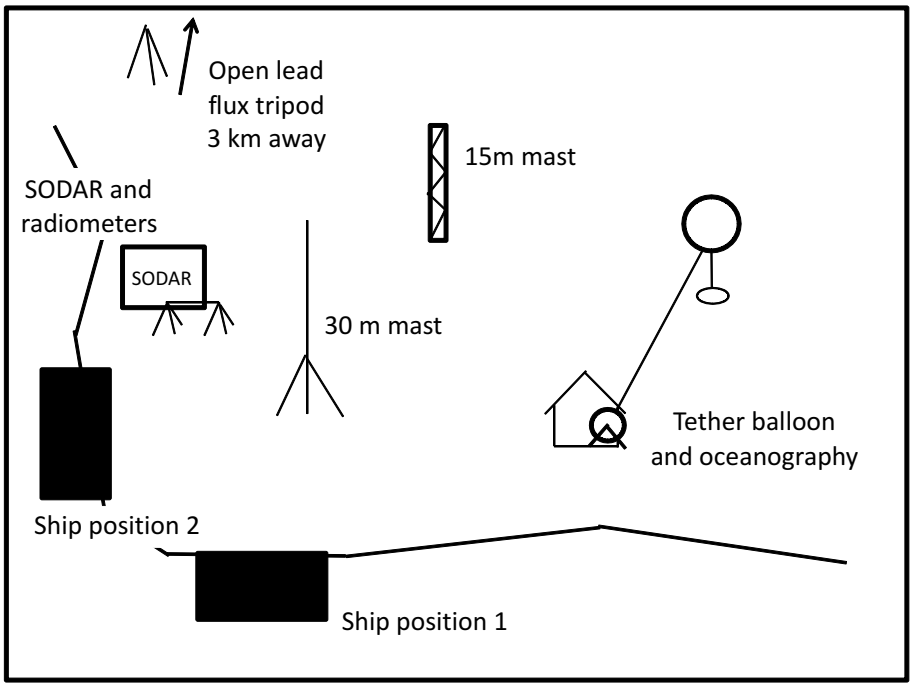

Figure 3.5: Plan view of the layout of instrumentation in Met Alley. Not to scale.

Figure 3.6: The Met alley site. From left to right: sodar, meteorological masts, oceanography tent and tether balloon.

although these instruments failed to work during the ice station. There were 5 levels of sonic anemometers; the two Gill instruments (at 3.25 and 15.40 m) were paired with high frequency Licor (LI-7500) open path H_20 and CO_2 analysers and the three Campbell (C-SAT3) sonic anemometers (at 0.94, 5.21 and 8.19m) were coupled with fine wire temperature sensors. The instrument heights were designed to give measurements on an approximate logarithmic scale. The 30 m mast was positioned between the 15 m mast and the ship and supported a single Metek sonic anemometer at the top.

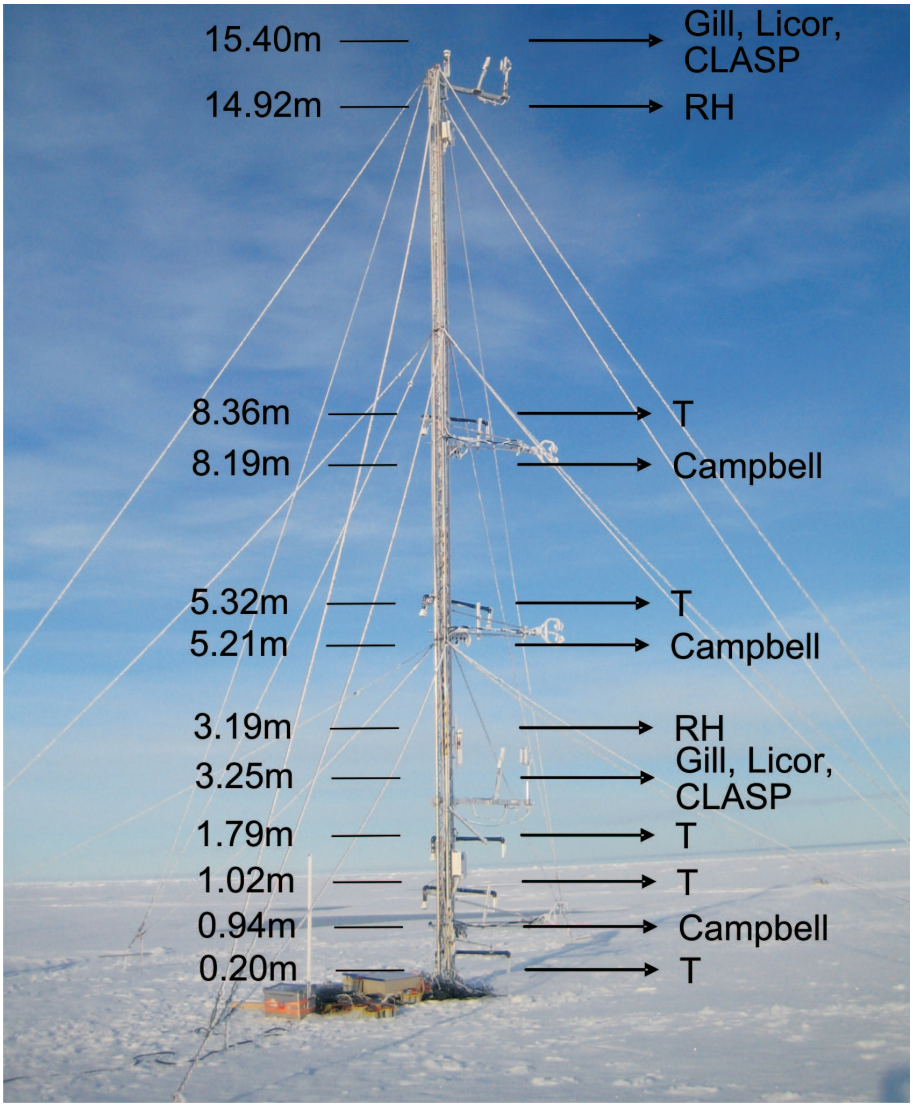

Figure 3.7: Instrumented 15 m meteorological mast

3.2.1.2 Radiometers

The radiation site was close to the meteorological masts and consisted of four Epply radiometers, measuring up and downwelling longwave and shortwave radiation (Figure 3.8). During the first part of the measurement period a number of mainly frozen melt ponds were within 10 m of the sites but during the second week of the ice camp these became completely frozen and covered in snow and remained in this state for the remainder of the campaign.

3.2.1.3 Thermocouples and flux plates

Three sets of 5 thermocouples were deployed for the duration of the ice camp to measure surface skin temperature and a profile of vertical ice temperature. Two sets were placed

Figure 3.8: Site of the radiometers

on the surface of the ice, half at the mast site and half at the radiation site. The remaining thermocouples were buried in the ice to depths of 5, 15, 40 and 100 cm. Two flux plates were also buried at the radiation site to a depth of 5 cm.

3.2.1.4 Tethersonde

The tethersonde instrument was suspended 10 m below a large helium balloon, which was attached by nylon tether to an electric winch (Figure 3.9). The instrument package consisted of a sonic anemometer head, along with temperature, pressure and humidity sensors and a CLASP instrument. Accelerometers were also included to allow instrument motion corrections of the sonic wind components. A tail at the rear of the instrument kept the sonic head pointing into wind.

The maximum height that can be gained by the balloon is dependant on atmospheric stability, wind speed and the balloon payload. In the summer Arctic environment, where convection and wind speed are both low, the balloon could reach approximately 500 m in altitude. The tethersonde was in near constant operation during the ice station; flights consisted of simple up and down profiles or stepped profiles stopping every 50 m for 30 minutes to acquire sufficient high frequency data for the computation of turbulent properties.

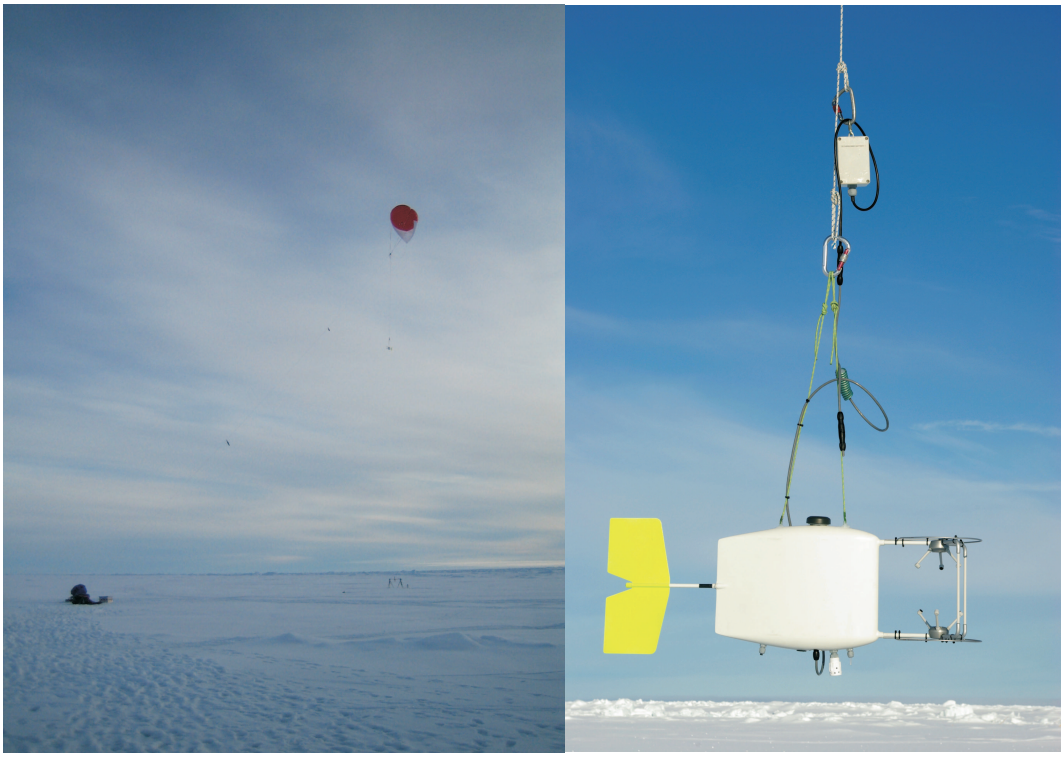

Figure 3.9: Left: tether balloon, right: tethersonde instrument (Photos by Ian Brooks).

Figure 3.10: Sodar instrument deployed on the ice

3.2.1.5 Remote sensing

A SOnic Detection And Ranging (SODAR) instrument was deployed at the Met Alley site. It measures atmospheric reflectivity of sound pulses, producing high resolution wind fields and turbulent properties (Figure 3.10). On board the ship there were an assortment of remote sensing antennas (Figure 3.11). These included a ceilometer to measure the height of cloud base, S- and K- band radars to observe precipitation, clouds and their ice properties. A microwave radiometer retrieved liquid water path and a scanning microwave radiometer retrieved vertical temperature profiles. A wind profiler, which makes good

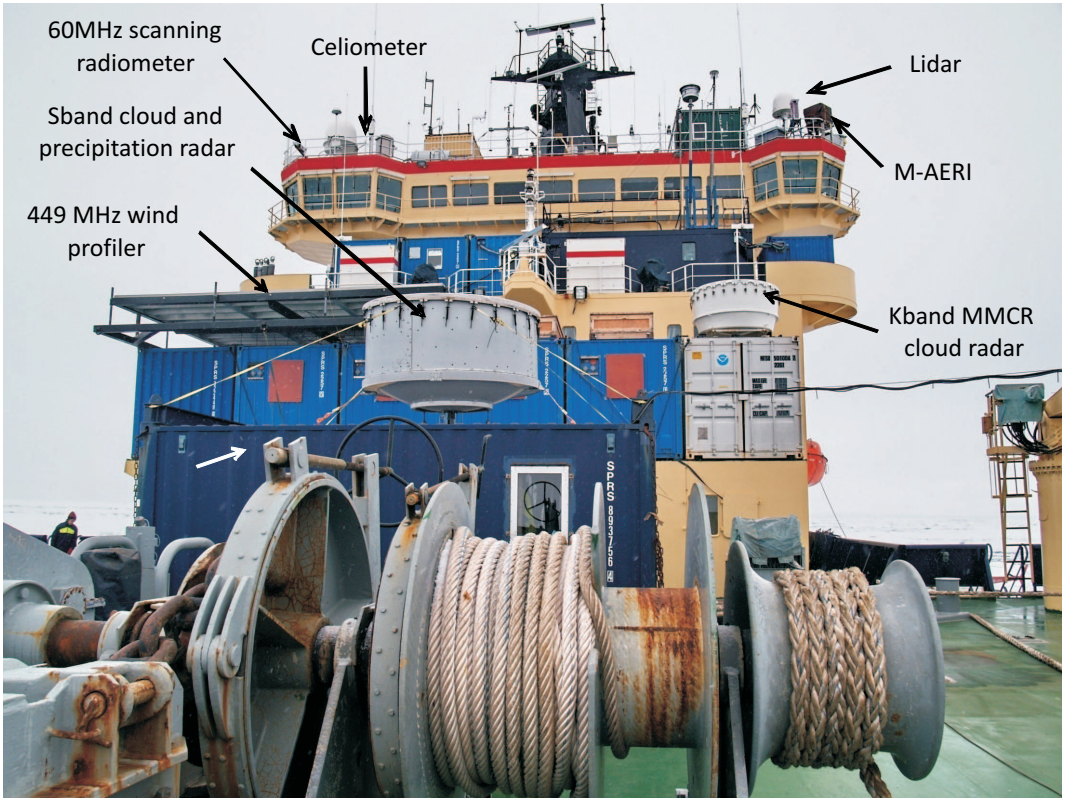

Figure 3.11: Remote sensing instruments on board Oden (Photo by Michael Tjernström)

quality measurements of wind speed up to 4-5 km, complements the wind profiles made by the sodar.

3.2.1.6 Open lead measurements

The open lead site was approximately 3 km away from the ship's harbour to avoid water contamination, which was important for the marine biology measurements (Figures 3.4 and 3.12). A flux tripod was deployed close to the edge of the lead and incorporated a CLASP, Licor and Gill sonic anemometer.

3.2.1.7 Additional atmospheric measurements

Radiosondes were launched from the ship's deck every six hours during the entire cruise and ice camp. On the upper deck of the ship additional downwelling long and short-wave radiation measurements were made, along with measurements of ice/water surface temperature via radiative emission from the Marine Atmosphere Emitted Radiance Interferometer (MAERI). Hemispheric photos of the sky were taken at regular intervals, from which an estimate of cloud fraction can be inferred. Data was also available from

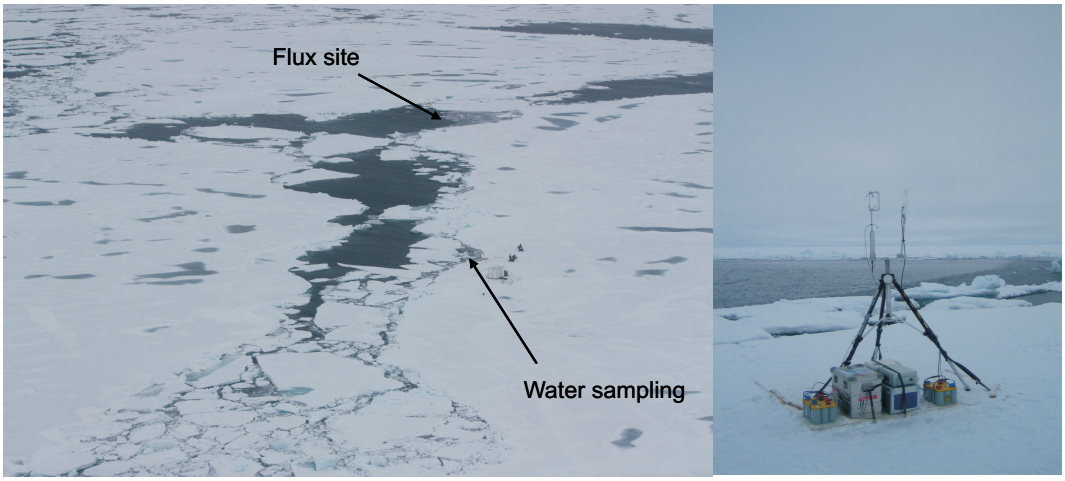

Figure 3.12: Aerial view of the open lead site and the open lead flux tripod

the ship's meteorological instruments, including GPS position coordinates, wind speed and direction, humidity, visibility and pressure.

3.2.2 Chemistry, aerosol and biology measurements

ASCOS was an interdisciplinary field campaign, involving meteorology, atmospheric chemistry, aerosol, biology and oceanography measurements. During the ice station the oceanography observations included half hourly temperature and salinity profiles down to approximately 500 m and constant heat and momentum flux profile measurements up to 10 m below the ice. A helicopter made regular flights during the campaign, profiling the atmosphere up to 3 km. Aerosol concentration profiles using CLASP and Condensation Particle Counter (4-500 nm diameter particles) instruments were made during the flights, as well as profiles of temperature, pressure and humidity. Air samples were also collected for analysis of dimethyl-sulphide.

The NASA DC-8 research aircraft made several flights over the ship during the ice camp period. The timing of these flights was designed to sample air profiles through frontal systems. Comprehensive meteorological, aerosol and chemistry measurements were made during these flights, which complement the static data sets.

On board Oden an air inlet and pump at the bow of the ship provided air for chemical and particle sampling. Aerosols in the size range 3 nm-10 μm diameter were sampled for their composition, number and their hygroscopic growth into ice and cloud nuclei using various sets of apparatus. Gas phase chemistry measurements were made via mass spectrometry techniques, plus more specific measurements of dimethyl-sulphide and ozone. Fog samples were also made on the upper deck of the ship and analysed for chemical composition.

At the open lead site twice daily samples of the water surface micro-layer were taken along with larger samples of water and ice to filter for biological material. A camera (Leifer *et al.*, 2002) was also deployed just below the surface of the lead, which captured imagery of any bubbles rising to the surface of the lead.

3.3 Data processing and quality control

Quality control and processing of the data from the two Gill sonic anemometers and two Licors on the 15 m mast, data from the Metek sonic anemometer on the 30 m mast and data from the Gill sonic and Licor at the open lead site was completed solely by the author. All other meteorological measurements made on the ice were processed by colleagues at the University of Leeds, Stockholm University and the University of Miami, namely Thorsten Mauristen, Joesph Sedlar, Ian Brooks, Michael Tjerström and Malagorzata Szczodrak. Products from the remote sensing measurements were provided by Matthew Shupe, from the National Oceanographic and Atmospheric Administration (NOAA) in Boulder, Colorado.

The flow charts in Figures 3.13 and 3.14 give an overview of the data processing, quality control and flux calculation methods that were used on the sonic anemometer and Licor data sets from the 15 and 30 m masts and open lead flux tripod. The sections below discuss stages of the process in more detail.

3.3.1 Sonic anemometer data processing

3.3.1.1 Instrument tilt corrections

If the transducer heads of a sonic anemometer are not aligned exactly with the true horizontal wind velocity, it is possible that significant errors will occur in the magnitudes of the computed fluxes because horizontal fluctuations in the wind speed can appear in the w velocity component. It is not usually practical to physically align the sonic with the true horizontal wind because the ground must be extremely flat and the sonic must be aligned to this with more than 0.1° accuracy (Kaimal & Haugen, 1969). It is more appropriate to use a streamline coordinate system, in which the wind is rotated so the local mean wind is parallel to the x axis. This has the advantage that over gentle slopes, where there is no separation, the system can be regarded as terrain following allowing the data to be used easily in models and other applications.

Wilczak *et al.* (2001) outlines three methods for the rotation of u, v and w into this coordinate system. The first two methods require a double or triple rotation of the

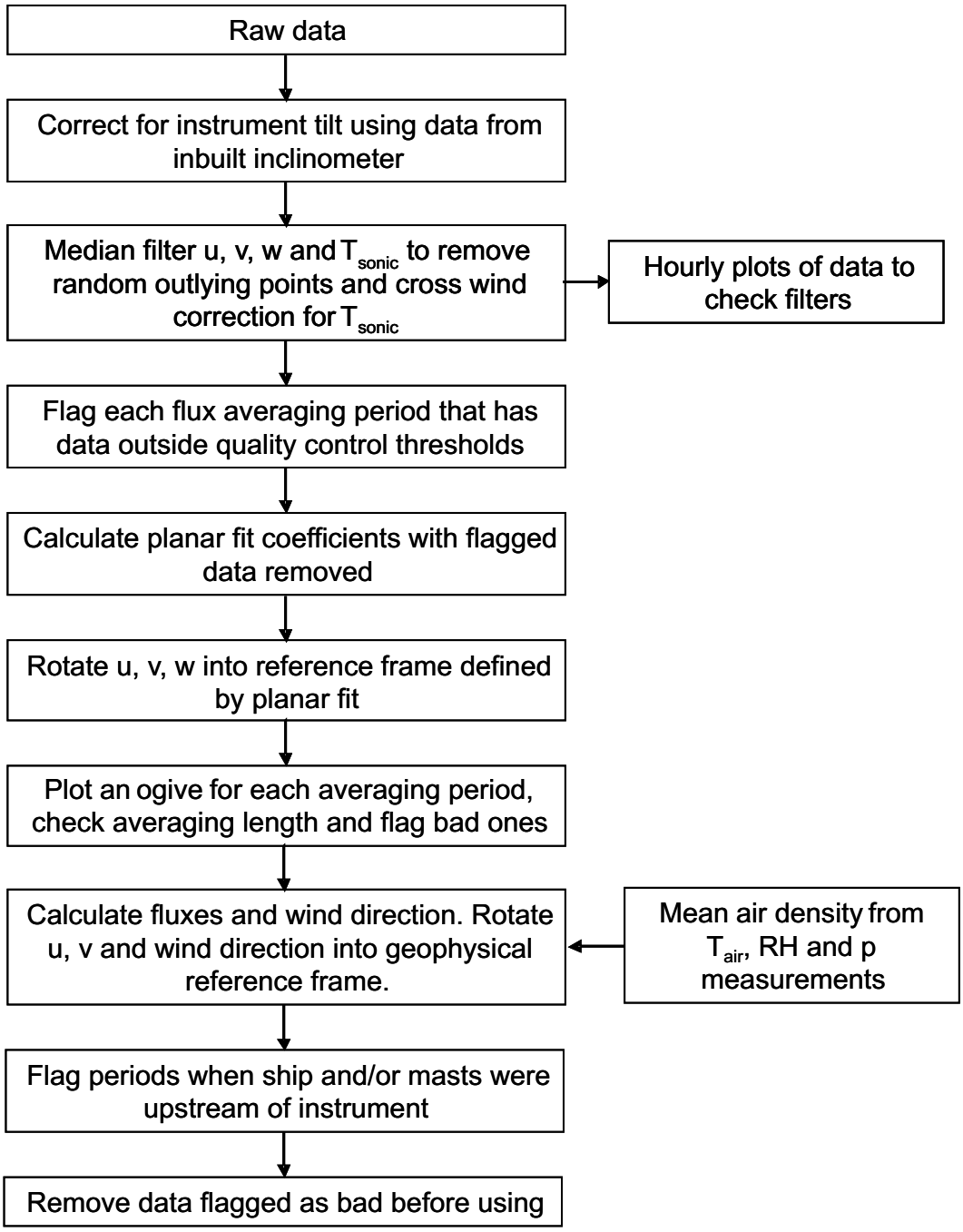

Figure 3.13: Data processing flow chart for Gill sonic anemometers. Metek sonic anemometer data was processed using the same method but no initial tilt corrections were applied since the Metek instruments do not contain an inbuilt inclinometer.

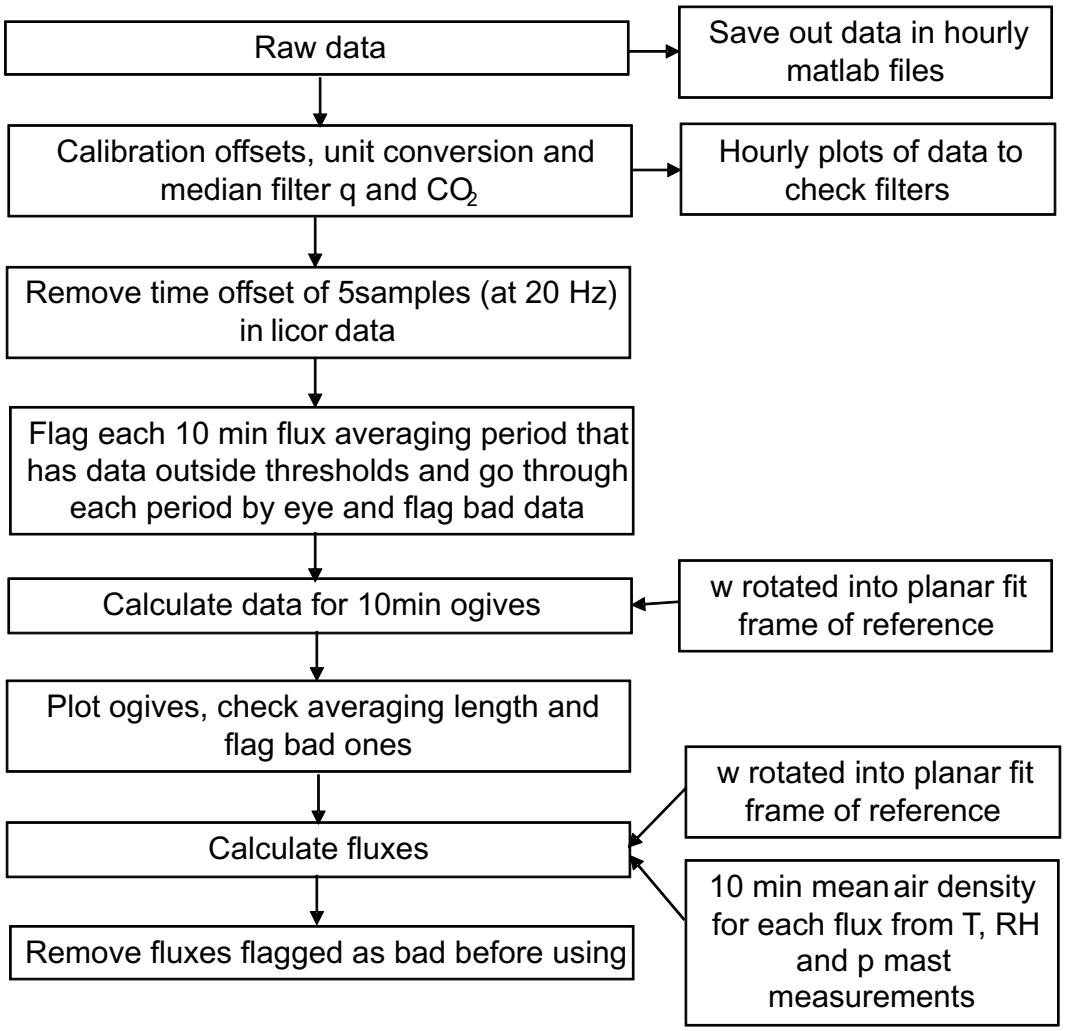

Figure 3.14: Same as Figure 3.13 but for the Licor data.

anemometer's axes. Although double rotation is the most commonly used method, since it is performed on a run-to-run basis (i.e. for every flux averaging period) sampling uncertainty in the mean vertical velocity can lead to large errors in the calculated stress. The third method calculates tilt angles using data from a large number of runs, which significantly reduces stress errors due to sampling uncertainty. Since a large amount of data is needed these values cannot be computed in real time, as can the first two methods (Wilczak *et al.*, 2001) but this was not necessary for the current application. It is important that the anemometer position does not change over the time of the calculation. For this study the tilt angles are calculated twice for the measurements made on the 15 m mast because it was lowered half way through the ice station for maintenance (24th August 14:45 - 15:15 UTC). It is also important to determine periods of suspect data such as when the instruments accumulated large amounts of ice or when the mast and ship were upwind of the instrument (see Section 3.3.3 for more details) and to disregard these periods of data during the planar fit calculation.

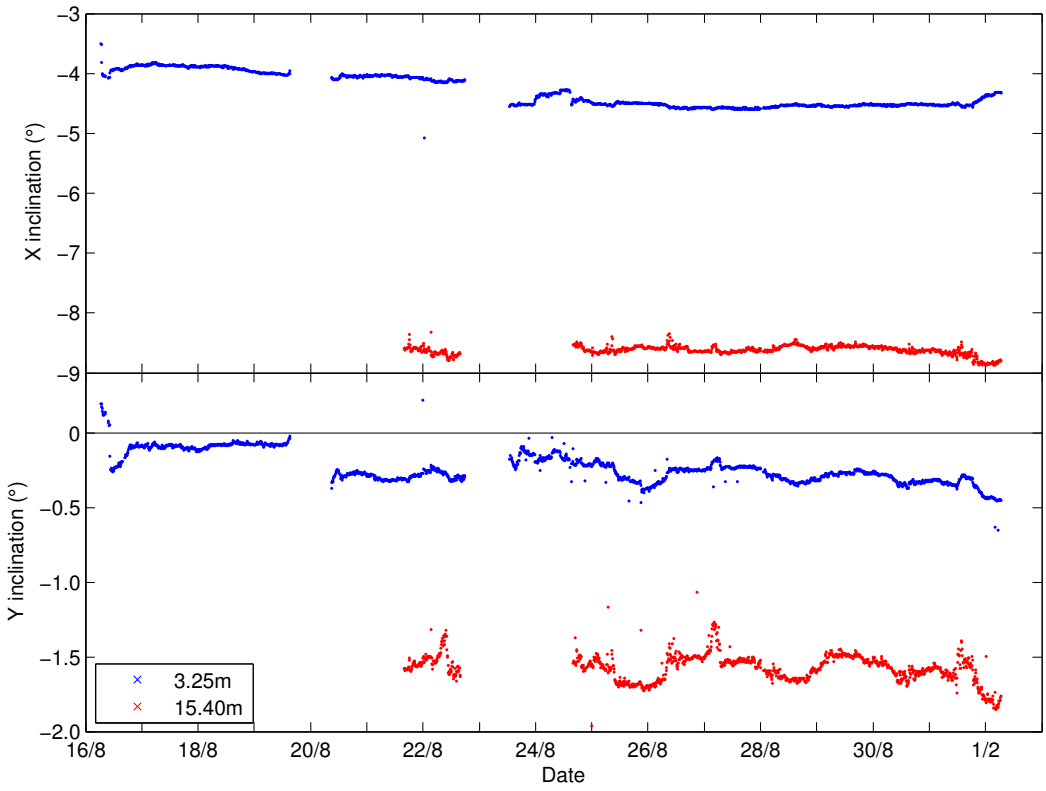

Figure 3.15: 5 minute mean tilt angles of the Gill sonic anemometers from true vertical and horizontal on the lower and upper levels of the 15 m mast using data from the inbuilt sonic inclinometers

Even when the wind components have been rotated into the streamline coordinate system to correct for the average tilt of the sonics, any conditions other than the lowest wind speeds can cause the mast to move, constantly changing the instruments' alignment. The data from the Gill sonic anemometers can be corrected for this using a measurement made by their inbuilt inclinometers. The Metek and Campbell anemometers however, do not incorporate this feature. It is therefore important to assess the extent to which instrument tilt variation affects the computed fluxes.

Figure 3.15 shows 5 minute mean measurements made over the entire ice station by the inclinometers in the Gill instruments on the upper and lower levels of the 15 m mast (3.25 m and 15.40 m respectively). These plots show a mean tilt in the alignment of the instruments; this arises because it is impossible to align the anemometer exactly with the true horizontal. Also apparent is a variation in tilt angle with time, related to movements of the mast caused by the wind. This is better illustrated by the increase in both the X and Y inclination angles with wind speed in Figure 3.16. At the lower level the instrument was tilted between -3.8 and -4.8° in the x direction and between 0 and -0.5° in the y direction. On the upper level the angles are larger; -8.3 and -8.9° in the x direction and -1.2 and -1.9° in the y direction.

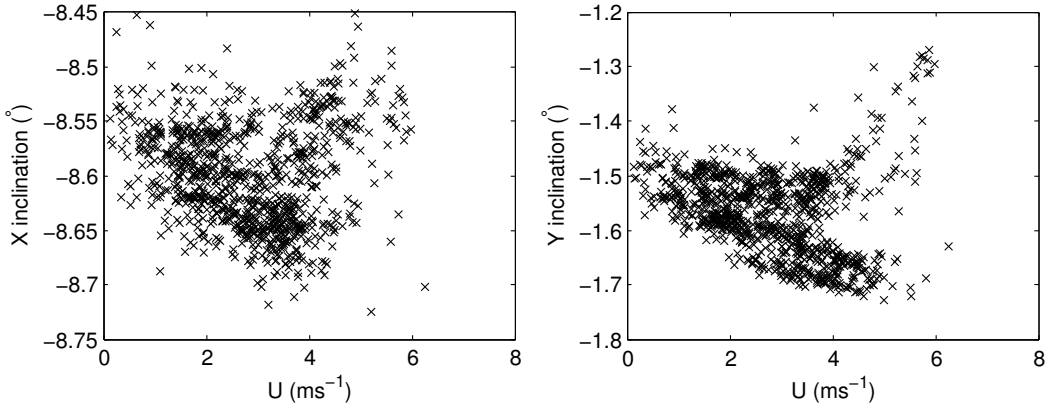

Figure 3.16: Relationship between wind speed and the sonic anemometer tilt angle at the upper level on the 15 m mast.

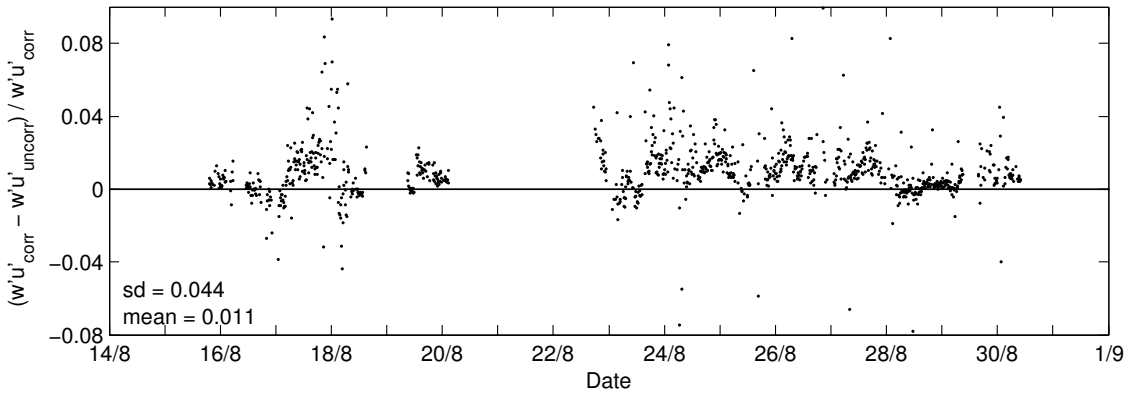

Figure 3.17: Fractional difference between tilt corrected and non tilt corrected $w'u'$ for the Gill sonic anemometer at 3.25 m. The mean and standard deviation over the entire measurement period are also shown.

Comparison of the kinematic momentum flux, $\overline{w'u'}$ measured by the Gill sonics with and without the tilt corrections (Figures 3.17 and 3.18) shows that the correction has only a small effect on the calculated fluxes. The mean difference between the tilt corrected and non tilt corrected fluxes is 1.1 % and 2.3 %, on the lower and upper mast level respectively. The Campbell anemometers were on the same mast as the Gill anemometers and therefore, it would be possible to infer a correction to the variation of instrument tilt with time using the inclinometers in the Gill instruments. The 15 m mast is constructed out of three 5 m sections; the Gill instruments were located on the first and third section and the Campbell instruments on the middle section. The three sections do not necessarily move in the same way due to potential bending at the joints and differing tensions on the guys at each level. Estimating a tilt correction for the Campbell sonics may therefore, introduce biases in the flux estimates. Since the tilt for the lower Campbell sonic is likley to be less than 1 % and for the two upper Campbell sonics between 1 % and 2 %, it seems adequate to neglect the high frequency tilt corrections for the Campbell instruments.

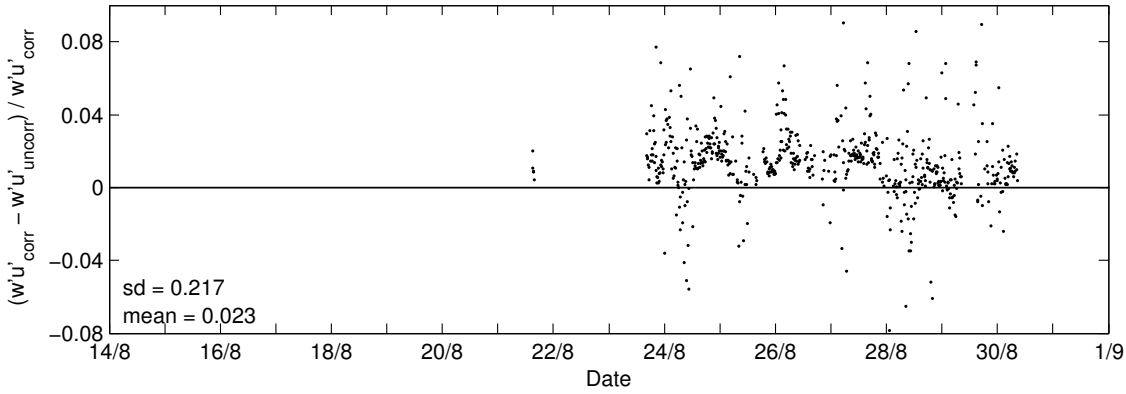

Figure 3.18: Same as Figure 3.17 but for the Gill sonic anemometer at 15.40 m.

3.3.1.2 Cross wind contamination correction for sonic temperature

Sonic anemometers estimate air temperature by taking an average of the time it takes to send a sound pulse between each of the three pairs of transducer heads. The time taken for the pulse to reach the receiving head depends on the speed of sound, which is a function of air density, in turn dependent on temperature and humidity, and can therefore be used to acquire a high frequency measurement of temperature (Schotanus *et al.*, 1983):

$$T_{sonic} \equiv \frac{l^2}{4\gamma R}\left(\frac{1}{t_1}+\frac{1}{t_2}\right)^2 \tag{3.1}$$

where T_{sonic} is the sonic temperature, l the separation between the transmitter and receiver, t_1 the transmission time of the first firing, t_2 the transmission time of the return pulse and γR is a physical constant which equals 403 $\mathrm{m^2 s^{-2} K^{-1}}$.

Air flow along the axis between transducers does not affect the measurement because the increased transit time of the pulse in one direction is cancelled by the decreased transit time of the pulse in the opposite direction. If however there is air flow across the transducer path, the pulse is carried away from the receiving head. Some sonic anemometer models, such as the C-SAT3 instruments used during ASCOS account for this internally but a correction needs to be applied to the Gill and Metek instruments. Schotanus *et al.* (1983) derived, by experiment, a relation between sonic temperature and a side-wind corrected estimate for the temperature of dry air:

$$T_{dry} = T_{sonic} + \frac{\nu_n^2}{\gamma R} \tag{3.2}$$

where ν_n is the single path, vertically orientated sonic anemometer side-wind. The way in which ν_n is related to u, v and w is dependent on instrument geometry. For the Gill

and Metek sonics it is (van Dijk *et al.*, 2004):

$$\nu_n^2 = \frac{3}{4}(u^2 + v^2) + \frac{1}{2}w^2 \tag{3.3}$$

3.3.1.3 Humidity correction for sonic temperature

The speed of sound through air depends on both air temperature and humidity. After the cross-wind corrections have been applied to the sonic temperature estimates, the water content of the air must be considered. van Dijk *et al.* (2004) present a correction to be applied before time averaging:

$$T = \frac{T_{dry}}{1 + 0.51q} \tag{3.4}$$

Alternatively, the equation below can be used to directly convert the covariance of sonic temperature with vertical velocity to the covariance of temperature with vertical velocity:

$$\overline{T'w'} = \overline{T'_{sonic}w'} - 0.51\overline{q}\overline{T'_{sonic}w'} - 0.51\overline{T'_{sonic}w'q'} \tag{3.5}$$

van Dijk *et al.* (2004) states that this correction is only important when $H < E$. Considering the lack of consistent good quality high frequency humidity observations and the fact observations from ASCOS show $H \approx E$, this correction was not performed on this data set.

3.3.1.4 Sonic and absolute temperature

Andreas *et al.* (2005) found that for observations over the Antarctic, $\overline{T'_{sonic}w'}$ is always within 5 % of $\overline{T'w'}$ and they reasoned that since random errors in $\overline{T'w'}$ are typically 10 %, $\overline{T'_{sonic}w'}$ can be used as the kinematic sensible heat flux in their study; the same is assumed here. In addition, considering Equation 3.4 and the relationship between temperature and virtual temperature in Equation 2.12, it is assumed $T_v \approx T_{sonic}$ for this data set.

3.3.2 Licor data processing

The accuracy of H_2O and CO_2 concentration measurements made by a the Licor H_2O and CO_2 analyzer are dependent on the time since the most recent factory calibration and when the internal chemicals were last changed. A total of four Licor instruments were taken on the ASCOS cruise, one of which (NOCS, provided by the National Oceanography Centre, Southampton) had been factory calibrated shortly before the field campaign. This instrument was used to calculate calibration offsets for the other three instruments. Of

Table 3.1: Mean H_2O measurements (mmols m^{-3}) made during laboratory tests along with the variance and calibration offset in comparison to NOCS instrument.

Time period 1				Time period 2			
Instrument	$\bar{x}_{obs}$	σ_x^2	Offset	Instrument	$\bar{x}_{obs}$	σ_x^2	Offset
NOCS	323.97	0.13	-	NOCS	313.43	0.15	-
NOAA1	308.31	0.08	15.66	NOAA1	301.18	0.09	12.26
NOAA2	368.95	0.16	-44.98	Leeds	308.52	0.14	4.90

Table 3.2: Same as Table 3.1 but for CO_2.

Time period 1				Time period 2			
Instrument	$\bar{x}_{obs}$	σ^2	Offset	Instrument	$\bar{x}_{obs}$	σ^2	Offset
NOCS	31.03	0.0072	-	NOCS	22.84	0.0020	-
NOAA1	30.69	0.0070	0.338	NOAA1	22.47	0.0016	0.371
NOAA2	30.47	0.0071	0.561	Leeds	23.03	0.0017	-0.194

the remaining three instruments one was provided by the University of Leeds (Leeds) and two by the National Oceanic and Atmospheric Administration (NOAA). All four instruments were left running under laboratory conditions for approximately one hour. A mean over the this period was computed for each instrument and the difference between this and the mean value measured by the NOCS instrument was used as the offset (Tables 3.1 and 3.2). For NOAA1, which was tested twice, an average of the differences between the means are used. The offsets for NOAA2 are the largest and thus this instrument is considered the least accurate and was used as the reserve instrument for the campaign. The instrument at the lower level on the 15 m was was NOAA1, at the upper level was the Leeds instrument and the NOC instrument was used at the open lead site. These calibration offsets were applied to the raw data before any other processing.

3.3.3 Quality control

The instruments on the 15 m mast were subject to the accumulation of hoar frost during the campaign (Figure 3.19). This occurred periodically throughout the ice station but was especially notable between 21st and 24th August, when temperatures were low and freezing fog occurred. On the 24th August the mast was lowered between 14:45 and 15:15 UTC to remove ice from the instruments. Ice was also removed periodically from the sensor heads on the lowest two levels of sonic anemometers and the lowest Licor instrument using a step ladder. The Metek anemometer, which was situated at the top of the 30 m mast and was out of reach for the entire ice station but did not suffer from

Figure 3.19: Ice accumulation on instrumentation

the same icing problems because it had heated sensor heads, preventing the accumulation of snow and ice.

The processing and quality control of the ASCOS turbulent flux data set is more challenging than data sets acquired under warmer conditions. Although ice was cleared as regularly as possible from the instruments' transducer heads, data quality is poor during some periods. A number of steps have been taken to ensure the maximum amount of data is available, without including suspect measurements. Firstly a median filter was applied to remove single points that are anomalously large or small. For each point in turn, a 3-point median is computed and if the absolute difference between the data point and the 3-point median is more than 3 times the standard deviation, the point is replaced with the median value. The next step was to create quality control flags for the data sets. For each 10 minute period (the shortest averaging period to be used) u, v, w, sonic temperature and H_2O concentrations from the Licor are flagged to be either good or bad using a series of thresholds. Since the Licor data were the most affected, human input was also utilised for this flag. Flags were also created for periods when the mast and ship were upwind of the sonic anemometers, to avoid errors from flow distortion.

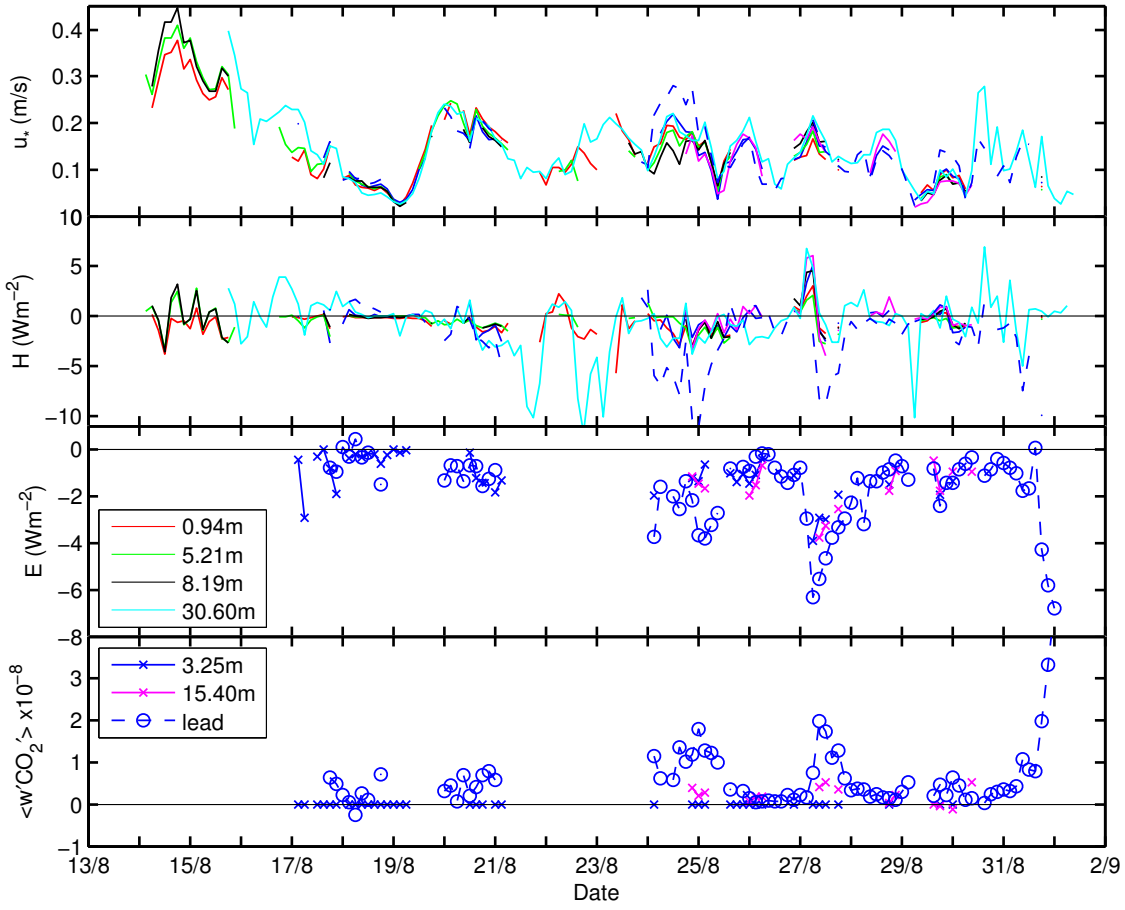

Figure 3.20: 3 hourly surface flux observations from ASCOS. A positive flux represents a transfer of energy to the surface.

3.3.4 Flux calculations

Ogive plots with various averaging periods were examined at each level. From this it was determined that in order to include all the turbulent frequencies the shortest averaging time that should be used is 10 minutes. The turbulent fluxes of momentum, sensible and latent heat were then computed using the covariances $\overline{u'w'}$, $\overline{w'T'}$ and $\overline{w'q'}$ and Equations 2.22. Values of air density were computed from air temperature, pressure and humidity measurements made on the 15 m mast. Since much of the data analysis involves the surface energy budget, the fluxes are, unless otherwise stated, defined such that a positive flux represents a gain in energy at the surface. This differs from the usual boundary-layer meteorology convention for fluxes. Figure 3.20 shows time series of the good quality 3 hourly averaged u_*, H and E available for the ASCOS ice station. Missing data is either due to instrument icing problems, periods of maintenance or periods when the masts and/or ship were upstream of the instruments. Oden was stationed at the ice camp for approximately 400 hours. Approximately 300 hours of good quality u_* and H data is available at 6 levels on meteorological masts and one level at the open lead site. There

are approximately 200 hours of E and CO_2 flux data available at two levels on the meteorological masts and one level at the open lead site. This forms a far more extensive data set than was acquired during AOE 2001, where approximately 150 hours of u_* and H data and approximately 75 hours of E data at only two levels is available.

3.4 Models

3.4.1 Met Office Unified Model

The Met Office Unified Model (MetUM) is a fully coupled ocean-atmosphere numerical model that supports both global and regional domains (Davies *et al.*, 2005; Staniforth *et al.*, 2006). It can be run on many temporal scales, making it suitable for both numerical weather prediction (NWP) and climate modelling. Although it is arguably more important to simulate the Arctic region accurately on a climate timescale, the NWP version of the MetUM is used in this study because there are a number of advantages in using this framework to infer systematic errors in the parameterisations of climate models (Phillips *et al.*, 2004). Firstly, the NWP short-range (12-36 hour) forecasts are run from initial states generated with state-of-the-art variational data assimilation (e.g. Lorenc *et al.* (2000)). There are very few in-situ observations available for assimilation over the Arctic region but those that do exist minimise errors in the large-scale synoptic flow. In addition, there are no large biases in the circulation due to remote forcing effects (e.g. tropical/extra-tropical/polar interactions). Such remotely forced biases in the circulation of a climate model make it difficult to ascribe errors to specific parametrised physical processes. While ascribing errors is still non-trivial in NWP models, detailed observational datasets from field campaigns, such as in this study, can be used to evaluate the physical processes at the scale of individual weather systems. Data from radiosondes launched from Oden were assimilated into the MetUM forecasts via the Global Telecommunications System. The result of this is that the validation data set is not independent of the forecast diagnostics but it does however minimise errors in regional circulation, allowing the focus of the model evaluation to be the parameterised processes. The MetUM is well placed to take advantage of this approach because the climate model (HadGEM1) and the global NWP version have a very similar dynamical and physical formulation (Martin *et al.*, 2006).

In Chapter 4 diagnostics from both the version (G42) of the global NWP model available in 2007, and the version operational during 2001 (G25) are used to help determine whether updates to the model physics since 2001 have improved the simulation of the Arctic region. UM(G25) has a dynamical core based on the Eulerian and hydrostatic formulation

described in Cullen & Davies (1991) and the physical formulation was similar to the HadAM3 climate version (Pope *et al.*, 2000). Data sets from this version of the model are comprised of 12-hour operational forecasts, initialised from 00 UTC and 12 UTC analyses, sampled at 3-hour forecast intervals (t + 3, 6, 9, 12 hours) and cover the entire August ice drift observation period. 3 hourly diagnostic data from every 12 hour forecast are concatenated to produce a continuous data series from August 3rd to 20th 2001.

Since 2001 both the NWP and climate versions of the MetUM have undergone a large number of developments. The Eulerian/hydrostatic dynamical core has been replaced by a semi-Lagrangian, semi-implicit and non-hydrostatic formulation (Davies *et al.*, 2005) and many of the physical parameterisations have been updated (Allan *et al.*, 2007). In addition the 3D-Var (three dimensional variational) data assimilation system (Lorenc *et al.*, 2000) has been replaced by a 4D-Var system (Rawlins *et al.*, 2007). The operational global NWP horizontal resolution for the UM(G42) version is 0.375° latitude by 0.5625° longitude, but was run here at the same horizontal resolution as UM(G25), 0.56° by 0.83° to simplify the comparison. UM(G42) was run for the 2001 observation period, with initial conditions provided by the European Centre for Medium-Range Weather Forecasts (ECMWF) 40 year reanalyses (ERA-40). The model forecast fields are output at 15 minute intervals out to 4 days. The second day of each forecast has been assembled in a similar way to the data in UM(G25) to obtain a continuous data set for the observation period. Using the second day of each forecast allows time for the necessary spin-up after model initialisation but keeps accumulated model errors to a minimum, allowing for optimum comparison with the older model version. In contrast, the UM(G25) data sets are from operational forecasts for which no spin-up time is required due to the ongoing nature of the forecast and data assimilation cycle. Although the same horizontal grid resolution is used with both versions of the model, the vertical resolution in UM(G42) is much greater: 12 vertical levels in the lowest 3km of the atmosphere, where the first 3 are at 10, 50 and 130 m, compared to UM(G25), which has 6 levels. Vertical grid box height is defined in pressure levels in the older version of the model, the first 3 roughly translate to a few meters above the surface, 330 and 530 m. Observations from all over the globe were assimilated into the ERA-40 and 2001 MetUM analyses used to initialise the forecasts. Radiosondes from the AOE 2001 field campaign were submitted to the Global Telecommunications System during the field campaign and were thus utilised in the ERA-40 and 2001 MetUM analyses.

The radiation scheme used in UM(G25) is described by Slingo & Wilderspin (1986) and Slingo (1989). The cloud scheme uses a prognostic method, where both cloud ice and water contents are diagnosed from the relative humidity (Smith, 1990). An improved radiation scheme based on the two-stream equations in both the longwave and shortwave spectral regions was introduced into UM(G42) following Edwards & Slingo (1996). This

allows for consistency in physical processes that are important in both spectral regions, such as overlapping cloud layers. It includes the treatment of the effects of non-spherical ice particles and allows multiple scattering between cloud layers. The cloud scheme in UM(G42) remains based on that by Smith (1990) but a cloud/precipitation microphysical scheme with prognostic ice was introduced (Wilson & Ballard, 1999), based on that by Rutledge & Hobbs (1983). Cloud ice water content is now advected, although cloud water content is still determined from a diagnostic relationship with relative humidity.

Both versions of the MetUM use a boundary-layer scheme based on Monin-Obukhov similarity theory and surface fluxes are computed following Louis (1979). The surface roughness length of momentum, z_0, is set at a constant value of 0.003 m and it is assumed the surface roughness lengths of heat, z_h and humidity, z_q, are equal to $z_0/10$. The surface albedo in both versions of the model depends on the surface temperature (Ingram *et al.*, 1989). When the ice surface temperature is at its maximum (273.15 K) the albedo is 0.5 and this increases to a maximum of 0.8 as the surface temperature decreases to 263 K. Although the MetUM can be run as a fully coupled ocean-atmosphere model, both NWP versions used here have fixed sea ice fractions over each forecast period. This far north both versions of the model assume 100 % sea ice cover. It is only in the marginal ice zone that an open lead fraction is simulated. Sea ice thickness is also constant, at 2 m.

In Chapter 6, consistent with the UM(G25) data set in Chapter 4, the time series of diagnostics from the MetUM are comprised of 12-hour operational forecasts, initialised from 00 UTC and 12 UTC analyses, sampled at 3-hour forecast intervals (t + 3, 6, 9, 12 hours) and cover the entire ASCOS ice camp period. 3 hourly diagnostic data from every 12 hour forecast are concatenated to produce a continuous data series from August 13th to September 2nd 2008. Model data is selected from the grid box containing the ship's location at each time step. The version of the MetUM used to produce these forecasts is model cycle G48, which was operational in August 2008. In contrast to 2001, data from the ASCOS radiosonde launches were submitted to the Global Telecommunications System but were not used in the MetUM forecast and data assimilation cycle.

3.4.2 HadGEM1

The Hadley Centre Global Environmental Model, Version 1 (HadGEM1) (Johns *et al.*, 2006; Martin *et al.*, 2006) is the climate version of the Met Office Unified Model; the atmospheric component is very similar in formulation to the recent versions of the global NWP MetUM described in the previous section. This version of the climate model was the first to incorporate the new non-hydrostatic atmospheric dynamical core (Davies *et al.*, 2005) that is now used in the operational NWP system. The horizontal resolution

is 1.25° latitude by 1.875° longitude and is run with 38 vertical levels, with the lowest at 20, 80 and 180 m.

Unlike the NWP version of the MetUM, the atmospheric component is coupled to an ocean and sea ice model. Daily mean parameters that are calculated in the ocean and sea components, such as surface currents, ice depths and the atmosphere-to-sea ice fluxes are passed to the atmosphere once a day (Johns *et al.*, 2006). The ocean component is based on the scheme by Bryan (1969) and Cox (1984); latitudinal resolution is 1° and the longitude varies between 1° at the poles to 1/3° at the equator. The sea ice component resolves sub grid-scale ice thickness distribution (Thorndike *et al.*, 1975; Lipscomb, 2001), where the evolution of the thickness is determined by thermodynamic growth and melt (Semtner, 1976), advection (Hunke & Dukowicz, 1997) and redistribution by ridging (Hunke & Lipscomb, 2004). The sea ice surface albedo is similar to the temperature dependent scheme in the NWP version but the minimum albedo for bare ice is set to 0.6 instead of 0.5, a dependency on snow cover is included and partial snow cover within a grid box can modify the bare ice albedo in a scheme similar to that by Cox *et al.* (1999).

For this study HadGEM1, Version 1 was run with fixed present day greenhouse gas forcing and land surface boundary conditions to allow the most straightforward comparison with the AOE 2001 and ASCOS observations. Daily mean data from a 7 year simulation were output and diagnostics were averaged over the 7 year period for each day in the 360 day year. Diagnostics from a grid box close to both the AOE 2001 and ASCOS measurement locations were selected for comparison with the observations.

3.4.3 COAMPS

The Coupled Ocean/Atmosphere Mesoscale Prediction System (COAMPS) was developed by the Naval Research Laboratory, USA (Hodur, 1997; NRL, 2003). It was run for AOE 2001 with an outer domain covering the whole pan-Arctic region, including the marginal ice zone and some open water and land. The outer domain had a resolution of 54 km while two inner domains were nested at 18 and 6 km resolution respectively. The innermost domain was centred around the AOE 2001 observation locations. All domains had the same vertical grid, with 45 vertical model levels in the lowest 3 km of the atmosphere; with the first three levels at 3, 10 and 17 m. Two-way nesting between domains was not implemented.

The fluxes at the surface were modelled with a surface energy-balance model adapted to sea-ice conditions. It is based on a simple force-restore concept with a fixed ice thickness of 2 m using a 'deep layer temperature' fixed at the freezing point of sea water, -1.7 °C. Ice cannot melt or accumulate in the model but ice extent and fraction was updated

every 24 hours during the model run from satellite observations. In the grid boxes as far north as the observation site, the surface is completely covered in ice, with no open lead fraction. The boundary-layer turbulence scheme is based on Mellor & Yamada (1974) and the surface turbulent fluxes are computed using a bulk Richardson number, based on the formulations presented in Louis (1979). z_0 is set at a constant value of 1.4x10^{-5} m and like the MetUM, it is assumed $z_h = z_q = z_0/10$.

At the surface a simplified snow model is applied, with a skin-surface temperature parameterisation. A fraction of any melted snow is retained as liquid inside the snow layer and is allowed to refreeze if the bulk snow temperature sinks below 0 °C. Snow albedo is set with a base value of 0.70 and a top value of 0.85. At each new snowfall, the surface albedo is reset to the top value and is then relaxed back to the base value with a relaxation time of a few days during the melt conditions. Each grid point is either ice covered or open water, as specified using Special Sensor Microwave Imager (SSM/I) satellite data.

The moist microphysics scheme is based on one developed by Rutledge & Hobbs (1983) and consists of a bulk cloud microphysical model (Lin *et al.*, 1983) and a single-moment prediction of mixing ratio for 5 microphysical variables (vapour, pristine ice, snow, rain and cloud water). The size distribution of Marshall & Palmer (1948) is used, along with Kessler auto-conversion (Kessler, 1969) and the Fletcher formulation for nucleation of pristine ice (Fletcher, 1962). The radiation scheme performs both longwave and shortwave transfer calculations, based on the work of Harshvardhan *et al.* (1987).

The outermost domain was forced by ERA-40 reanalysis data, which has a resolution of 1.5° latitude and 1.5° longitude. In contrast to the MetUM model runs, COAMPS was run in a "climate mode". The simulation, covering the entire AOE 2001 ice drift period, was run without any constraints from assimilation of observational data, except for that contained in the ERA-40 data used at the outermost boundary. It should be noted however, that the ERA-40 data does include the assimilation of the AOE 2001 radiosonde observations. With an outer domain covering the entire Arctic Ocean it is expected that the exact development of the atmospheric circulation will deviate more from the observations than those in the MetUM simulations. Systematic model errors present in all models are here allowed to fully develop over time and the chaotic nature of the atmospheric system and the size of the domain ensures conditions well away from the lateral boundaries of the outermost domain deviate from reality. It is important to realise that such differences need not be erroneous in a physical sense but are an expression of the stochastic nature of the atmosphere. Due to these differences, the relative success of how the MetUM and COAMPS capture individual events cannot be assessed with confidence. Statistical comparisons however are useful, since biases over a longer period of time indicate fundamental differences in the model climates. It is more informative

to compare MetUM model cycles G25 and G42 since these data sets were produced in a much more similar way and a comparison will give insight into whether changes to the MetUM that were implemented between 2001 and 2007 have increased its accuracy in the Arctic region.

Chapter 4

An evaluation of MetUM and COAMPS using AOE 2001 observations

4.1 Introduction to evaluation

When evaluating either global or regional scale models against observations a comparison of single point observations must be made with grid box averaged model diagnostics. Some care must be taken interpreting such comparisons since, for at least some of the variables, the two may represent rather different physical properties.

The main meteorological mast was located on a large ice floe, 300 m from the open water around the Oden and a significantly larger distance from open leads in all other directions. All observations discussed here were made either on or near the mast, apart from measurements made by the ceilometer and S-band radar, which were located on board the Oden and by the ISFF stations, which were made on separate ice floes. The observations will represent conditions over the local pack ice, rather than conditions averaged over a region the size of a grid box, which will in reality contain a fraction of open leads. Compared to the pack ice, open leads can be a significant source of moisture, meaning conditions in their immediate vicinity can be quite different to those over the ice. Having said that, the ice and lead temperatures during August are much more similar than at other times of the year and the Arctic sea ice is relatively homogeneous compared to land surface types at lower latitudes. Figure 4.1 shows near-surface air temperature measurements from the main meteorological mast and the three ISFF stations, one of which was located next to an open lead. This shows air temperature did not vary significantly over small distances on the main ice floe or between the middle and the edges of the ice floe.

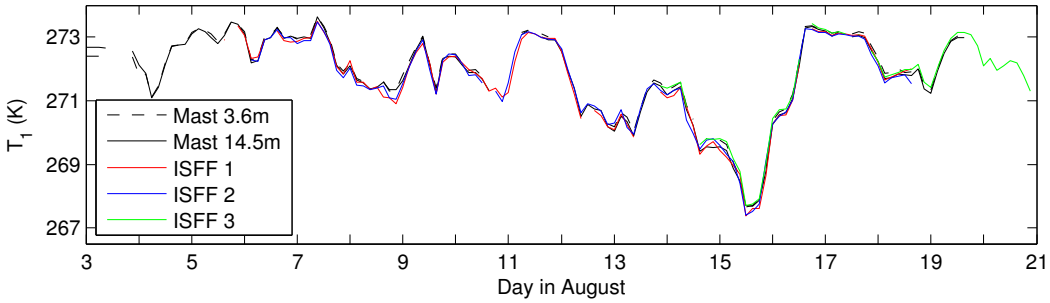

Figure 4.1: 3 hourly averages of near-surface air temperature observations from the meteorological mast and the 3 ISFF stations.

In addition to this, none of the three models include an open lead fraction in grid boxes this far north and the variability in diagnostics between the selected grid box and the surrounding ones was found to be very small in both models. Consequently, providing these issues are appreciated, it seems adequate to compare the observations and models in this way.

Figure 4.1 also shows there is negligible difference between the air temperature measurements at 3.6 and 14.5 m on the mast. Since the measurements made at the upper mast height are more continuous, they are used in comparisons with modelled T_1, which refers to 1.5 m and 3 m above the surface in the MetUM and COAMPS respectively. This is also true of the humidity measurements (not shown). Observed 10 m wind speed was derived by interpolation of the wind speed at the 7.1 and 12.9 m measurement levels for comparison with modelled wind speed at this height.

The albedo and radiation measurements were made over undisturbed snow on the pack ice and therefore do not fully represent a region of sea ice on spatial scales the size of a model grid box, which includes a fraction of open leads and melt ponds. Without further radiation measurements over these various surface types, the effect of an open water fraction on the surface albedo is difficult to quantify. For this study however, both models assume the sea ice fraction is 100 % at 88-89°N and thus evaluating the model data using radiation measurements over ice surfaces only is considered valid and adequate for the methods of analysis used here.

The comparisons in this study are conducted using either time series or time-height cross-sections of the variables under consideration. To complement this, a basic statistical analysis is also presented in Table 4.1, which compares 117 three-hourly mean model and observational data points. The absolute bias is the mean difference between each observed and modelled parameter. The mean observation is also given, along with the standard deviation, σ of the differences between each 3 hourly observation and modelled value. Models that reproduce the observations to a high degree of accuracy should

have a low absolute bias and a low standard deviation. When testing for the degree of correlation, a model could produce the correct signal even if it is out of phase with the observations, returning a low or even negative correlation coefficient. For this reason both the correlation coefficient, R and the 'Index of Agreement', IoA have been computed. IoA is an alternative to R that takes into account phase differences between two signals. As an example, the correlation coefficient between two sine functions that are a quarter of a wavelength out of phase is zero, whereas the IoA is about 0.4, and so similarity can be detected even in poorly correlated signals (Tjernström *et al.*, 2005). IoA is defined as:

$$\text{IoA} = 1 - \frac{\sum_1^n (P - O)^2}{\sum_1^n (|P - \overline{O}| + |O - \overline{O}|)^2} \tag{4.1}$$

where P and O are the predicted and observed values respectively, n is the number of observations and an overbar indicates a time average (Tjernström *et al.*, 2005).

4.2 Basic Meteorological Fields

Figure 4.2 shows a time-height cross-section comparing air temperature from radiosonde observations with that diagnosed by the models. There are two obvious warm periods above 500 m between August 9-12 and 15-18, which all three models reproduce more or less accurately. Warmer air was also observed up to 1500 m between August 4.5-7.5, which is less well represented by the two MetUM models and not at all by COAMPS. A cold period occurs throughout the lowest 3 km of the atmosphere between August 12-16, with a distinct region of cold air in the lowest 400 m on August 14-15. The MetUM simulates the cold air aloft with reasonable accuracy, with UM(G42) producing the best results. The cold air close to the surface however, is not reproduced at all in either version of the model. This is also illustrated in Figure 4.3a, which shows T_1 over the entire ice drift period. The observed cold period on August 15 is not at all evident in UM(G42), which keeps the temperature fairly constant, very close to 273 K, the freezing point of fresh water and UM(G25) produces only a slight decrease in temperature. COAMPS produces a drop in temperature close to the surface on August 15 but for a much shorter duration than the observed cold event. All three models have a mean positive bias in T_1 (i.e. the models are too warm), with UM(G42) showing the largest discrepancy (Table 4.1). None of the models are well correlated with the observations.

Ice surface temperature, T_{ice}, measurements were derived from the surface longwave radiation flux following Persson *et al.* (2002b). Observed T_{ice} ranges between 273 and 267 K (Figure 4.3b) and T_1 follows a similar variation over time. All three models show a positive mean bias in T_{ice} of at least 1 K. UM(G42) performs the worst, where T_{ice}

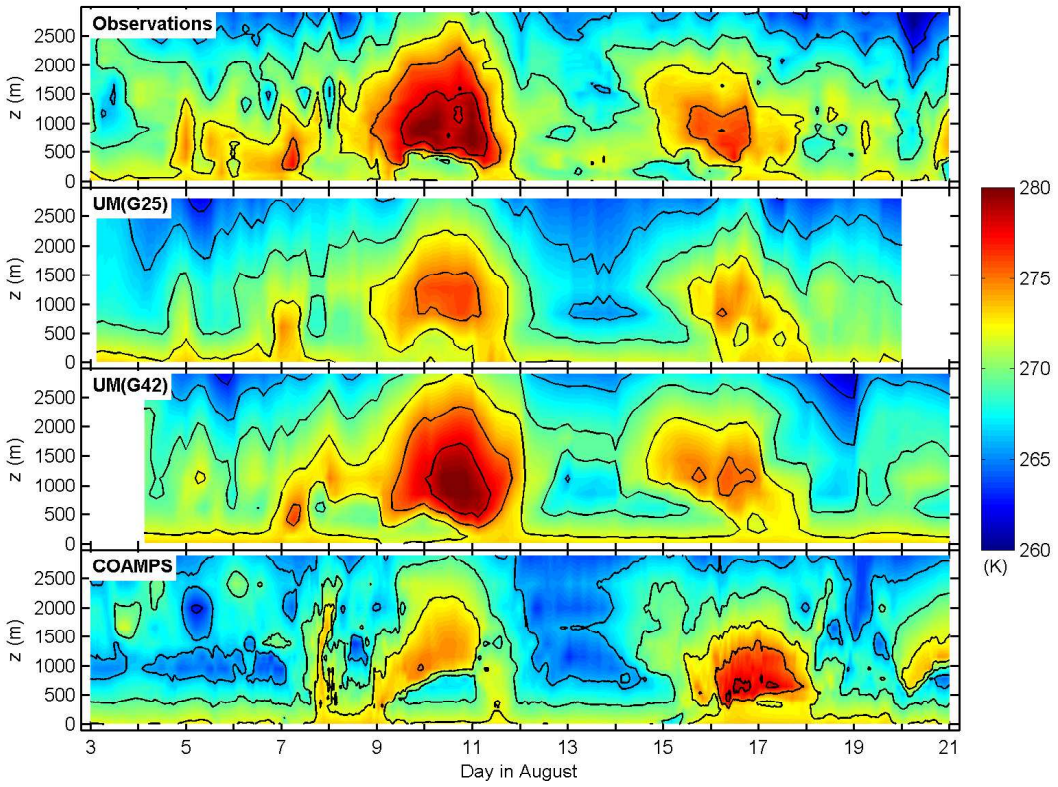

Figure 4.2: Air temperature measurements from the 6 hourly radiosondes compared to model diagnostics during the AOE 2001 observation period. Isopleths are at 3 K intervals.

remains at 273.1 K for almost the entire duration of the observation period, except for a very small decrease on August 15. COAMPS produces a similar magnitude of error in T_{ice} and none of the models are correlated well with the observations.

Table 4.1: Statistics of model diagnostics compared to observations using 3 hourly averages. The absolute bias (a.b.) is the mean difference between each observed and modelled parameter. A positive bias implies that for a given parameter, the model produces a value of higher magnitude than that observed. The mean observation over the entire field campaign ($\bar{x}_{obs}$), the standard deviation (σ) of the difference between each 3 hourly averaged observation and modelled value, the correlation coefficient (R) and the 'Index of Agreement' (IoA) are also given.

			UM(G25)				UM(G42)				COAMPS			
	unit	$\bar{x}_{obs}$	a.b.	σ	R	IoA	a.b.	σ	R	IoA	a.b.	σ	R	IoA
p	hPa	1004.16	0.24	1.25	0.98	0.99	0.52	1.70	0.97	0.98	-2.21	3.31	0.86	0.89
U_{10m}	m s^{-1}	4.39	-0.56	1.32	0.71	0.81	-0.16	1.62	0.67	0.80	0.60	2.58	0.37	0.58
u_*	W m^{-2}	0.19	0.05	0.08	0.70	0.78	0.02	0.05	0.84	0.90	-0.05	0.10	0.21	0.49
q_1	g kg^{-1}	3.38	0.06	0.26	0.69	0.73	0.17	0.26	0.71	0.69	-0.03	0.35	0.45	0.68
T_1	K	271.77	0.79	1.19	0.50	0.54	1.33	1.30	0.25	0.47	0.53	1.32	0.39	0.59
T_{ice}	K	271.72	0.99	1.26	0.28	0.47	1.38	1.30	0.53	0.44	1.03	1.49	-0.16	0.37
$cldfrac$	-	0.79	0.01	0.31	-0.01	0.34	0.19	0.27	0.15	0.46	-	-	-	-
LW_{dn}	W m^{-2}	296.50	-9.34	14.62	0.60	0.71	8.90	17.84	0.18	0.48	-11.02	27.68	0.00	0.27
LW_{up}	W m^{-2}	309.10	4.49	6.01	0.13	0.45	6.51	5.93	0.31	0.44	4.71	6.79	-0.16	0.37
SW_{dn}	W m^{-2}	135.23	16.15	51.63	0.63	0.74	-35.76	40.17	0.49	0.60	24.60	53.13	0.38	0.57
SW_{up}	W m^{-2}	107.58	-23.19	35.28	0.60	0.70	-57.83	31.81	0.49	0.48	12.80	41.50	0.46	0.65
LW_{net}	W m^{-2}	-12.60	-13.83	16.10	0.42	0.57	2.39	16.14	0.08	0.35	-15.73	25.98	-0.11	0.19
SW_{net}	W m^{-2}	27.66	39.34	27.46	0.40	0.30	22.07	16.96	0.33	0.40	11.80	14.87	0.19	0.41
Rad_{net}	W m^{-2}	15.06	25.51	21.69	-0.08	0.27	24.46	16.18	0.04	0.32	-3.93	19.11	0.11	0.37
H	W m^{-2}	-2.07	0.49	6.75	0.52	0.59	2.35	5.51	0.37	0.53	0.32	5.00	0.27	0.52
E	W m^{-2}	-5.09	-9.99	8.83	0.14	0.34	-4.00	7.85	0.07	0.37	2.97	5.20	0.06	0.40
tot_{hflx}	W m^{-2}	7.09	16.01	18.92	-0.07	0.34	22.81	17.61	0.22	0.42	-0.64	18.00	0.31	0.46

The radiosonde observations show that relative humidity with respect to water was constantly above 90 % in the lowest 100 m of the atmosphere, which all three models simulate well (Figure 4.4). There are periods of high humidity throughout the lowest 3 km of the atmosphere on August 3-7, 11, 16 and 19, which are also represented well in the models. The observations show two prolonged periods of low humidity aloft, occurring between August 9-11 and 12.5-16 and there are additional shorter low humidity periods throughout the measurement period. UM(G25) and UM(G42) simulate most of the low humidity events well (e.g. August 10) but neither produce low enough humidities between August 14-16. COAMPS generally represents the timing of low and high humidity periods accurately but away from the surface there is a general bias towards higher humidities than those observed. The near-surface specific humidity, q_1 (Figure 4.3d and Table 4.1) is positively biased in both versions of the MetUM and negatively biased in COAMPS but the bias is small and all three models show at least reasonable correlation to the observations.

Observed wind speeds up to 3 km in altitude were often below 5 m s^{-1} but there are notable periods of stronger winds on August 5-9, 12 and 16 (Figure 4.5). Both versions of the MetUM capture the high wind events with reasonable accuracy, although there is a tendency to underestimate the speed. COAMPS reproduces the magnitude of the high wind events with some accuracy but these events are often phase shifted in time. This is not unexpected since COAMPS is free to develop without daily assimilated observations, apart from at the model boundaries. Both these points are highlighted in the 10 m wind speed, U_{10m} in Table 4.1 and Figure 4.3e; both versions of the MetUM show a negative bias, although it is much smaller in UM(G42). The wind speed in COAMPS is positively biased and has a lower correlation coefficient than the MetUM. Modelled surface pressure is by far the best simulated diagnostic (Figure 4.3f), where the bias is notably larger and the correlation notably less in COAMPS than in either version of the MetUM.

The p, U_{10m} and q_1 fields and air temperatures away from the surface are represented reasonably well in all three models. This is not surprising since the AOE 2001 radiosonde observations were utilised in the UM(G25) forecasts and to produce the ERA-40 data used to initialise the UM(G42) forecasts. The models should therefore be expected to reproduce these basic meteorological fields with at least reasonable accuracy. COAMPS performs notably worse than the MetUM in these basic parameters because it was run without any constraints from assimilation of observational data, except for at the outermost boundaries. The fact that the difference between the correlation coefficient and the IoA for U_{10m} and q_1 is much greater in COAMPS than the MetUM indicates that the general signal is correct but it is out of phase with the observations. Errors in the surface flux and cloud diagnostics produced by inaccuracies in the larger scale circulation rather than in the physical parameterisations will occur in all three models but are likely

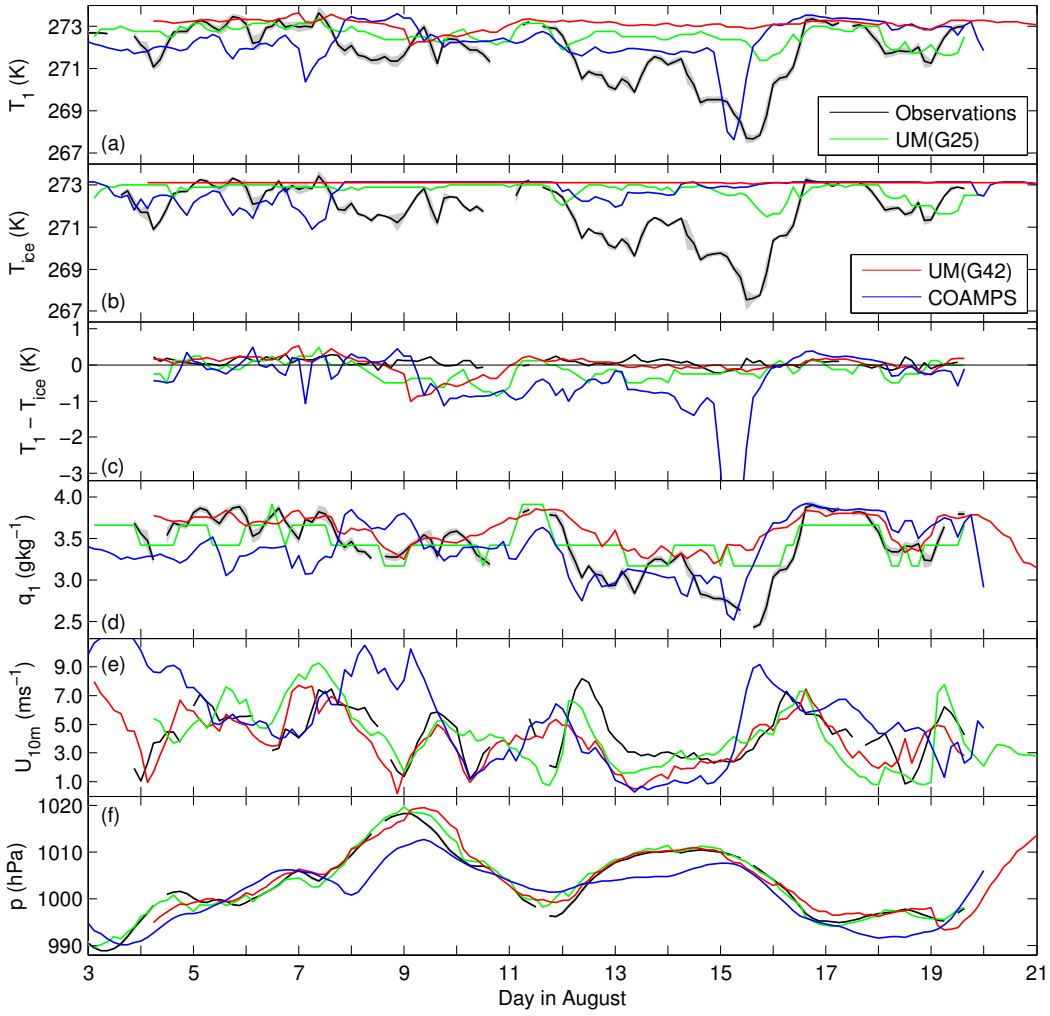

Figure 4.3: Three hourly mean observations and model comparisons during the AOE 2001 observation period. 3 hourly mean (a) near-surface air temperature, T_1 (b) ice surface temperature, T_{ice} (c) T_1 - T_{ice} (d) near-surface specific humidity, q_1 (e) 10 m wind speed, U_{10m} and (f) surface pressure, p. All measurements, except for T_{ice} were made on the meteorological mast. The grey area represents ± 1 standard deviation about each 3 hour mean observation.

to be more significant in COAMPS. It is therefore important to assess the success of a model compared to the observations based on mean values over extended periods of time rather than on its representation of individual weather events and that MetUM-COAMPS comparisons should be made with caution due to the fundamental differences in model set-up.

4.3 Surface Turbulent Fluxes

Observed and modelled friction velocity u_*, and the turbulent fluxes of sensible, H and latent, E heat are presented in Figure 4.6, along with a statistical analysis in Table 4.1.

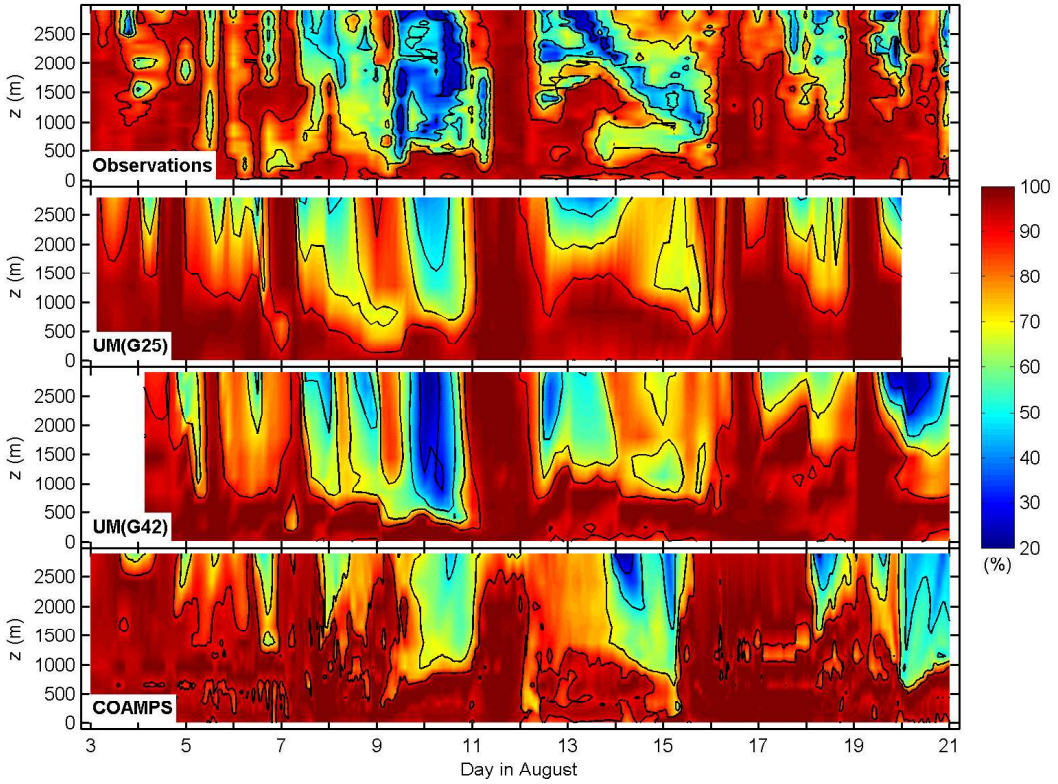

Figure 4.4: Same as Figure 4.2, but for the relative humidity with respect to water. Isopleths are at 20 % intervals.

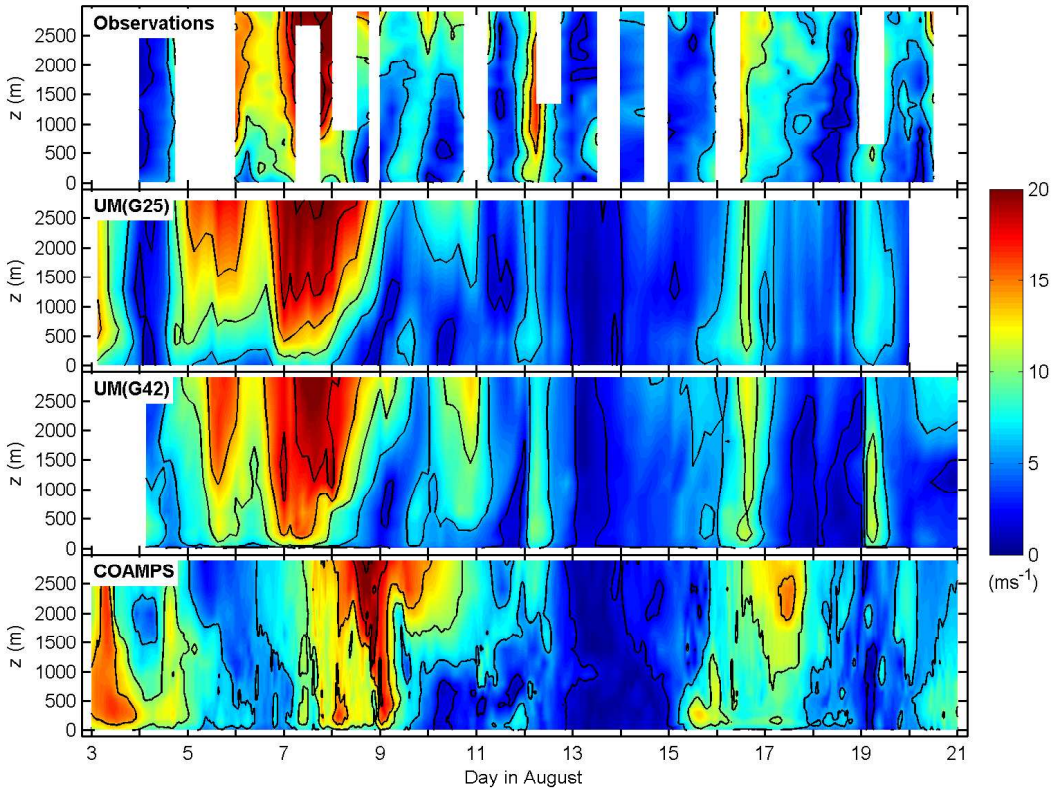

Figure 4.5: Same as Figure 4.2, but for wind speed. Isopleths are at 4 m s^{-1} intervals. Missing observations are due to instrument failure.

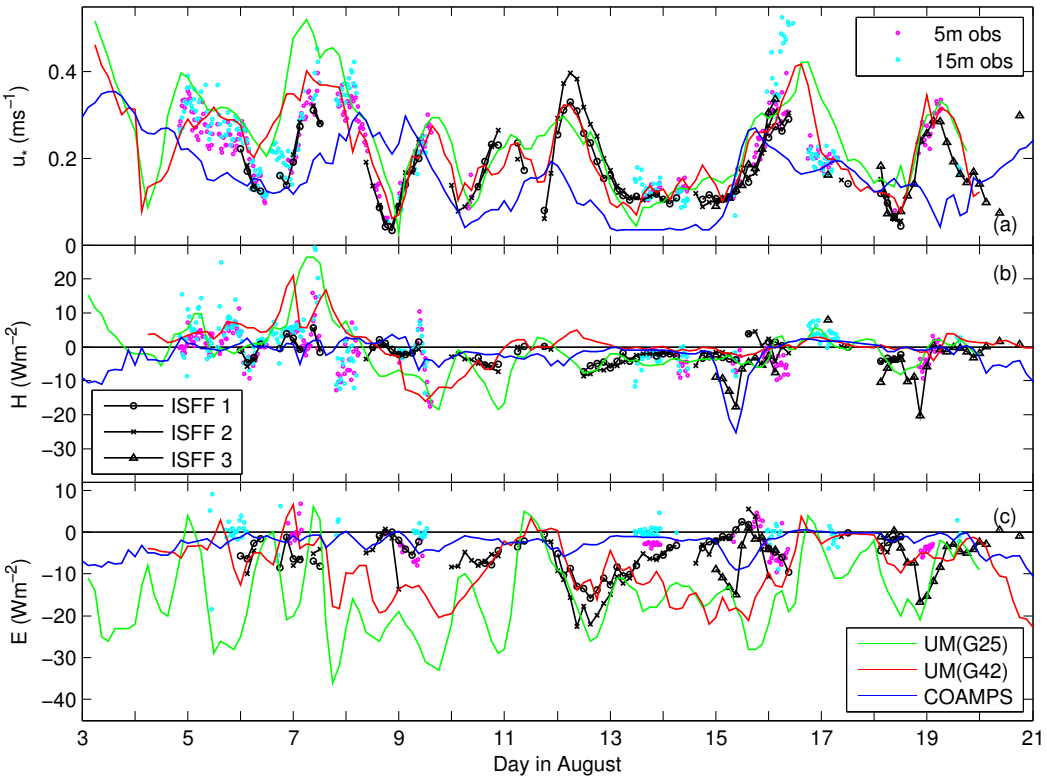

Figure 4.6: Surface flux observations and model diagnostics, (a) friction velocity, (b) sensible heat, (c) latent heat. Model diagnostics and measurements from the ISFF stations are presented as 3 hourly averages and the measurements from the meteorological mast are half hourly averaged fluxes. A positive flux represents a transfer of energy to the surface.

Throughout this chapter, the surface radiative and turbulent fluxes are defined such that a positive flux represents a transfer of energy to the surface. Comparing model diagnostics to the observed turbulent fluxes requires an assumption that the flux sampling error is small and can be neglected. As discussed in Section 2.1.5, typical flux sampling errors are estimated at 12 to 31 % (Finkelstein & Sims, 2001). The use of observations from the three ISFF stations, in addition to those from the meteorological masts illustrates the spatial variability in the observed fluxes and therefore, gives an indication of the possible extent of the sampling error. There are some differences between the observations made at each of the sites but the general trend is consistent between all locations.

There were significant problems with ice and condensation forming on the sensing heads of the sonic anemometers and Krypton hygrometers on the meteorological mast during AOE 2001, limiting the turbulent flux data set that is available for analysis. The measurements from the three ISFF stations are however more extensive and there is reasonably good agreement between these and the mast data, giving confidence that the measurements used from each location are representative of average conditions over the whole region.

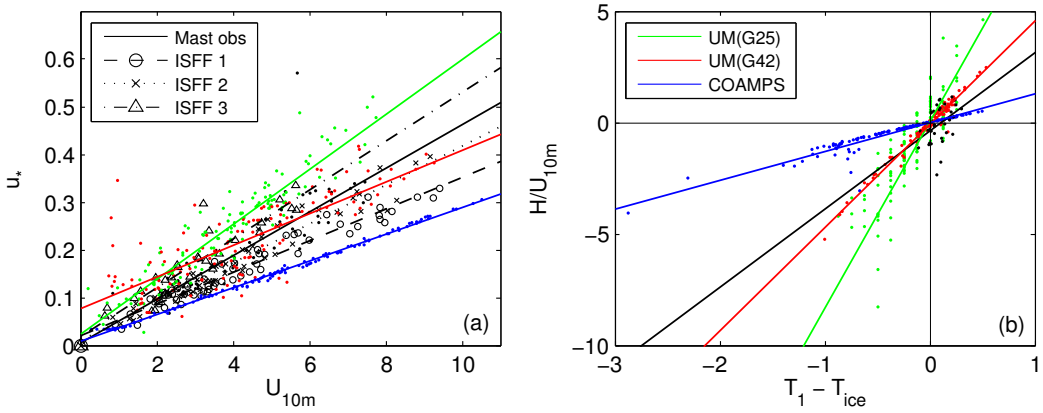

Figure 4.7: Modelled and observed 3 hourly averaged (a) u_* against U_{10m} and (b) H/U against $T_1 - T_{ice}$. The observations are represented by the black symbols and the model diagnostics by coloured dots. The straight lines are linear regressions of the observations or model data. The gradients of the lines are directly related, but not equal to the transfer coefficients.

The values of u_* produced by UM(G25) and UM(G42) are well correlated with the observations, which is expected since the correlation between modelled and observed U_{10m} is also high. Both versions of the MetUM produce a small positive bias in u_*, even though the wind speeds show a small negative bias. Figure 4.7 compares the value of u_* to the value of U_{10m}, where the gradient of each line is representative of the transfer coefficient at 10 m above the surface. The range of gradients produced by the observations is most likely indicative of the spatial variation in roughness length over the measurement sites. The scatter of model data around the model linear regressions is due to the variation in atmospheric stability. Tjernström (2005) estimated the mean value of z_0 during the AOE campaign at 0.003 m. This is an order of magnitude higher than the value computed for SHEBA (Persson *et al.*, 2002b), although that value represents average conditions over the entire 12 month campaign rather than over the summer months only. z_0 is set to a constant value of 0.003 m in the MetUM, equal to that observed. The transfer coefficient produced by UM(G25) is too large, explaining the slight positive bias in u_*. Since the value of z_0 is accurate in the model this bias could be explained by its representation of atmospheric stability. The transfer coefficient produced by UM(G42) is closer to the observations, accounting for the smaller bias in u_*.

The correlation between observed u_* and that produced by COAMPS is poor compared to that between the MetUM and the observations. This is most likely due to the lower correlation between the modelled and observed wind speeds. COAMPS produces an overall negative bias in u_*, even though the overall bias in U_{10m} is positive. Figure 4.7 suggests this is due to an underestimation of the transfer coefficient, consistent with the low value of z_0 used in COAMPS ($1.4\text{x}10^{-5}$ m); two orders of magnitude lower than that observed during AOE 2001.

All three models show good agreement in the sensible heat flux during many periods of the field campaign (Figure 4.6b), although there is a tendency towards magnitudes that are too small (Table 4.1). Correlation between the models and the observations is generally low and the standard deviation of the bias high. The correlation coefficient in UM(G42) is similar to that produced by the other two models but the mean absolute bias is much larger.

Figure 4.7b shows H/U_{10m} plotted against $T_1 - T_{ice}$ for each model. Observations include measurements made from the meteorological mast only due to the lack of T_{ice} or upwelling longwave radiation flux measurements at the ISFF stations. In COAMPS $T_1 - T_{ice}$ (Figure 4.3c) is mostly too large in magnitude and on average over the entire observation period is the wrong sign compared to the observations. This should lead to an overestimation of the magnitude of H compared to the observations. However, the transfer coefficient is much smaller than that produced by the observations. This compensates for the overestimation of $T_1 - T_{ice}$. Both versions of the MetUM overestimate the transfer coefficient for H but the magnitude of H produced by the models is underestimated due to the low values of $T_1 - T_{ice}$.

Model biases in the latent heat flux, E are much larger than in either H or u_* and the correlation between each model and the observations is very low (Table 4.1). Both versions of the MetUM produce a negative bias in E (too much energy lost from the surface), which is consistent with other modelled and observed latent heat flux comparisons such as by Brunke *et al.* (2006) and Tjernström *et al.* (2005). COAMPS however produces magnitudes of E that are lower than the observations, at least in part due to the low value of z_q.

Another potential source of error in both modelled H and E is the representation of snow and ice in the models. In reality the surface temperature of sea ice adjusts very rapidly to changes in atmospheric forcing caused by, for example, variations in the radiative fluxes due to changing cloud conditions. Since neither the MetUM nor COAMPS incorporate a fully coupled ice model, the force-restore method used within them requires a relatively thick layer of ice at the surface to change temperature. This process may not occur quickly enough in the models, meaning the surface temperature reacts too slowly to changes in surface forcing and thus potentially causes errors in the modelled surface turbulent fluxes, which are forced by processes on synoptic or shorter time scales.

4.4 Cloud occurrence

Cloud fraction is a difficult quantity to measure and represent accurately. Observations were derived from ceilometer measurements, which retrieved cloud base height at a single point in the sky at a frequency of 4 samples per minute. A cloud fraction parameter was then computed from this by taking a time-average of the measurements over a 3 hour period. The cloud fraction variable determined by the MetUM is a parameterised spatial average, where cloud fraction on each model level in a grid box is used to compute a total fraction assuming maximum overlap (this type of cloud field is unavailable from COAMPS). A comparison of modelled and observed cloud fraction is, however, still worthwhile since a temporal average of clouds moving over a single point in the sky should have a quantitative relationship to a spatially averaged model parameter. The top panel of Figure 4.8a and Table 4.1 show these quantities. UM(G42) generally over-predicts cloud fraction, keeping it at 100 % for the majority of the time but it does reproduce some periods of decreased cloud fraction found in the observations, such as on August 18-19. This is in agreement with the findings of Tjernström *et al.* (2008), who found regional scale models produce clear conditions less frequently than what was observed during SHEBA. Over the whole observation period UM(G25) produces a lower absolute bias than UM(G42), although it shows a lower correlation with the observations.

Success in the representation of cloud occurrence cannot be assessed using only cloud fraction, since in theory a model could generate a perfect annual cycle of cloud fraction but still produce cloud at incorrect heights and with the wrong radiative properties. A more informative way of assessing modelled cloud is through the cloud ice and liquid water concentrations. Figure 4.8b,c show time series of ice water path (IWP) and liquid water path (LWP) for each of the three models and Table 4.2 presents the mean modelled IWP, LWP and total cloud water over the entire period. Since observations of these variables are not available from AOE 2001, mean values observed when clouds were present during August at SHEBA (Shupe *et al.*, 2006) are used as representative values for comparison. Additionally, mean cloud base measurements from the ceilometer and back-scatter from the S-band cloud and precipitation radar can be compared to the model time-height cross-sections of total cloud water concentrations (Figure 4.8d-f). Although patchy, the S-band radar shows several periods in which cloud extends to above 3 km, for example on August 11. These deeper clouds are associated with the passage of synoptic scale frontal systems, which included some precipitation. Low-level clouds or fog, which are too close to the surface for the S-band radar to observe, are indicated by the ceilometer cloud base measurements; cloud base was typically between 100 and 200 m.

Both versions of the MetUM show distinct periods during which cloud extends up to approximately 7 km (e.g. August 11, 16.5-17.0 and 19.0-19.5) and where radar data is

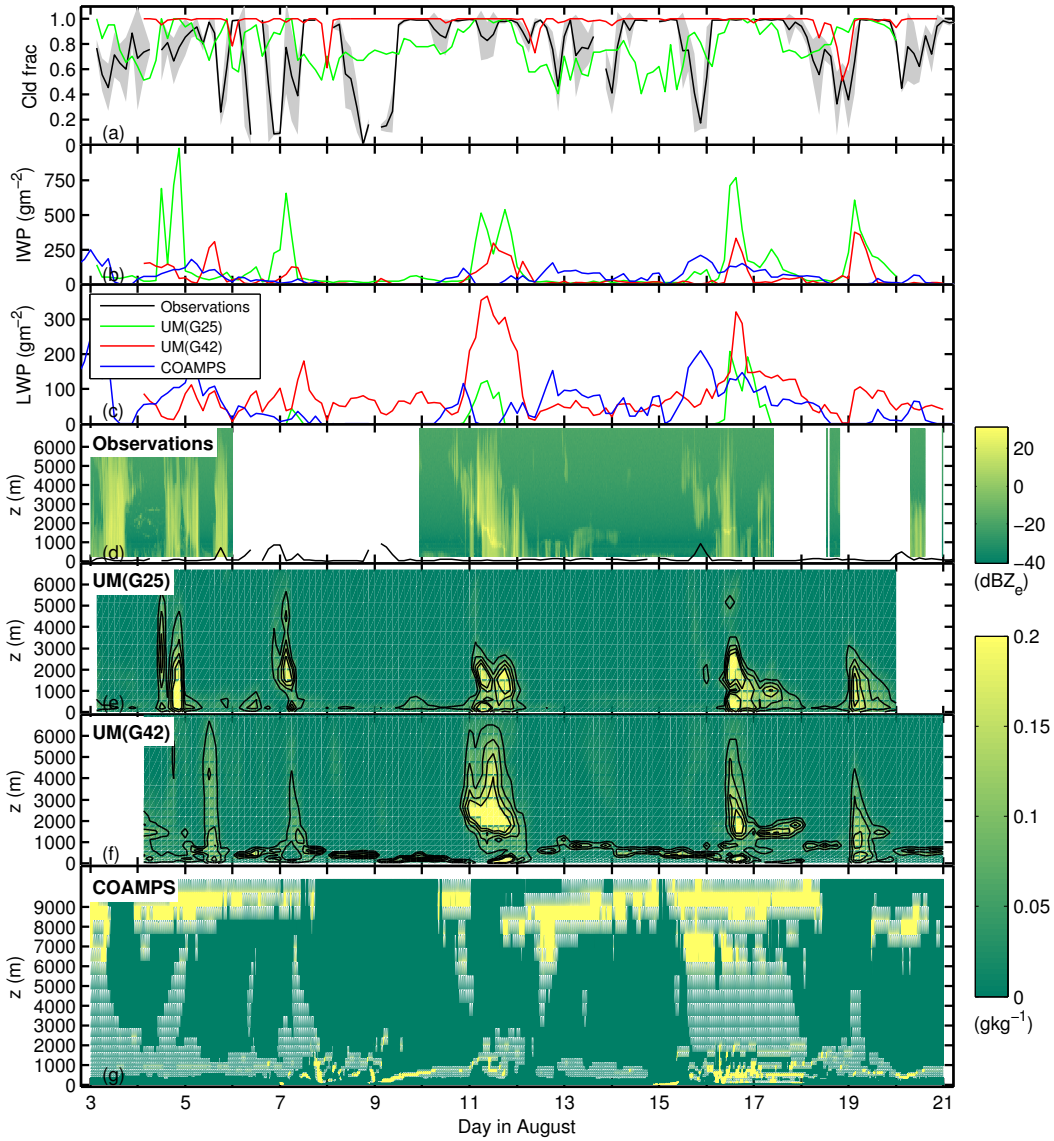

Figure 4.8: Cloud observations and model diagnostics, (a) 3 hourly averaged cloud fraction. The grey area represents ±1 standard deviation about each 3 hour mean observation. (b) modelled ice water path (no observations available) (c) modelled liquid water path (no observations available) (d) radar backscatter from the S-band cloud and precipitation radar. Backscatter is proportional to the amount of condensate in the atmospheric column, where the threshold at approximately 0 to +5 dBZ$_e$. The black line shows 3 hourly averaged mean cloud base measurements derived from the ceilometer. (e) UM(G25) profile of modelled total frozen plus liquid cloud water concentration. Isopleths are at 0.05 g kg^{-1} intervals. (f) same as (e) but for UM(G42), (g) same as (e) but for COAMPS.

Table 4.2: Mean modelled liquid and ice water paths (g m^{-2}) compared to mean observations during periods where clouds were present for the month of August from SHEBA (Shupe *et al.*, 2006).

	obs	G25	G42	COAMPS
IWP	50-60	116	51	51
LWP	70-90	11	83	15
IWP + LWP	120-150	127	134	66

available, the timing of these events is correct. The most obvious difference in cloud between the two versions of the MetUM is the near persistent cloud layer below 1 km in UM(G42) (e.g. August 12-15). In general, UM(G25) under-predicts low cloud and UM(G42) produces a layer of low level cloud which occurs too frequently compared to the observations and is not necessarily correct in its altitude, thickness or radiative properties. During the periods with deeper clouds both models produce peaks in IWP and LWP, although the magnitude of the LWP (IWP) peaks are significantly larger (smaller) in UM(G42). Furthermore, the LWP is between 25-100 g m^{-2} in UM(G42) and near zero in UM(G25) during the low-cloud periods such as August 12-16. The partition between ice and liquid cloud water in UM(G42) is consistent with the SHEBA data (Table 4.2). UM(G25) however, underestimates the value of liquid water and overestimates the value of ice water.

COAMPS produces high concentrations of cloud water at single grid points and zero cloud water at others, producing a sharp gradient between grid boxes containing high and zero cloud water concentrations, which accounts for the peculiar-looking profiles. The model produces cloudy skies for the greater part of the observation period, with cloud up to 10 km for the majority of the time. There is a distinct segregation of ice and liquid cloud water, where cloud water below 5 km is liquid and water above 5 km is ice. The IWP is similar to the observations during SHEBA, though the mean LWP is significantly lower.

4.5 Radiation and the total heat flux

To produce accurate climate predictions it is critical that the surface energy budget, including the radiative fluxes, are modelled correctly. Cloud fraction, thickness, and optical and microphysical properties all significantly influence the radiation balance at the surface. An evaluation of the modelled surface radiation budget, whilst important in its own right, will also give further insight into the success of cloud representation in the models.

As noted in Section 3.1, the sensor measuring SW_{up} at the mast site failed during the field campaign. Albedo is calculated from a second set of SW_{dn} and SW_{up} measurements, that were made periodically during the campaign. From this data, the albedo of the surface is estimated using a polynomial fit to the data clusters. To avoid unrealistic values produced by an extension of the polynomial to times before the first albedo observations were made, a constant value of 0.9 (the mean of the first observation cluster) is used for the previous day (August 4). The albedo is then used to calculate SW_{up} using SW_{dn} measurements from the first set of sensors. This process introduces some uncertainty in the radiation flux estimates. To assess the extent of this error the mean and standard deviation of each cluster of albedo data points is computed. The mean albedo measurement ± 1 standard deviation is 0.796 ± 0.02. This is then used to calculate the error range in the values of mean observed SW_{up}, SW_{net} and Rad_{net}, which are 107.58 ± 2.7, 27.66 ± 2.7 and 15.06 ± 2.7 Wm^{-2} respectively. The error is relatively small and even the uncertainty in the radiation fluxes calculated by the standard deviation of the cluster means (0.06, producing an uncertainty of ± 8.2 Wm^{-2}) is not significant enough to change the general relationship between each model and the observations.

Table 4.1 lists the mean absolute biases in the radiation components and Figure 4.9 shows scatter plots of the modelled and observed individual component and net surface radiative fluxes. The net surface radiative fluxes are defined such that a positive flux represents a transfer of energy to the surface. An important result from both the statistics and Figure 4.9 is the lack of correlation with the observations in all three models. The correlation is generally better in the separate upwelling and downwelling long and shortwave radiation components than in the net radiation fluxes, where the accumulation of errors in the separate components produces large biases. Since the downwelling radiation fluxes, LW_{dn} and SW_{dn}, are the important fluxes when considering the effects of cloud on the radiation balance, these are considered first.

Both UM(G25) and COAMPS overestimate SW_{dn} and underestimate LW_{dn} (Table 4.1). Shupe & Intrieri (2004) have found that the radiative properties of clouds with LWP values that are less than 20-50 g m^{-2} depend strongly on the value of the LWP, whereas clouds with larger LWPs behave almost as black bodies and thus the absolute value of the LWP is of less importance. In both UM(G25) and COAMPS the mean LWP is less than 20 g m^{-2} and much lower than expected based on the SHEBA data. This is the most likely cause of overestimated SW_{dn} and underestimated LW_{dn}. UM(G42) overestimates LW_{dn} and underestimates SW_{dn}; mean IWP and LWPs are much closer to the expected values and therefore the positive bias in cloud fraction is a more likely cause for the biases in downwelling radiation.

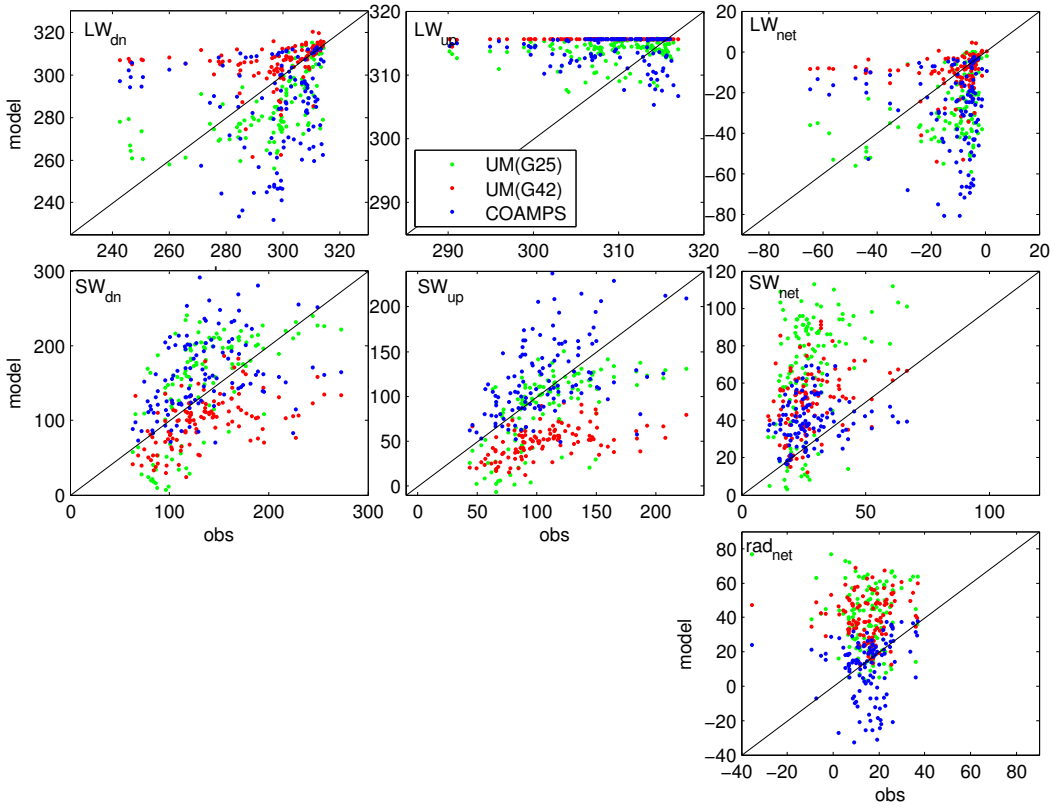

Figure 4.9: Comparison of 3 hourly averaged modelled and observed radiative fluxes. A positive flux in LW_{net}, SW_{net} and rad_{net} represents a transfer of energy to the surface.

LW_{up} is dependent on the temperature of the surface and is overestimated in all three models due to the positive bias in T_{ice}. These errors are however, small compared to those in SW_{dn} and LW_{dn} due to the relatively small temporal variation in T_{ice} during August. The value of modelled SW_{up} depends on the magnitude of SW_{dn} and the albedo of the surface. Figure 4.10 shows surface albedo observations made over the duration of the field campaign. The albedo over sea ice in the MetUM can vary between a minimum of 0.5 and a maximum of 0.8, depending on the temperature of the surface. Due to the overestimation of T_{ice} the albedo produced by both versions of the MetUM is too small and the error in UM(G42) is especially prominent; its almost constant value of 0.5 is obviously unrealistic. For UM(G25), the overestimation of SW_{dn} partially compensates for the underestimation of albedo, leading to a smaller underestimation of SW_{up}. The surface albedo in COAMPS is based on the amount of time elapsed since the last snowfall, rather than T_{ice} and produces the highest and most realistic values for albedo of all the models and therefore values of SW_{up} with the smallest bias.

Rad_{net} is overestimated in UM(G25) and UM(G42) by 25.5 and 24.5 Wm^{-2} respectively. The error in LW_{net}, and more specifically in LW_{dn} dominates in COAMPS and is reflected by an underestimation in Rad_{net} of 3.9 Wm^{-2}. The bias in LW_{dn} and SW_{dn} in COAMPS are similar to those in UM(G25), indicating both models produce a similar

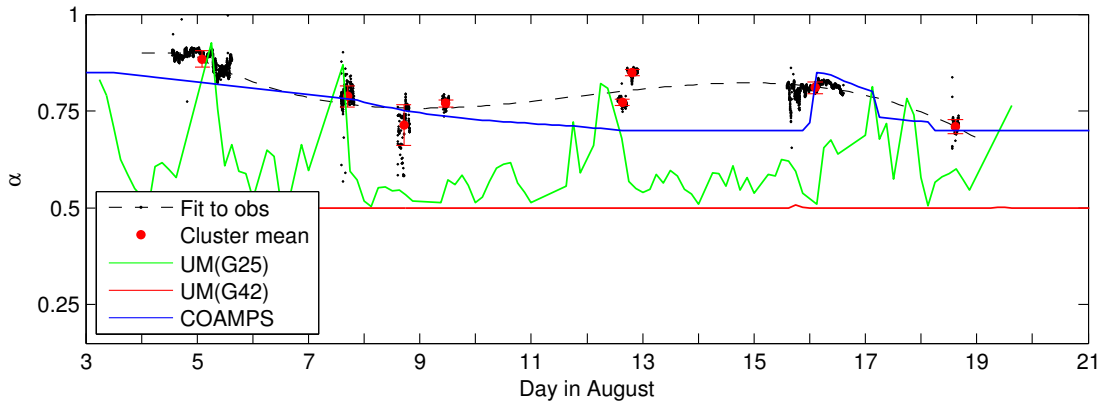

Figure 4.10: One minute averaged measurements of surface albedo made over an undisturbed snow surface and 3 hourly averaged model diagnostics.

magnitude of error from cloud forcing. This suggests the cause of the large bias found in Rad_{net} in UM(G25) and thus in UM(G42) is dominated by the unrealistic surface albedo parameterisation in the MetUM, with errors in cloud radiative forcing having a smaller but still important effect.

Table 4.1 shows that the mean observed net heat flux at the surface is +7.1 W m^{-2}. This is about half the value observed at SHEBA during the month of August (+15-19 W m^{-2}) (Persson *et al.*, 2002b). SHEBA measurements were made at a lower latitude and thus experience slightly higher insolation. UM(G25) and UM(G42) overestimate the observed value by +16.0 and +22.8 W m^{-2} respectively, even though the biases in the latent heat flux compensate for the errors in Rad_{net} to some extent. T_{ice} is calculated iteratively in the models from the turbulent heat fluxes and radiative terms in the surface energy budget. If any of these terms cause too much energy to be absorbed by the surface, modelled T_{ice} is overestimated. Since the albedo of the surface in the MetUM is based on T_{ice}, this causes an important feedback at the surface in the model. Errors in the model radiative fluxes cause an overestimation of the total heat flux; T_{ice} is positively biased and the albedo is underestimated. This underestimation causes too much SW_{dn} to be absorbed at the surface, further increasing the error in the total heat flux and T_{ice}. In UM(G42) this locks the albedo at its lowest value of 0.5. In UM(G25) the same feedback occurs but to a lesser extent due to the smaller bias in the total heat flux.

This conclusion is reinforced by results from a run of the MetUM Single Column Model (SCM). The SCM version of the MetUM encompasses all the parameterisations used in the global NWP version but allows the meteorology to be constrained by observations. Vertical profiles of the advective terms of wind, temperature and humidity are necessary to fully constrain the SCM at each timestep. These terms are not available from the AOE 2001 observations, although measurements of wind, temperature and humidity are available from the 6 hourly radiosonde launches. For each radiosonde launch the SCM was

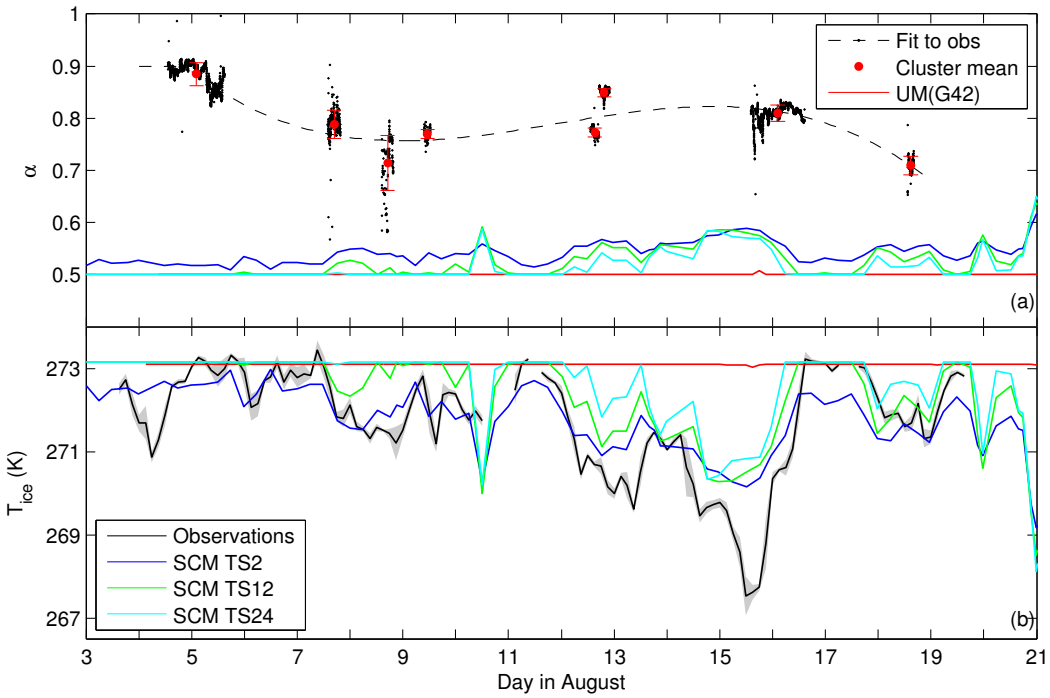

Figure 4.11: Albedo and T_{ice} diagnostics from the MetUM Single Column Model at time steps 2, 12 and 24, UM(G42) operational data and observations.

initialised using the observations and was allowed to run unconstrained for 24 timesteps (6 hours, 15 minute time steps). Data from a specific time step in each SCM run can be concatenated to form a continuous time series of data. This process was carried out for the 2nd, 12th and 24th timesteps. The albedo and T_{ice} diagnostics are shown in Figure 4.11. Shortly after initialisation with the observations (TS2) the albedo is significantly higher because the observed near-surface air temperature forces T_{ice} to below 0 °C. After the SCM has run unconstrained for 3 hours (TS12) the feedback is already apparent; T_{ice} increases due to errors in the surface energy budget causing the albedo to decrease, reinforcing the errors in the surface energy budget. After 6 hours (TS24) this bias has progressed even further. Since very few relevant observations are assimilated into the global NWP MetUM, T_{ice} is essentially unconstrained and therefore becomes locked at 0 °C during the summer season.

In reality, when an ice surface is at 0 °C additional heat input would melt the ice. In these models, where ice extent is prescribed and ice thickness is constant, an imbalance in the heat flux cannot cause the ice to melt and disappear. However, in a version of the model with a fully coupled ice model where ice extent and thickness are explicitly simulated, this imbalance could cause excess ice melt over the course of the summer season producing inaccuracies in future predictions of sea ice extent and other variables. The albedo parameterisation in the climate version of the MetUM (Hadley Centre Global Environment Model, HadGEM1) is similar but includes a snow depth dependency and

the minimum albedo is set to 0.6 instead of 0.5. The significance of these differences in terms of the surface energy budget are assessed in Section 6.4.

In COAMPS the underestimation of Rad_{net} is offset largely by biases in the turbulent heat fluxes, producing only a small under-estimation of the total heat flux. There is however a large positive bias in T_{ice} and T_1, a result which is not expected. This is discussed in more detail in the following section.

4.6 Case Study

Here we examine a period of relatively low temperatures observed in the lowest 3 km of the atmosphere between August 12.0 and 16.0 (Figure 4.2). Tjernström *et al.* (2004a) show that during the summer months, the near-surface air temperature is most frequently at 0 °C or -1.7 °C, the melting points of fresh and seawater respectively. This indicates strong control of the near-surface air temperature by a surface consisting of snow, ice, open leads and melt ponds. If colder air is advected over a sea ice surface, the surface warms the atmosphere through the release of sensible heat and then through latent heat as melt ponds and sea water begin to freeze. For the regional average air temperature to drop below -1.7 °C for a significant amount of time a layer of ice must form on top of a sufficient fraction of melt pond and open lead surfaces, significantly reducing the magnitude of the heat fluxes. Formation of a thin layer of ice on top of melt ponds and open leads was observed visually during 12-16 August.

Figure 4.12 shows 5 day back trajectories ending at the observation site at an altitude of 800 m together with a plot of sea ice extent from the UM(G25) analyses, in which sea ice fraction is diagnosed from the assimilation of satellite data. The start of the observed temperature decrease (August 11.75) coincides with a change in air mass origin, from air originating over warmer, open ocean, to air that has spent at least 5 days over the pack ice. This suggests that the cold air results from advection from another region of the Arctic rather than local cooling; this is supported by the fact that colder temperatures were observed up to 3 km, rather than only at the surface. If this temperature decrease was caused by local radiative cooling at the surface, the observed heat fluxes would be positive (downward). Over the entire cold period the observed sensible heat flux is negative, only returning to positive once the air temperature recovered on August 16 (Figure 4.6) and the observed total heat flux remains positive (Table 4.3), at 2.47 Wm^{-2} even though T_{ice} decreases significantly, which is contrary to what is expected. This disparity is most likely due to uncertainties in the observed values that make up the surface energy budget. The maximum uncertainty in the net radiation measurements is 8.2 Wm^{-2}. This, along with a typical uncertainty of 20 % in the eddy-covariance measurements of sensible and

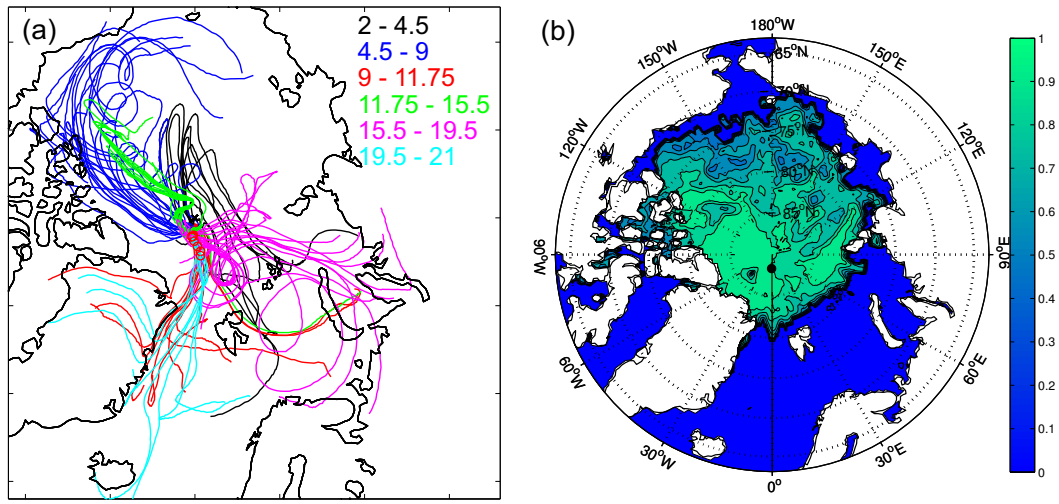

Figure 4.12: (a) 5 day back trajectories ending at the observation site at an altitude of 800 m during AOE 2001, calculated with the McGrath (1989) 3D trajectory model utilising ECMWF analyses. The time of arrival of the air masses at the observation site are in decimal days in August. (b) Sea ice fraction from UM(G25), which is diagnosed from satellite observations. The black dot marks the location of the AOE 2001 observation site.

latent heat (e.g. DeCosmo *et al.* (1996)) results in a potential total heat flux down to -6.63 Wm^{-2} for the cold period, which could easily have caused the decrease in observed surface temperature.

During the periods August 12-14 and August 14-15 cloud was observed up to 2000 m and 400 m respectively (Figure 4.8d). The ceilometer observations show a near constant layer of low-level cloud, apart from a period with decreased cloud cover during the second half of August 15, coinciding with the coldest T_{ice} and T_1 observations (Figure 4.8d and 4.3a,b). During this decrease in cloud cover, Rad_{net} decreases and becomes negative for a short time (Figure 4.13c), indicating radiative cooling of the surface, thus further enforcing the cold period.

Figure 4.2 shows decreased air temperatures above the surface in all three models during the cold period, indicating that they have, to some extent, reproduced the advection of cold air over the observation site. This cold period is not seen in modelled T_1 and T_{ice}, except briefly in COAMPS, due to errors in the surface energy budget, where the representation of clouds play a significant role. The observations show that low-level clouds prevail during the cold period. The properties of these clouds and their impact on the radiation budget during the cold period are now assessed using a comparison with periods where different cloud conditions are prevalent. For this we use a number of periods when the passage of synoptic scale frontal systems produced cloud that extended to above 3 km (August 11.0-12.0, August 16.5-17.0 and August 19.0-19.5). The absolute

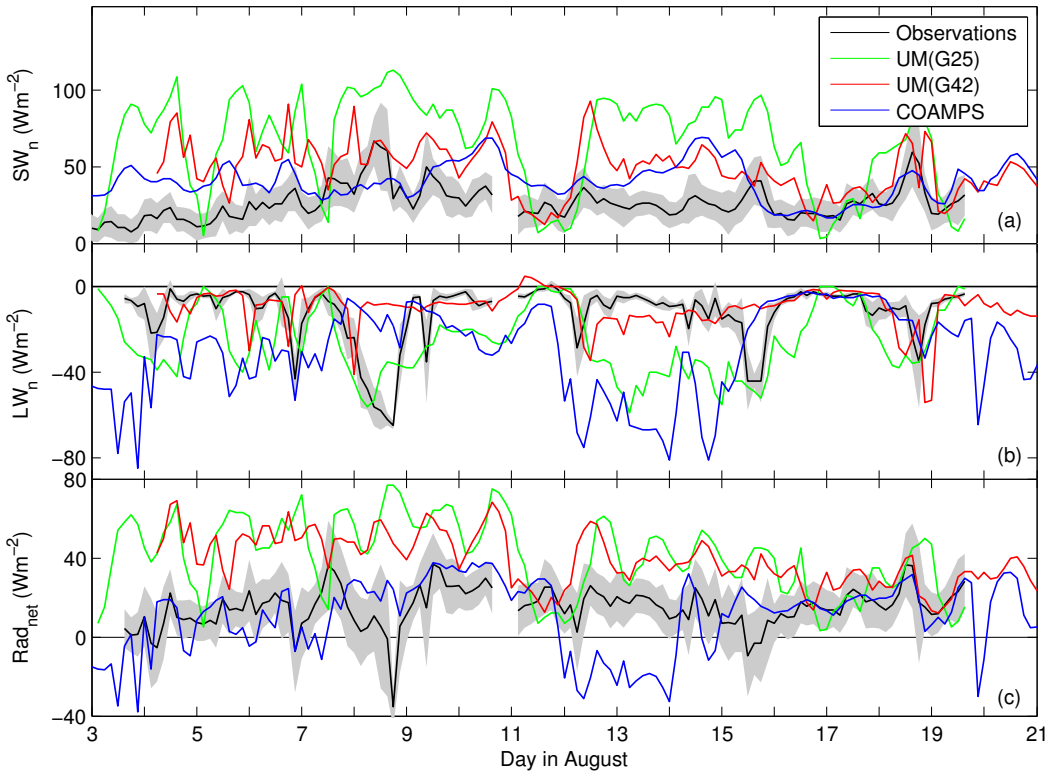

Figure 4.13: Three hourly averaged surface radiative flux observations and model comparisons, showing (a) net shortwave (b) net longwave and (c) net radiation. A positive flux represents a transfer of energy to the surface. The grey area represents ±1 standard deviation about each 3 hour mean observation and for SW_{net} and Rad_{net}, includes an estimate of the error produced in the computation of SW_{up} of 8.2 W m^{-2}.

model biases for T_{ice}, T_1 and the radiation and turbulent fluxes, computed in the same way as those in Table 4.1 are presented for the 'cold period' (August 12-15.5) and the 'deep cloud' periods in Table 4.3.

At times when deep clouds were observed, the biases for almost all variables in all three models are smaller than during periods where only low-level cloud was present. This is because all three models simulate the passage of the frontal systems and the occurrence and radiative properties of the associated deep clouds with reasonable accuracy and the radiative fluxes are less sensitive to the precise values of LWP and IWP when their magnitudes are large. It must be noted however, that although the simulated cloud fractions are accurate during these periods, the absolute biases in SW_{up} and SW_{dn} are still large and it is the result of the difference in these errors that produces the small error in SW_{net}. The direction of the biases in SW_{up} and SW_{dn} in COAMPS are also of the opposite sign to those in the MetUM. The resulting values of modelled Rad_{net} are all within 4.1 W m^{-2} of that observed. The predominately negative biases in the sensible and latent heat fluxes lead to a small negative bias in the total heat flux in all three

Table 4.3: Mean observed values and model absolute biases of temperature, radiation and heat flux diagnostics during the cold period and during periods with deep cloud cover.

		Cold period				Deep cloud periods			
	unit	$\bar{x}_{obs}$	G25	G42	COAMPS	$\bar{x}_{obs}$	G25	G42	COAMPS
T_1	K	270.20	2.17	2.88	1.29	272.77	-0.32	0.43	0.10
T_{ice}	K	270.16	2.47	2.93	2.52	272.70	-0.26	0.40	0.41
$cldfrac$	-	0.80	-0.15	0.17	-	0.91	0.06	0.06	-
LW_{dn}	W m^{-2}	288.61	-12.52	13.12	-25.22	309.56	-4.94	1.12	-9.81
LW_{up}	W m^{-2}	302.04	11.57	13.54	11.47	313.61	-1.05	2.01	1.87
SW_{dn}	W m^{-2}	141.40	39.13	-36.81	11.26	86.70	-43.01	-34.91	30.66
SW_{up}	W m^{-2}	115.01	-10.93	-62.70	-7.98	65.74	-48.94	-39.85	21.03
LW_{net}	W m^{-2}	-13.43	-24.09	-0.42	-36.69	-4.05	-3.89	-0.89	-11.67
SW_{net}	W m^{-2}	26.39	50.06	25.88	19.24	20.96	5.92	4.93	9.63
Rad_{net}	W m^{-2}	12.96	25.98	25.46	-17.45	16.91	2.03	4.04	-2.05
H	W m^{-2}	-3.50	-0.67	2.92	-0.96	-0.37	-0.12	0.86	-1.76
E	W m^{-2}	-6.99	-10.32	-6.20	3.83	-4.58	-6.58	-2.75	-2.01
tot_{hflx}	W m^{-2}	2.47	14.99	22.18	-14.58	11.96	-4.67	2.15	-5.82

models and simulated T_{ice} and T_1 are within 0.5 K of the observed values during these periods.

During the cold period, UM(G25) produces unrealistic clear conditions, seen in Figure 4.8e and in the cloud fraction bias in Table 4.4. Over the entire observation period, incorrect partitioning of mean ice and liquid cloud water also prevails. A combination of these factors causes an underestimation of LW_{dn} and an overestimation of SW_{dn} by the model. UM(G42) produces a near constant layer of low-level cloud during the cold period, which perhaps looks fairly realistic, although the biases in Table 4.3 show the cloud fraction in this version of the model is overestimated. Since the partitioning of ice and liquid water is approximately correct, the cause of the overestimated LW_{dn} and underestimated SW_{dn} is the over-prediction of low-level clouds. Biases in SW_{dn} and LW_{dn} due to errors in cloud occurrence and cloud radiative forcing, coupled with a large negative bias in SW_{up} caused by errors in the parameterisation of the surface albedo produces a positive bias in Rad_{net} of 25 W m^{-2} in both versions of the model. Errors in H and E act to compensate for these errors to some extent but a positive bias remains in the total heat flux of 15.0 and 22.2 W m^{-2} in UM(G25) and UM(G42) respectively. These large errors account for the large biases in T_{ice} and T_1.

The errors produced by COAMPS during the cold period are large, seem unphysical and have a large effect on the mean statistics for the model over the month of August. The separation of statistics for this model into the 'deep cloud' and 'cold' periods in the same way as the MetUM and the production of a set of statistics for all times other than the cold period (Table 4.4) is therefore especially helpful. During the periods with

Table 4.4: Mean observed values and model absolute biases of temperature, radiation and heat flux diagnostics for COAMPS at all times except the cold period.

	unit	$\bar{x}_{obs}$	COAMPS
T_1	K	273.44	0.12
T_{ice}	K	272.38	0.37
LW_{dn}	W m^{-2}	299.19	-6.35
LW_{up}	W m^{-2}	312.05	1.75
SW_{dn}	W m^{-2}	135.87	29.90
SW_{up}	W m^{-2}	106.95	20.46
LW_{net}	W m^{-2}	-12.86	-8.11
SW_{net}	W m^{-2}	28.91	9.44
Rad_{net}	W m^{-2}	16.05	1.33
H	W m^{-2}	-1.39	0.93
E	W m^{-2}	-3.99	2.47
tot_{hflx}	W m^{-2}	10.67	4.73

deep clouds the biases in COAMPS are similar to those in the MetUM, causing a small negative bias in the total heat flux and fairly accurate T_{ice} and T_1. The same can be said during periods of the field campaign other than during the cold period. This shows that the representation of cloud forcing, surface albedo and the turbulent fluxes in the model are generally reasonable enough to produce T_{ice} and T_1 with only a small positive bias.

During the cold period, errors in the up and downwelling radiation components are generally smaller in COAMPS than those produced by the MetUM, apart from the significant underestimation of LW_{dn}. This error is most likely caused by the relatively small amount of warm, low level cloud produced by the model during this period (Figure 4.8g) or too low LWP (Table 4.2), and results in a value of mean Rad_{net} that is of the wrong sign. This is offset to some extent in the total heat flux by the bias in E, producing a total heat flux that is both too large in magnitude and of the wrong sign; a large amount of heat is emitted from the surface by the model compared to a small amount of heat absorbed at the surface in the observations. Large negative biases in T_{ice} and T_1 would therefore be expected, but this is not the case.

In COAMPS, grid boxes containing sea ice can consist of a fraction of bare and snow covered ice. The model computes T_{ice} using a weighted average of the snow and bare ice surface temperatures. When the total heat flux becomes large and negative on August 11, T_{ice} and T_1 begin to decrease as expected. At the start of August 13 there is a decrease in the fraction of the surface that is covered in snow. This alters the weighting in the computation of T_{ice} and since the sea ice surface temperature in the model is higher than the snow surface temperature this decrease in snow cover increases T_{ice} to values above what would be expected due to the changes in radiative fluxes alone. This overestimation of T_{ice} during August 13 and 14 keeps the decrease in T_1 moderate until August 15, when

a pool of very cold air is advected over the observation site in the model. This is visible in plots of near-surface air temperature fields over the Arctic region (not shown) and in the large negative sensible and latent heat fluxes produced by the model. The observed decrease in T_1 on August 15 is not accompanied by a decrease in T_{ice} (Figure 4.3). This is because an increase in Rad_{net} of approximately 20 W m^{-2} occurs on August 15th, offsetting the loss of energy from the surface through the turbulent heat fluxes.

4.7 Summary

AOE 2001 field observations made over the Arctic pack ice during August 2001 are used to evaluate two versions of the global NWP version of the MetUM and the mesoscale model, COAMPS. The UM(G25) data set is comprised of forecasts from the U.K. Met Office archives, produced by the version of the model that was in operation in 2001. UM(G42) is the most recent version of the model that was available in 2007, which contains a large number of developments to its formulation and physical parameterisations. Daily forecasts were produced for August 2001 using initial conditions from ERA-40 data. COAMPS was run with an outer domain covering the whole pan-Arctic region and contained two nested inner domains, the smallest of which was centred around the AOE 2001 observation site. The outermost domain was forced by ERA-40 data and in contrast to the MetUM model data, COAMPS was run in a 'climate mode' for the entire AOE 2001 ice drift period, without any constraints except those at the outermost boundaries.

The wind speed, surface pressure and relative humidity fields are at least reasonably represented in all three models. This is expected since the radiosonde observations made during AOE 2001 were assimilated into the UM(G25) forecasts and into the ERA-40 data used to initialise UM(G42) and as boundary conditions in COAMPS. In these fields, biases are larger and correlation with the observations is worse in COAMPS. This is due to the reduced constraints used in this model run. The air temperature in all three models away from the surface is represented with reasonable accuracy but close to the surface there are large positive biases. UM(G42) shows the largest bias, where T_1 and T_{ice} remain close to 273 K for the duration of the observation period.

u_* is represented reasonably well in all three models, though with some explainable errors. The observed surface sensible and latent turbulent heat fluxes are negative (heat emitted from the surface) but small in magnitude. The MetUM underestimates the magnitude of the sensible heat flux, likely due to biases in T_1 and T_{ice}, and the bias in the latent heat flux is large in both versions of the MetUM. The direction of the sensible and latent heat fluxes in COAMPS are correct but the magnitudes of both are underestimated, which

is due to the small roughness lengths used in the parameterisations compared with the MetUM and those suggested by the observations.

The MetUM computes the surface albedo as a function of T_{ice}. When the ice surface temperature is at its maximum (273.1 K) the albedo is 0.5 and this increases to a maximum of 0.8 with decreasing T_{ice}. The albedo in both versions of the model is underestimated due to the positive bias in T_{ice}. This affects the value of modelled SW_{up} and thus the entire radiation balance, creating an important feedback of errors. The climate version of the MetUM (HadGEM1) uses a slightly different albedo scheme, which computes the surface albedo based on both surface temperature and snow cover.

All three models reproduce the occurrence and radiative properties of deep cloud, associated with synoptic scale frontal events with reasonable accuracy. During periods where only low level cloud was observed, UM(G25) under-predicts cloud fraction and both it and COAMPS produce too little cloud liquid water compared to that observed during the SHEBA experiment. This causes an underestimation of LW_{dn} and an overestimation of SW_{dn}. The partitioning of ice and liquid cloud water in UM(G42) is more representative of typical conditions and unlike UM(G25), the newer version of the model produces a layer of low-level cloud for the majority of the observation period, possibly due to the increased vertical grid resolution in this version of the model. Although it 'looks' as though it reproduces the observations with greater accuracy, cloud fraction is over-predicted, leading to an overestimation of LW_{dn} and a underestimation of SW_{dn}. Similar biases in SW_{dn} and LW_{dn} produced by UM(G25) and COAMPS suggest errors in cloud forcing are similar in both models. The larger bias in Rad_{net} in UM(G25) and UM(G42) compared to COAMPS is therefore most likely dominated by the surface albedo parameterisation rather than cloud forcing. The bias in the surface turbulent heat fluxes act to offset the overestimation of Rad_{net} to some extent but the total heat flux in the MetUM remains overestimated in both versions of the model.

The changes in model formulation between versions G25 and G42 of the MetUM have made little difference to the accuracy of modelled surface pressure, relative humidity, wind speed fields and air temperature away from the surface, since these diagnostics were already reproduced with high accuracy. The production of more low level clouds in UM(G42), although seemingly more accurate has lead to increased biases in the surface radiation balance and thus in T_{ice} and T_1. The bias in H has increased, most likely due to the increased errors in T_{ice} and T_1 but the bias in E has decreased by approximately 50 %.

Although there are significant errors in both SW_{up} and SW_{dn} in COAMPS, at all times other than during the cold period COAMPS produces only a small bias in the net radiation flux. This and the small biases in H and E lead to only a small errors in the average

total heat flux and thus T_{ice} and T_1 are reproduced reasonably accurately. During the cold period, errors originating from cloud representation and in the reproduction of surface snow and liquid water processes at the surface produce a large positive bias in T_{ice} and T_1 during this period. This bias has a large effect on the statistics for COAMPS for the whole month of August.

In all three models errors in the turbulent heat fluxes compensate for errors in the net radiation flux in the total heat flux, therefore improving one aspect of the model will not necessarily improve overall model performance. Since accurate representation of all components of the surface energy budget is central to accurate climate predictions, it is imperative to improve model parameterisations of the surface heat fluxes and of cloud properties. Improvements to simulated Arctic cloud occurrence and radiative properties in regional and global scale models generally is challenging. Progress in this area has been limited by a lack of in-situ observational data. The processes that cause the formation and persistence of summer low-level Arctic clouds are not well understood and therefore polar specific parameterisations have not been fully developed. The Arctic Summer Ocean Cloud Study (ASCOS), whose observations are discussed in detail in the following two chapters was conducted with the aim of solving some of these issues.

Chapter 5

ASCOS turbulence observations

The previous chapter highlighted some large biases in the turbulent surface fluxes produced by the MetUM, although the investigation was limited to a large extent by the quality and number of observations. The measurements of turbulent properties made during ASCOS are far more extensive and complete. This new data set is used to assess the performance of model surface turbulent flux parameterisation schemes and investigate whether the assumptions made by the parameterisations hold for the late summer/early freeze-up conditions observed in the central Arctic Ocean. Section 5.1 evaluates the success of the MetUM parameterisation scheme in reproducing the observed fluxes. The following two sections investigate whether Monin-Obukhov similarity theory can be applied in this type of boundary layer using the similarity functions and spectral analysis of the turbulence data. Section 5.4 computes values for the roughness length scale for the turbulent transfer coefficients using the observations and compares them to those used in models. Finally, a state-of-the-art surface flux parameterisation scheme, developed using observations from the Surface Heat Budget of the Arctic Ocean (SHEBA) experiment is tested using the ASCOS observations in Section 5.5.

5.1 Surface turbulent fluxes estimated by the MetUM

Figure 5.1 shows statistics of 3 hourly averaged friction velocity, u_* and the sensible, H and latent, E heat fluxes computed from observations at each level on the 15 and 30 m masts and those diagnosed by the MetUM. The model data points are grid box averages that contain the observation location, as described in Section 3.4.1. The frequency of occurrence of the observed fluxes is similar at all measurement levels. The MetUM overestimates the occurrence of periods where u_* is greater than approximately 0.2 m s^{-1} and underestimates the occurrence of the smaller friction velocities. The same is true for

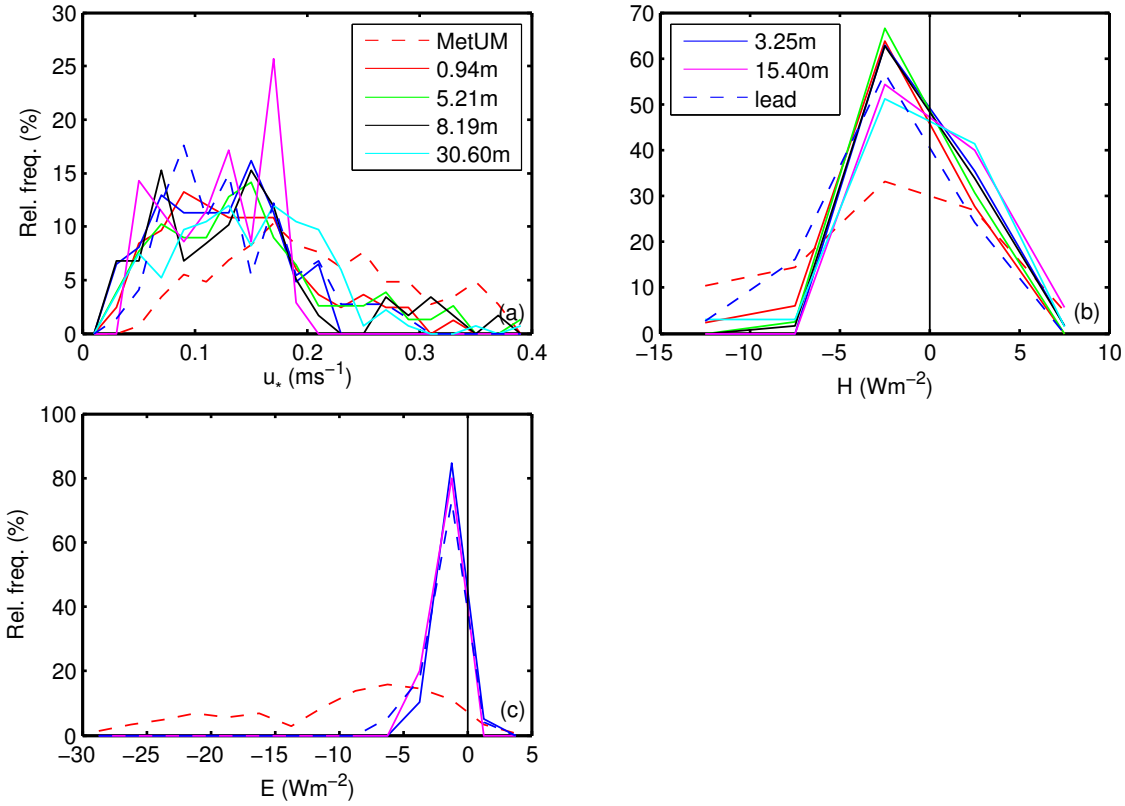

Figure 5.1: Frequency of occurrence of 3 hourly averaged (a) u_*, (b) H and (c) E observed during ASCOS and diagnostics from the MetUM. A positive flux is defined as the transfer of energy into the surface.

the sensible and latent heat fluxes, where the model overestimates the occurrence of the larger magnitude fluxes; for the latent heat flux it produces fluxes of magnitudes up to -10 to -40 Wm^{-2}, several times larger than the maximum observed values. The biases in u_*, H and E are all related since the overestimation of u_* suggests that turbulent mixing is too strong in the model.

Plots of observed and modelled u_* and scaled H and E are shown in Figure 5.2, analogous to Figure 4.7 for the AOE 2001 data. These plots allow an assessment of the success of the turbulent flux parameterisation schemes without the complication of whether or not the modelled surface temperature and near-surface wind speed, temperature and humidity are accurate. A caveat of this approach is that it assumes all the observation levels were within the surface (constant flux) layer; there is evidence presented later in this chapter that suggests this is not the case. In light of this it is best to compare the model diagnostics with the observations from the lowest level only and use the other levels as an indication of variability with height. The ASCOS turbulence data set is far more extensive than that from AOE 2001 and it is possible to apply linear fits to the observations at several levels for all the fluxes. It is obvious from the plot that the model overestimates the magnitude of the fluxes.

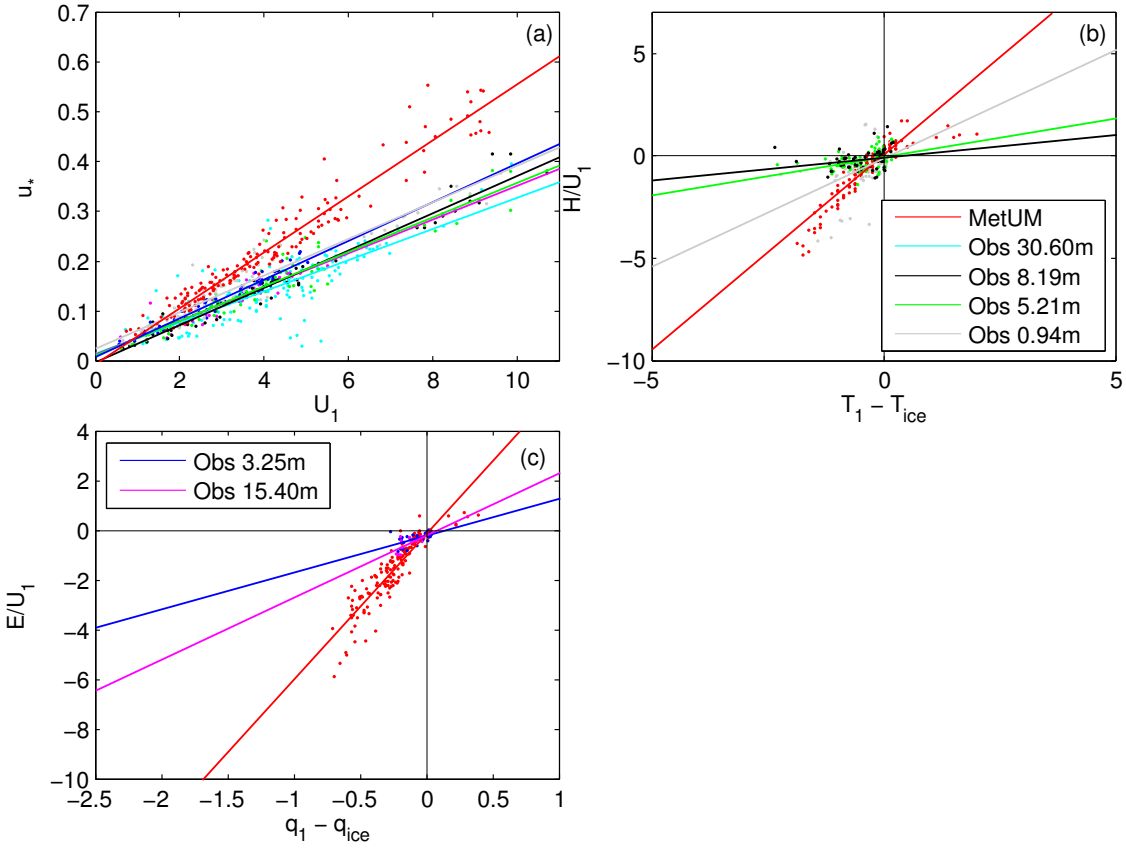

Figure 5.2: Scatter plot of 3 hourly averaged (a) u_* vs. U_1, (b) H/U_1 vs. $T_1 - T_{ice}$ and (c) E/U_1 vs. $q_1 - q_{ice}$. T_1 (q_1) is the temperature (specific humidity) at each observation or first model level. q_{ice} for both the model and observations is computed as the saturation humidity with respect to ice at T_{ice} and U_1 is the wind speed at each observation or first model level.

The gradients of the lines in the plots are directly related (but not equal) to the value of the transfer coefficients for momentum, C_{Dr}, temperature, C_{Hr} and humidity, C_{Er}. To quantify the model bias the gradients of the linear fits to the observations and the model are presented in Table 5.1. The 'factor' in the last column indicates by how much the MetUM overestimates the transfer coefficient. For example, the model's estimation of C_{Df} for u_* is 1.58 times that suggested by the observations. Two values are given for the sensible heat flux due to the large difference in gradients of the linear fits to the data from the 0.94 m and 5.21 and 8.19 m levels. The values of 0.30 and 1.06 for H in the second column of the table are the mean of C_{Df} from the 5.21 and 8.19 m levels and the value of C_{Df} from the 0.94 m level respectively. The transfer coefficient for the latent heat flux is overestimated by a factor of 2.94, which is smaller than the factor for the sensible heat flux even though the bias in the modelled latent heat fluxes are much larger than for the sensible heat flux. This suggests that for the latent heat flux errors in modelled $q_1 - q_{ice}$ are a significant factor as well as the transfer coefficients.

Table 5.1: Comparison of observed and model surface flux transfer factors, C_{Df} (gradient of lines in Figure 5.2). This parameter is not C_{DN10} or C_{Dr} but is directly related to them. Factor = MetUM C_{Df} / observed C_{Df}. Two values for mean observed C_{Df} for H are given; an average of the upper two levels and the value of the lower level because the difference in gradient between the first level and the upper two levels is large. The number in brackets in the second and third columns are the correlation coefficients, R between, for example U_1 and u_* in Figure 5.2a, for each measurement height or the model diagnostics.

z (m)	Obs C_{Df}	MetUM C_{Df}	Factor
u_*			
0.94	$3.68\text{x}10^{-2}$ (0.95)		
3.25	$3.90\text{x}10^{-2}$ (0.97)		
5.21	$3.48\text{x}10^{-2}$ (0.97)		
8.19	$3.74\text{x}10^{-2}$ (0.98)		
15.40	$3.39\text{x}10^{-2}$ (0.91)		
30.60	$3.14\text{x}10^{-2}$ (0.80)		
Mean	$3.56\text{x}10^{-2}$	$5.63\text{x}10^{-2}$ (0.97)	1.58
H			
0.94	1.06 (0.48)		
5.21	0.38 (0.40)		
8.19	0.22 (0.24)		
Mean	0.30 - 1.06	1.90 (0.90)	1.79 - 6.32
E			
3.25	1.48 (0.58)		
15.40	2.50 (0.67)		
Mean	1.99	5.86 (0.90)	2.94

This analysis has shown that even if the model produces accurate estimates of the surface and near-surface quantities the fluxes are still overestimated due to a positive bias in the transfer coefficients. This is a significant problem since errors in the modelled surface heat fluxes can cause errors elsewhere, such as in atmospheric stability, surface evaporation and the near-surface air temperature. The transfer coefficients in the MetUM surface flux parameterisation scheme are a function of the stability functions, φ_m and φ_h and the roughness lengths z_0, z_t and z_q (Equations 2.41 to 2.43). The accuracy of the estimates for the roughness lengths used in the MetUM, and in models generally, is evaluated in this chapter. An assessment of whether the necessary assumptions for surface flux parameterisation schemes can be applied to the central Arctic boundary layer during the late summer melt and early freeze-up periods is also investigated.

5.2 Evaluation of the Monin-Obukhov similarity function for momentum

A large part of this chapter is based around Monin-Obukhov similarity theory, where atmospheric stability plays an important role; it is therefore useful to illustrate the range and frequency of stabilities encountered during the ASCOS field campaign. Figure 5.3

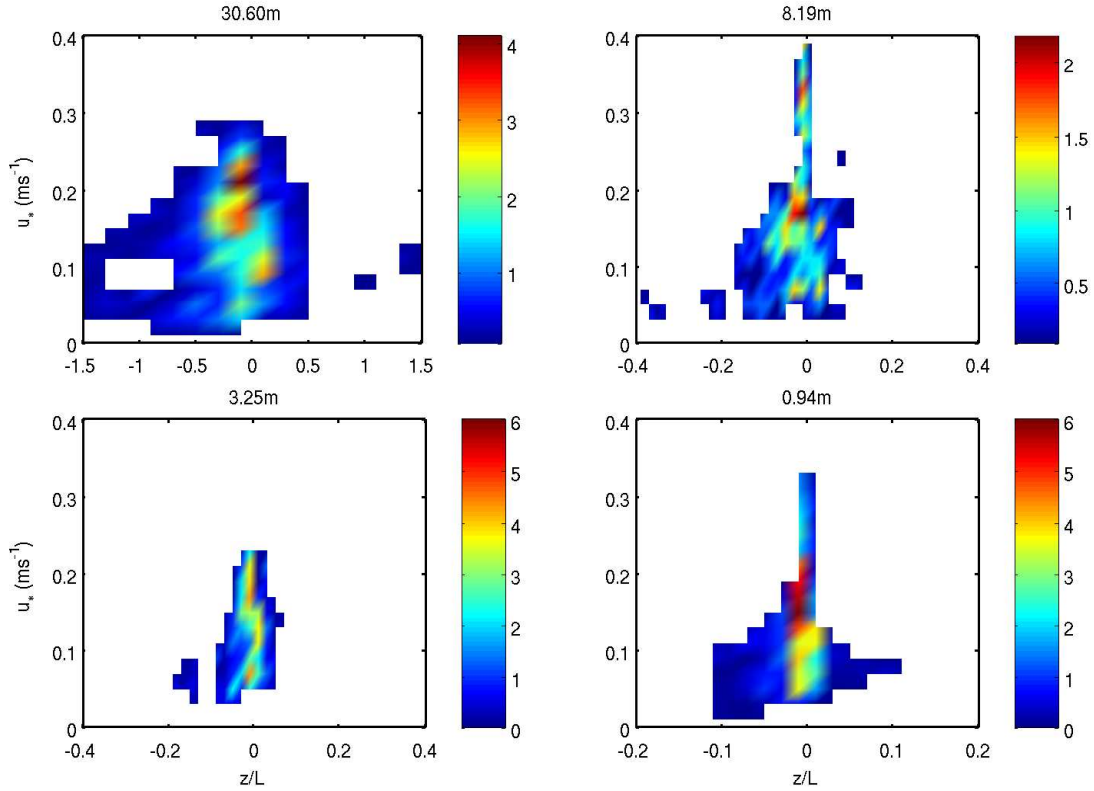

Figure 5.3: Frequency of occurrence (%) of z/L as a function of u_* at 4 different levels. z is the measurement height and L is computed using measurements from the 0.94 m level in all four panels. Bin size is 0.02 for u_*, 0.2 for z/L at the 30.60 m level and 0.02 for z/L at the other levels. Note the change of scale on the z/L axes and colour bars.

shows the range of values of the stability function, z/L, that occurred during the ice station, calculated using Equation 2.26 and the measurement height, z, at four levels on the meteorological masts. At all levels the most common range of z/L is close to zero ($-0.1 \geq z/L \leq 0.1$), indicating neutral or weakly stable/unstable conditions. This range of z/L occurred for almost the entire duration of the observation period at the lowest level but the departure of z/L from this range increases with distance from the surface.

Equation 2.30 gives the non-dimensional form of the stability function for momentum, φ_m; this describes the rate of change of wind speed with height in the surface layer as a function of stability. This function is vital for the computation of the momentum flux in bulk flux parameterisations schemes (see Section 2.1.7). It can be tested using the ASCOS data set by plotting φ_m against z/L calculated from the observations and then comparing it to previously established forms of the functions.

φ_m is computed from the observations by rearranging Equation 2.30:

$$\varphi_m = (kz/u_*)(dU/dz) \tag{5.1}$$

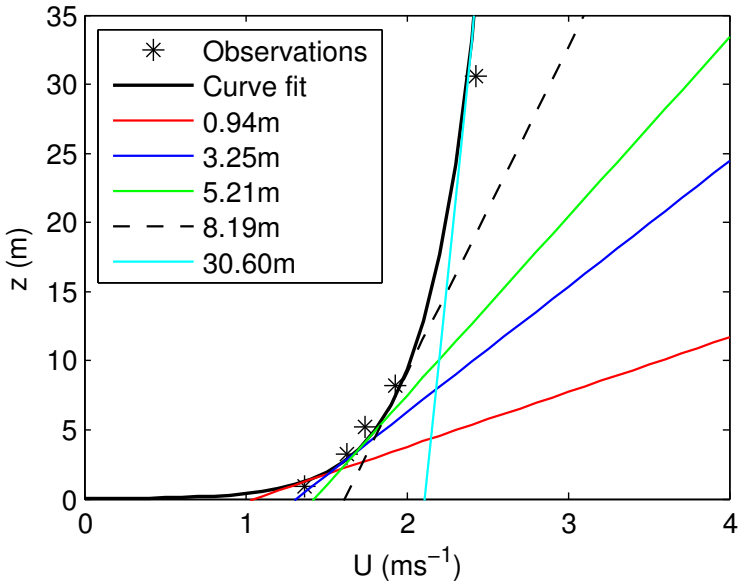

Figure 5.4: Method for the derivation of dU/dz for a 10 minute period on 18th August 2008. Note data from the 15.40 m level is not included during the fitting of the curve.

where u_* is computed from the eddy covariance measurements using Equation 2.23, z is the measurement height of the sonic anemometer and dU/dz is the rate of change of wind speed with height at z. dU/dz was derived by fitting an exponential curve to 10 minute averaged wind speed observations from each height on the 15 and 30 m masts and then taking the gradient of the tangent to the curve at each sonic anemometer height (Figure 5.4). During the data processing stage measurements of u, v and w from the Gill sonic anemometer at 15.40 m were found to be positively biased (although u', v' and w' appeared unbiased) and therefore, data from this level was not included in the curve fit.

Figure 5.5a shows φ_m computed from 10 minute averaged observations at each measurement height on the masts, where L is computed from Equation 2.26 using observations from the 0.94 m measurement level. During the computation of dU/dz the correlation coefficient between U and $\ln(z)$ was calculated. This indicates how well the exponential curve fits the observations. If the correlation coefficient was less than 0.97, the data was assumed to be poor quality; these periods are marked as grey points in Figure 5.5a. Due to the large variability in such data sets, bin averaging of a large amount of data is required to identify relationships between variables (Figure 5.5b). In this case bin averaging is performed using a median value, so a few anomalously small or large values do not adversely affect the average. A threshold is also applied, requiring a minimum number of data points in each bin for an average to be accepted. The value of this threshold is optimised in order to maximise the number of discrete bin averages but to keep the standard deviation about each bin average as low as possible.

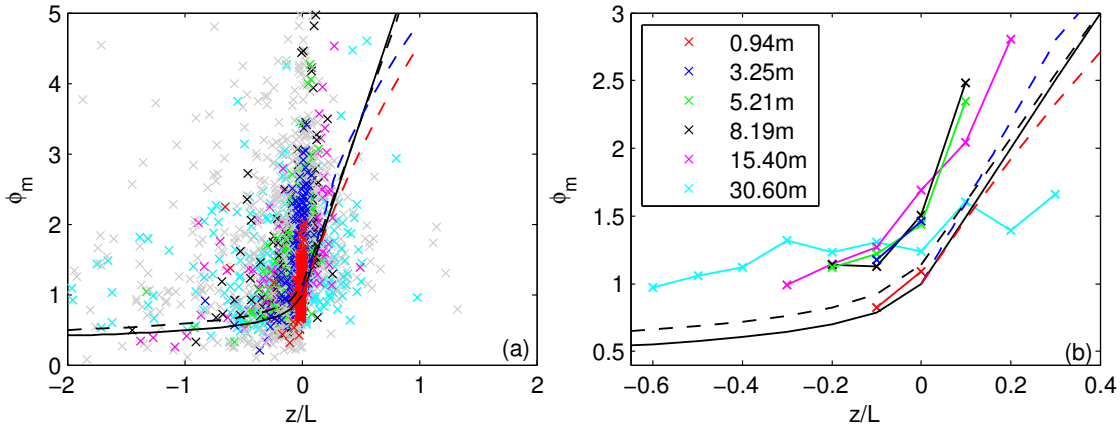

Figure 5.5: Similarity function, φ_m plotted against z/L. L is computed from Equation 2.26 using observations from the 0.94 m measurement level. (a) 10 minute mean values calculated from the observations at each measurement height. The grey points are considered poor quality and are not used in the bin averaging. Four different forms of φ_m are shown for comparison; Kaimal & Finnigan (1994), refined through comparison between a number of observational data sets (solid black line), Businger *et al.* (1971) (dashed black line), Yamamoto (1975) (dashed blue line) and Grachev *et al.* (2007) (dashed red line) (b) median bin values of φ_m for each measurement height. Bin size is $z/L = 0.1$ and a threshold of at least 10 observations in each bin was applied. Note the change in axis scale between panels (a) and (b).

Along with the form of φ_m given in Kaimal & Finnigan (1994), a number of different forms of the function are also shown in Figure 5.5. There is only a relatively small difference between these functions at moderate stabilities. Apart from the measurements made at the upper-most level, the general shape of the observed curves agree reasonably well with the forms of the function found by the previous experiments. The curve representing the 0.94 m level agrees well with the form of φ_m given in Kaimal & Finnigan (1994). However, for a given value of z/L, the curves representing the 3.25, 5.21, 8.19 and 15.40 m levels suggest a higher value of φ_m than the forms of the function taken from the literature. This can be interpreted as follows: under the conditions observed during ASCOS, turbulence at a certain value of z/L behaves like that observed under more stable conditions during previous experiments. The curve from the 30.60 m level is notably different to the others; the rate of increase in φ_m with increasing z/L is much lower than that shown by both the ASCOS observations at the lower levels and by the curves found by previous experiments. This suggests that the turbulence at the upper-most level is behaving differently to that at the other levels.

Figure 5.6 shows boundary-layer and mixed-layer depths estimated from the radiosonde and tethersonde observations. For each radiosonde launch or tethersonde flight vertical profiles of potential temperature, relative humidity with respect to water and wind speed were used to diagnose the top of the boundary layer. Figure 2.3 shows expected profiles

of these variables in a classic boundary layer. These features were not always obvious in the observed profiles. In these cases a best-estimate of boundary-layer depth was made using the author's judgement of any features that were illustrated in the profiles.

The depth estimates from the radiosondes agree well with those from the tethersonde profiles during some periods but there is a tendency for the radiosonde estimates to be larger. This is because there are several disadvantages in using the radiosonde measurements to make boundary-layer depth estimates. The radiosondes were launched from the ship at 16 m above the surface, which is high considering boundary-layer depth is often very shallow. The launch site was within the heat island of the ship and sometimes sheltered from the wind and thus the radiosonde measurements immediately after the launch may be biased. The resolution of the observations is coarser than those made by the tethersonde (5 m resolution compared to less than 1 m) and because the ascent is rapid compared to the tethersonde, the response of the sensors will be slightly lagged. This has the potential to smooth out important features of the vertical structure or to cause them to appear at slightly higher altitudes than in reality. The tethersonde estimates are therefore, more likely to be representative of observed conditions and the radiosonde estimates are included simply for comparison and to provide an estimate when observations from the tethersonde are not available.

The observations suggest that boundary-layer depth was less than 200 m for the majority of the ASCOS period, which is very shallow compared to a typical fair weather boundary layer (see Figure 2.2). In addition, mixed-layer depth was often zero and rarely above 50 m, even though near-surface stability was near-neutral for the majority of the time. The surface (constant flux) layer is usually assumed to be 10 % of the boundary-layer depth (Stull, 1988). Under the conditions observed during ASCOS the surface layer was therefore rarely deeper than 20 m and often less than 10 m.

The famous Kansas experiments are the basis for the Kaimal & Finnigan (1994) form of φ_m (Haugen *et al.*, 1971; Businger *et al.*, 1971; Wyngaard & Coté, 1972). Conditions observed during these experiments were very different to those observed in the central Arctic; daytime, fair weather boundary layers in Kansas are of order several kilometres deep, which is associated with a surface layer depth of several hundred metres. Under conditions observed during summer in the central Arctic, the boundary layer and surface layer are much shallower. Our hypothesis is therefore: if the boundary layer in the central Arctic during late summer is less than 200 m deep and the surface layer is less than 20 m, for much of the ASCOS period measurements made on the upper levels of the mast will be outside of the surface layer. This could explain the differences between the φ_m functions from different measurement heights in Figure 5.5.

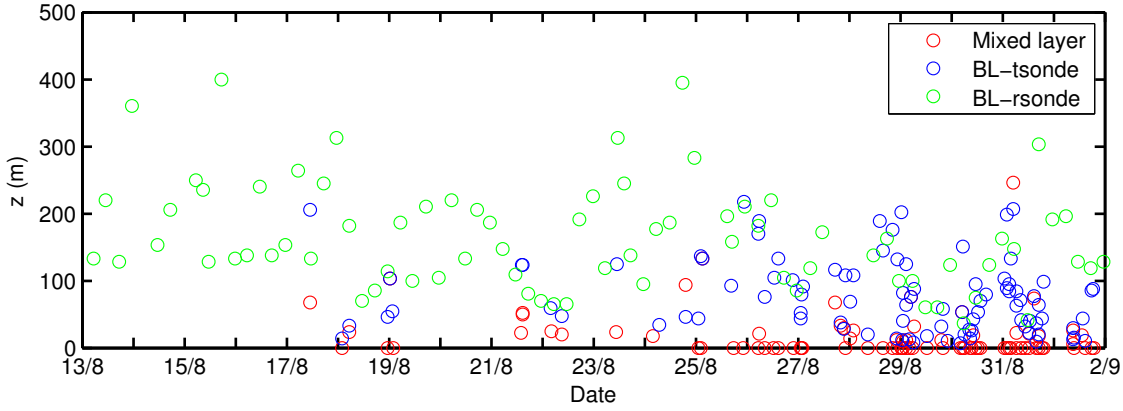

Figure 5.6: Mixed layer and boundary-layer depth estimates diagnosed from potential temperature, wind speed and humidity profiles. The red circles are the mixed layer depth estimates diagnosed from the tether balloon measurements. The blue and green circles are boundary-layer depth estimates made from the tether balloon and radiosonde measurements respectively.

The range of stabilities observed during ASCOS was relatively small and the scatter in φ_m is large. This limits the type of analysis illustrated in Figure 5.5. A different approach is necessary to consider this hypothesis in greater detail. Turbulence characteristics can be analysed in more detail by examining the spectra and cospectra of the observations (see Section 2.1.5), where a large range of z/L values is not essential. The following section uses this analysis technique.

5.3 Spectral and cospectral analysis

5.3.1 Monin-Obukhov scaling

Monin-Obukhov similarity scaling predicts that turbulence spectra will follow some universal shape when scaled appropriately and this can be used to assess the validity of similarity theory in the lower atmosphere. Kaimal *et al.* (1972) showed that data from the Kansas experiments collapsed onto a series of curves according to z/L. Frequency is normalised through multiplication by z/U, where z is the measurement height of the turbulence data and U is the wind speed measured at z. The normalised frequency-weighted spectral energy density for the three wind components, u, v and w is defined as:

$$fS_x/u_*^2\phi_\epsilon^{2/3} \tag{5.2}$$

where S_x is the spectral energy density, x is u, v or w, u_* is the surface friction velocity, which is estimated from $\overline{u'w'}$ measured at the 0.94 m level and ϕ_ϵ is a dimensionless dissipation rate for turbulent energy, which is included to ensure collapse of the curves

in the inertial subrange (Kaimal *et al.*, 1972):

$$\phi_\epsilon = \kappa z \epsilon / u_*^3 \tag{5.3}$$

where κ is von Karman's constant. ϵ is the turbulent dissipation rate, which using Taylor's hypothesis (i.e. assuming 'frozen' turbulence) (Yelland *et al.*, 1994) is:

$$\epsilon = \frac{S_u^{3/2} f^{5/2}}{K^{3/2} \left(\frac{U}{2\pi}\right)} \tag{5.4}$$

where K is the Kolmogorov constant ($= 0.55$).

S_{uw} is normalised as (Kaimal *et al.*, 1972):

$$-f S_{uw} / u_*^2 G(z/L) \tag{5.5}$$

where:

$$G(z/L) = \begin{cases} 1 & -2 \leq z/L \leq 0 \\ 1 + 7.9 z/L & 0 \leq z/L \leq 2 \end{cases} \tag{5.6}$$

and finally, S_{wT} is normalised as (Kaimal *et al.*, 1972):

$$-f S_{wT} / u_* T_* H(z/L) \tag{5.7}$$

where:

$$H(z/L) = \begin{cases} 1 & -2 \leq z/L \leq 0 \\ 1 + 6.4 z/L & 0 \leq z/L \leq 2 \end{cases} \tag{5.8}$$

Each 60 minute fS_x, fS_{uw} and $-fS_{wT}$ were bin averaged by frequency using bins at equal intervals in log space and then normalised using the methods described above. It was necessary to specify the range of frequency values in the inertial subrange to calculate ϵ. This was taken as the range of frequencies for which spectral energy density decreases with increasing frequency with a gradient of -5/3 (Kolmogorov, 1941).

Figures 5.7 to 5.10 show the normalised spectra and cospectra for u, w, uw and wT. The dots represent the individual 1 hourly normalised velocity (co)spectra, split into three stability regimes: unstable ($-2 < z/L < 0$), weakly stable ($0 < z/L < 0.1$) and moderately stable ($0.1 < z/L < 0.5$). The red and blue lines show these data bin-averaged by normalised frequency. The black curves are the generalised or 'universal' spectra, derived from experiment by Kaimal *et al.* (1972) and the values of z/L for which the curves apply are indicated in panel (f) in each of the figures.

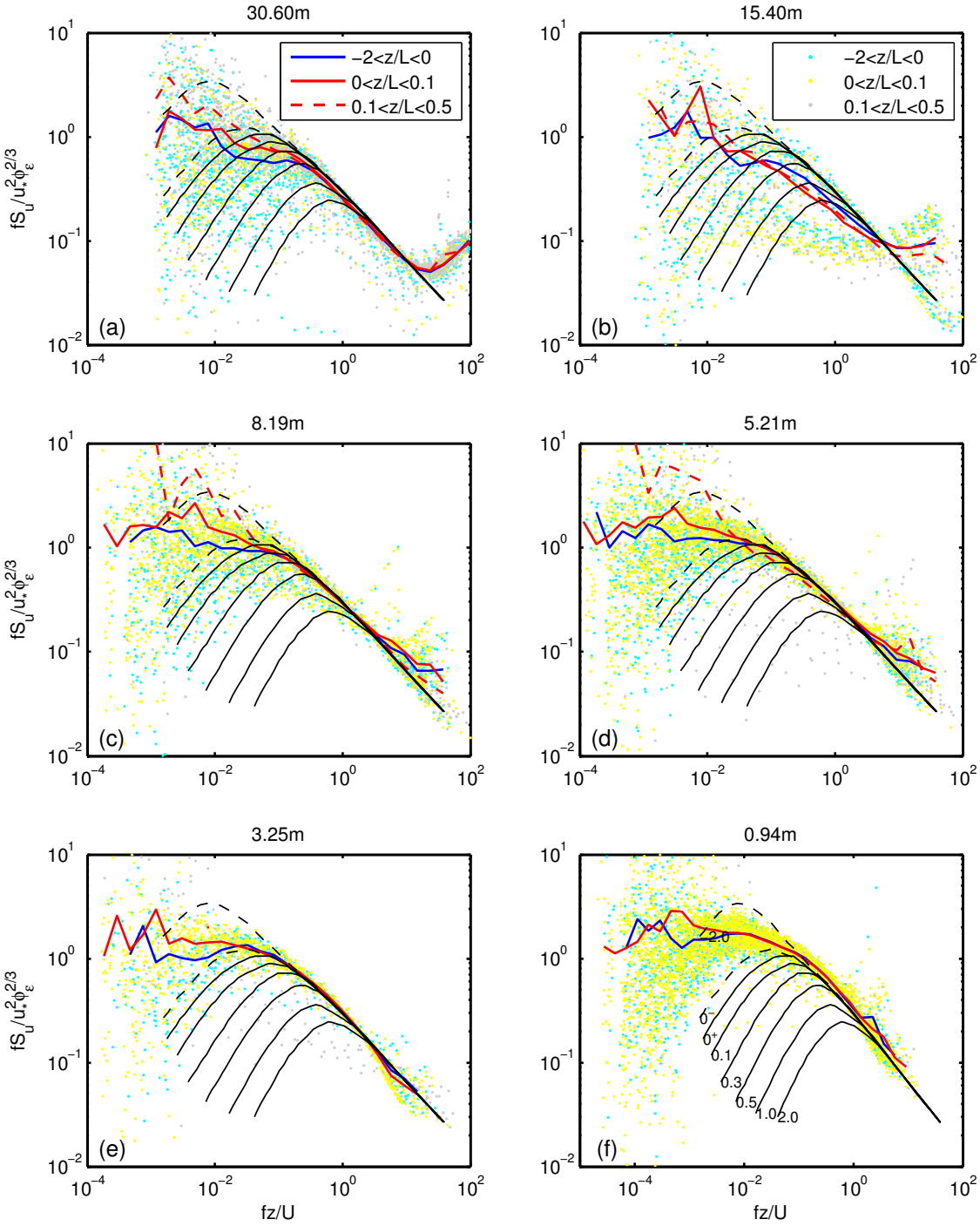

Figure 5.7: Normalised spectra of wind velocity component u, scaled according to z/L. Observations are 1 hour averages shown for each measurement level on the 15 m and 30 m masts. The blue and red curves represent the spectra in three stability ranges, bin averaged by frequency. The black curves are the generalised spectra for various z/L values, derived from experiment by Kaimal *et al.* (1972). The values of z/L for which these curves apply are indicated in panel (f).

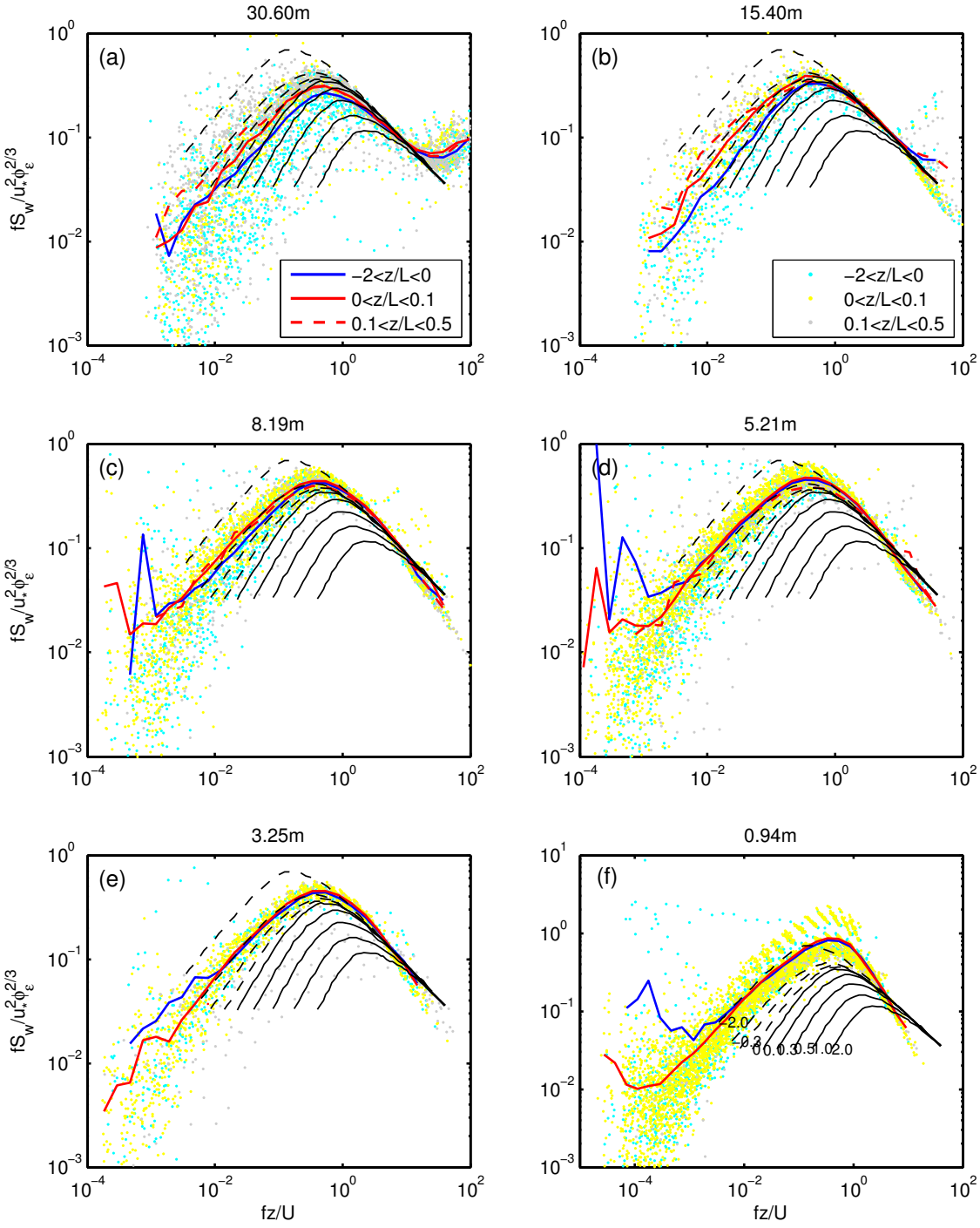

Figure 5.8: Same as Figure 5.7 but for w.

The normalised spectra for u and w show good agreement with the Kaimal *et al.* (1972) curves in the inertial subrange at all measurement levels (Figures 5.7 and 5.8), which illustrates the success of using ϕ_ϵ to collapse the curves in this region of frequency space. It is important to note that the range of observed z/L values is smaller at the lower measurement levels (Figure 5.3), which explains the lack of data in the moderately stable regime in all of the spectra and cospectra at these levels. Another obvious characteristic of the u and w spectra is the upwards tail at the highest frequencies apparent at the 30.60 m level and to a smaller extent at the 15.40 and 3.25 m levels. This is caused by the aliasing of high frequency information to lower frequencies. The tails are most significant in the observations made by the Metek anemometer (30.60 m level) because this instrument simply samples at the chosen rate. The Gill instruments (15.40 and 3.25 m levels) sample at 100 Hz and then average this to the chosen sample rate, which reduces the aliasing effect. The Campbell instruments sample at 60 Hz and then apply a low pass filter before averaging to 20 Hz, which explains why tails are not apparent at the 8.19, 5.21 and 0.94 m levels. These tails do not occur in the covariance of uw and wT curves (Figures 5.9 and 5.10) because the aliasing in the two variables is not necessarily correlated. It is important to note that the aliasing does not compromise the variance and covariances and therefore, the fluxes calculated from them because the variance and covariance calculations are not frequency dependent but are a measure of a signal's total variation or two signals' total covariation (Campbell Scientific Inc, 2009).

Although there is large scatter in the data, the observed u spectra do not show the downward trend at low frequencies, suggested by the Kaimal *et al.* (1972) curves. This causes the data from the weakly stable and moderately stable regimes to lie in the unstable region produced by the Kaimal *et al.* (1972) curves. Many of the observed u spectra from the 15.40 m level disagree significantly with the Kaimal *et al.* (1972) curves and seem to have large regions of aliasing, which is illustrated by the large tails at high frequencies. This instrument was shown during quality control of the data to overestimate the wind speed. The poor agreement may be related to this or, since the tails are so long, part of them may have been included in the calculation of ϕ_ϵ in some of the spectra and thus the shift to collapse the curves in the inertial subrange may have produced this bias. Unlike the u spectra, the observed w spectra do show a downward trend at low frequencies, in agreement with the Kaimal *et al.* (1972) curves. At all the measurements levels both the stable and unstable curves are within the unstable Kaimal *et al.* (1972) region.

The uw and wT cospectra in Figures 5.9 and 5.10 produce more scatter than the u and w spectra. The scatter is so large in the wT spectra that no bin averaged curves for the observations could be added to the plot. This large scatter is at least in part due to the small magnitude of the fluxes. The absolute value of the sensible heat flux observed during ASCOS was never greater than 10 Wm^{-2} (Figure 3.20). This is compared to typical

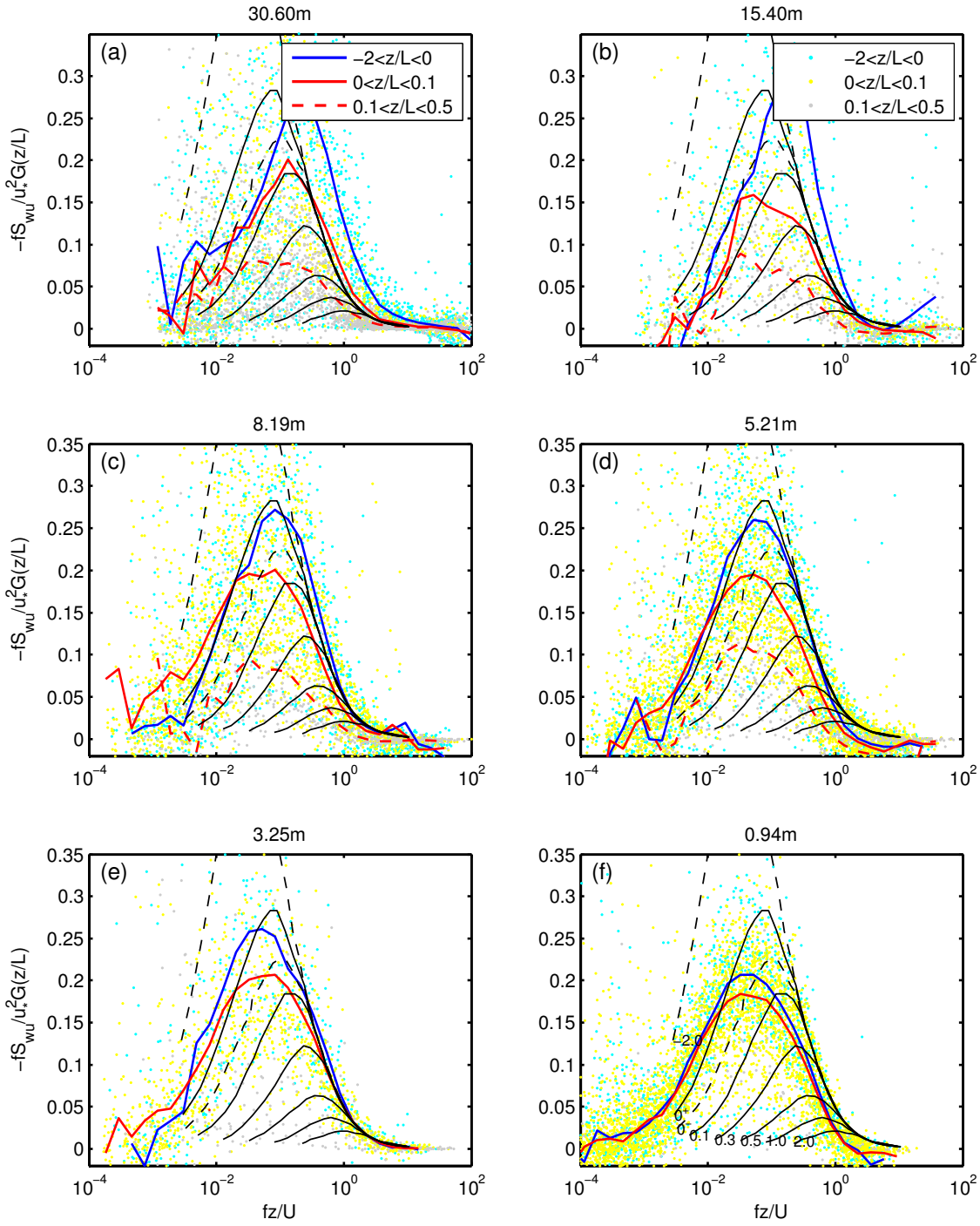

Figure 5.9: Same as Figure 5.7 but for uw.

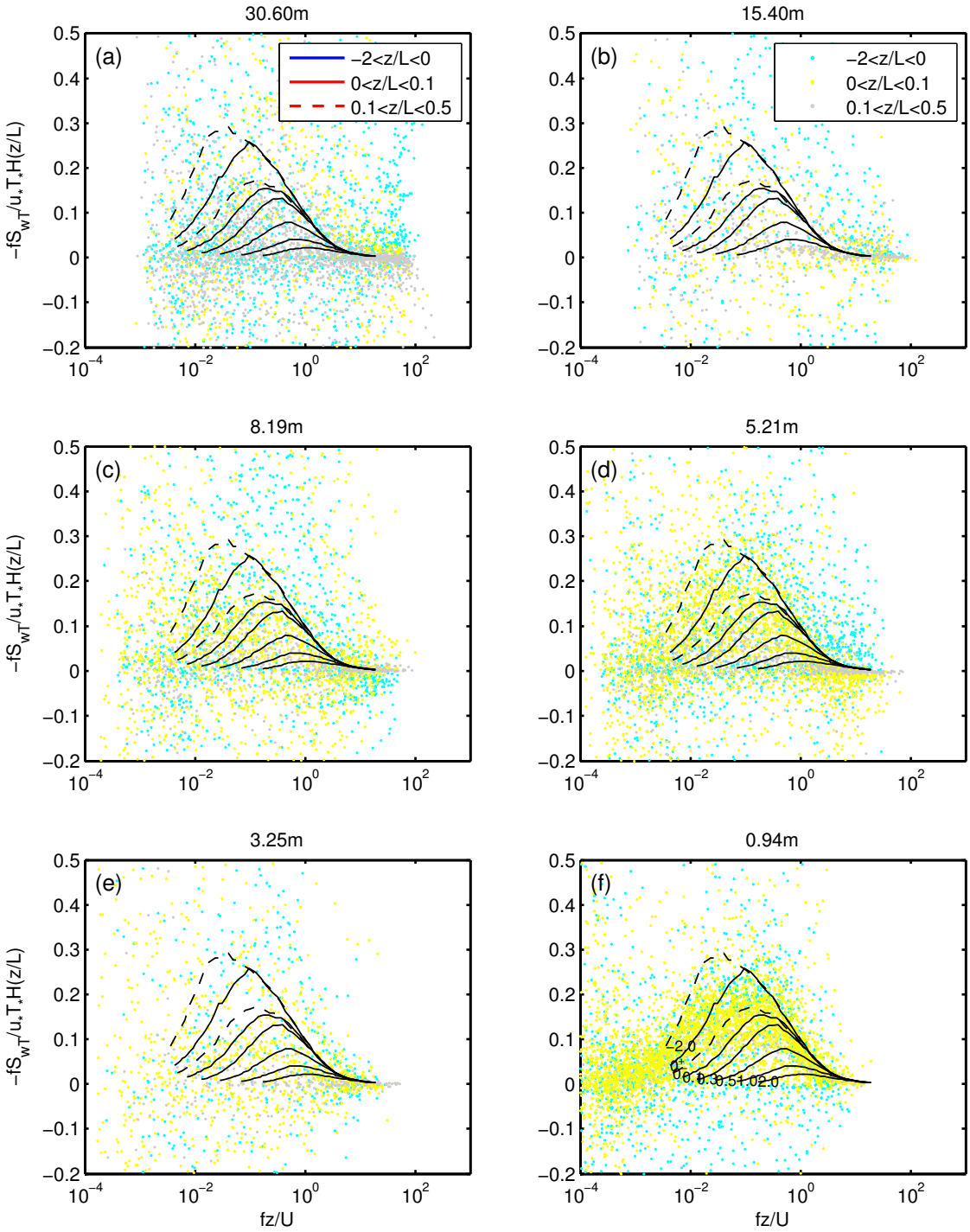

Figure 5.10: Same as Figure 5.7 but for wT.

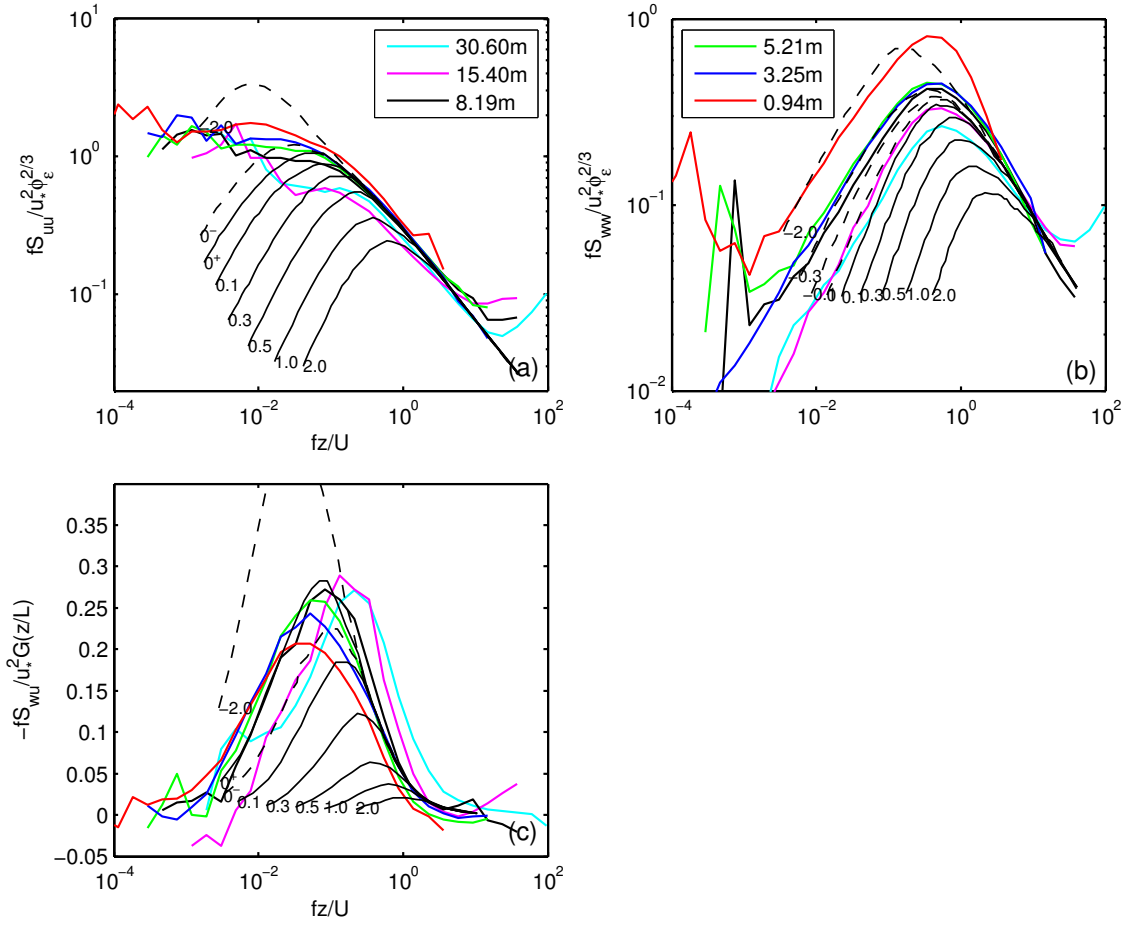

Figure 5.11: Normalised spectra and cospectra of (a) u, (b) w and (c) uw at each measurement height under unstable conditions (-2.0 $\geq z/L \leq$ 0).

daytime values over arid grassland of 100-200 Wm^{-2} (e.g. Ortega-Farias *et al.* (1996)). With such small magnitudes observed it is not surprising large scatter is produced when S_{wT} is normalised by T_* and u_*. Unlike the u and w spectra, the bin averaged curves for the uw spectra show some differences between stability regimes. The shapes of the observed curves agree reasonably well with the Kaimal *et al.* (1972) curves, although there are variations in the location of the peaks on the fz/U axis, which appear to be at least in part related to measurement height.

The bin averaged curves for u, w and uw at all measurement heights are shown on the same plots in Figure 5.11 for the unstable cases, Figure 5.12 for the weakly stable cases and Figure 5.13 for the moderately stable cases. The curves representing the u, w and uw spectra from the 0.94 to 8.19 m measurement levels are reasonably similar to each other in the unstable cases (Figure 5.11). The exception to this is the w data from the 0.94 m, which was discussed above in comments regarding Figure 5.8. The upper two levels however, behave differently in all three plots. The peaks in the curves are shifted towards more stable conditions compared to the data from the lower levels and

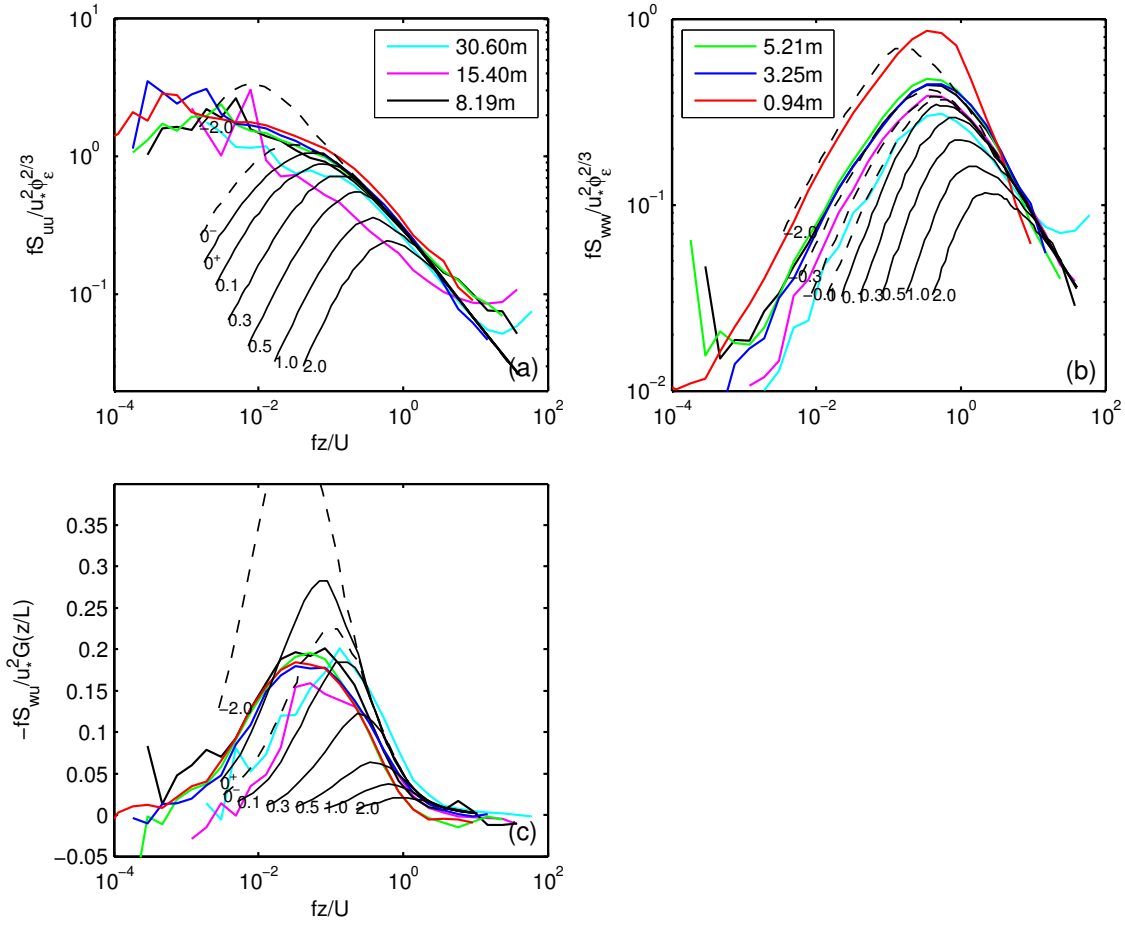

Figure 5.12: Normalised spectra and cospectra of (a) u, (b) w and (c) uw at each measurement height under weakly stable conditions ($0 \geq z/L \leq 0.1$).

the Kaimal *et al.* (1972) curves. This can be interpreted as follows: at the upper two levels a larger fraction of the energy is associated with higher frequencies (smaller eddies) than at the lower levels and compared with the Kansas experiments, i.e. the turbulence behaves as would be expected under more stable conditions. The differences between the lower and upper measurement levels for unstable values of z/L support the hypothesis that they are outside the constant flux layer for the majority of the observation period.

The u and w spectra under weakly stable conditions (Figure 5.12) are similar to that in the unstable regime. Most of the curves lie within the unstable region of the Kaimal *et al.* (1972) curves. The very small differences in turbulent structure between the unstable and weakly stable cases is likely due to the small range of z/L values that exist in the unstable regime. Although the regime includes all z/L values between -2 and 0, Figure 5.3 shows that, especially at the lowest levels, most of the values are actually between -0.1 and 0. In reality both these categories are 'near-neutral' and there is little difference in turbulent characteristics between the two. It is more revealing to compare the curves from the unstable and weakly stable cases with those from the moderately stable cases. Figure

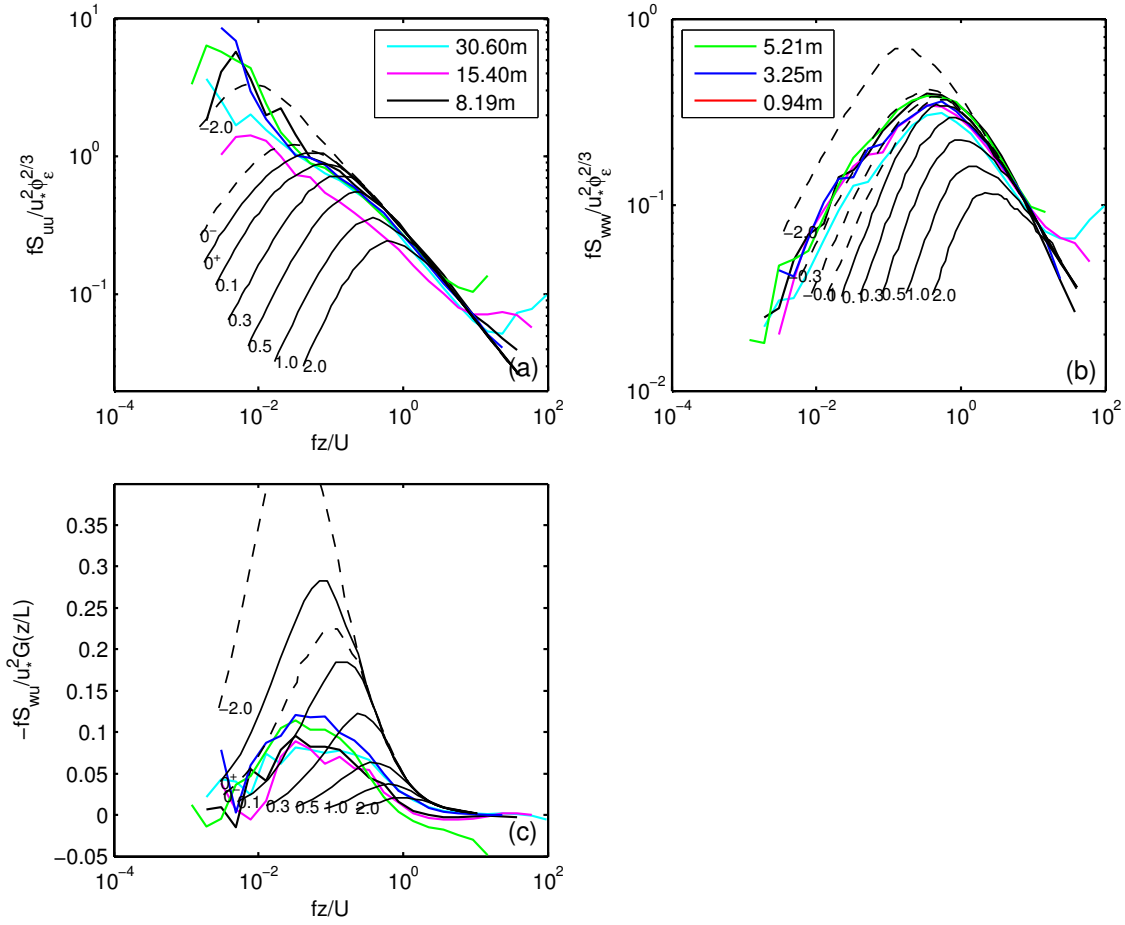

Figure 5.13: Normalised spectra and cospectra of (a) u, (b) w and (c) uw at each measurement height under moderately stable conditions ($0.1 \geq z/L \leq 0.5$).

5.13 shows that for u and w, although the curves are still within the unstable region of the Kaimal *et al.* (1972) curves, there is better agreement between all measurement levels. The same is true of uw, the height of the peaks in the curves is in better agreement with the Kaimal *et al.* (1972) curves for $0.1 > z/L > 0.5$ and the peaks from each level is at the same frequency. This illustrates an alternative regime in the differences between turbulent characteristics at each level when the boundary layer is moderately stable compared to when it is near-neutral.

The hypothesis proposed at the end of the previous section suggested that due to the shallow boundary-layer depths observed in the central Arctic during ASCOS, the surface (constant flux) layer is also extremely shallow (often < 20 m) and this could explain differences in turbulent characteristics between the upper and lower measurement levels. The spectral analysis using Monin-Obukhov similarity scaling has shown that when normalised, turbulent spectra from all six measurement levels do not all collapse onto the 'universal' set of curves suggested by Kaimal *et al.* (1972). The analysis does however, suggest that the lower-most four levels show similar turbulent characteristics and the

upper-most two levels show similar turbulent characteristics, and that these two sets of characteristics are different to each other. This supports the hypothesis that the constant flux layer does not always extend up to 30 m over sea ice in the central Arctic during the late summer months.

Bulk turbulent flux parameterisation schemes, which are often based on Monin-Obukhov similarity theory, assume that turbulent fluxes are constant in the surface layer. The parameterisation schemes use model diagnostics from the lowest vertical model level to compute the surface fluxes. If this first model level is outside the surface layer, similarity theory is invalid and the surface flux parameterisation scheme will not provide accurate estimates of the surface turbulent fluxes. As an example, the first model level in the MetUM is at 20 m for temperature and humidity and 10 m for wind components, which are likely to be outside of the surface layer under the majority of conditions observed during ASCOS. This goes some way in explaining why the transfer coefficients are overestimated by the MetUM (Figure 5.2).

The results from this analysis are however, not pronounced or straightforward, largely due to the large scatter in the turbulent spectra, which is a consequence of a narrow range of conditions and a limited volume of good quality turbulence data measurements. Observations were made for only three weeks and significant amounts of the data were removed during quality control (see Section 3.3.3). As discussed in Chapter 3, this is a consequence of the measurement environment, where a balance must be found between removing ice accumulation from instruments and making continuous measurements. The spectral analysis has suggested reasons for why the values for φ_m in Figure 5.3 are too high for a given z/L at the upper two levels but does not explain why only the measurements from the lowest level agree well with results from previous experiments. Nevertheless, the conclusions are revealing and useful and should be used to inspire further research.

5.3.2 Local scaling

Since the normalised spectra and cospectra from the ASCOS observations do not scale well using Monin-Obukhov similarity theory, it is appropriate to test a different scaling method. Local similarity theory was developed by Nieuwstadt (1984) and Sorbjan (1986) to scale characteristics of turbulence in the stable boundary layer. Frequency-weighted spectral or cospectral energy density for each 10 minute averaging period is normalised by the relevant mean variance or covariance (e.g. $-fS_{uw}/\overline{u'w'}$) and as with Kaimal *et al.* (1972) scaling, the frequency is normalised by the measurement height and the mean wind speed (fz/U), but then divided by a reduced frequency, f_m. The data should then

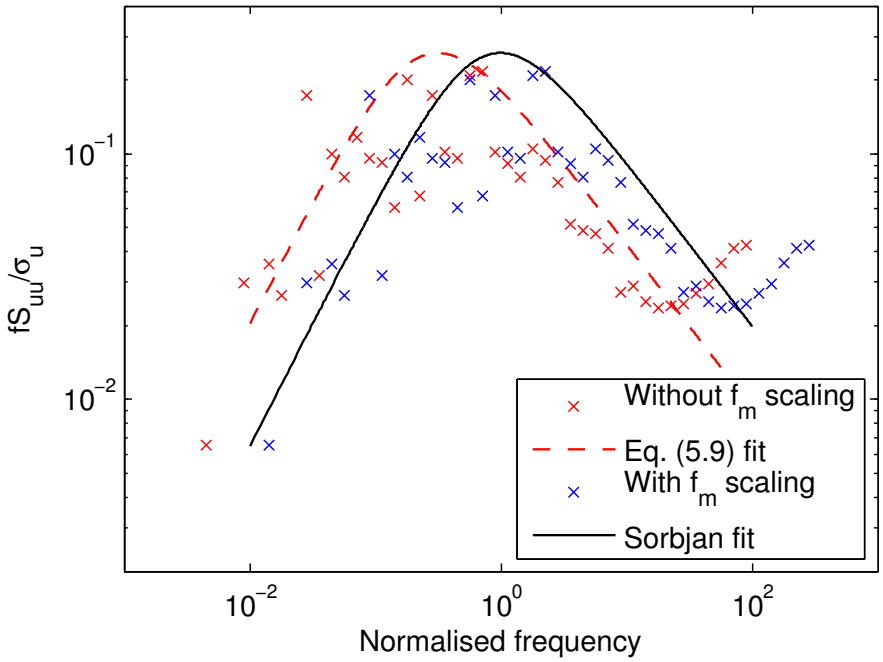

Figure 5.14: Method for finding f_m: an example using one 10 minute period of turbulence data. The red crosses represent the normalised frequency-weighted spectral energy density, bin averaged by frequency plotted against fz/U, the red dashed line is the selected fit of Equation 5.9 to this data (see text for further explanation). The blue crosses present the normalised frequency-weighted spectral energy density, bin averaged by frequency plotted against $(fz/U)/f_m$ and the black line is the Sorbjan (1986) universal curve.

collapse onto a universal curve, which for u, v, w and T has the form:

$$f(f_n/f_m) = \frac{0.644(f_n/f_m)}{1 + 1.5(f_n/f_m)^{5/3}} \tag{5.9}$$

and for uw and wT has the form:

$$f(f_n/f_m) = \frac{f_n/f_m}{[1 + 0.75(f_n/f_m)]^{5/3}} \tag{5.10}$$

where f_n is the normalised frequency, $f_n = fz/U$.

The reduced frequency, f_m normalises the spectra and cospectra so that the peak of each curve is at $f_n/f_m = 1$. The value of f_m must be deduced for every 10 minute period of data and considering the volume of data involved it must be determined in an automated way. Figure 5.14 is used to illustrate how this was achieved, using the spectra of u as an example. For every 10 minute averaging period bin averaged $-fS_u/\sigma_u$ is plotted against the normalised frequency, f_n (red crosses). A form of the curve described by Equation 5.9 is then fitted to this data (red dashed line). The form of this curve is determined by performing a least squares fit on the data points and a range of curves of the same shape

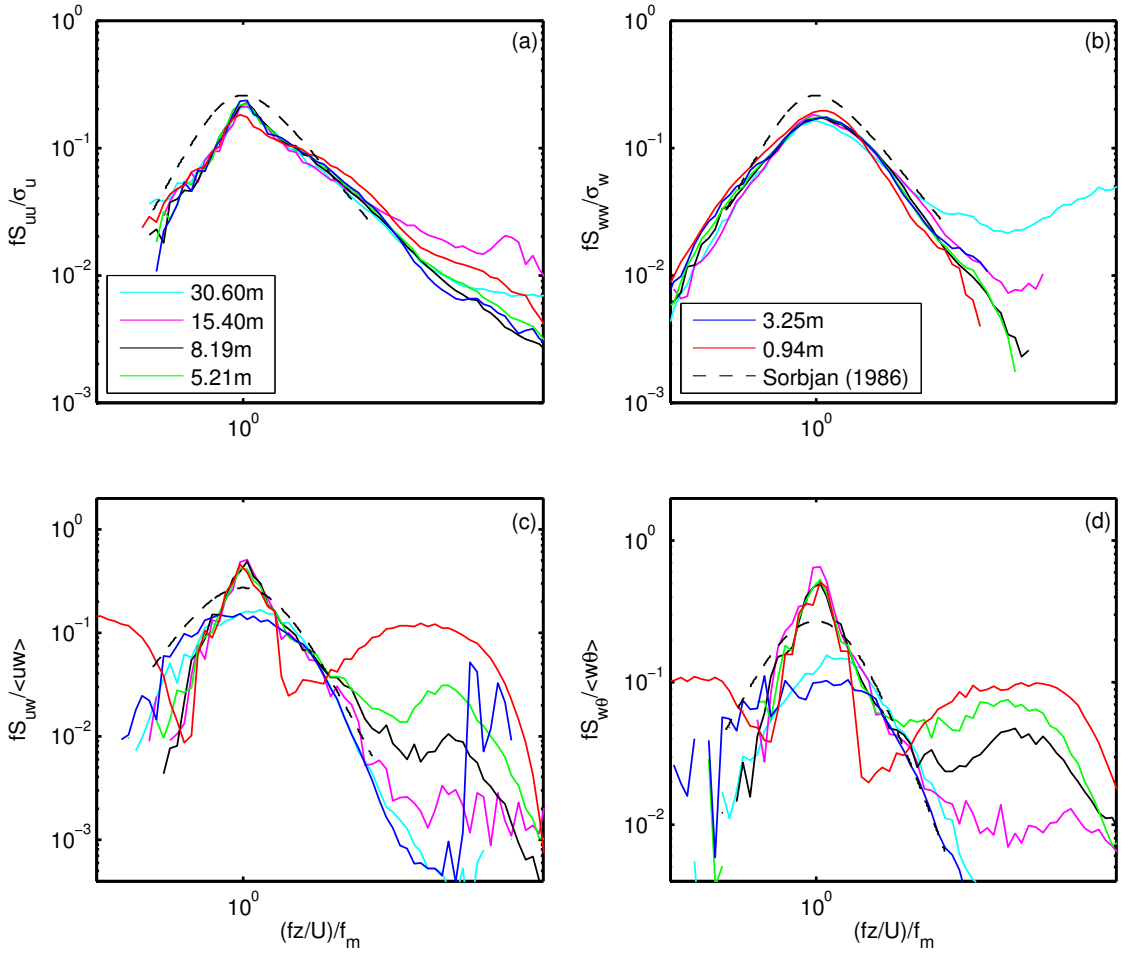

Figure 5.15: Spectra and cospectra of (a) u, (b) w, (c) uw and (d) wT, scaled according to local similarity theory Sorbjan (1986).

as Equation 5.9, but that are displaced left or right on the frequency axis by different amounts. These curves are formed by taking a range of values for f_m in Equation 5.9; the curve with the best least squares to the data points is then selected (red dashed line) and the normalised frequency at the curve maxima is found. This frequency is set to f_m and thus the data points can be plotted against f_n/f_m (blue crosses). The peak in the bin averaged, normalised spectra now lies at $f_n/f_m = 1$, in agreement with the Sorbjan (1986) universal curve (black line). The example in Figure 5.14 is however, an ideal case. Many of the bin averaged, normalised cospectral do not produce an adequate fit to a form of Equation 5.9 and thus errors in the diagnosis of f_m can occur. This error is minimal in the variances but for the covariances the effect is much larger because there is more scatter in the bin averaged normalised spectra data. The automation of this process causes a sub-optimal form of Equation 5.9 to be selected for some periods, which produces a value of f_m that is often too small. This causes some of the spectra to be shifted too far to the right, which accounts for the second peak in the curves in Figure 5.15c,d.

Figure 5.15 shows the normalised spectra and cospectra from all measurement heights on the 15 and 30 m masts. The normalised spectra for u and w match the curve formed by Equation 5.9 very well and the curves from all the measurement levels collapse onto the same curve. The normalised cospectra for uw and $w\theta$ generally agree well with Equation 5.10 although there is an obvious second peak at higher frequencies; the reasons for which have already been explained. This result is expected since the derivation of f_m from the spectra guarantees that the peaks of the spectra are aligned with $f_n/f_m = 1$. Unfortunately, this method is not an alternative to Monin-Obukhov similarity theory for model bulk surface turbulent flux algorithms because the value of f_m cannot be computed within the model.

5.4 Surface roughness

5.4.1 Calculation of the roughness lengths and transfer coefficients

Representative values of the transfer coefficients are vital for the surface flux parameterisation schemes that are described in Section 2.1.7. The transfer coefficients depend on the roughness lengths z_0, z_t and z_q and the stability functions φ_m and φ_h. In this section, values for the roughness lengths are estimated and their application in surface flux parameterisation schemes is considered. In order to compute the roughness lengths from observations Equations 2.41 to 2.43 are rearranged following Andreas *et al.* (2005) to give:

$$z_0 = z \exp\left(-\kappa C_{Dr}^{-1/2} + \varphi_m(z/L)\right) \tag{5.11}$$

$$z_t = z \exp\left(-\kappa C_{Dr}^{1/2} C_{Hr}^{-1} + \varphi_h(z/L)\right) \tag{5.12}$$

$$z_q = z \exp\left(-\kappa C_{Dr}^{1/2} C_{Er}^{-1} + \varphi_h(z/L)\right) \tag{5.13}$$

where z is the measurement height and $\varphi_m(z/L)$ and $\varphi_h(z/L)$ are the Businger-Dyer (Businger *et al.*, 1971; Dyer, 1974) forms of the stability functions. There are in fact various forms of the functions but Figure 5.5 shows that at moderate stabilities there is negligible difference between them. The transfer coefficients are calculated by rearranging Equations 2.38 to 2.40 to give:

$$C_{Dr} = \frac{-\overline{u'w'}}{U_r^2} \tag{5.14}$$

$$C_{Hr} = \frac{\overline{w't'}}{U_r(T_s - \theta_r)} \tag{5.15}$$

$$C_{Er} = \frac{\overline{w'q'}}{U_r(q_s - q_r)} \tag{5.16}$$

$\overline{u'w'}$, $\overline{w't'}$ and $\overline{w'q'}$ are from sonic anemometer and Licor measurements made at height $z = r$, U_r is the wind speed at z and θ_r and q_r are measurements from aspirated temperature and relative humidity sensors in close proximity to the sonic anemometers. The surface temperature, T_s is estimated from the mean of measurements made by 10 thermocouples at 2 different locations near the 15 m mast and q_s is the surface saturation humidity with respect to ice at T_s, calculated using Equation 2.10.

Figure 5.16 shows z_0 calculated at each measurement height on the 15 and 30 m masts and from measurements made at the open lead site. The red points represent periods where the data is rejected due to data quality issues, discussed in Section 3.3 or periods when the masts and/or ship were upwind of the instruments. The blue data points represent good quality data, the black crosses are bin averaged values over 30 ° intervals and the error bars are ± 1 standard error from each median value. It is obvious from the plots that the scatter in the data is high since the error bars are large even on a log scale. Although Andreas *et al.* (2005) also found large variability in the roughness lengths calculated from the Ice Station Weddell data, the variability was smaller than produced by the ASCOS data. Reasons for this could be that the data points used in the Andreas *et al.* (2005) study were hourly averages and the data set is longer. Another possibility is that the sea ice was more spatially homogeneous than that found in the Arctic. This is because a large fraction of southern hemisphere sea ice melts every summer and therefore contains fewer large roughness features, such as pressure ridges (NSIDC, 2009). 10 minute averages have been chosen for the ASCOS data set to maximise the number of points available for each bin since the data set is much smaller.

Despite the problems discussed above a relationship is apparent between the bin averaged values of z_0 calculated from the ASCOS observations and the wind direction. Figure 5.17 shows a comparison of the bin averaged values from each measurement height. z_0 at the open lead site shows the most variability with wind direction; the magnitude of z_0 varies by two orders of magnitude, between 1x10^{-4} and 1x10^{-2} m and there are two peaks in the z_0 measurements at approximately 180° and 360°. z_0 computed from the mast measurements are generally smaller and only vary by one order of magnitude with wind direction. There is also some indication of slightly higher values when the wind direction is greater than 270° and less than 100°.

Apart from the most recent studies the transfer coefficients, rather than the roughness lengths were used to quantify the roughness of sea ice. A general form of C_{Dr} is the 10 m neutral drag coefficient, C_{DN10} and in near-neutral stability it can be derived from

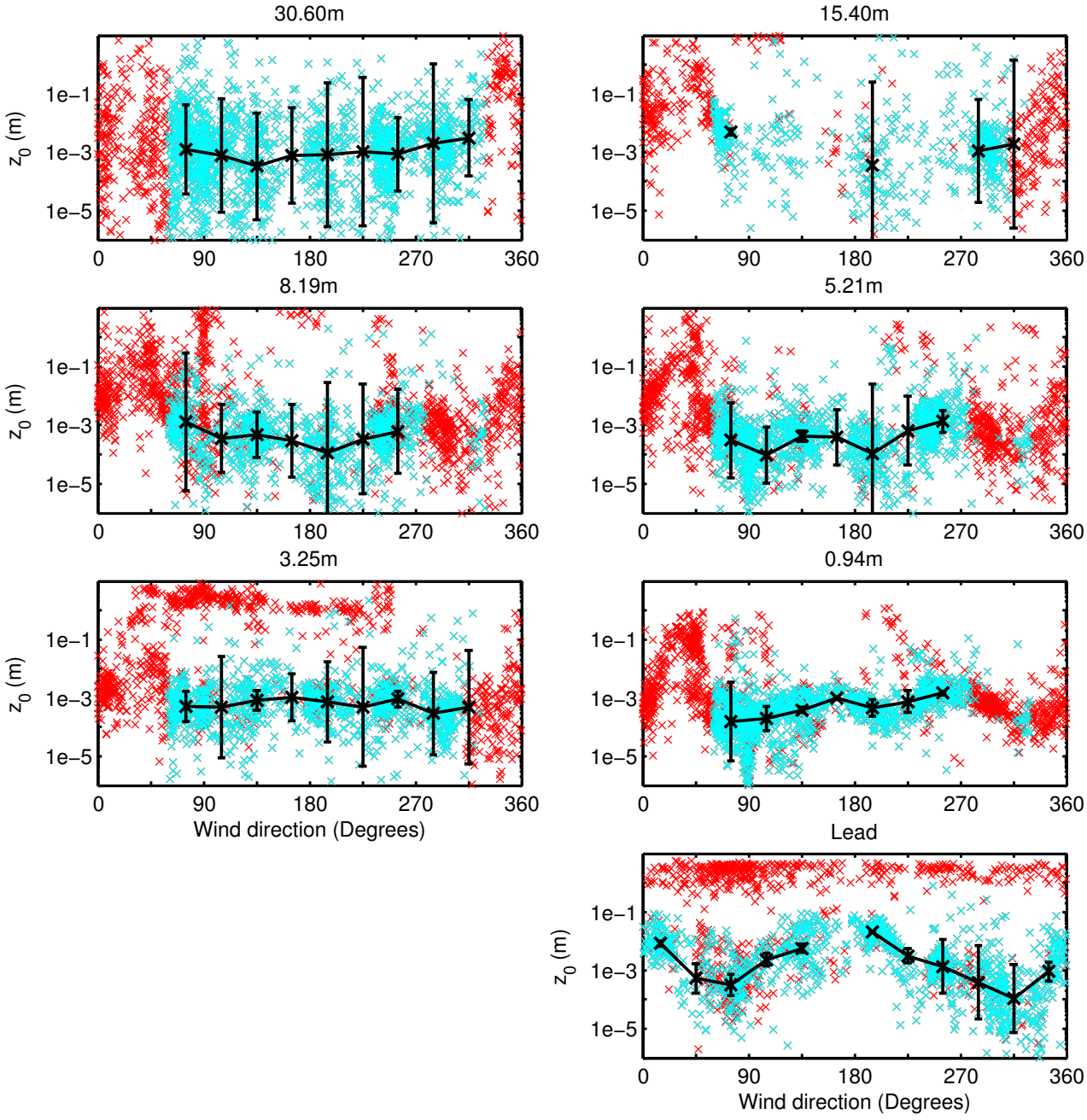

Figure 5.16: 10 minute averaged z_0 computed for all instrument heights on the 15 m and 30 m masts and at the open lead site. The red points represent periods that are unusable due to data quality issues or periods when the masts and/or ship were upwind of the instruments. The black crosses are bin averaged values over 30° intervals and the error bars are ± 1 standard error from each median value.

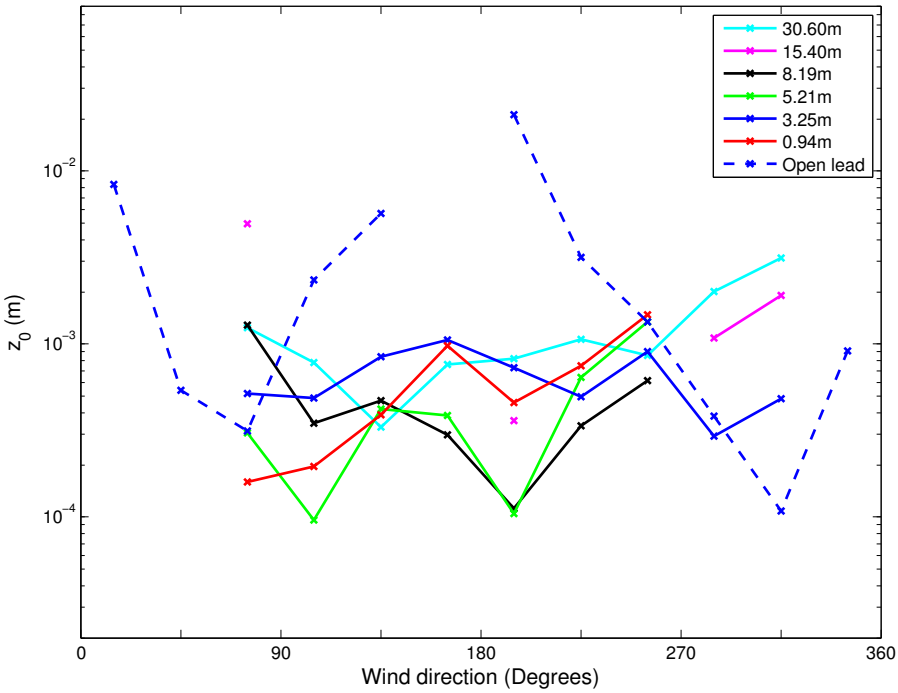

Figure 5.17: Bin averaged z_0 data from Figure 5.16 for each instrument height.

Equations 2.38 and 2.23 (Andreas & Claffey, 1995):

$$C_{DN10} = (u_*/U_{10})^2 \tag{5.17}$$

To allow easy comparison with previous studies C_{DN10} is calculated from the observations at each measurement height for periods of near-neutral conditions ($-0.1 < z/L < 0.1$) (Figure 5.18). As one would expect, the wind direction sectors with the highest z_0 also produce the largest values of C_{DN10} and the variability at the open lead site is larger than at the mast site.

5.4.2 Interpretation in terms of surface features

A flux footprint illustrates the upwind area in which the atmospheric flux measured by an instrument is generated. The three main factors that determine the size and shape of the footprint are the measurement height, surface roughness and atmospheric stability. Lower measurement heights, increased surface roughness and stronger stabilities produce smaller footprints and move the peak contribution closer to the instrument. Knowledge of the flux footprint for each measurement height will help to explain the variation in z_0 or C_{DN10} with wind direction. Flux footprints calculated by Andreas Held for the 6 measurement levels on the meteorological masts, using a model by Schmid (1994) are shown in Figure 5.19. The source area for 90 % of the measured flux is within 60 m of the

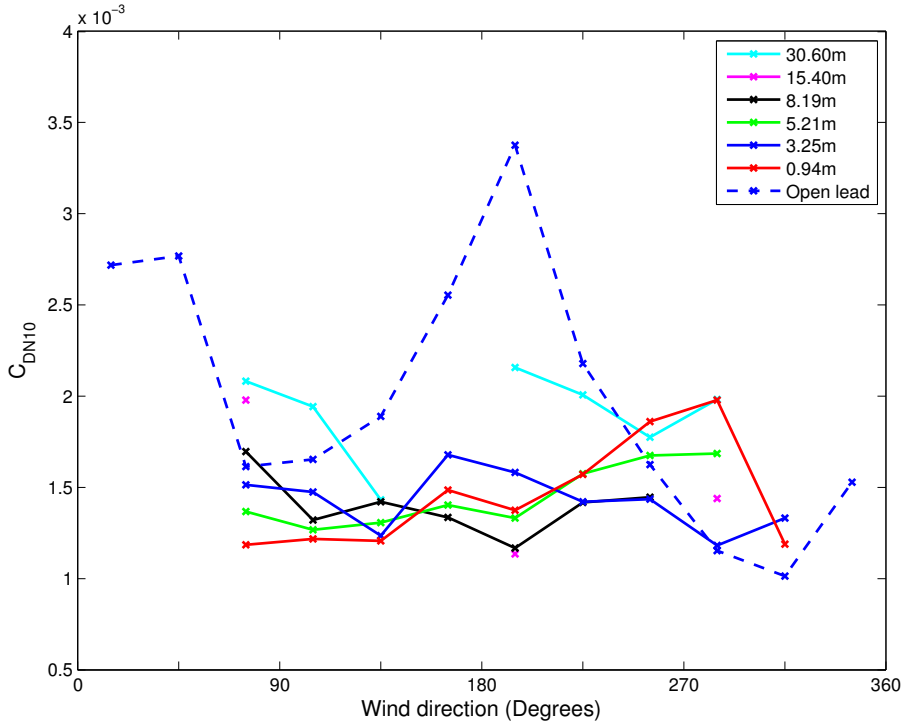

Figure 5.18: Same as Figure 5.17 but for C_{DN10}.

instrument at the 0.94 m measurement level. This distance increases with measurement height; at the 30.60 m level the 90 % source area extends up to 3 km away from the instrument.

The approximate outer limits of the 90 % source areas for the instruments at 8.19, 15.40 and 30.60 m are illustrated on an aerial photo of the ASCOS ice camp station in Figure 5.20. When the wind direction is between 100 and 270° the entire source area for all levels is over the large ice floe. For all other wind directions at least a fraction of the source area is over the smaller floes or open leads. A comparison with Figure 5.17 shows that z_0 computed for the 8.19, 15.40 and 30.60 m levels is generally larger for wind directions less than 100° or more than 270° and smaller for wind directions 100-270°. At the lower levels this trend is less apparent because the limits of the 90 % source areas are almost entirely over the local ice floe. Table 5.2 summarises these results, in which the values for z_0, C_{Dr} and C_{DN10} are means computed from the bin averages in Figures 5.17 and 5.18. Over all wind directions the value of z_0 generally increases with increasing measurement height. This is consistent with the fact that the source areas of the upper levels include a larger fraction of rough ice and open leads than the lower levels. For periods when only the large ice floe is upwind of the instruments z_0 at the upper levels is decreased but the values for the lower levels remain similar to their overall means.

The results from Sections 5.2 and 5.3 suggest that the surface layer is often very shallow and that the upper measurement levels may not always be inside this layer. This questions

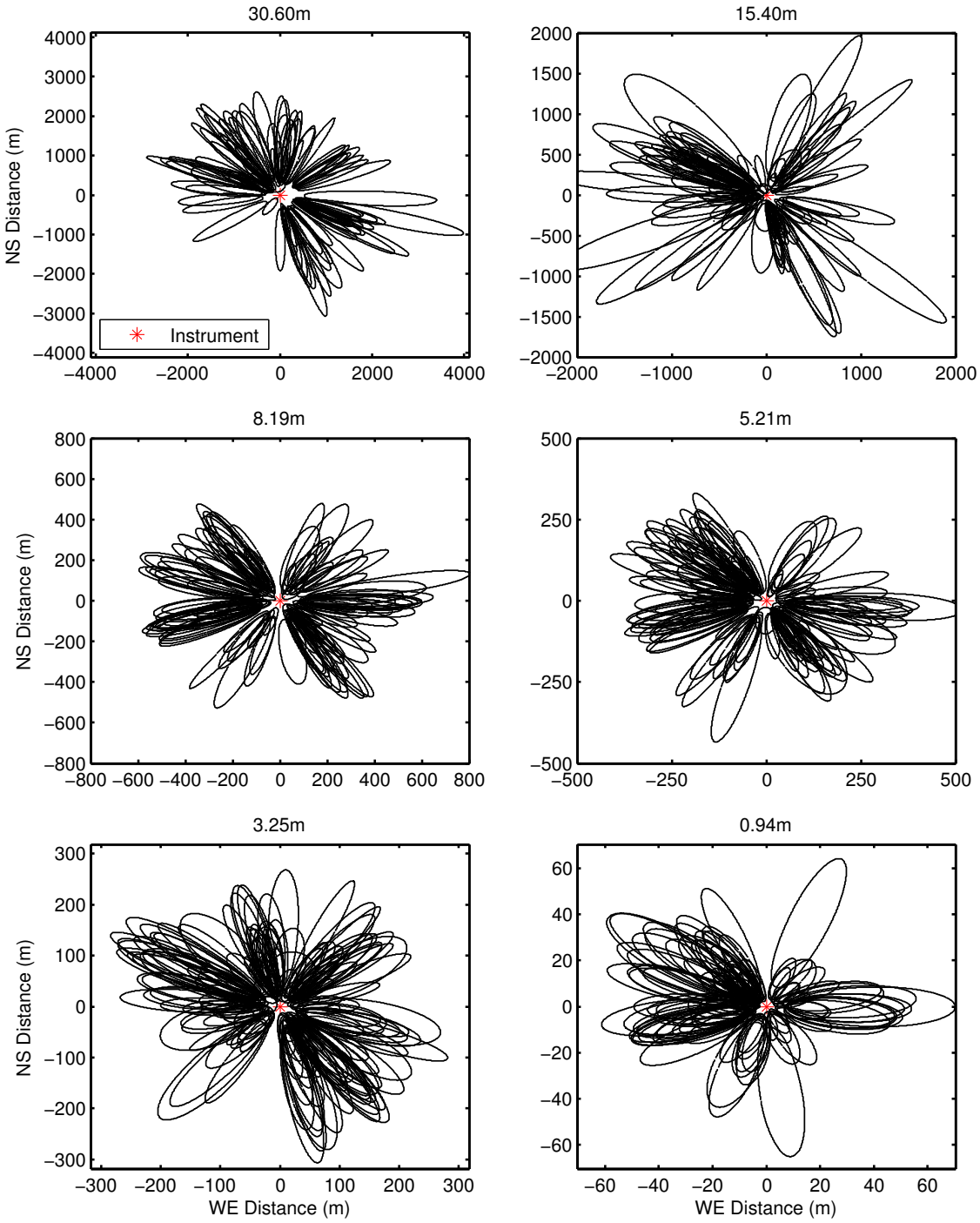

Figure 5.19: Flux footprints for each instrument height on the 15 and 30 m masts. Each ellipse represents the source area for 90 % of the measured flux. Footprints were calculated using 10 minute averaged data but only one in every 10 footprints are shown. Note the differences in axis scale. Data provided by Andreas Held, using the Schmid (1994) flux footprint model.

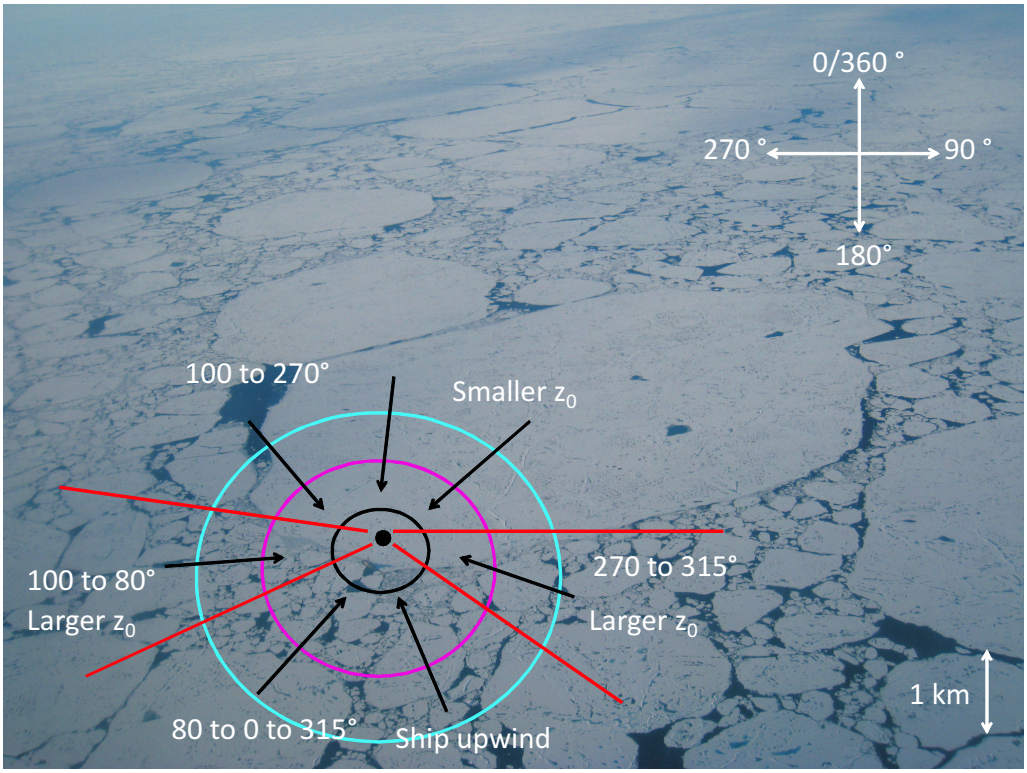

Figure 5.20: z_0 measurements in terms of the local floe. Arrows point in the direction the wind is blowing. The cyan, magenta and black circles represent the approximate limit of the 90 % flux source area for the instruments at 30.60 m, 15.40 m and 8.19 m respectively.

whether the values of z_0 that are computed from measurements made at the upper levels on the masts are actually representative of the surface layer. Under very stable conditions, which were not common during ASCOS, the instruments may not 'feel' the surface directly, but respond only to the local stability and wind sheer. Since heights of 15 to 30 m are still relatively close to the surface, an indirect link via continuous turbulence from the surface to the upper levels, probably means the wind stress is related to the surface roughness indirectly. The majority of conditions observed during the ice station were near-neutral ($-0.1 > z/L > 0.1$) and under these conditions the wind stress measured at the upper levels is very likely to be dependent on the surface roughness, even if these levels are not in the surface layer. For these reasons it will be assumed that the values of z_0 computed from observations at the upper levels are representative of the surface roughness.

Similar conclusions can be drawn from the measurements made at the open lead site. Figure 5.21 shows that the 90 % source area of the lead extends up to 200 m away from the instrument. Wind direction is split into 6 sectors in Figures 5.22 and 5.23 and the mean values of z_0 and C_{DN10} for each sector are summarised in Table 5.3. The sectors with the smallest values are C and D, in which the ice floe is upwind. The values of z_0

Table 5.2: Values of C_{DN10} and z_0 measured at the Met Alley site. The second column represents z_0 computed using data only from periods when the large ice floe was upwind (i.e. wind direction = 100-270°).

z (m)	z_0 100-270°	z_0	n_{obs}	C_{Dr}	n_{obs}	C_{DN10}	n_{obs}
30.60	$7.6\text{x}10^{-4}$	$1.2\text{x}10^{-3}$	1749	$1.1\text{x}10^{-3}$	1871	$1.91\text{x}10^{-3}$	537
15.40	$3.6\text{x}10^{-4}$	$2.1\text{x}10^{-3}$	512	$1.3\text{x}10^{-3}$	539	$1.52\text{x}10^{-3}$	230
8.19	$3.6\text{x}10^{-4}$	$4.9\text{x}10^{-4}$	932	$1.3\text{x}10^{-3}$	960	$1.40\text{x}10^{-3}$	607
5.21	$5.0\text{x}10^{-4}$	$4.7\text{x}10^{-4}$	1218	$1.4\text{x}10^{-3}$	1237	$1.45\text{x}10^{-3}$	992
3.25	$9.3\text{x}10^{-4}$	$8.0\text{x}10^{-4}$	1025	$1.7\text{x}10^{-3}$	1029	$1.43\text{x}10^{-3}$	876
0.94	$7.1\text{x}10^{-4}$	$6.3\text{x}10^{-4}$	1311	$2.2\text{x}10^{-3}$	1316	$1.45\text{x}10^{-3}$	1119

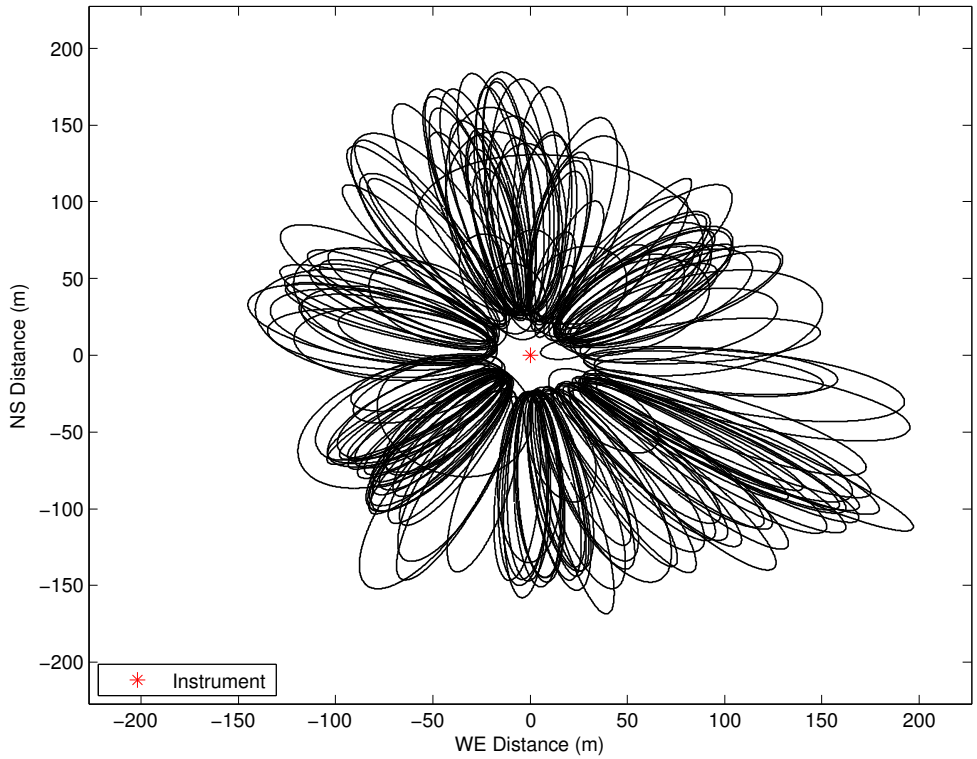

Figure 5.21: Flux footprints for the open lead site. Each ellipse represents the source area for 90 % of the measured flux. Footprints were calculated using 30 minute averages but one in every two footprints is shown. Data provided by Andreas Held, using the Schmid (1994) flux footprint model.

observed in the other four sectors are almost an order of magnitude higher. These sectors include open leads, the ice edge and broken ice. Even though sectors A and F contain mostly water, z_0 is comparable to that measured in sectors B and E, which contain broken ice floes. This is most likely due to the close proximity of the ice edge to the instrument, which is a significant roughness element.

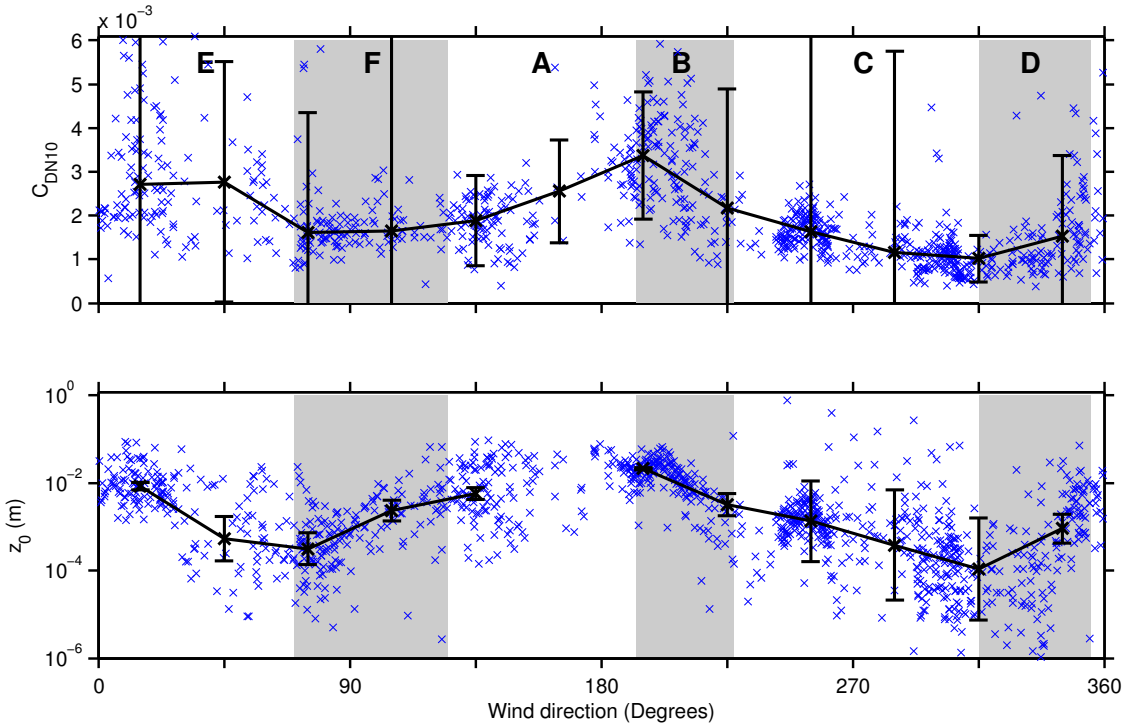

Figure 5.22: z_0 and C_{DN10} computed from measurements made at the open lead site. The bottom panel is reproduced from a figure by Andreas Held.

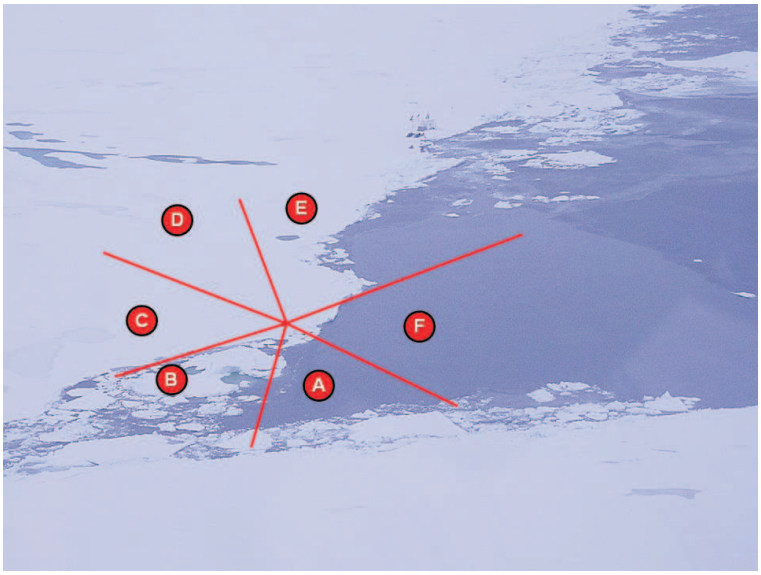

Figure 5.23: Plan view of ice conditions at the open lead site. Provided by Andreas Held.

Table 5.3: Values of C_{DN10} and z_0 measured at the open lead site.

Sector	Ice type	C_{DN10}	z_0
A	Open lead/ice edge	$2.22\text{x}10^{-3}$	$5.7\text{x}10^{-3}$
B	Rough ice	$2.78\text{x}10^{-3}$	$3.2\text{x}10^{-3}$
C	Ice floe	$1.26\text{x}10^{-3}$	$6.1\text{x}10^{-4}$
D	Ice floe	$1.53\text{x}10^{-3}$	$9.1\text{x}10^{-4}$
E	Fairly rough ice	$2.74\text{x}10^{-3}$	$4.4\text{x}10^{-3}$
F	Open lead/ice edge	$1.63\text{x}10^{-3}$	$1.3\text{x}10^{-3}$

5.4.3 Comparison with previous observations

Table 5.4 compares values of z_0 calculated from the ASCOS data with values found by previous experiments and some examples of z_0 used in global circulation models. The values of z_0 measured over rough and smooth ice at the ASCOS mast and open lead sites agree reasonably well. The value calculated by Tjernström (2005) for all wind directions from the AOE 2001 data is similar to that measured over rough ice during ASCOS. The roughness lengths calculated from the SHEBA data over an entire year (Persson *et al.*, 2002a) are similar to those measured over smooth ice during ASCOS. This is likely to be because outside of the summer months snow cover reduces the surface roughness and the ice floes are generally larger, with less broken ice surrounding the main floes. Observations over ice in the Weddell Sea, Antarctica during autumn and early winter show a similar range of magnitudes to those in the Northern Hemisphere. Several expeditions to the Arctic Ocean before the 1990's computed values of C_{DN10} instead of z_0. Overland (1985) gives an overview of measurements made before 1985 and in addition, Guest & Davidson (1991) provide values of C_{DN10} calculated from a number of experiments in the late 1980's in the Spitsbergen Archipelago. The estimates from ASCOS over large, smooth ice floes agree well with measurements made over smooth ice during the other experiments and the estimates from ASCOS for rough ice are similar to the other estimates for rough multi-year ice.

Table 5.4 presents two examples of the value of z_0 used in global circulation models. The version of the MetUM operational in August 2008 uses $3.0\text{x}10^{-3}$ m for the entire year over all ice types and the Polar Weather Research and Forecasting (WRF) model assumes $1.0\text{x}10^{-3}$ m. Both these estimates are within the range of measurements made during the field experiments listed in Table 5.4, although both are at the upper limit of the observed values. This is consistent with the fact that this value is designed to represent all ice conditions, including ice in the marginal ice zone at grid box scales of 10-100 km, which the observations in Table 5.5 show to be rougher than the larger ice floes further north. The observations used to calculate z_0 from the experiments in Table 5.4 were made on a mast located on a relatively large ice floe, which is unlikely to be

Table 5.4: Values of z_0 found from various field experiments. AOE 2001 (Tjernström, 2005), SHEBA (Persson *et al.*, 2002b) Ice Station Weddell (Andreas *et al.*, 2005), Met Office Unified Model (MetUM) (Essery *et al.*, 2001) and Polar Weather Research and Forecasting (WRF) model (Bromwich *et al.*, 2009). The observed rough ice value from the mast is a mean of z_0 measured from the 30.60 and 15.40 m levels during periods when the rough ice sectors were upstream. The observed smooth ice value is a mean of z_0 measured under all wind directions (apart from when the ship was upstream) at the 0.94 to 8.19 m levels and from measurements on the upper two levels during periods when the large ice floe was upstream. For the open lead the rough ice value is a mean of z_0 from sectors A, B, E and F and the smooth ice value is a mean from sectors C and D from Table 5.3.

Experiment	Latitude	Time of year	Ice type	z_0 (x10^{-3} m)
ASCOS	87 °N	Aug/Sept	Large ice floe (mast site)	0.59
			Rough ice/leads (mast site)	2.40
			Large ice floe (lead site)	0.76
			Rough ice (lead site)	3.70
AOE 2001	88-89 °N	Aug	Large floe/broken ice/leads	3.00
SHEBA	74-81 °N	Whole year	Large ice floe	0.31 (2.2 m), 0.46-0.60 (8.9-18.2 m)
Ice Station Weddell	66-72 °S	Feb-June	Antarctic sea ice	∼0.10-1.00 (for $u_* = 0.1$-0.3 m s^{-1})
MetUM	All	Whole year	All types	3.00
Polar WRF	All	Whole year	All types	1.00

representative of ice in a 10 km region around the measurement site and even less likely to be representative of sea ice throughout the Arctic. To make observations of surface roughness over an area representative of a meso or global scale model grid box the flux footprint of the measurement would need to be at least 10 km, requiring a measurement height much greater than 30 m. Section 5.3 showed that measurement levels above 5 to 10 m are very often outside the surface layer and therefore it impossible to a make accurate measurements of surface characteristics at levels above this height on a mast. Measurements would be better made with low-flying aircraft.

5.5 Evaluation of the SHEBA bulk flux algorithm

The SHEBA bulk turbulent flux algorithm (Andreas *et al.*, 2009) was developed using observations from the SHEBA experiment to predict surface turbulent fluxes of momentum, sensible and latent heat over sea ice. It is based on the same principles as the schemes in most mesoscale and global atmospheric models (see Section 2.1.7) and is therefore a useful tool for investigating the success of these types of schemes in modelling the surface turbulent fluxes. The scheme takes a similar form to Equations 2.38 to 2.40, except U_r is replaced with P_r, which is an effective wind speed that incorporates the enhancement

Table 5.5: Values of C_{DN10} from various field experiments: Spitsbergen seas (Guest & Davidson, 1991) and pre-1985 composite when $T_1 \sim 0$ °C (Overland, 1985). ASCOS means calculated using the same method in Table 5.4.

Experiment	Latitude	Time of year	Ice type	C_{DN10} (x10^{-3})
ASCOS	87 °N	Aug/Sept	Large ice floe (mast site)	1.45
			Broken ice/leads (mast site)	1.87
			Large ice floe (lead site)	1.40
			Rough ice (lead site)	2.34
Spitsbergen seas	73-85 °N	Various	Smooth multi-year	2.2
			Rough multi-year	3.4
			Very rough multi-year	4.6
			Extremely rough multi-year	8.0
Pre-1985 composite	Various	Various	Smooth ice	1.5
			Arctic pack (ice>90%)	1.7
			Marginal seas	2.2
			Inner MIZ	2.6
			Outer MIZ	2.8

of turbulent exchange by wind gustiness. In stable stratification P_r is of the form:

$$P_r = U_r + 0.5\text{sech}(U_r) \tag{5.18}$$

and in unstable stratification it is of the form:

$$P_r = (U_r^2 + \beta_g^2 w_*^2)^{1/2} \tag{5.19}$$

where $\beta_g = 1.25$ (Fairall *et al.*, 1996) and w_* is Deardorff's convective velocity scale (Deardorff, 1970):

$$w_* = u_* \left(-\frac{z_i}{\kappa L}\right)^{1/3} \tag{5.20}$$

where z_i is the depth of the convective boundary layer.

Two different versions of the algorithm were tested with the ASCOS observations. The first is that designed for use outside of the melt season (i.e. 'winter' season) and it computes the transfer coefficients using Equations 2.41 and 2.43 with a parametrised value for z_0 (Andreas *et al.*, 2009):

$$z_0 = 0.135\frac{\nu}{u_*} + 2.30\text{x}10^{-4}\tanh^3(13u_*) \tag{5.21}$$

where ν is the kinematic viscosity. Figure 1 in Andreas *et al.* (2010) illustrates the form of this function. z_t and z_q are then computed through the expression (Andreas, 1987):

$$\ln(z_x/z_0) = b_0 + b_1 \ln R_* + b_2(\ln R_*)^2 \tag{5.22}$$

where z_x is either z_t or z_q, R_* is the roughness Reynolds number, $R_* = u_* z_0 / \upsilon$ and b_0, b_1 and b_2 are polynomial coefficients defined in Andreas *et al.* (2005).

The second version was designed specifically for summer sea ice and the marginal ice zone (i.e. 'summer' season). It is applied on the assumption that drag associated with the vertical edges of leads and melt ponds dominates momentum exchange in summer and that the 10 m neutral transfer coefficient, C_{DN10} is a function only of sea ice concentration, C_i. The expression for C_{DN10} was derived by Andreas *et al.* (2009) using SHEBA measurements and observations made in the Arctic and Antarctic marginal ice zone:

$$10^3 C_{DN10} = 1.500 + 2.233 C_i - 2.333 C_i^2 \tag{5.23}$$

Figure 5.24 shows values of C_{DN10} derived from measurements made during SHEBA and a number of field campaigns in the marginal ice zone, and the quadratic fit to the data (Equation 5.23). The values of observed C_{DN10} for rough and smooth ice at the mast and open lead sites from Table 5.5 have been added to the plot. The blue square, representing data over large, smooth ice floes (C_i=1) from both the open lead and mast sites agrees well with the value predicted by Equation 5.23. The values of C_i over rough ice at the mast and open lead sites were estimated from the aerial photographs in Figures 5.20 and 5.23 at 80 % near the mast site and 40 % near the open lead site. The value of C_{DN10} from the mast site (red square) agrees well with the parameterisation but the value from the open lead site (green square) is larger than the predicted value. The ASCOS observations are however, consistent with the other observations when C_i is between 30 and 55 %.

The success of the summer parameterisation for C_{DN10} is compared to the results from the winter version of the SHEBA bulk flux algorithm in Figure 5.25. To simplify the analysis results are given only for periods when the wind direction was between 100 to 270°. This is because the observed values of z_0 were shown to vary significantly with wind direction and this particular sector was selected because it only includes periods when the large, fairly uniform ice floe was upwind of the measurements. The grey dots represent the observations, where $\tau/\rho = \overline{u'w'}$; U and $\overline{u'w'}$ are derived from measurements made by the sonic anemometers at each level and the grey line is a linear fit to the data. The green dots represent results using the summer sea ice parameterisation, for which it was necessary to compute C_{Dr}. Equations 2.29 and 5.17 were equated, z was set to 10 m and the expression was rearranged to give (Andreas & Claffey, 1995):

$$C_{DN10} = \frac{\kappa^2}{[\ln(10/z_0)]^2} \tag{5.24}$$

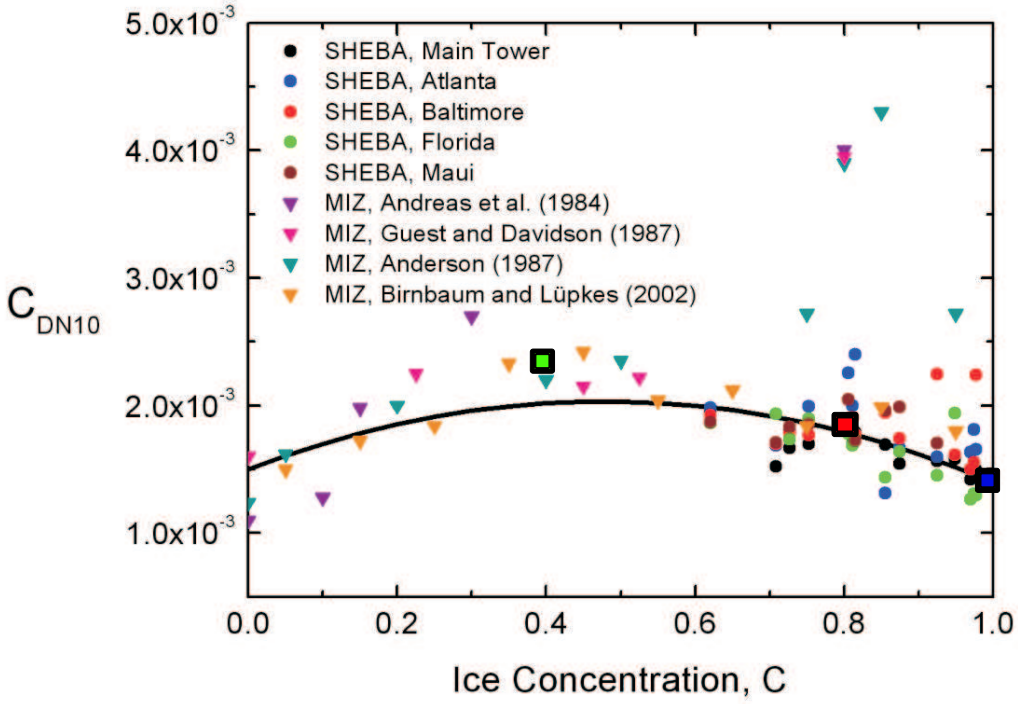

Figure 5.24: Summertime parameterisation for C_{DN10} over sea ice. The black line is a quadratic fit (Equation 5.23) to observations from the SHEBA experiment, observations in the Antarctic marginal ice zone by Andreas *et al.* (1984) and observations in the Arctic marginal ice zone by Guest & Davidson (1987), Anderson (1987) and Birnbaum & Lüpkes (2002). Original plot taken from Andreas *et al.* (2009). Values of C_{DN10} calculated from ASCOS observations have been added to the plot; rough ice at the mast site (red square), rough ice at the open lead site (green square) and smooth ice from the open lead and mast sites (blue square).

Rearranging this forms an expression for z_0:

$$z_0 = \frac{10}{\exp\left(\frac{\kappa}{{C_{DN10}}^{1/2}}\right)} \tag{5.25}$$

C_{DN10} was then computed from Equation 5.23 for $C_i = 1$, to represent surface conditions over the large ice floe. C_{Dr} was then computed using the value of z_0 calculated from the expression above and Equation 2.41. Finally, the momentum flux was calculated from Equation 2.38 using observations from each measurement level.

The red, blue and black data sets in Figures 5.25 to 5.27 represent data produced by the SHEBA bulk flux algorithm using various assumptions for the values of z_0, z_h and z_q. These data sets can be compared to the observed (eddy covariance) fluxes at each measurement height, which are represented by the grey dots. The gradient of each of the linear regressions is directly related, but not equal to, the bulk flux algorithm transfer coefficients. For all three of these tests observed long and short wave downward radiation fluxes, surface pressure and surface temperature are input into the algorithm, along with

observations of wind speed, air temperature and specific humidity from the relevant measurement level. The red dots represent results from the winter version of the SHEBA bulk flux parameterisation, in which z_0 is parametrised according to Equation 5.21 and z_t and z_q according to Equation 5.22. The black dots represent results from the SHEBA bulk flux parameterisation scheme, in which the value of z_0 was constant and equal to the observed value at each level (see Table 5.2). It is assumed that $z_t = z_q = z_0/10$ because z_t and z_q could not be computed accurately from the observations.

The dark blue dots represent results from the SHEBA bulk flux algorithm scheme, in which z_0 was kept at a constant value of $3\text{x}10^{-3}$ m and $z_t = z_q = z_0/10$. This test was designed to assess the impact of the values of z_0, z_t and z_q used by the MetUM on the turbulent fluxes calculated in the SHEBA parameterisation. Finally, the light blue dots represent diagnostics from the operational version of the MetUM. The values of τ, H and E from the model are all estimates for the surface. The lowest model level in this version of the MetUM is at 10 m for U and ρ and at 20 m for T and q. This difference is due to the way the model splits variables onto ρ and θ levels. None of the measurement levels are at exactly these heights and therefore, the operational data is plotted on the figures at the height closest to 10 m for the momentum flux and closest to 20 m for the sensible and latent heat fluxes. This limitation must be considered during the analysis.

The results from the winter and summer versions of the algorithm are very similar at $C_i = 1$ and these versions produce values of τ/ρ that agree best with the observations (Figure 5.25). The winter version of the algorithm predicts the fluxes at the lowest two levels with reasonable accuracy but above this the accuracy decreases with increasing measurement height, until the 30.60 m level, which again appears reasonably accurate compared to the observations. Results from Section 5.3 suggest that the surface (constant flux) layer is only a few metres deep for the majority of the observation period. This means that fluxes computed from measurements made at the levels above 3.25 m are likely not estimates of the surface fluxes, but of the local flux. The SHEBA bulk flux algorithm is designed to compute the surface fluxes, which is likely to be the reason why the algorithm is increasingly less accurate with distance from the surface. The high accuracy at the 30.60 m level could be due to other reasons. This level is almost always above the surface layer and has a larger flux footprint than the other levels. The turbulence may, therefore be influenced by surface properties further upstream, where, according to Figure 5.20, the surface is rougher and therefore, the associated momentum flux larger.

The values of τ/ρ produced using the observed values of z_0 are larger than both the observations and the predictions from the 'winter' and 'summer' versions of the algorithm. This again questions the validity of Monin-Obukhov similarity theory because the bulk

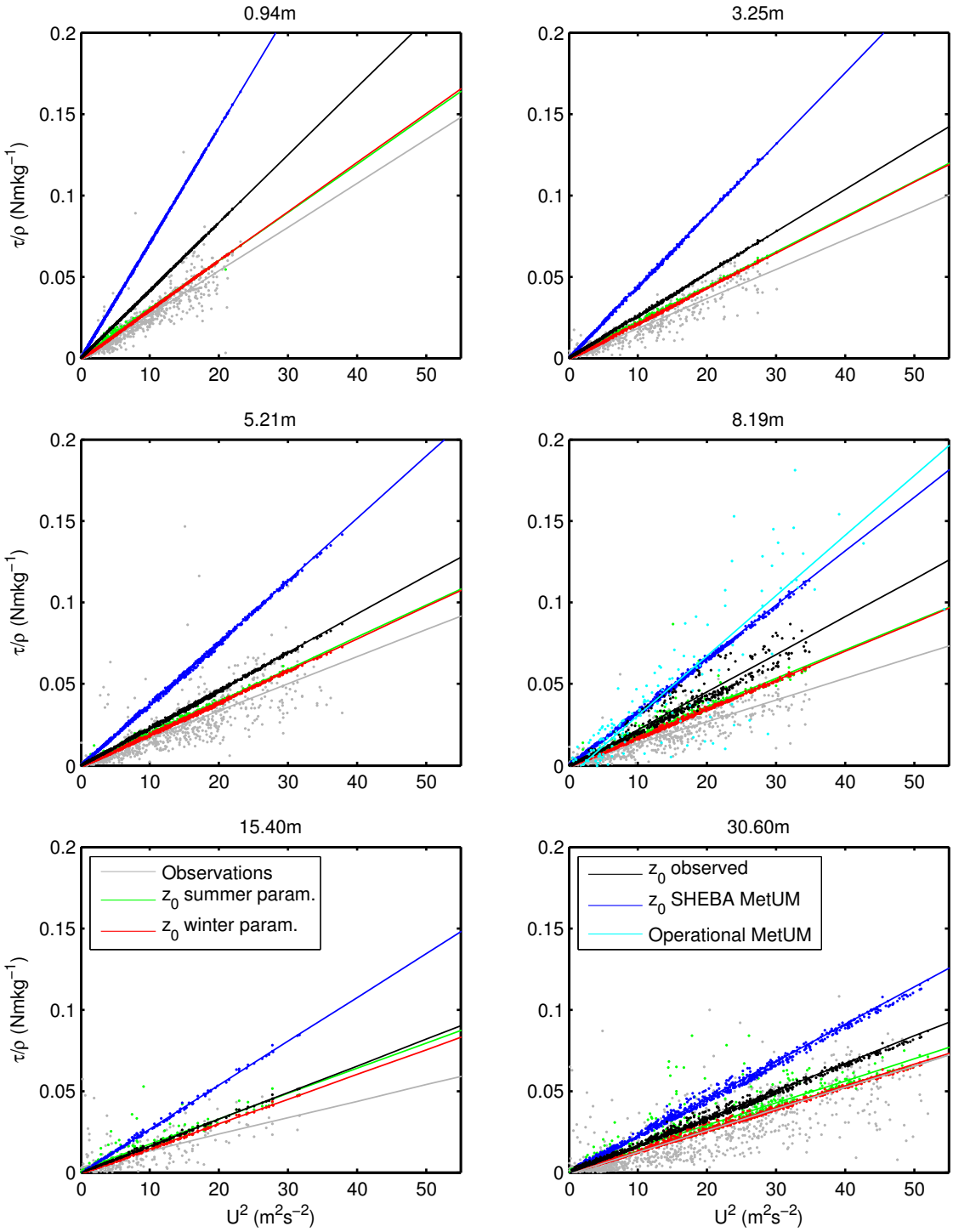

Figure 5.25: τ/ρ vs. U^2: observations, results from the SHEBA bulk flux algorithm and comparisons with the MetUM. Grey dots are the observations and the red, green, dark blue and black dots represent results from the SHEBA bulk flux algorithm using various assumptions for the value of z_0. The light blue dots show data from the operational version of the MetUM (only on the 8.19 m panel). The lines are linear fits to each set of data. Data is used only from periods when the the ice floe is upstream (wind direction = 100-270°).

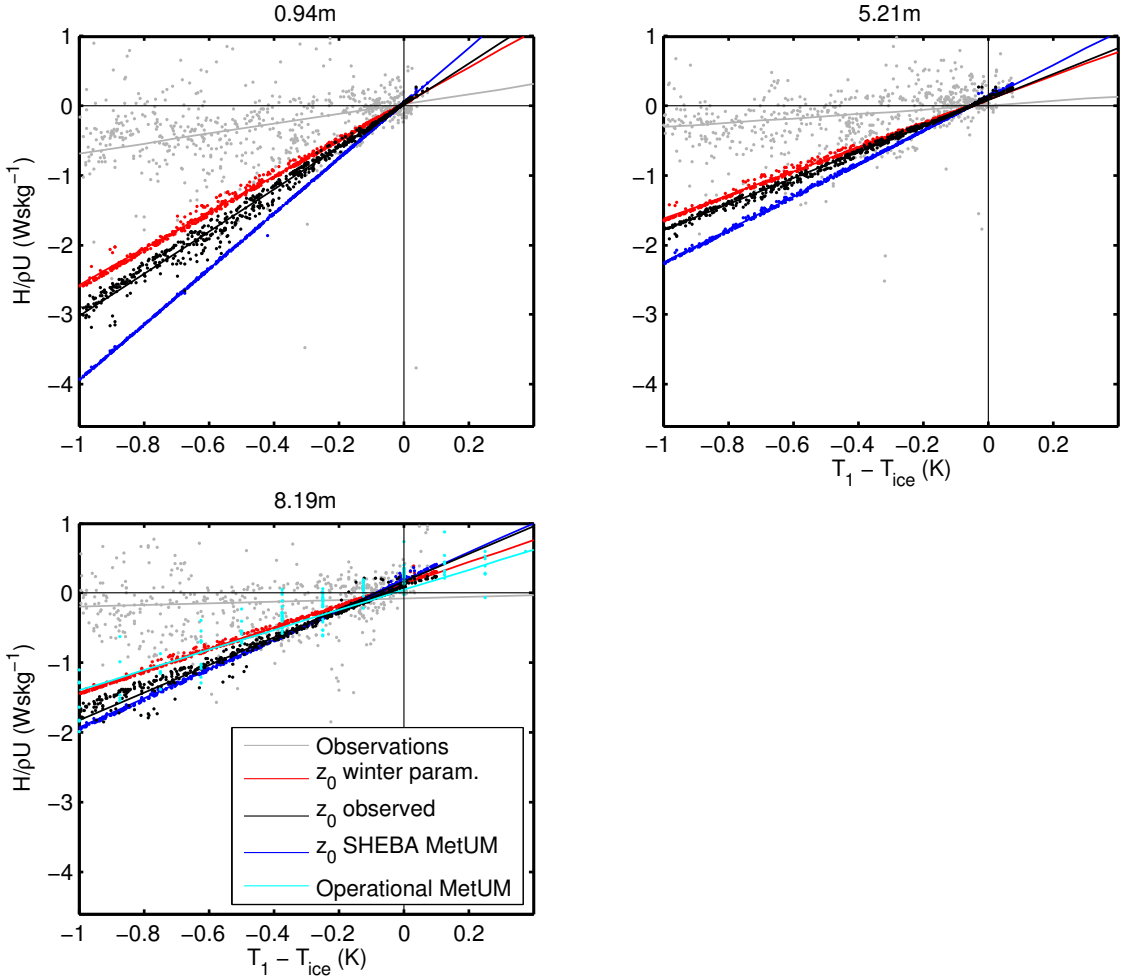

Figure 5.26: Same as Figure 5.25 but for the sensible heat flux.

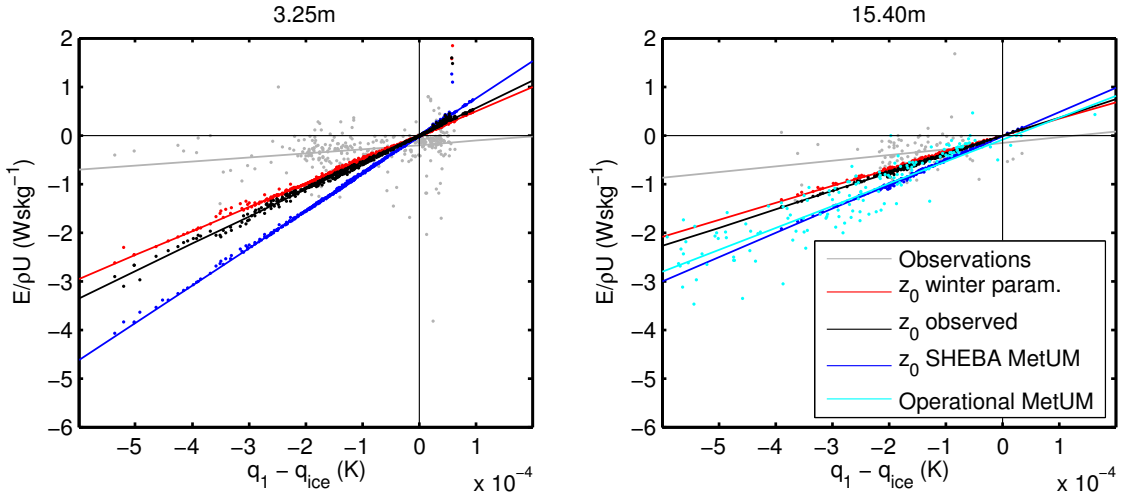

Figure 5.27: Same as Figure 5.25 but for the latent heat flux.

flux algorithm, which is based on the theory over predicts the fluxes even when accurate values of z_0 are used. The results from the SHEBA bulk flux algorithm, in which z_0 is set to a constant value of $3\text{x}10^{-3}$ m are very similar to those produced by the MetUM itself. This shows that the basic formulation of the SHEBA parameterisation is similar to that in the MetUM and the most significant difference between the two schemes is the way z_0 is represented. Both sets of results show that τ/ρ is overestimated, which is probably because the value the MetUM uses for z_0 is constant and is designed to represent the roughness of the surface for all ice conditions and over an area the size of a model grid box. The flux footprints of the measurements contain a large, relatively flat ice floe, which is consistent with the fact that the parameterisations overestimate the surface roughness and thus the momentum flux. Results from the ASCOS data set show that the value of z_0 can vary by several orders of magnitude, depending on surface type and therefore, a constant value of $z_0 = 3\text{x}10^{-3}$ m is not appropriate for all seasons of the year at all latitudes that contain Arctic sea ice.

The performance of the operational version of the MetUM is similar to that of the winter version of the SHEBA parameterisation for the sensible heat flux, H (Figure 5.26). There is also a reasonably large difference between the operational data and the results from the SHEBA algorithm in which $z_0 = 3\text{x}10^{-3}$ m and $z_t = z_q = z_0/10$ (the values used in the MetUM). Both these results are most likely a consequence of comparing data from the model level of 20 m with observations from the measurement level at 8.19 m. This is because in the surface layer the gradients of the linear fits to the observations are expected to decrease with increasing distance from the surface; because whilst U (or $T_1 - T_{ice}$ or $q_1 - q_{ice}$) increase with height, the value of the flux should remain constant. In comparison, the results from the operational MetUM for the latent heat flux are much more similar to the results from the SHEBA algorithm where $z_0 = 3\text{x}10^{-3}$ m and $z_t = z_q = z_0/10$, because the measurement level is closer to that in the model (Figure 5.27).

Similar to the results for the momentum flux, the 'winter' version of the SHEBA parameterisation performs the best in the prediction of H and E out of the various versions tested. This suggests that the parameterisations for z_t and z_q, as well as that for z_0 in the SHEBA algorithm are superior to using constant values. The sensible and latent heat fluxes do however, remain significantly overestimated by the SHEBA algorithm. It is difficult to explain this error, other than to suggest that it is likely to be a combination of the very shallow surface layer causing Monin-Obukhov similarity theory to be invalid and the uncertainties in the values used for z_t and z_q.

5.6 Summary

This chapter uses the ASCOS data set to assess the performance of model surface turbulent flux parameterisation schemes over sea ice in the central Arctic region. Comparisons between the surface turbulent flux measurements and diagnostics from the MetUM show that the model overestimates the momentum and sensible and latent heat fluxes, with the latent heat flux suffering the largest bias. These errors can be at least partly explained by the positive bias in the transfer coefficients computed by the model. The possible causes of this bias have been examined, including whether or not the assumptions of Monin-Obukhov similarity theory are valid under the observed conditions and the accuracy of the representation of surface roughness in the parameterisation scheme.

Various forms of the similarity function for momentum, φ_m, derived from previous sets of observations were compared to the ASCOS turbulence observations from each measurement level. Apart from at the very lowest level, the observed value of φ_m at a given value of z/L was greater than that predicted by the accepted forms of the function. This suggests turbulent properties under the conditions observed during ASCOS are similar to those observed under more stable conditions during other experiments. Spectra and cospectra, normalised by Monin-Obukhov similarity scaling were used to investigate this is more detail. Under weakly unstable/stable (i.e. near-neutral) conditions the peaks of the normalised u, w and uw spectra from the upper two measurement levels (15.40 and 30.60 m) were shifted to the right on the frequency axis. This can be interpreted as follows: a larger fraction of the total energy is associated with higher frequency turbulence (smaller eddies) than was observed during previous experiments. This is in agreement with the results from the φ_m analysis, although the spectral analysis only illustrates this for the upper two levels, whereas the φ_m analysis suggests that this is the case for all levels other than the lowest.

The shallow boundary and surface layers observed in the Arctic are an explanation for the vertical variation in turbulent properties observed during ASCOS. Boundary-layer depths were observed to be less than 200 m and often below 100 m, with associated surface layer depths of less than 20 m. This suggests that the upper two measurement levels were above the surface layer for much of the observation period. It is important to note that the majority of the ASCOS observations were made under near-neutral stabilities and therefore, under conditions different to those observed in classic stable boundary layers, where the surface layer is also very shallow. Cases representative of a classic stable boundary layer were also observed during ASCOS and are illustrated in the moderately stable regime. The turbulent spectra in this regime show much greater agreement between measurement levels.

Surface turbulent flux parameterisation schemes are based on Monin-Obukhov similarity theory, which is only valid in the surface layer. The MetUM's first model level is at 10 m for the wind speed diagnostic necessary to compute the momentum flux and at 20 m for the temperature and humidity diagnostics needed for the sensible and latent fluxes. These model levels are above the surface layer for much of the ASCOS observation period, which would cause Monin-Obukhov similarity theory to predict higher turbulent intensity than is observed. This is one explanation for why the MetUM surface turbulent flux parameterisation scheme over-predicts the transfer coefficients that are used to compute the turbulent fluxes.

The transfer coefficients are also a function of the values used for the roughness lengths for momentum, heat and humidity. Values of the momentum roughness length, z_0, computed from the ASCOS observations were found to vary by an order of magnitude depending on surface type; from 3.7x10^{-3} m over rough, broken ice to 5.9x10^{-4} m over the large, relatively smooth ice floe. The MetUM uses a value of 3.0x10^{-3} m over all types of ice for all seasons. Whilst this may be valid in areas with a large fraction of rough ice, it is too high to represent ice conditions at the ASCOS observation site. This conclusion is reinforced through the use of the SHEBA bulk flux algorithm. It was used to compute the momentum flux using observations from each level on the masts with various assumptions for the value of z_0. The fluxes produced by the algorithm when z_0 was equal to the observed values were in better agreement with the observations than when a constant value of 3.0x10^{-3} m was assumed.

The SHEBA bulk flux algorithm was also tested using a parameterisation for z_0 that was developed by Andreas *et al.* (2009). For the momentum flux, this produced better results than those computed by the algorithm when the mean observed values for z_0 were used. At the lowest levels the computed fluxes match those observed reasonably well. Agreement between the modelled and observed fluxes did however, decrease with increasing measurement height, which is most likely caused by the breakdown of similarity theory at the upper levels. In contrast, the SHEBA bulk flux algorithm significantly overestimated the values of the sensible and latent heat fluxes, although the values produced by the algorithm using the Andreas *et al.* (2009) parameterisation for the roughness lengths produced slightly better heat fluxes than those produced by the algorithm when $z_t = z_q = z_0/10$. It is still uncertain why the sensible and latent heat fluxes are significantly overestimated by both the models in this study and others. It is unlikely to be completely due to the break down of Monin-Obukhov similarity theory at distances of a few metres above the surface because the SHEBA bulk flux algorithm did not perform well even compared to observations from the lowest levels. Unfortunately, the Andreas *et al.* (2009) parameterisation for z_t and z_q cannot be explicitly tested because these values could not be calculated from the observations. A longer observational

data set is necessary to reduce the large variability in the values of z_t and z_q in order to produce reasonable estimates of them.

Chapter 6

Evaluation of the MetUM using ASCOS observations

The previous two chapters have highlighted some systematic errors in output from the Met Office Unified Model (MetUM) over the central Arctic region. This chapter presents a brief general evaluation of the MetUM using the ASCOS observations, similar to that in Chapter 4, and a more detailed evaluation of boundary-layer structure and clouds. Several sensitivity tests using the MetUM, which modify the surface albedo, roughness length for momentum, and vertical resolution are also presented. These experiments reinforce some of the conclusions made about model errors in the analysis and help to assess possible solutions. The final section presents a brief evaluation of diagnostics from the climate version of the MetUM, the Hadley Centre Global Environmental Model (HadGEM1) using both AOE 2001 and ASCOS observations to assess whether the same biases and errors appear in both the numerical weather prediction (NWP) and climate versions of the model.

6.1 Evaluation of the MetUM operational data set

6.1.1 Surface energy budget

Four distinct periods, with different conditions, were observed during the ice station; these are illustrated by the temperature observations in Figure 6.1. During the first week of the ice station temperatures were close to 0 °C, the freezing point of fresh water and were similar to those observed during the majority of the AOE 2001 observation period. Considering the relatively high temperatures, this period is named the 'melt period'. This period experienced the passage of a number of synoptic scale frontal systems, which

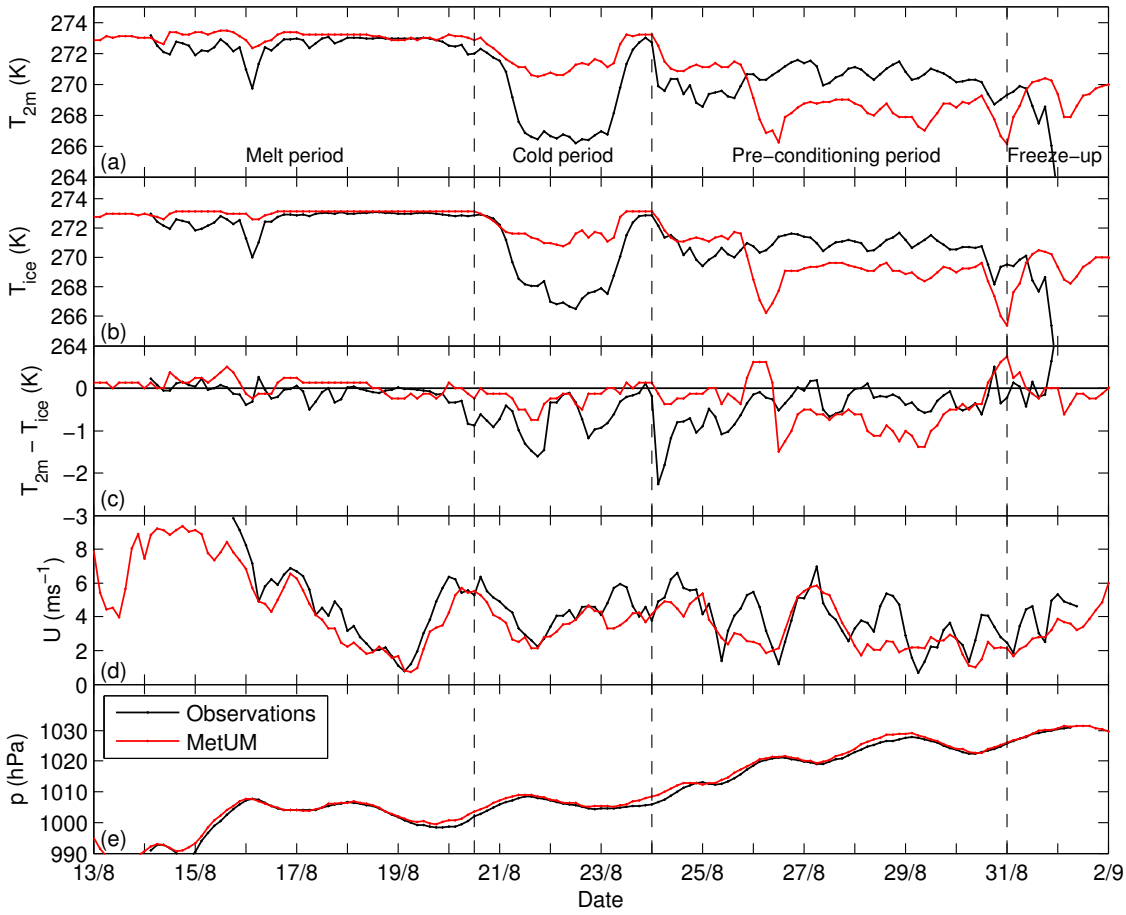

Figure 6.1: 3 hourly averaged basic meteorological variables observed during ASCOS and diagnostics from the MetUM. (a) 2 m air temperature (b) surface temperature (c) difference between 2 m air temperature and surface temperature, (d) wind speed; model diagnostics are from the first model level (10 m) but observations are from the 30 m mast, since this instrument produced the most continuous set of observations and (e) surface pressure. The dashed lines represent the approximate limits of the four main periods.

brought relatively high wind speeds, some precipitation and a large amount of cloud that extended above 2000 m. This was the largest number of weather systems to pass over the region at this time of year for the last 10 to 15 years, which shows it was climatologically unusual. This was followed by a 'cold period' between 21st and 23rd August that is similar to the cold period that occurred between 12th and 17th August in 2001. Temperatures then increased but did not return to 0°C; instead they remained at approximately -1.7 °C, the freezing point of sea water. These conditions ended abruptly on 31st August when temperatures decreased rapidly to below -10°C; indicating the onset of freeze-up conditions.

The idea of splitting the observations into four periods is supported by the surface energy budget observations shown in Figure 6.2. During the melt period the sensible and latent heat fluxes were negative (energy lost from the surface) but small and due to the large

amount of cloud cover (Figure 6.3), the surface cooled only a small amount through the emission of longwave radiation. The shortwave radiation flux dominated, the total heat flux was positive and it was possible to maintain temperatures up to 0 °C. Longwave cooling was larger during the cold period due to the clearer skies. This coupled with increased cooling by the turbulent heat fluxes caused the total heat flux to be about zero, explaining the decrease in near-surface air temperatures. Fresh water (wet snow, melt ponds etc) were visually observed to freeze during the cold period and therefore, between 24th and 31st August temperatures were maintained at approximately -1.7 °C because the only latent heat processes to occur involved saline water in the open leads. A layer of low level cloud was observed for almost the entire period between 24th and 31st August (Figure 6.3), which reduced the amount of longwave cooling at the surface and prevented any rapid cooling of the surface. This period is therefore named the 'pre-conditioning period', since it is likely that the onset of the freeze-up was prevented by this cloud layer. Clearer conditions prevailed on 31st August and 1st September and the surface began to cool strongly through the emission of longwave radiation. This caused the total heat flux to be negative for the first time and temperatures to decrease rapidly to below -10 °C, indicating the beginning of freeze-up conditions.

An evaluation of global operational diagnostics from the MetUM (model cycle G48, see Section 3.4.1 for more details) during the first three periods is performed using the same method used for the AOE 2001 data in Chapter 4. Statistics for the 'freeze-up' period are not given in Table 6.1 due to the short period that it was observed and the lack of quality turbulence data. Figure 6.4 shows that during the melt period air temperature away from the surface is well represented by the model, although the surface temperature, T_{ice} and the 2 m air temperature, T_{2m} remain close to 273.15 K (Figure 6.1a,b). This does not precisely agree with the observations but is similar to what was found for most of the AOE 2001 period. Model biases in the up and downward radiative fluxes are relatively small except for the large negative bias in SW_{up}, produced by the negative bias in the surface albedo. This causes too much radiation to be absorbed at the surface, but is largely offset by the biases in the turbulent heat fluxes. During the cold period the temperature observations in Figure 6.4 and in Figure 6.1a show a region of cold air adjacent to the surface. The model does reproduce this to some extent but it is too high and does not extend to the surface. This is similar to what was found for the cold period observed during 2001 and is due to the same reasons: the positive bias in the net radiation flux keeps the surface and near-surface air temperatures high causing a feedback of errors, which locks the temperature-dependent surface albedo at 0.5.

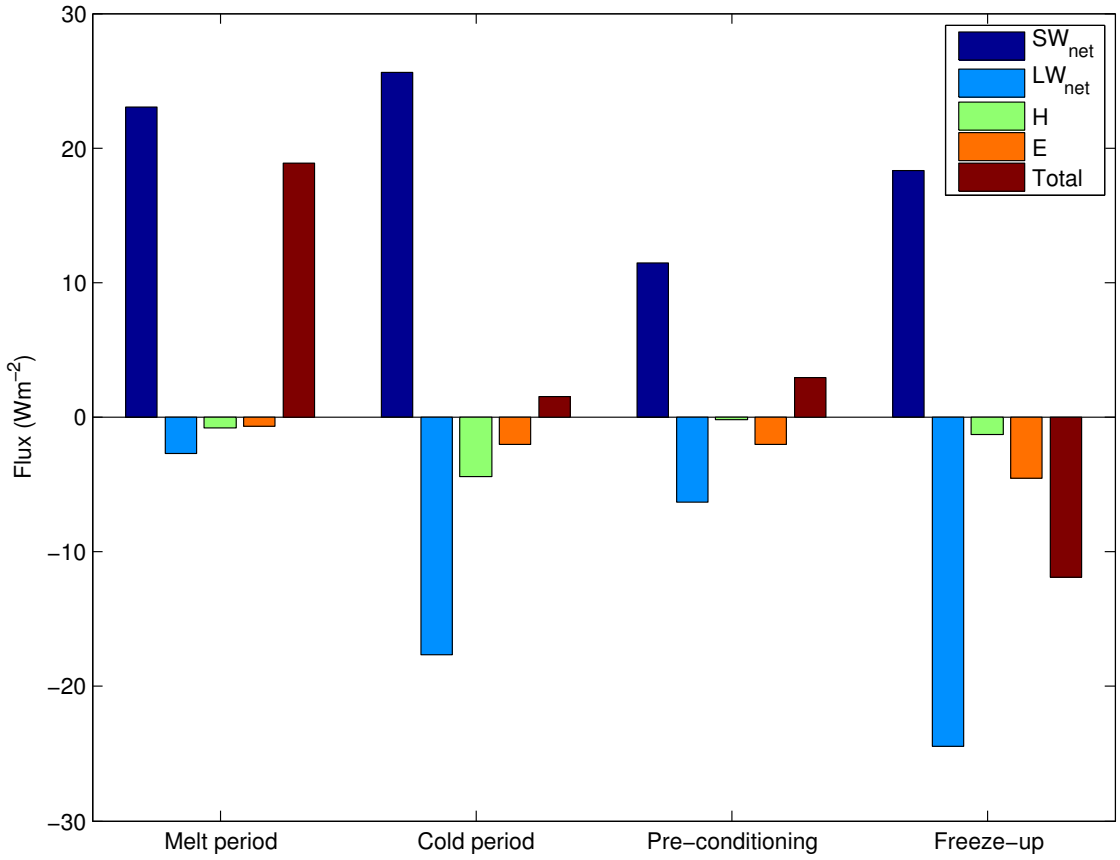

Figure 6.2: Surface energy budget measurements split into the four main periods observed during ASCOS. To avoid including times of transition between the main periods the limits are defined as 17th 00:00 UTC to 21st 00:00 UTC for the 'melt period', 21st 00:00 UTC to 23rd 12:00 UTC for the 'cold period', 26th 18:00 UTC to 30th 12:00 UTC for the 'pre-conditioning period' and 31st August 12:00 UTC to 1st September 22:00 UTC for the 'freeze-up period'. Due to a lack of observations the latent heat flux is estimated at a constant value of -2 Wm^{-2} during the cold period. A positive flux is defined as energy absorbed at the surface. Reproduced from a figure originally by Thorsten Mauritsen.

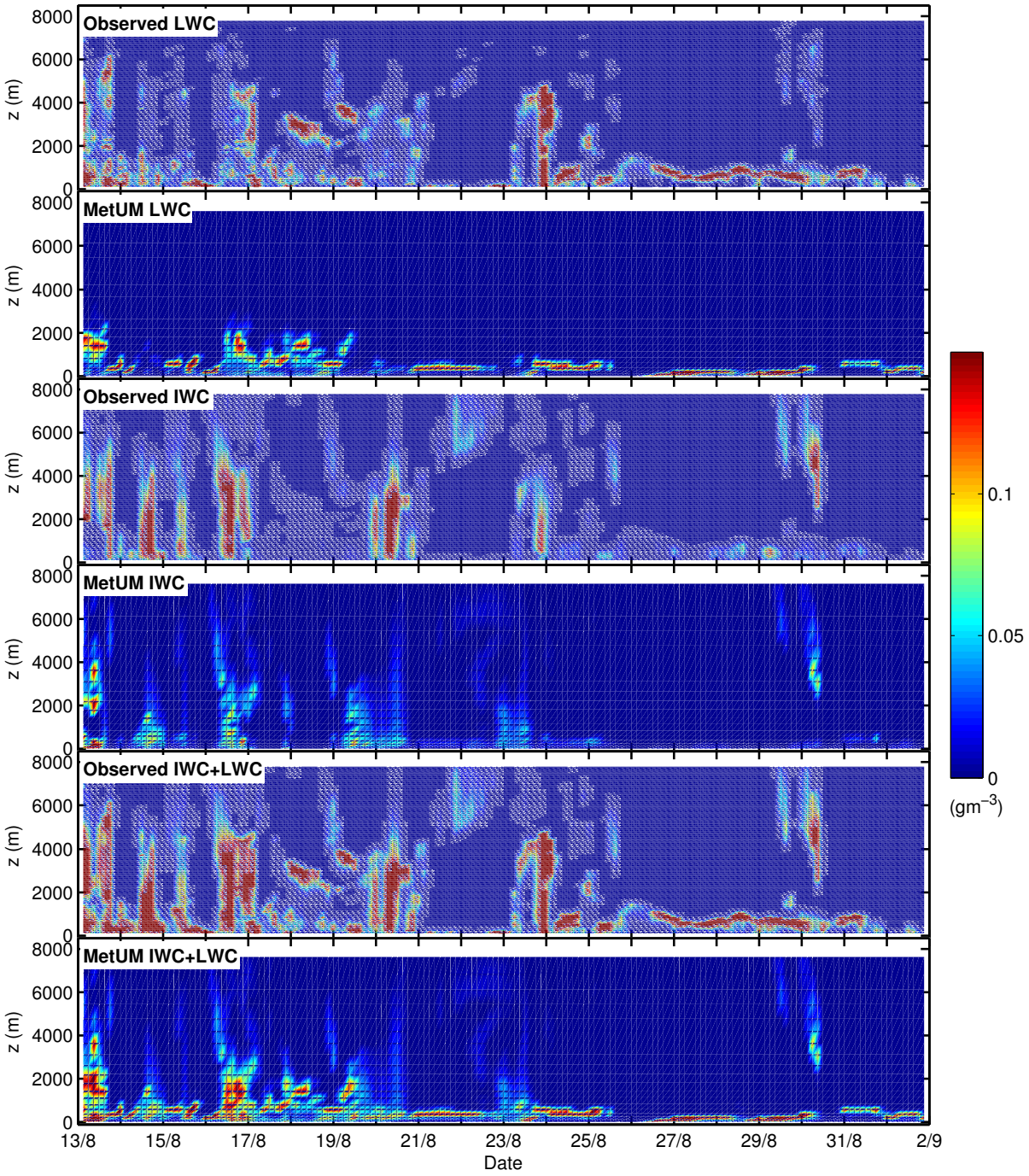

Figure 6.3: 3 hourly liquid, ice and total cloud water concentrations observed during ASCOS and diagnostics from the MetUM. Observations are a product derived from measurements made by the remote sensing instruments. The methods employed to retrieve these properties are discussed in Section 6.1.2. Isopleths are at 0.05 gm^{-2} intervals.

Table 6.1: Statistics of model diagnostics compared to ASCOS observations using 3 hourly averages. The absolute bias (a.b.) is the mean difference between each observed and modelled parameter. A positive bias implies that for a given parameter, the model produces a higher value than that observed. The mean observation over the entire field campaign ($\bar{x}_{obs}$), the standard deviation (σ) of the difference between each 3 hourly averaged observation and modelled value and the correlation coefficient (R) are also given. The limits of the periods are the same as those used in Figure 6.2.

		Entire ice station					Melt period			Cold period			Pre-conditioning		
	unit	$\bar{x}_{obs}$	a.b.	σ	R	n_{obs}	$\bar{x}_{obs}$	a.b.	n_{obs}	$\bar{x}_{obs}$	a.b.	n_{obs}	$\bar{x}_{obs}$	a.b.	n_{obs}
U_{10m}	m s^{-1}	3.44	0.17	0.91	0.84	68	3.09	-0.12	27	4.16	-0.40	3	3.03	0.52	19
T_1	K	270.48	0.41	2.36	0.44	139	272.70	0.34	33	267.67	3.63	21	270.74	-2.29	31
T_{ice}	K	270.80	0.31	2.26	0.46	139	272.94	0.12	33	268.41	3.14	21	271.02	-1.79	31
α	-	0.79	-0.24	-	-	143	0.75	-0.26	33	0.77	-0.23	21	0.84	-0.23	31
LW_{dn}	W m^{-2}	300.35	-8.86	20.03	0.45	113	313.41	-8.02	32	279.98	15.42	11	299.65	-12.00	28
LW_{up}	W m^{-2}	308.10	-1.25	7.47	0.59	113	316.13	-0.80	32	298.02	11.29	11	306.09	-8.08	28
SW_{dn}	W m^{-2}	89.18	-4.48	24.44	0.60	113	89.53	-6.33	32	108.69	-16.34	11	74.70	-2.99	28
SW_{up}	W m^{-2}	70.78	-24.24	18.28	0.53	113	66.89	-25.91	32	84.17	-35.10	11	62.86	-18.85	28
LW_{net}	W m^{-2}	-7.75	-7.61	-	-	113	-2.74	-7.22	32	-18.04	4.13	11	-6.44	-3.92	28
SW_{net}	W m^{-2}	18.40	19.76	-	-	113	22.64	19.58	32	24.52	18.76	11	11.84	15.86	29
Rad_{net}	W m^{-2}	10.65	12.15	-	-	113	19.90	12.36	32	6.48	22.89	11	5.40	11.94	28
H	W m^{-2}	-0.67	-1.36	7.53	-0.16	83	-0.41	0.60	30	-1.00	-2.75	15	-0.06	-11.72	15
E	W m^{-2}	-1.68	-7.51	8.12	0.20	74	-0.74	-11.02	17	-0.88	-21.12	1	-2.02	-5.73	27
tot_{hflx}	W m^{-2}	8.30	3.28	-	-	74	18.75	0.74	17	4.60	-0.98	1	3.32	-5.51	27
LWP	g m^{-2}	109.6	-66.88	225.77	0.21	145	149.2	-89.80	33	31.9	-0.42	21	78.4	-40.91	31
IWP	g m^{-2}	88.7	-51.1	166.30	0.65	145	126.1	-65.22	33	44.6	4.73	21	72.5	-51.65	31

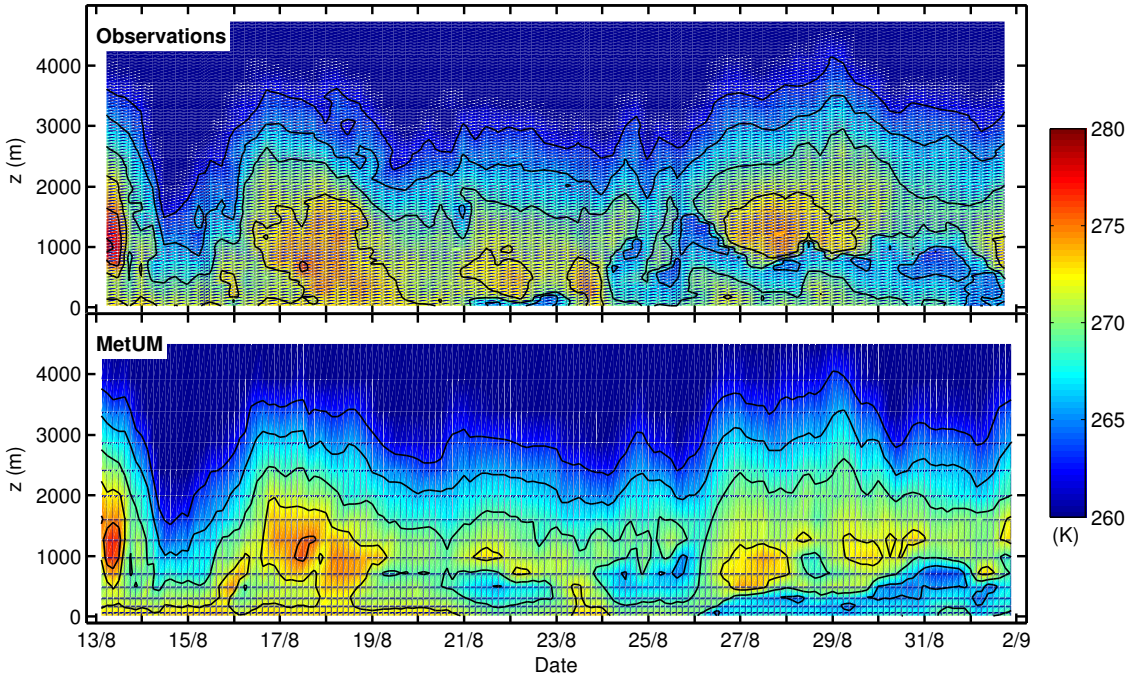

Figure 6.4: 2D air temperature from the ASCOS radiosonde observations and 3 hourly diagnostics from the MetUM. Isopleths are at 3 K intervals.

There is a distinct change in error regime during the pre-conditioning period; for the first time the 2 m air temperature decreases below that observed. Modelled near-surface air temperature remained above that observed until 25th August, when the model value decreased below that observed and remained so until 31st August (Figure 6.1a). At the start of this period the model produced a decrease in temperature of approximately 5 °C between 25th and 26th of August, which was not seen in the observations. This is associated with an erroneous clear period on 25th August (Figure 6.3) that caused an increase in both shortwave warming and longwave cooling (Figure 6.5). The sum of these changes produced significant radiative cooling at the surface, decreasing the surface temperature and increasing the albedo by a small amount (Figure 6.5d), which reinforced the cooling effect. The layer of low cloud returned in the MetUM on 26th August and the net radiative flux returned to positive. T_{ice} and T_{2m} did not however, return to the observed values for several days. At approximately midday on the 26th the difference between T_{ice} and T_{2m} (Figure 6.1c) increased, causing an erroneously large negative sensible heat flux. This, along with the large bias in the latent heat flux produced a negative total heat flux (Table 6.1), which reinforced the negative bias in T_{ice}. The surface temperature drives the near-surface air temperature (note the lag in the minimum temperature between T_{ice} and T_{2m} on 26th August) and therefore the near-surface air temperatures also remained negatively biased throughout the pre-conditioning period. These errors are linked to the region of cold air produced by the MetUM close to the surface from 26th August onwards (Figure 6.4). A layer of cloud is associated with this

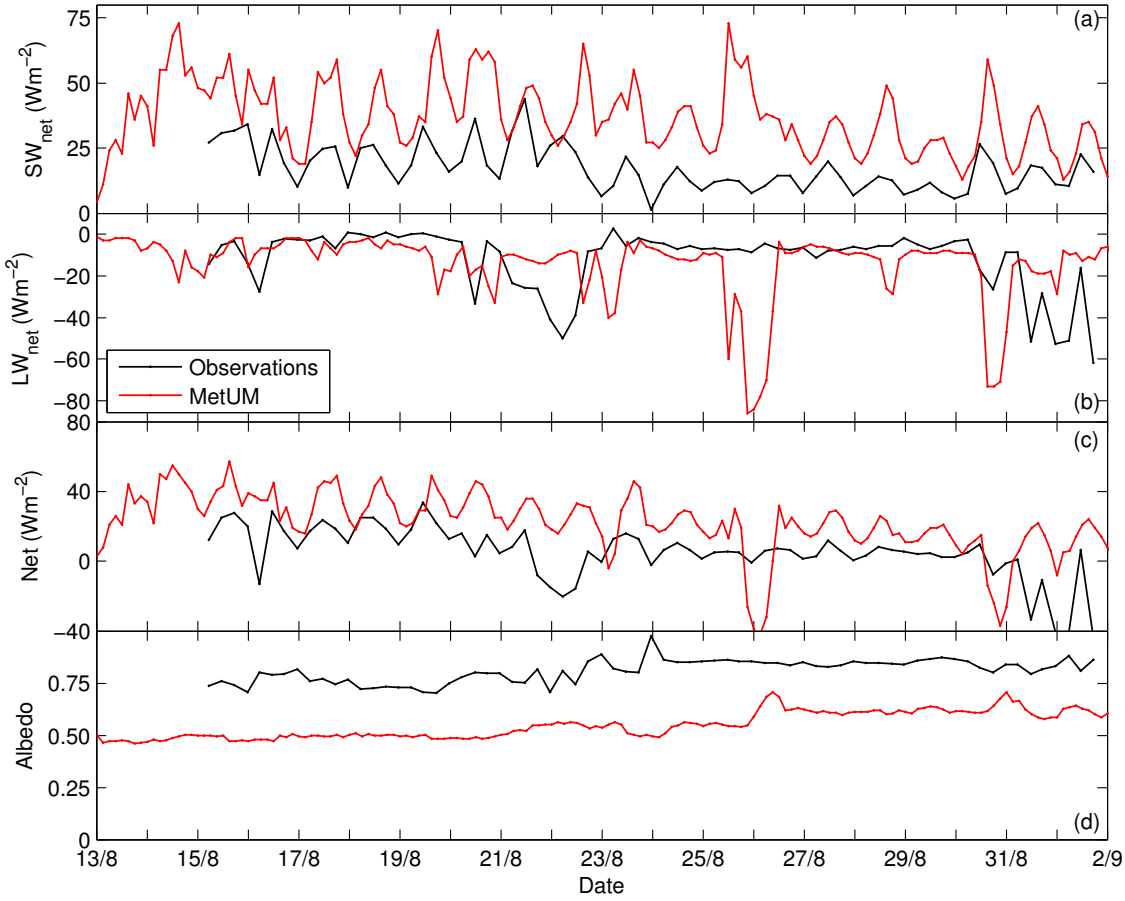

Figure 6.5: 3 hourly averaged (a) net shortwave radiation, (b) net longwave radiation, (c) net radiation and (d) albedo observed during ASCOS and diagnostics from the MetUM. A positive flux is defined as energy absorbed at the surface.

cold air in both the observations and the model, whose formation is discussed in more detail in Section 6.2.

6.1.2 Cloud properties and occurrence

Estimates of liquid and ice cloud water concentrations, derived from a combination of the remote sensing measurements are shown in Figure 6.3. To retrieve these properties the cloud phase must first be classified using radar reflectivity, mean Doppler velocity and spectrum width, along with vertical temperature profiles from the radiosondes and the liquid water path derived from the microwave radiometer (Shupe, 2007). Liquid water path (LWP) can be diagnosed relatively easily from the microwave radiometer, with a root mean square error of approximately 25 gm^{-2} (Westwater *et al.*, 2001). Liquid properties are derived from the cloud phase classification, the LWP, the radiosonde vertical temperature profiles, cloud base derived from the ceilometer measurements and cloud top derived from the radar measurements. Ice properties were derived from the 34 GHz

radar reflectivity retrievals using an Arctic specific retrieval coefficient and the cloud phase classification (Shupe *et al.*, 2005, 2006). The vertical extent of liquid layers (cloud top and base) and the LWP can be retrieved with reasonable accuracy during periods without precipitation but the relative vertical distribution within the cloud layers is not certain and is assumed to be adiabatic (M. D. Shupe, personal communication). The vertical extent of ice layers can also be retrieved with reasonable accuracy. In contrast to the liquid properties, the relative vertical distribution of ice within the cloud boundaries is well diagnosed but the total magnitude (IWP) is not (M. D. Shupe, personal communication). The potential error in the magnitude of IWP is a factor of two, which is obviously very large. This, and the other limitations of the data set should be taken into account during the comparisons with the model.

Although the model can distinguish between the cloud produced by the frontal systems during the first half of the observation period and the single, low-level cloud layer observed during the latter half, the modelled cloud is not correlated well with the observations. During the first half of the ice station the observed liquid cloud extends up to 6 km, but to only 2 km in the model and the position of the cloud patches do not resemble those in the observations in either time or space. The timing of periods in which a large amount of ice water was observed is reasonably well represented by the model. Modelled ice water path (IWP) is however, significantly overestimated at all times other than during the cold period (Table 6.1), although this conclusion is questionable due to the uncertainty in the observed values. The single layer of low level cloud observed between 25th and 30th August is reproduced by the model but the layer is too thin and too close to the surface. The observations show some periods with fewer clouds (e.g. just before midday on 26th) but the model produces more prolonged clear periods that are not always correlated with those observed.

Since clouds are the single most important factor influencing the surface energy budget (Curry *et al.*, 1996), it is important to assess the effect of errors in modelled cloud on the radiation budget. Shupe & Intrieri (2004) found that when LWP is greater than 20-50 gm^{-2} clouds behave like blackbodies and thus the absolute value of the LWP has little effect on the amount of longwave radiation it emits. The mean values of LWP derived from the ASCOS observations were greater than this threshold apart from during the cold period. The values for LWP computed by the model are significantly negatively biased and are therefore often close to or under this threshold. This is consistent with the negative bias in modelled surface LW_{dn}.

At all times, other than during the cold period, SW_{dn} is underestimated which implies the modelled atmosphere is optically too thick. This is inconsistent with the fact LWP is underestimated by the model; although the same discrepancy has been found for other

models over the Arctic (e.g. Tjernström *et al.* (2008)). Since the biases in SW_{dn} are small (less than 7 % of the observed values), this discrepency could be explained by biases in the SW_{dn} observations or by the comparison of mean model grid box diagnostics with point measurements. It could however, also be due to the representation of cloud radiative properties in the model. In the pristine environment of the central Arctic, aerosol concentrations are much smaller that at lower latitudes (Covert *et al.*, 1996; Bigg, 1996; Jiang & Cotton, 2000), which produces low CCN number concentrations and larger but fewer cloud droplets. The operational NWP version of the MetUM, like many models, assumes a fixed cloud condensation nuclei (CCN) number concentration that is representative of marine stratocumulus at lower latitudes but not of Arctic clouds. Previous studies have shown that at least part of the inability of regional and global models to reproduce the radiative properties of Arctic cloud is caused by the use of aerosol and cloud droplet number concentration parameterisations formed using empirical data from lower latitudes (Prenni *et al.*, 2007). If the MetUM overestimates the aerosol and cloud droplet number concentration, modelled cloud albedo will be too high, SW_{dn} will be too strongly attenuated and the downward shortwave surface radiation flux will be too low even though modelled LWP is significantly underestimated.

Another possibility is linked to the negative bias in modelled surface albedo. Fitzpatrick *et al.* (2004) showed that due to multiple reflections between the surface and the cloud layers, the magnitude of SW_{dn} is a strong function of surface albedo over ice surfaces. The highly reflective surface significantly increases the amount of shortwave radiation that is involved in the multiple reflections and thus increases SW_{dn}. Since the surface albedo is underestimated by the model, this could reduce the effect of these reflections and cause SW_{dn} to be underestimated.

A different combination of errors occur during the cold period, which are largely associated with cloud occurrence. The biases in modelled LWP are relatively small even though LW_{dn} is significantly overestimated and SW_{dn} is significantly underestimated by the model. These errors can be explained by the layer of low level cloud that is produced by the model for the majority of the cold period, when the observations suggest reasonably clear conditions. The mean model value for LWP remains similar to that observed due to the low level patch of cloud that occurs in the observations at 00:00 UTC on 23rd August; this biases the mean value of observed LWP that occurs in an otherwise relatively cloud-free period.

6.2 Case study: the pre-conditioning period

The previous section highlighted some significant errors associated with the way the MetUM represents the layer of cloud during the pre-conditioning period. This type of cloud is typical of conditions in the lower atmosphere during the summer in the central Arctic but different to the type of stratocumulus observed at lower latitudes (e.g. Sedlar & Tjernström (2009)). For this reason, the pre-conditioning period of the ASCOS observational data set is used to perform a more detailed analysis of cloud occurrence and boundary-layer structure in the MetUM. Three 7-day forecasts that represent the pre-conditioning period are used to illustrate some problems with the data assimilation process in the MetUM in the central Arctic region and then the forecasts are used to investigate the link between clouds and vertical atmospheric structure in the model.

6.2.1 Sensitivity to initial conditions

Figures 6.6 and 6.7 show observations, two sets of diagnostics from the operational MetUM (model cycle G48) and diagnostics from three 7-day forecasts. The first set of operational diagnostics are from 12 hour forecasts, initialised from 00 and 12 UTC analyses, sampled at 3 hourly intervals and concatenated to produce a continuous data set (this data is used throughout this chapter unless otherwise stated). The second set of operational diagnostics are from the 24 to 36 hour forecasts, initialised from the same 00 and 12 UTC analyses and concatenated to produce a continuous data set. The 7-day forecasts were produced in September 2009 using the latest version of the MetUM (model cycle G49). Updates to some of the model parameterisations were implemented between model cycles 48 and 49 but none of these involved major changes to the dynamics, such as the changes made between model cycles G25 and G42 (S. Milton, personal communication). The new forecasts were initialised from analyses at 12:00 UTC on 23rd, 24th and 25th August and were run unconstrained for 7 days.

There is little difference in the air temperature and cloud water diagnostics between the two sets of operational forecasts. This is because within a 36 hour forecast, the model does not evolve significantly differently when constrained or unconstrained by data assimilation. In contrast, there are large differences between each of the three 7-day forecasts and large differences between each 7-day forecast and the operational data. The first two 7-day forecasts were initialised at times when low cloud was present. They both maintain this through time and reproduce the vertical distribution of cloud to a higher degree of accuracy than the operational forecasts. These forecasts also produce temperature profiles that are more similar to the observations than those from the operational forecasts. The region of cold air above the surface (Figure 6.7) and the near-surface air

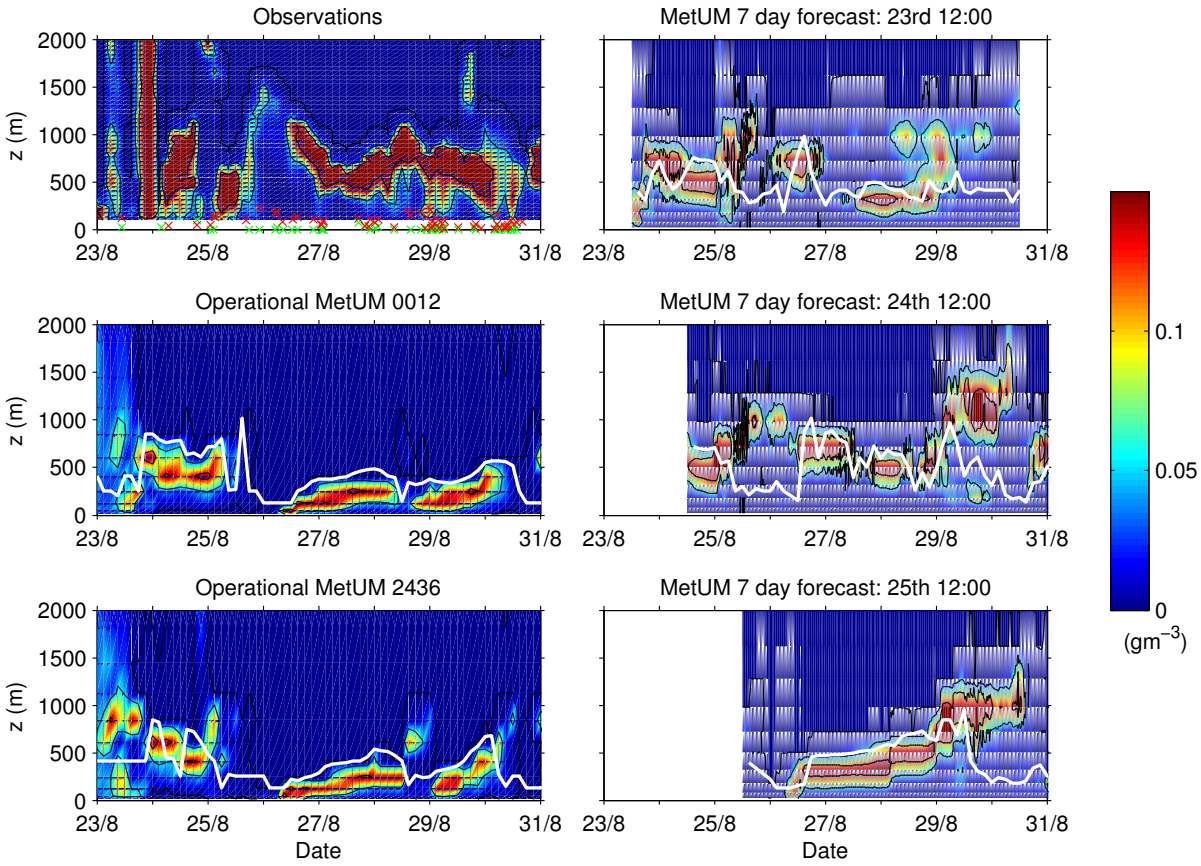

Figure 6.6: 3 hourly liquid and ice water concentrations and boundary-layer depth observed during ASCOS and diagnostics from the MetUM. Two time series of concatenated operational forecasts and three 7-day unconstrained forecasts are shown (see text for explanation). Modelled boundary-layer depth is represented by the white lines and observed boundary-layer depth (red crosses) and mixed-layer depth (green crosses) are estimated from the temperature, wind and humidity profiles measured by the tethersonde. Isopleths are at 0.05 gm^{-2} intervals.

temperature is closer to that observed (Figure 6.8) and the cloud layer, which is related to the temperature structure, is also in closer agreement with that observed. The third forecast was initialised during a short period with no cloud. It maintains clear conditions for too long and when cloud appears it initially follows a similar evolution to that in the operational forecasts. On the 28th August the cloud layer begins to increase in altitude and by the 29th it is more similar to the observed cloud layer than that produced by the operational forecasts. The altitude of the cloud layer does however, increase on the 30th and 31st to heights greater than observed.

The 7-day forecasts show that when unconstrained by data assimilation, the model is capable of producing a layer of cloud similar to that observed and that the forecasts are highly sensitive to the initialisation conditions. The operational forecasts do not reproduce the cloud layer as accurately, even though observations are assimilated into the

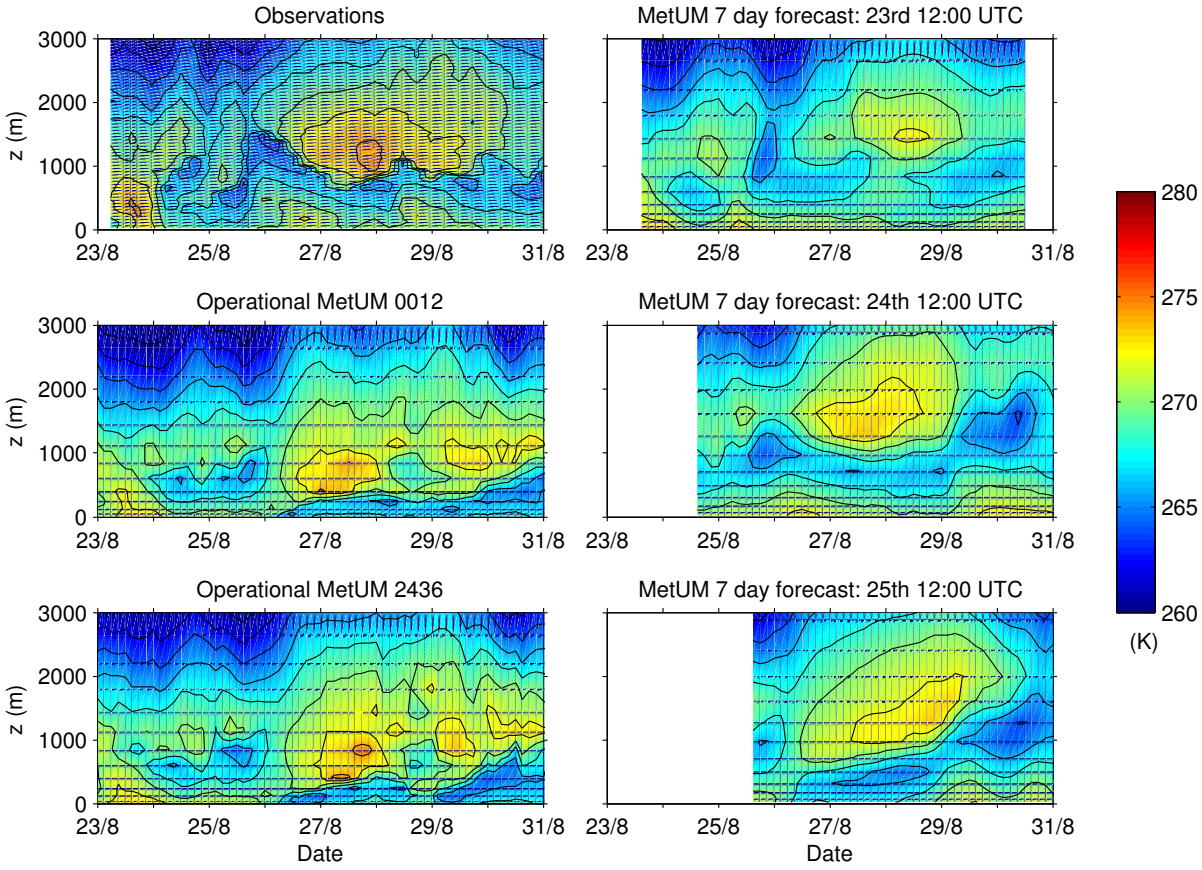

Figure 6.7: 3 hourly air temperature observed during ASCOS and diagnostics from the MetUM. Two time series of concatenated operational forecasts and three 7-day unconstrained forecasts are shown. Isopleths are at 3 K intervals.

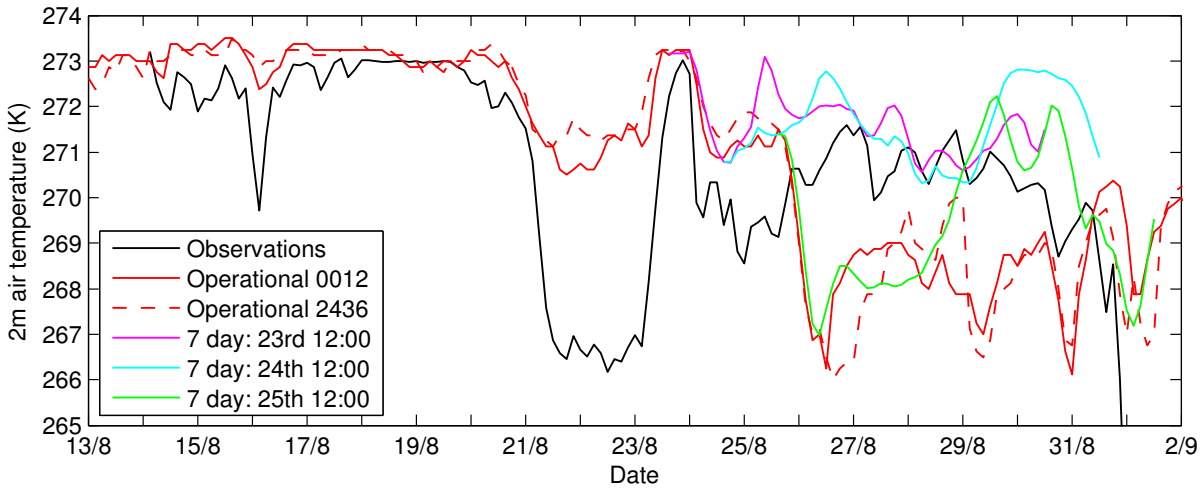

Figure 6.8: 3 hourly near-surface air temperature observed during ASCOS and MetUM diagnostics. Two time series of concatenated operational forecasts and three 7-day unconstrained forecasts are shown (see text for explanation).

forecasts. This indicates that there is a problem with the forecast and data assimilation cycle in the MetUM over the central Arctic region. The cloud layer in the operational data is able to evolve over each 12 hour period but then seems to be 'reset' back to a preferred state during the data assimilation process. The cause of this problem is not obvious and requires further investigation that is beyond the scope of this study and therefore, the remainder of this study will focus on diagnostics from the 7-day unconstrained forecasts.

6.2.2 Cloud and boundary-layer structure

Figure 6.6 suggests that the boundary layer in the MetUM is almost always too deep compared to estimates from observations and that for much of the pre-conditioning period the cloud layer is within the boundary layer, which does not occur in the observations. This implies that the evolution of cloud and boundary-layer depth in the MetUM are dynamically coupled, as is expected for a cloud-topped boundary layer. This is not the case in the observations because the cloud layer is well above the boundary layer. This coupling is discussed in detail in this section.

Figure 6.9 shows boundary-layer depth estimates using potential temperature, relative humidity with respect to water and wind speed profiles from the tethersonde and radiosonde observations, diagnosed in the same way as described in Section 5.2. The plot also shows model boundary-layer depth estimates, diagnosed from model vertical profiles in the same way as the observations and model boundary-layer depth diagnosed by the boundary-layer parameterisation scheme. There are differences between the model boundary-layer depths estimated from the vertical profiles and those diagnosed by the model parameterisation. This is most apparent during the pre-conditioning period when the depth diagnosed by the parameterisation scheme is approximately 100 m greater than that estimated from the model profiles. This is not unexpected since the diagnosis of boundary-layer depth from vertical profiles is very subjective and the diagnosis of the depth from the parameterisation scheme uses a different set of conditions. Even after taking these differences into consideration, the evidence from Figure 6.9 suggests that the boundary layer in the MetUM is too deep for the majority of the ice station. Considering the limitations of comparing modelled and observed boundary-layer depth the reminder of this analysis focuses on the structure of the lower atmosphere and the type of boundary layer simulated in the model.

The MetUM diagnoses 7 different types of boundary-layer structure to allow the use of two turbulent closure schemes for different conditions (Lock *et al.*, 2000). In stable layers a local Richardson number based scheme is applied, which relates turbulent fluxes to the local mean gradients using a value for the eddy diffusivity, K, that is related to the local

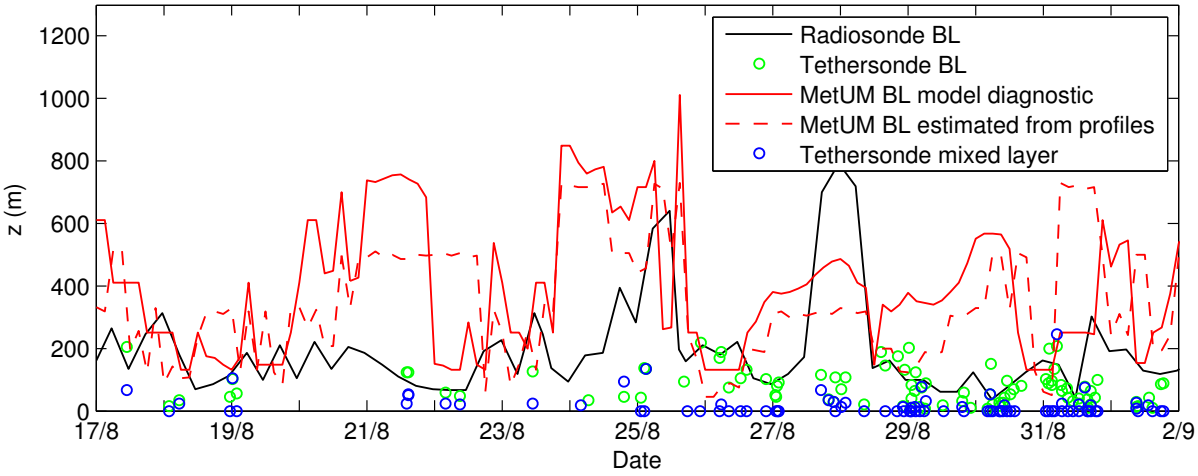

Figure 6.9: Boundary-layer depth diagnosed from the radiosonde and tethersonde observations, diagnosed by the MetUM in the boundary-layer parameterisation scheme and a visual estimate of boundary-layer depth from the MetUM vertical profiles. Mixed-layer depth estimates from the tethersonde observations are also shown.

stability. In unstable layers a non-locally specified profile scheme is used, where the eddy diffusivity is not related to local gradients but to a prescribed profile. The structure of the 6 main boundary-layer types are shown in Figure 6.10; the 7th boundary-layer type is an optional addition, defined as a shear-dominated unstable layer, in which wind-shear is able to cause deeper turbulent mixing in unstable boundary layers than the thermodynamic profiles alone would suggest. The category of a boundary layer is determined by moving a parcel constructed using the liquid-ice water potential temperature and the specific total water content up and downwards in the boundary layer (Lock *et al.*, 2000). If the parcel is lifted upwards from the surface allowing for latent heat effects, the top of the surface-based mixed layer is the height at which the parcel is neutrally buoyant relative to the environment. The presence and depth of any mixed layer driven by buoyancy forces at cloud top is then diagnosed by moving a second parcel downwards from cloud top (Lock *et al.*, 2000).

Boundary-layer type diagnosed by the MetUM in the three 7-day forecasts varies sometimes on an hourly basis but often a single type is maintained for a few days (Figure 6.11) and the most frequently produced type is a well-mixed boundary layer. The 7-day forecast initialised on 25th August is helpful in an investigation of boundary-layer structure because the diagnostics show the development of a single cloud layer (Figure 6.6). At the very start of the forecast there is a clear period, in which cooler temperatures (Figure 6.8) occur due to longwave cooling and a stable boundary layer is formed (Figure 6.11). The cloud layer develops upwards from the surface on 26th August, initially within the boundary layer. Boundary-layer depth decreases on 29th August and the cloud layer begins to increase in altitude outside of the boundary layer; to show more

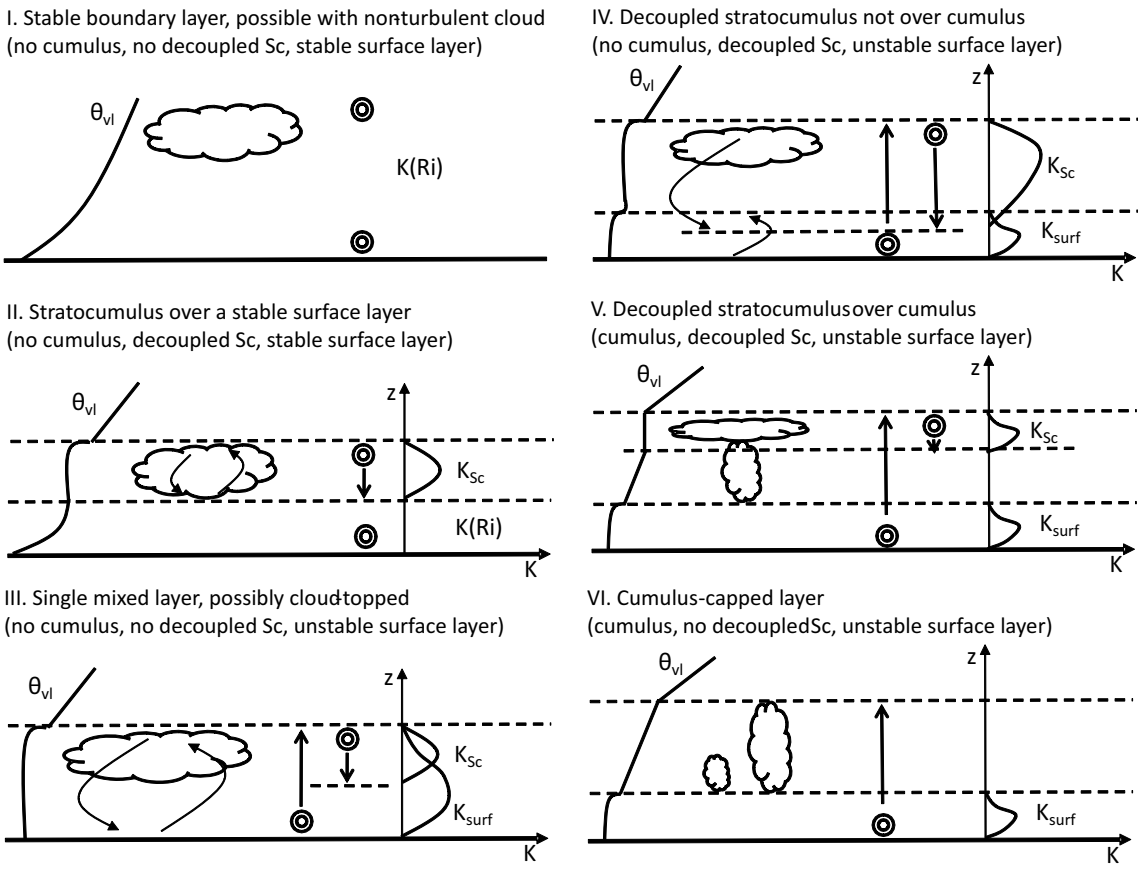

Figure 6.10: Schematic representation of the six boundary-layer types in the MetUM. θ_{vl} is a conserved variable equal to θ_v in cloud-free air, Sc is an abbreviation for stratocumulus, the concentric circles represent the air parcels and $K(Ri)$, K_{Sc} and K_{surf} are the Richardson, stratocumulus and surface eddy diffusivities respectively. Reproduced from Figure 1 in Lock *et al.* (2000).

agreement with the observations. This transition occurs with a change in boundary-layer type, from 'well-mixed' (III) to 'stratocumulus over stable' (II) and then to 'decoupled stratocumulus not over cumulus' (IV). The reduction in boundary-layer depth also shows more agreement with the depth estimated from the observations.

Figure 6.12 shows modelled and observed profiles of potential temperature, relative humidity and wind speed, along with the mean observed and modelled boundary-layer depth, cloud base and cloud top estimates for three periods when the model diagnosed different boundary-layer types. These periods are 27th 00:00 UTC to 28th 00:00 UTC (well-mixed), 29th 00:00 to 12:00 UTC (stratocumulus over stable) and 30th 05:00 to 12:00 UTC (decoupled stratocumulus not over cumulus). For the entire pre-conditioning period the observed conditions are reasonably stationary. The lower atmosphere is weakly stable with a stronger inversion beginning at 600 to 800 m, the relative humidity is very high and often 100 % in the lowest 600 to 800 m and the wind speeds are more variable. Boundary-layer depth, as diagnosed from the potential temperature, relative humidity

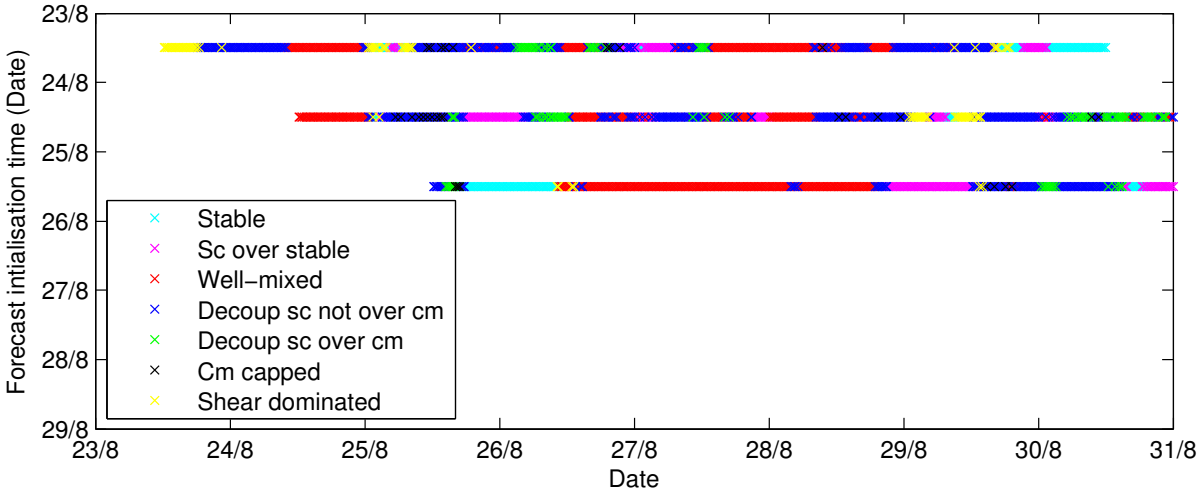

Figure 6.11: Boundary-layer type diagnostic from the MetUM. Data from 7-day forecasts initialised at 12:00 UTC on the 23rd, 24th and 25th August.

and wind speed vertical profiles, is at approximately 100 m and the position of the cloud layer varies but generally lies between 200 and 800 m.

On 27th August the model identifies the boundary-layer type as well-mixed and this prevents the cloud layer from extending above boundary-layer top. Even though the boundary layer in the model is very deep compared to the observations, the cloud layer is too low and too thin. Between 00:00 and 12:00 UTC on 29th August boundary layer type is identified as 'stratocumulus over stable'. This model regime agrees better with the observations; a layer of cloud over a stable layer. The potential temperature and relative humidity profiles in both the model and observations show a weakly stable and very humid layer up to approximately 800 m and the height of the cloud layer produced by the model at least overlaps the observed cloud layer. On 30th August between 05:00 to 12:00 UTC the boundary layer is identified as 'decoupled stratocumulus not over cumulus'. Under these conditions the cloud layer becomes decoupled from the surface, with a mixed layer capped by an inversion below. Under this regime the surface mixed layer is too deep, causing the cloud layer to be too far above the surface. These results indicate that the creation of a new boundary-layer type for summertime Arctic stratocumulus could improve model performance. This requires further investigation.

A more general result from Figure 6.12 regards the inversion that occurs in the observations between 500 and 1000 m throughout the period 27 - 30th August. The model consistently reproduces this inversion but to varying degrees of accuracy. The boundary-layer depths diagnosed from the observations were found to be very shallow under the conditions experienced during the ASCOS ice station; it was almost always less than 200 m and often around 100 m deep. The lowest four model levels in the version of the MetUM examined here are at 20, 80, 130 and 180 m and therefore very few levels are

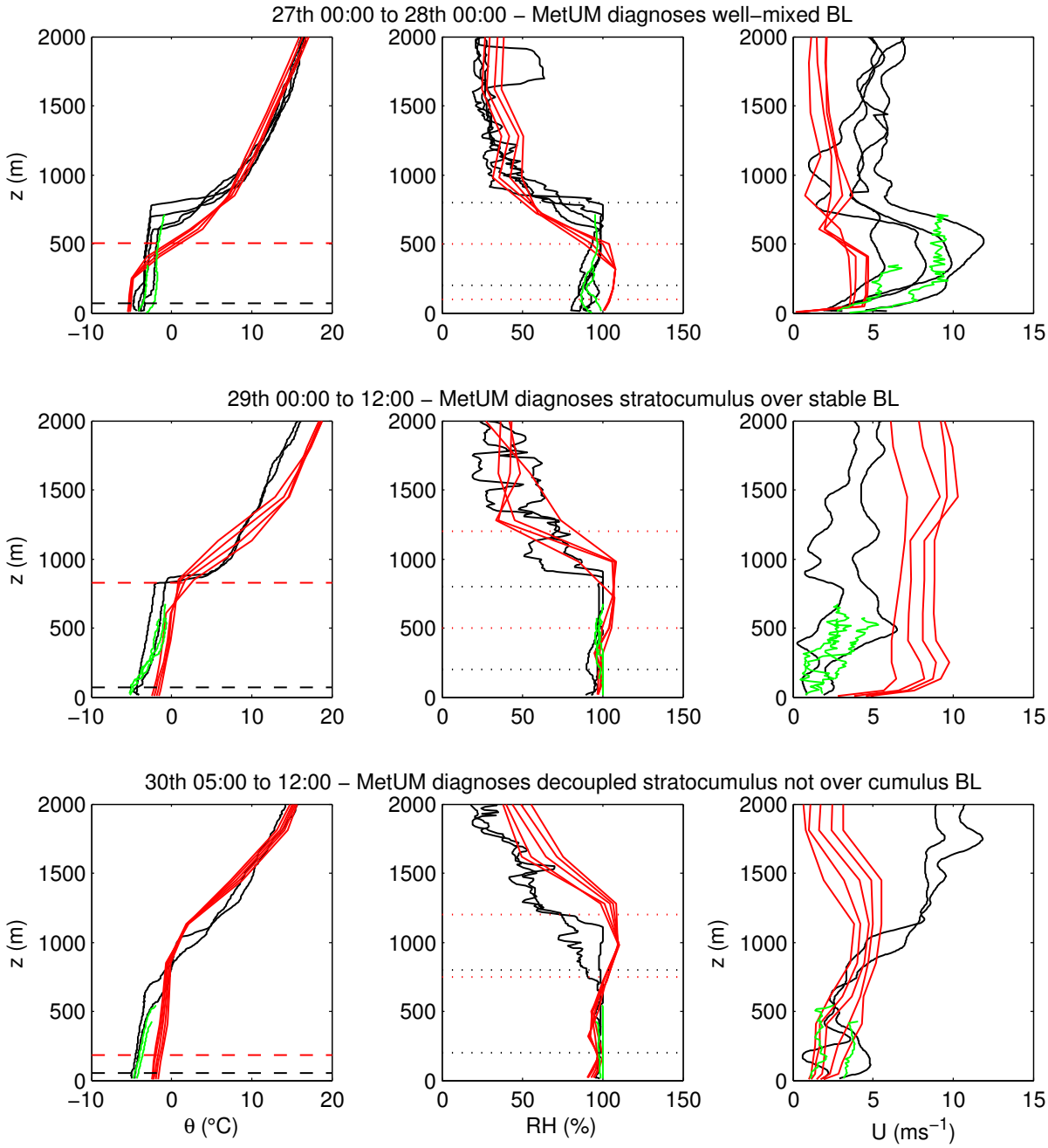

Figure 6.12: Observed and modelled profiles of potential temperature, relative humidity with respect to water and wind speed in the lower atmosphere for various boundary-layer types. The solid black lines are measurements from every radiosonde launch during each period; the solid green lines are measurements from selected tethersonde flights during each period. The red lines are profiles at regular intervals throughout each period from the MetUM 7-day forecast initialised at 00:00 UTC 25th August. Observed and model mean boundary-layer depth are shown by the black and red dashed lines respectively and the dotted black and red lines represent mean cloud base and top.

at altitudes low enough to be within the depth of the observed boundary layer. The vertical structure of a very shallow boundary layer cannot be resolved by the model and consequently it often diagnoses a mixed layer between the surface and the top of the main inversion, which is not seen regularly in the observations. This is investigated in more detail in a model sensitivity test with increased vertical resolution.

6.2.3 Summary

Comparisons between the operational MetUM forecasts and the ASCOS observations have reinforced what was found from the study using the AOE 2001 data set. The positive bias in modelled surface temperature was found to exist during both the AOE 2001 and ASCOS observation periods. This is caused by a feedback of errors involving the surface albedo and surface energy budget; errors in cloud occurrence cause too much radiation to be absorbed at the surface, which causes the surface temperature to be overestimated and the temperature-dependent albedo to be underestimated. More shortwave radiation is thus absorbed at the surface, which locks the surface temperature at 0 °C and the albedo at 0.5. Unlike the AOE 2001 period, a different set of model errors occur in the pre-conditioning period of the ASCOS observations. The onset of these errors was caused by an erroneous clear period in the model, which significantly cooled the surface. Large biases in the turbulent heat fluxes then offset the positive bias in the radiation budget and thus surface temperature became colder than that observed for the first time.

Cloud occurrence was found to be generally represented poorly by the model and therefore, the pre-conditioning period was used as a case study to investigate it in more detail. The modelled cloud layer that existed during this period was too thin and too low in the operational forecasts compared to the observations. This was caused by two distinct problems in the model. Firstly, a problem with the operational forecast-assimilation cycle prevented the cloud layer from evolving and moving higher in altitude. Every 12 hours the model is forced back into a preferred state, which does not agree well the observations from the ASCOS campaign. The cause of this is not obvious from the analysis and requires further investigation. The 7-day unconstrained forecasts did however, demonstrate that the model is able to develop a cloud layer that is similar to the observations. The second problem involved the interaction between modelled clouds and vertical atmospheric structure. The model produced a boundary layer that was always too deep and almost always too well-mixed, due at least in part to the low model vertical resolution. Unlike the observations, the modelled cloud was often within the boundary layer, which caused the cloud layer to be too low even though boundary-layer top was too high. During some periods the model produced a stratocumulus layer that was decoupled from

a stable surface layer. This is much closer to the type of boundary layer observed and during these times the cloud layer agreed better with the observations.

6.3 MetUM sensitivity tests

This study has highlighted some major failings of the MetUM over the central Arctic Ocean during late summer. The largest errors produced by the model are associated with the unphysical radiation-albedo-surface temperature feedback, overestimated surface turbulent fluxes, and errors in cloud occurrence and boundary-layer structure. This section presents some sensitivity tests performed using the MetUM, designed to refine some of the conclusions made in this study and to indicate possible ways of reducing some of the model errors. The MetUM was used to produce sets of 7-day unconstrained forecasts with increased minimum albedo, increased vertical resolution and decreased roughness length for momentum. The diagnostics from these forecasts are compared to those from 7-day control forecasts that are initialised at the same time using the same analyses.

6.3.1 Increased minimum albedo

Chapter 4 highlighted an important feedback process between model errors in the surface energy budget and albedo parameterisation. Errors in cloud occurrence or cloud radiative properties cause the amount of radiation and thus the total amount of energy absorbed at the surface to be overestimated by the model. This causes a positive bias in the surface temperature and a negative bias in the surface albedo. More shortwave radiation is absorbed at the surface, creating a feedback loop that locked the surface albedo at 0.5 and the surface temperature at 273.15 K for the majority of the AOE 2001 observation period and the ASCOS melt period. The ice surface albedo is computed in the MetUM through a temperature-dependant parameterisation scheme (e.g. Curry *et al.* (2001), where the albedo is set to a maximum value of 0.8 at $T_{ice} \leq 263.1$ K. The albedo then decreases linearly with increasing surface temperature to a minimum value of 0.5 at $T_{ice} = 273.1$ K.

The MetUM (model cycle G49) was initialised at 12:00 UTC on 18th, 19th and 20th August 2008 and run unconstrained for 7-days with the minimum surface albedo, α_{min} increased from 0.5 to 0.6. These dates were chosen to cover the ASCOS cold period, in which T_{ice} was overestimated by the model even though it reproduced the cold temperatures aloft with reasonable accuracy. In addition, the model errors during this period were similar to the errors produced by the model during the AOE 2001 cold period. The

albedo measurements from ASCOS were made over a snow surface and are therefore not representative of an area the size of a grid box. The aerially averaged albedo is lower than the observed value due to the presence of open leads and melt ponds. An estimate for this albedo can be derived using the estimated ice (80 %) and open water (20 %) surface fractions made from the aerial photograph in Figure 5.20. Cogley (1979) showed that for direct radiation, the albedo of water increases with increasing solar zenith angle. The solar zenith angle is always relatively large during the summer months in the central Arctic but because there is a near-persistent cloud layer the amount of direct radiation incident on the surface is small. A value of 0.04 is therefore assumed for the open water albedo and a fractional average of 0.64 was computed from this and the mean observed albedo (0.79). This value is in broad agreement with that observed during the SHEBA experiment in the later half of August (Figure 2.12). A value of $\alpha_{min} = 0.6$ was selected for the sensitivity test, since this is both a modest adjustment but also represents the observations reasonably well.

Figure 6.13 compares results from the control and increased α_{min} forecasts initialised on the 18th, 19th and 20th August 2008. At almost every timestep in all three forecasts the amount of radiation absorbed by the surface has decreased by up to 10 Wm^{-2} and T_{ice} has decreased by approximately 1 K. The blue outlying points on both the net radiation and T_{ice} plots are caused by a period of clear conditions on 25th August that appeared only in the forecast initialised on the 19th August. Figure 6.14 compares time series of observed T_{ice} with that produced by the operational forecasts and the three forecasts with increased α_{min}. It is obvious that this change to the albedo parameterisation improves the representation of T_{ice} in the model during the cold period. The near-surface air temperature is driven strongly by T_{ice} and therefore this is also improved with the increase in α_{min} (not shown). Figure 6.13c shows that there is very little change in $T_1 - T_{ice}$ with increased α_{min} because T_1 and T_{ice} have both decreased by the same amount. This suggests that the modification of α_{min} has little impact on the sensible heat flux because it is the difference between T_1 and T_{ice}, rather than their absolute magnitudes that are important in the sensible heat flux parameterisation.

Adjusting the constants in an existing parameterisation is often only a short term solution for reducing model errors. In the future it is recommended that the albedo parameterisation is changed to a more sophisticated scheme. Prognostic schemes with a decay factor for the albedo of melting/ageing snow have been shown to perform better than temperature dependent schemes by Curry *et al.* (2001) and Pedersen & Winther (2005) and through the comparison of the MetUM and COAMPS in this study. An albedo scheme with snow depth dependency already exists in the climate version of the MetUM (HadGEM1); this has been shown to perform reasonably well over the central Arctic (McLaren *et al.*, 2006) and could easily be implemented in the operational NWP version.

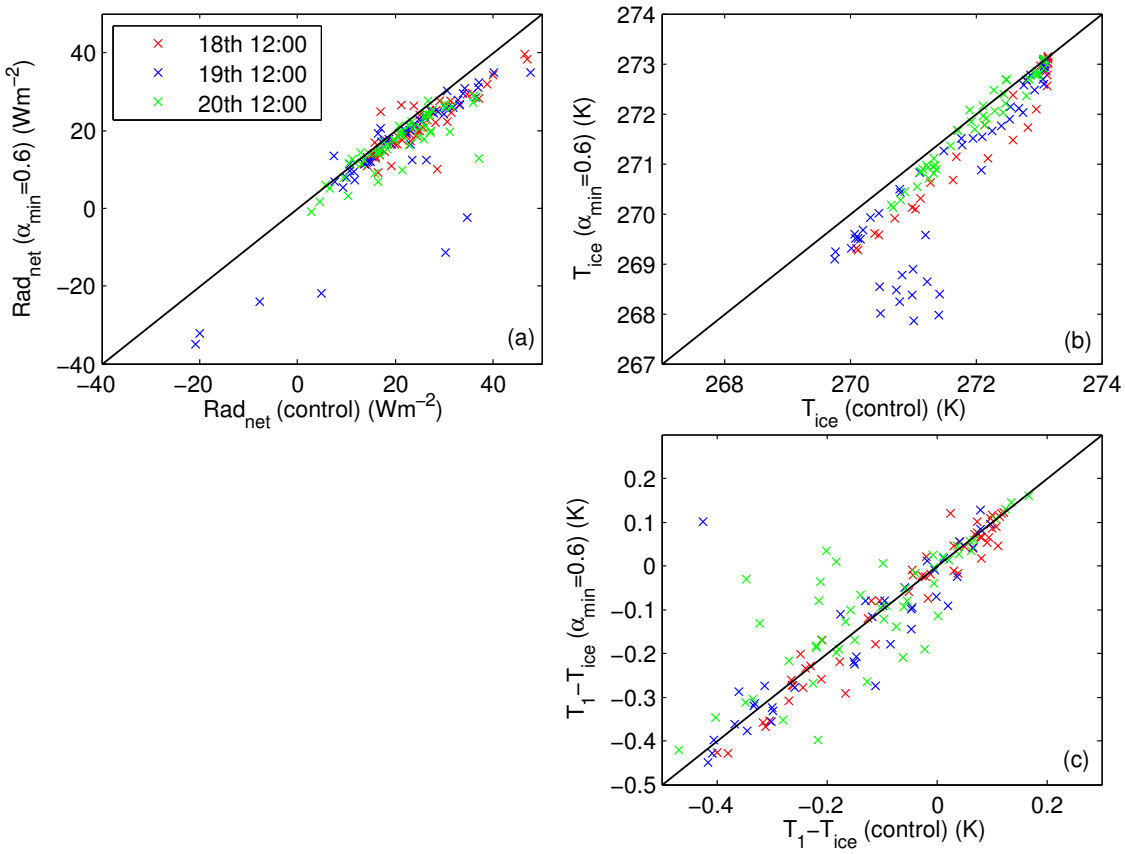

Figure 6.13: Effect of increased α_{min} from 0.5 to 0.6 on (a) net radiation, (b) surface temperature and (c) $T_1 - T_{ice}$. The three colours represent three 7-day forecasts, initialised at 12:00 UTC on 18th, 19th and 20th August.

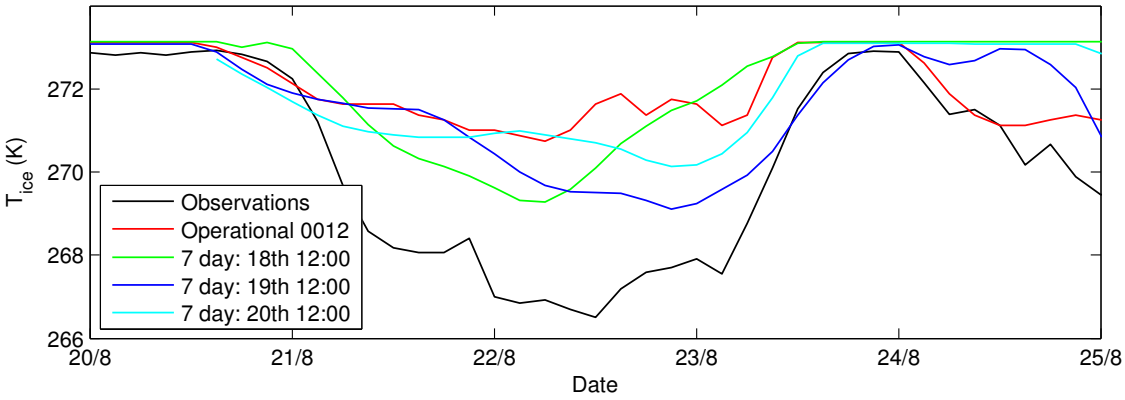

Figure 6.14: Effect of increased α_{min} from 0.5 to 0.6 on surface temperature. The observations, data from the operational model and data from the three 7-day forecasts are shown.

Although more complicated to implement, the ideal solution would be to incorporate a more sophisticated scheme that is based on observations, such as that by Bromwich *et al.* (2009), which has been shown to perform well in the Polar Weather Research and Forecasting (WRF) model (see Section 2.4.5 for more details).

6.3.2 Decreased roughness length for momentum

The analysis in Chapter 5 highlighted large biases in the transfer coefficients used by the model to compute the surface turbulent fluxes. The results suggest that the modelled transfer factors (gradients of the lines in Figure 5.2) were 1.58 times greater than that derived from the observations for u_*, and 6.32 and 2.94 times greater for the sensible and latent heat fluxes respectively. One conclusion was that the roughness length for momentum, z_0 (and possibly for temperature and heat, z_t and z_q) used by the MetUM is too large. To test the sensitivity of the model to z_0 unconstrained 7-day forecast runs, initialised at 12:00 UTC every day between 18th and 26th August were produced using model cycle G49, with z_0 reduced from the standard value of $3\text{x}10^{-3}$ m to $5\text{x}10^{-4}$ m. This value was selected from Table 5.4 to represent the value of z_0 observed over the large ice floe at the mast site. The MetUM assumes that $z_t = z_q = z_0/10$ and this also applies in the forecasts with modified z_0.

The results from these forecasts, along with the control runs and the observations are shown in Figure 6.15, which uses the same method of analysis as Figure 5.2. Decreasing the value of z_0 has a large impact on the accuracy of u_* predicted by the model. The transfer coefficient is almost exactly the same as that produced by the observations at the lowest model level. For the sensible and latent heat fluxes decreasing z_0 (and thus z_t and z_q) does show some improvement to the fluxes computed by the model but not to the same extent as for u_*. Unfortunately, due to the large spread in z_t and z_q computed from the observations using Equations 5.12 and 5.13, it was not possible to derive good estimates of these quantities from the AOE 2001 or ASCOS data set. The spread in z_t and z_q estimates computed from observations over sea ice has been shown previously to be large by Andreas *et al.* (2005) and therefore a large volume of data is needed to enable mean values to be calculated with a reasonable standard error. The AOE 2001 and ASCOS data sets were found to be too short for this type of analysis and therefore, no observed values of z_t and z_q are available to compare to the model values. The analysis in Section 5.5 does however, suggest that using the parameterisation of Andreas (1987) for z_t and z_q (Equation 5.22) does reduce the positive bias in the transfer coefficients.

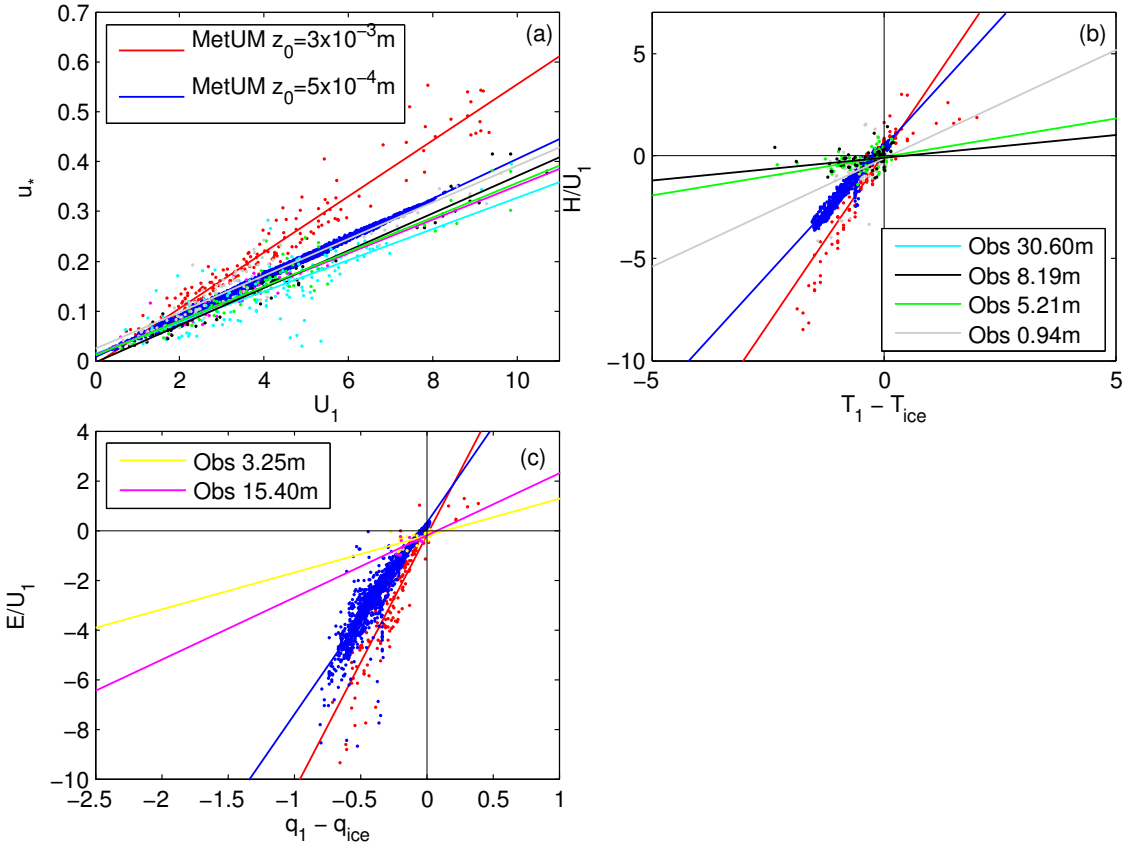

Figure 6.15: Effect of reducing z_0 from 3x10^{-3} m to 5x10^{-4} m on the surface turbulent fluxes. z_t and z_q are equal to $z_0/10$ in both the control and reduced roughness length forecasts. The plot shows 3 hourly averaged (a) u_* vs. U_1, (b) H/U_1 vs. $T_1 - T_{ice}$ and (c) E/U_1 vs. $q_1 - q_{ice}$. T_1 (q_1) is the temperature (specific humidity) at each observation (or first model) level. q_{ice} for both the model and observations is assumed to be the saturation humidity with respect to ice at T_{ice} and U_1 is the wind speed at each observation (or first model) level.

There are no immediately obvious easy ways of improving the turbulent fluxes produced by the MetUM over the central Arctic Ocean during the summer months. Small improvements would be possible through further sensitivity tests by optimising the value of z_0 and altering its simple relationship to z_t and z_q. Reducing the value of z_0 to 5x10^{-4} m will probably improve the accuracy of the modelled turbulent fluxes during the summer months. Further evidence to support this is given in Chapter 4; the transfer coefficients used in COAMPS are z_0 =1.4x10^{-5} m and $z_t = z_q = z_0/10$, two orders of magnitude smaller than those used in the MetUM. Whilst this value for z_0 is smaller than any of the values observed during ASCOS, the turbulent fluxes produced by COAMPS have a significantly smaller bias than those produced by the MetUM.

In reality the values of the roughness lengths are not constant in time or space over sea ice and therefore, a better solution would be to incorporate a bulk flux algorithm, specifically developed for use over sea ice that uses a parameterisation for the roughness lengths based

on observations. The SHEBA bulk flux algorithm is an obvious choice but this has been only very recently developed and is yet to be tested in a general circulation model. In addition, it is questionable whether Monin-Obukhov similarity theory, on which most bulk flux algorithms are based, is even valid in this context. Considering the evidence in Chapter 5 it is unlikely that a first model level more than a few metres from the surface is within the surface layer during the summer months, suggesting similarity theory is often not valid in the model flux calculations under the types of conditions observed during the ASCOS ice station.

6.3.3 Increased vertical resolution

Section 6.2 highlighted issues associated with the vertical structure of the lower atmosphere and cloud occurrence in the MetUM. The analysis suggested that boundary-layer depth is almost always overestimated by the model and that the model often produces a well-mixed boundary layer when the observations suggest a weakly stable boundary layer with an extremely shallow or non-existent mixed layer. The vertical profiles were found to have a significant impact on the evolution of modelled cloud and since the presence of cloud has a large impact on the surface energy budget (Curry *et al.*, 1996), it is important to look at ways to improve the representation of cloud in the model. One possible issue is that the vertical resolution of the MetUM is too coarse to adequately capture the vertical structure of the atmosphere and many of the processes that occur in the low-level stratocumulus clouds. During 2008 the version of the global NWP MetUM that operational ran with 50 vertical levels (model cycle G48 and G49). In 2009 a newer version of the model became available with 70 levels (model cycle G50), in which most of the extra levels were in the lower atmosphere. The lowest levels in this version of the model were at 10, 37, 77, 130, 197, 277, 370, 477 and 598 m compared to 10, 50, 130, 250, 410 and 610 m in G48 and G49. 7-day unconstrained forecasts were produced using the 70 level version of the model, initialised at 12:00 UTC on 18th to 22nd August and 25th August; these can be compared to control runs from the 50 level version, initialised using the same analyses.

A comparison between the observations and the cloud produced by the 50 level (control) version of the model and the 70 level version of the model is shown in Figure 6.16. The general form of the cloud that the model produces is similar in the 50 and 70 level versions but there are some obvious differences in diagnosed boundary-layer depth. For example, the forecasts that were initialised on the 19th produce a layer of cloud on the 21st and 22nd of August. In the 50 level version of the model this cloud layer is within the boundary layer but in the 70 level version boundary-layer depth has decreased significantly; the cloud layer is above it and at slightly higher altitude. The same effect is also apparent to

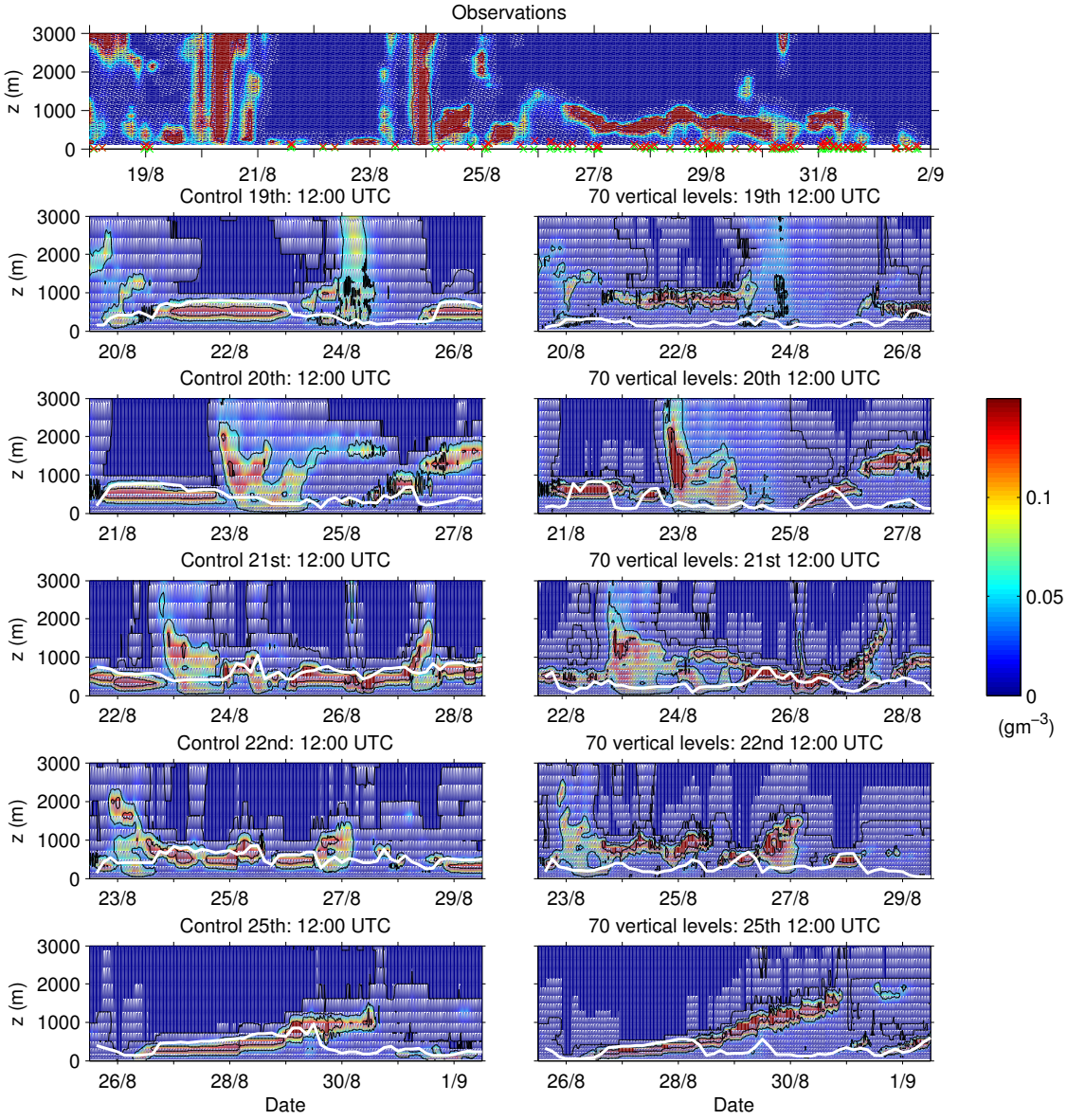

Figure 6.16: Effect of increased vertical resolution on cloud and boundary-layer depth. The top panel shows total cloud water concentration derived from measurements made by the remote sensing instruments. The lower panels compare total cloud water and boundary-layer depth (white line) over five 7-day forecasts initialised at 12:00 UTC on 18th to 22nd August. Isopleths are at 0.05 gm^{-2} intervals.

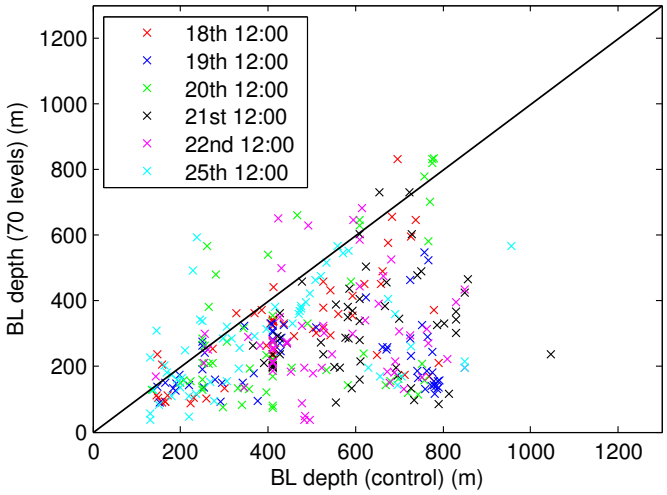

Figure 6.17: Effect of increased vertical resolution on boundary-layer depth. Comparison of boundary-layer depth diagnosed by the model from six 7-day forecasts initialised at 12:00 UTC on 18th to 22nd August and 12:00 UTC on 25th August.

some extent in the forecasts that were initialised on 20th to 22nd August. The forecasts initialised on the 25th show a single layer of cloud that evolves during the 7-day period. In the 70 level version of the model boundary-layer depth decreases sooner and the cloud layer increases further in altitude. The effect of increased vertical resolution on boundary-layer depth is shown more clearly in Figure 6.17. It is obvious that boundary-layer depth has decreased by a large amount.

Figure 6.18 compares vertical profiles produced by the 50 and 70 level versions of the model from forecasts initialised on the 25th with observations from the tethersonde and radiosondes. Figure 6.19 shows the differences in boundary-layer type produced by the model in all the available forecasts. During the first few days of the forecast that was initialised on the 25th both versions of the model produce similar temperature, humidity and wind speed profiles and the boundary-layer type is stable during the clear period on the 26th and then mostly well-mixed until 28th August. During 27th August and the first half of the 29th there are also few differences between the two versions of the model, except that boundary-layer depth decreases and moves below the cloud layer earlier in the 70 level forecast. By the 30th August the strong temperature inversion that begins at 900 m in the 50 level version has increased in altitude to approximately 1200 m in the 70 level version and the point at which the relative humidity begins to decrease has also increased. This causes the cloud layer in the 70 level forecast to be even higher than that in the 50 level version and in the observations. Boundary-layer type has also changed from mostly 'well-mixed' to a 'shear dominated unstable' or 'decoupled stratocumulus not over cumulus'. A general observation of the boundary-layer types produced in the forecasts by both the 50 and 70 level versions is that the boundary layer is most often

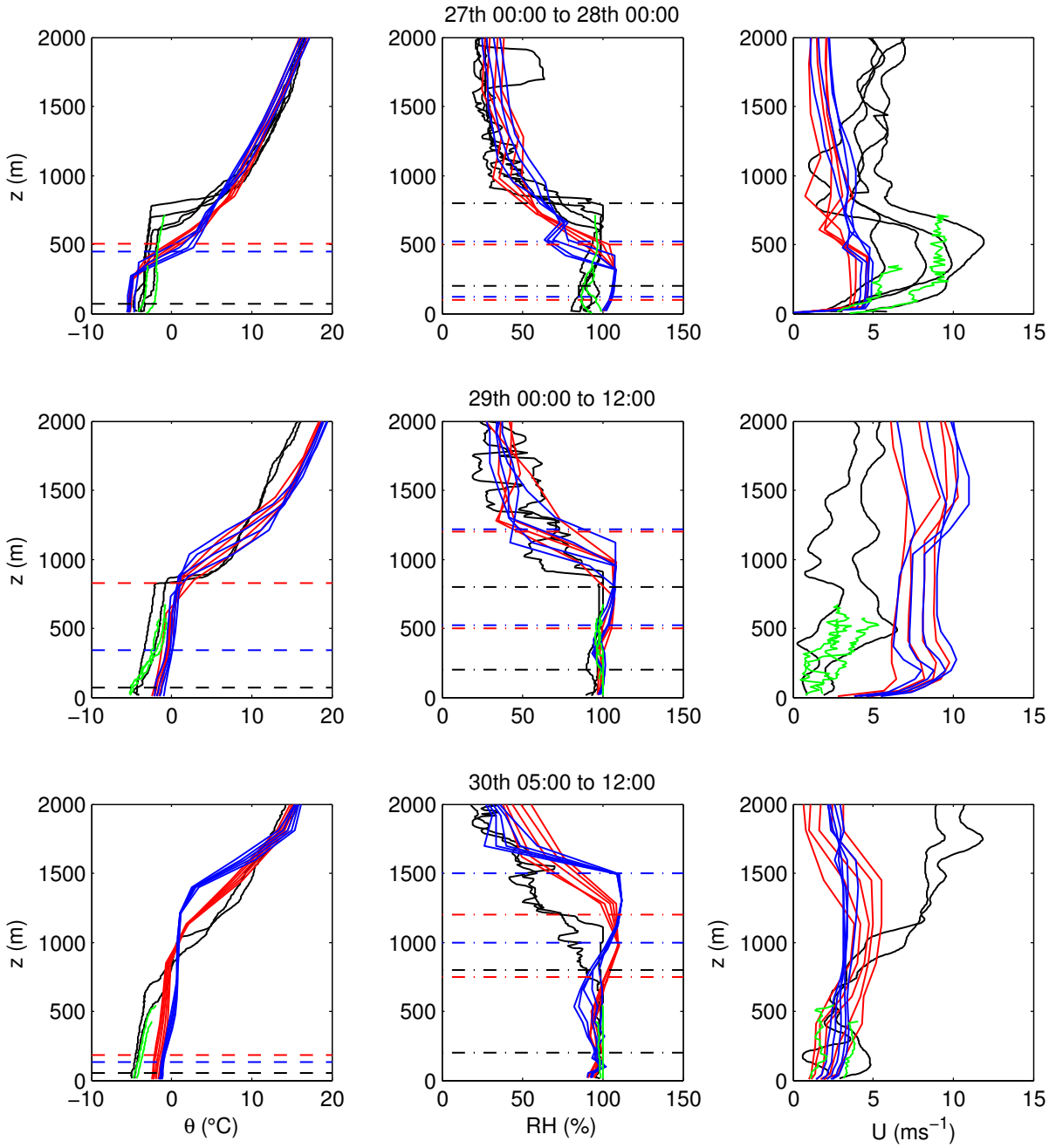

Figure 6.18: Same as Figure 6.12 but including data from the 70 level version of the MetUM (blue).

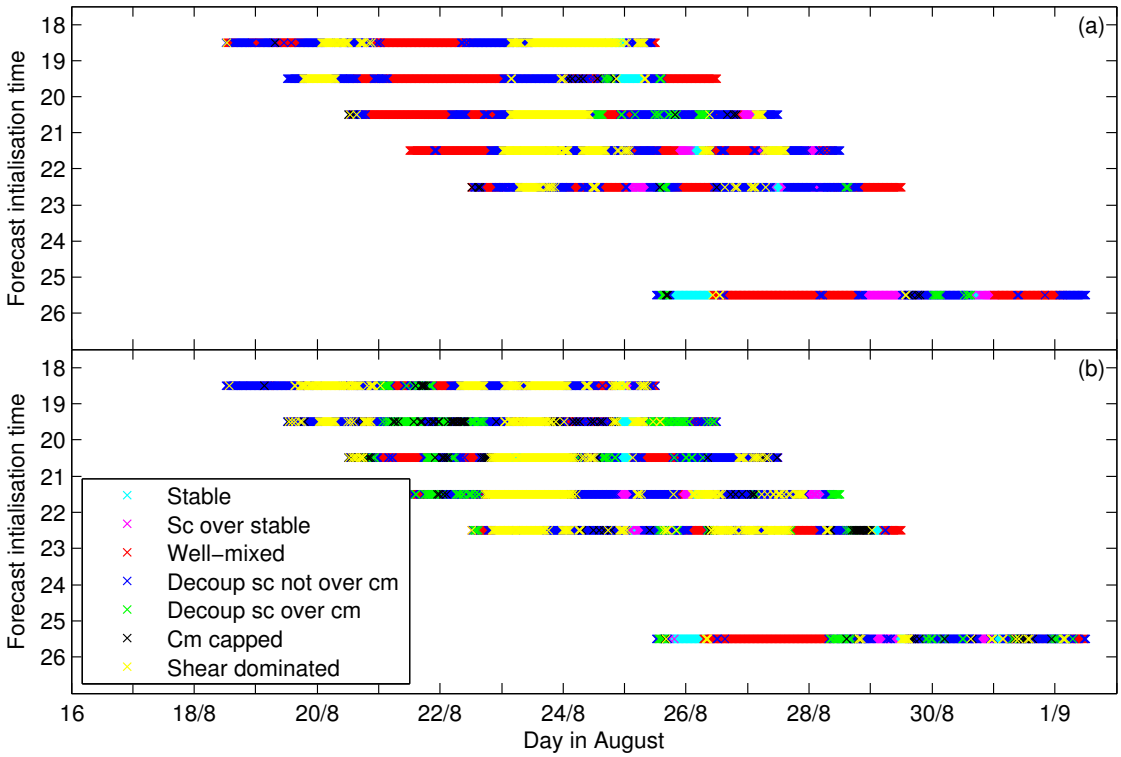

Figure 6.19: Effect of increased vertical resolution on boundary-layer type. Comparison of boundary-layer type diagnosed by the model from six 7-day forecasts initialised at 12:00 UTC on 18th to 22nd August and 12:00 UTC 25th August. Panel (a) shows data from the control run with 50 levels and (b) shows data from the 70 level version of the model.

well-mixed or shear dominated unstable. This is obviously not an accurate representation since Figure 6.9 shows that observed mixed-layer depth was always less than 200 m and in many cases there was no mixed layer.

This sensitivity test has shown that increasing the vertical resolution of the model does not significantly affect cloud occurrence, although it does reduce boundary-layer depth since more near-surface processes can be resolved. The modelled mixed-layer that is in contact with the surface remains too deep and there is little improvement in the representation of the observed vertical profiles in Figure 6.18. There is some evidence to suggest that because the boundary-layer depth is decreased, cloud can exist above the boundary layer more easily, be at a higher altitude, and be in better agreement with the observations. A good example of this is the cloud layer that exists between 21st and 23rd August in the forecasts initialised on 19th August. Despite this, the forecasts initialised on the 25th suggest that the increased resolution causes the cloud layer to increase to altitudes higher those observed. Creating a new Arctic specific boundary-layer type for the MetUM could improve the simulation of the observed cloud.

6.4 Comparison with HadGEM1 data

This study has concentrated on evaluating the global NWP version of the MetUM over the central Arctic Ocean. Detailed reasons for evaluating the NWP version, rather than a climate version are given in Section 3.4.1. In brief, using a NWP version allows an investigation of the physical parameterisations without the complication of large errors in the large-scale flow. It also enables an evaluation of individual weather systems rather than a purely statistical approach, which would be difficult with an observational data set that spans only a few weeks. The Hadley Centre Global Environmental Model (HadGEM1) is a climate version of the Met Office Unified Model; the atmospheric component is very similar in formulation to the global NWP version used in this study. Due to the wealth of evidence that the Arctic climate is changing rapidly (Section 2.2), it is arguably more important to produce accurate simulations of the region on climate rather than NWP timescales. This section briefly compares diagnostics from HadGEM1 with both the AOE 2001 and ASCOS observations, to assess whether the problems and errors in the NWP version highlighted in this study are also apparent in the climate version.

Figures 6.20 to 6.23 compare daily averaged observations from AOE 2001 and ASCOS with data from a 7 year climate simulation using HadGEM1 with fixed present day greenhouse gas forcing. The daily model data is averaged over the same day from each of the 7 years, are plotted with a representation of the standard deviation about each mean and the minimum and maximum daily mean from the 7 year period. Firm conclusions from this type of analysis are difficult due to the limitations of the observational data set and the methodology. Measurements are available over periods of only a few weeks and from only two seasons; a good representation of the inter-annual variability is thus impossible to achieve. The measurements are also made at a single location, and thus unlikely to be representative of an area the size of a model grid box. Since the surface of the central Arctic Ocean is reasonably homogeneous compared to other types of surface and the MetUM shows little variability in diagnostics between grid boxes that contain ice at this latitude this method of model evaluation should however be informative, providing the limitations are taken into account during the analysis.

Figure 6.20 shows modelled and observed near-surface air temperature, surface temperature, near-surface relative humidity and near-surface wind speed for the months of July, August and September. The surface and air temperature diagnostics from the model show the obvious transition into freeze-up that begins in the middle of August. What is assumed to be the beginning of freeze-up in 2008 occurred earlier than in any of the years in the model, although it is not possible to say how representative the ASCOS year was of average conditions. Observed temperatures are generally within one standard deviation of the daily inter-annual model means but the temperatures observed during the cold

periods in 2001 and 2008 decrease to well below the lowest daily temperatures that were diagnosed by the model in the 7 year period. This suggests that a similar issue to that in the operational NWP version of the model exists in the climate model; errors in the surface energy balance cause the surface and thus near-surface air temperatures to be positively biased.

The near-surface relative humidity produced by the model gradually increases with time through the 3 month period and is between 85 and 100 % during the observation periods. The model statistics agree well with the observations during the second half of the ASCOS observations but the results from before the 20th August suggest that the modelled relative humidity is too low, although this could be due to the positive bias in the temperature fields. The 10 m wind speed varies in the model between about 1 and 9 m s^{-1} during July to September agreeing closely with the observations.

Modelled and observed turbulent heat fluxes, albedo and modelled ice fraction are shown in Figure 6.21. Up to the end of August the sensible heat flux varies between -10 and +10 Wm^{-2} in the model, which matches the observations very well. The latent heat flux is negative during July and August in the model and becomes small in September. The observations from both field campaigns suggest that the modelled latent heat fluxes are of the correct sign but are too large. This is a conclusion that is common in evaluations of other models over the central Arctic during summer (Tjernström *et al.*, 2005; Brunke *et al.*, 2006). This also agrees with what was found in the global NWP version of the MetUM.

The surface albedo over sea ice is parameterised in HadGEM1 using a similar temperature-dependent scheme to that in the NWP version of the MetUM, except that the minimum albedo for bare ice is set to 0.6 and a dependency on snow cover is included. Unlike the NWP version, sea ice fraction is not prescribed through satellite observations in HadGEM1 but is calculated through the coupled sea ice model. This allows the grid box mean ice fraction to be lower than 100 %, whereas the NWP version assumes complete sea ice cover at such high latitudes. The albedo of the ice fraction of the grid box remains at 0.6 during July and the first half of August and then increases to 0.8 by the end of September (Figure 6.21). The grid box mean surface albedo, which includes the albedo of the open water fraction, is lower than this by approximately 0.05. The ice surface albedo observations are between 0.7 and 0.9, much higher than the modelled value for the ice surface. This is because the values set in the model parameterisation account for melt ponds on the ice surface. According to visual observations made during the ASCOS ice station, all the melt ponds had become frozen and covered in snow by about the 21st August. This suggests that the ice albedo in HadGEM1 is too low during late August.

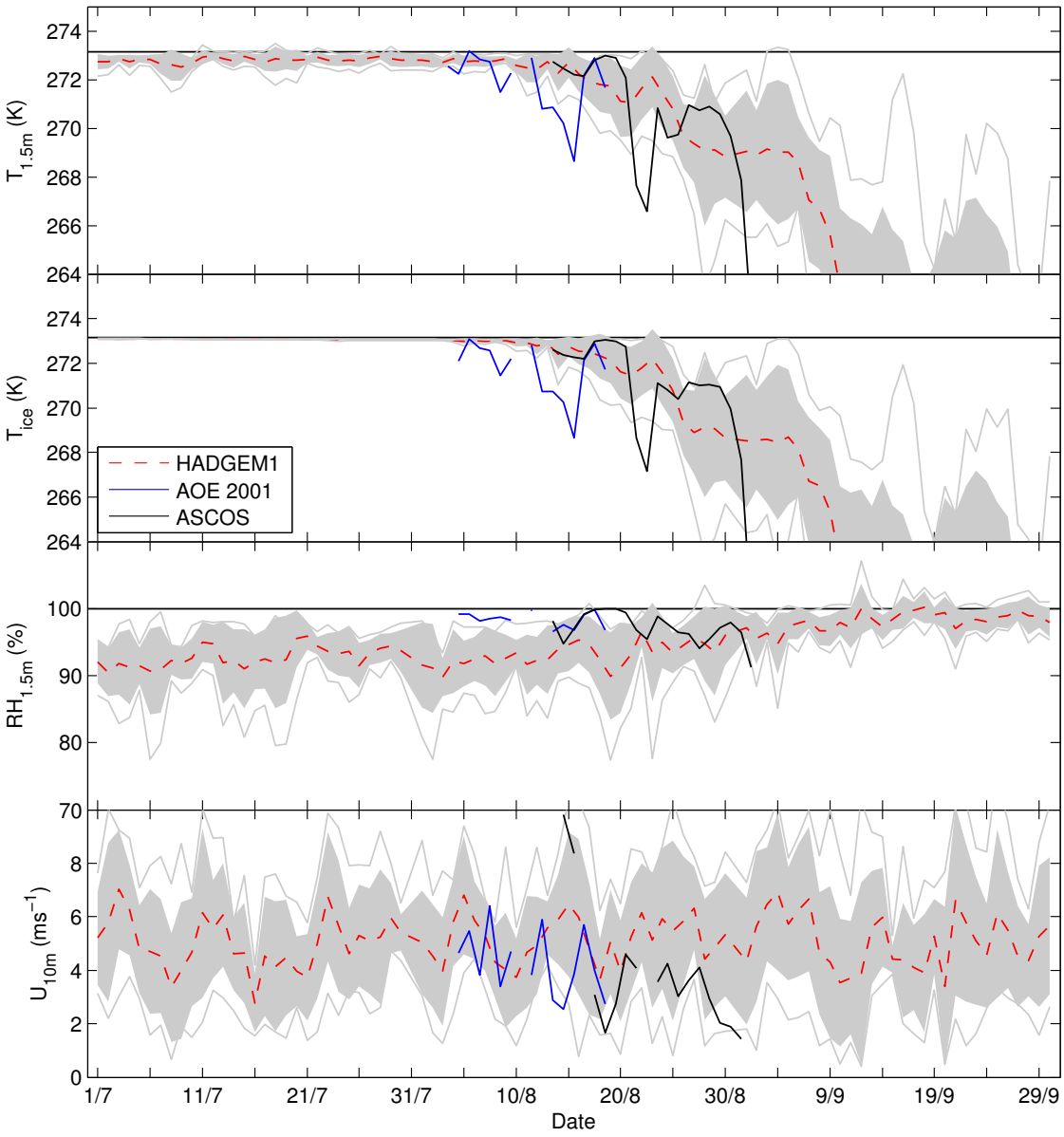

Figure 6.20: Daily mean temperature, relative humidity and wind speed observations and diagnostics from HadGEM1. Observations are daily means from the AOE 2001 and ASCOS campaigns and data from HadGEM1 are daily means, averaged over the 7 years of model data. The grey area represents ±1 standard deviation from the daily mean model value and the grey lines represent the minimum and maximum year.

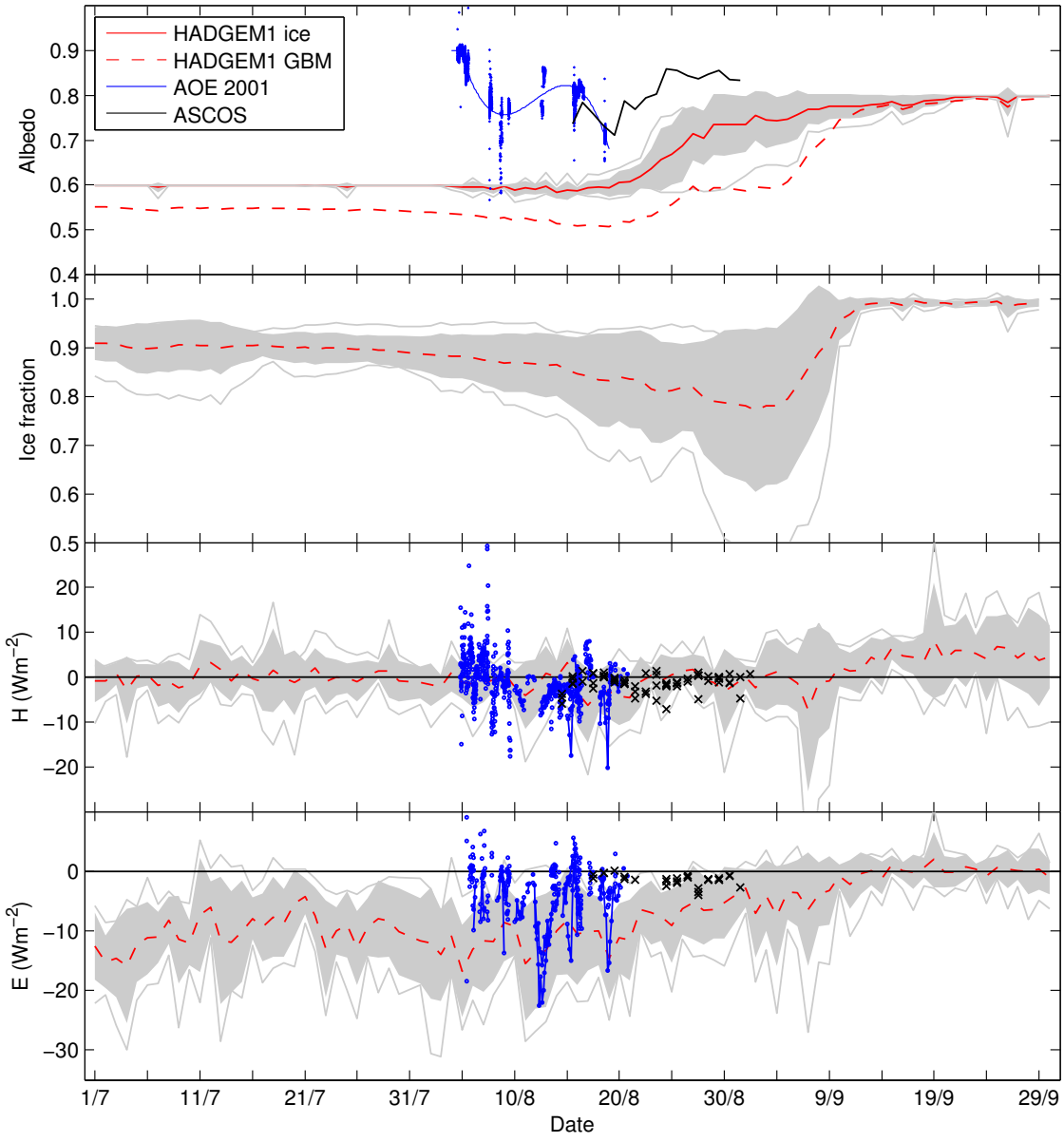

Figure 6.21: Same as Figure 6.20 but for albedo, ice fraction and turbulent heat fluxes. In the top panel the thick red line represents the modelled ice albedo and the dashed red line the grid box mean albedo. A positive flux is defined as energy absorbed at the surface.

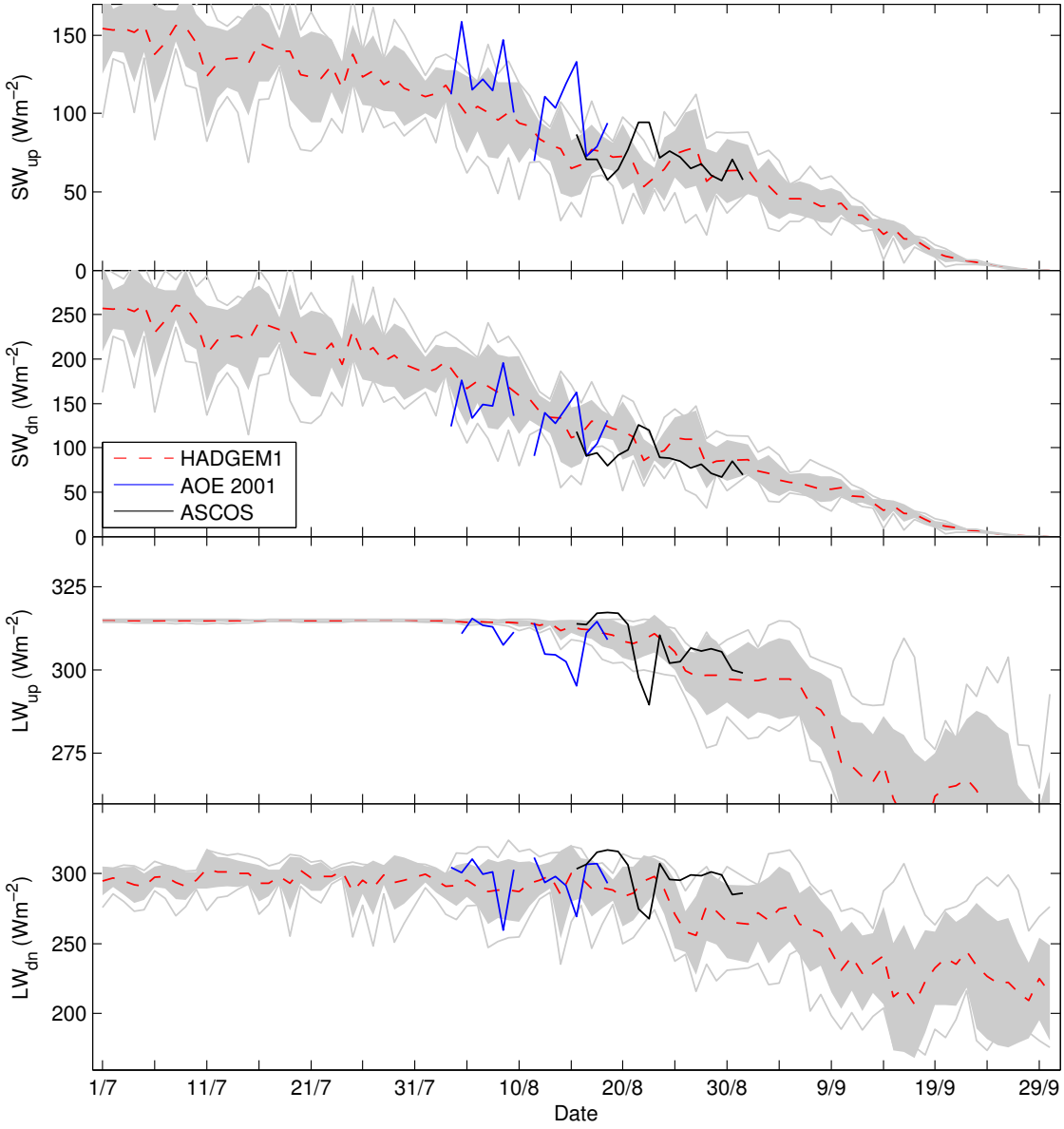

Figure 6.22: Same as Figure 6.20 but for the up and downward radiation fluxes. A positive flux is defined as energy absorbed at the surface.

The effect of biases in surface albedo and cloud occurrence can be assessed using the surface radiation fluxes in Figure 6.22 and 6.23. The magnitude of modelled SW_{dn} is reasonable compared to both sets of observations but there are indications that the magnitude of SW_{up} is too low in the model, similar to the NWP version. The upward and downward components of the longwave radiation flux are reasonable, apart from periods in LW_{up} when the observations are lower than the model minimum daily averages. This is related to the underestimation of surface temperature by the model. Figure 6.23 suggests that the magnitude of both SW_{net} and LW_{net} are overestimated by the model, in agreement with results from the NWP version. The observed daily mean total heat flux from AOE 2001 is generally smaller than the minimum daily means produced by the

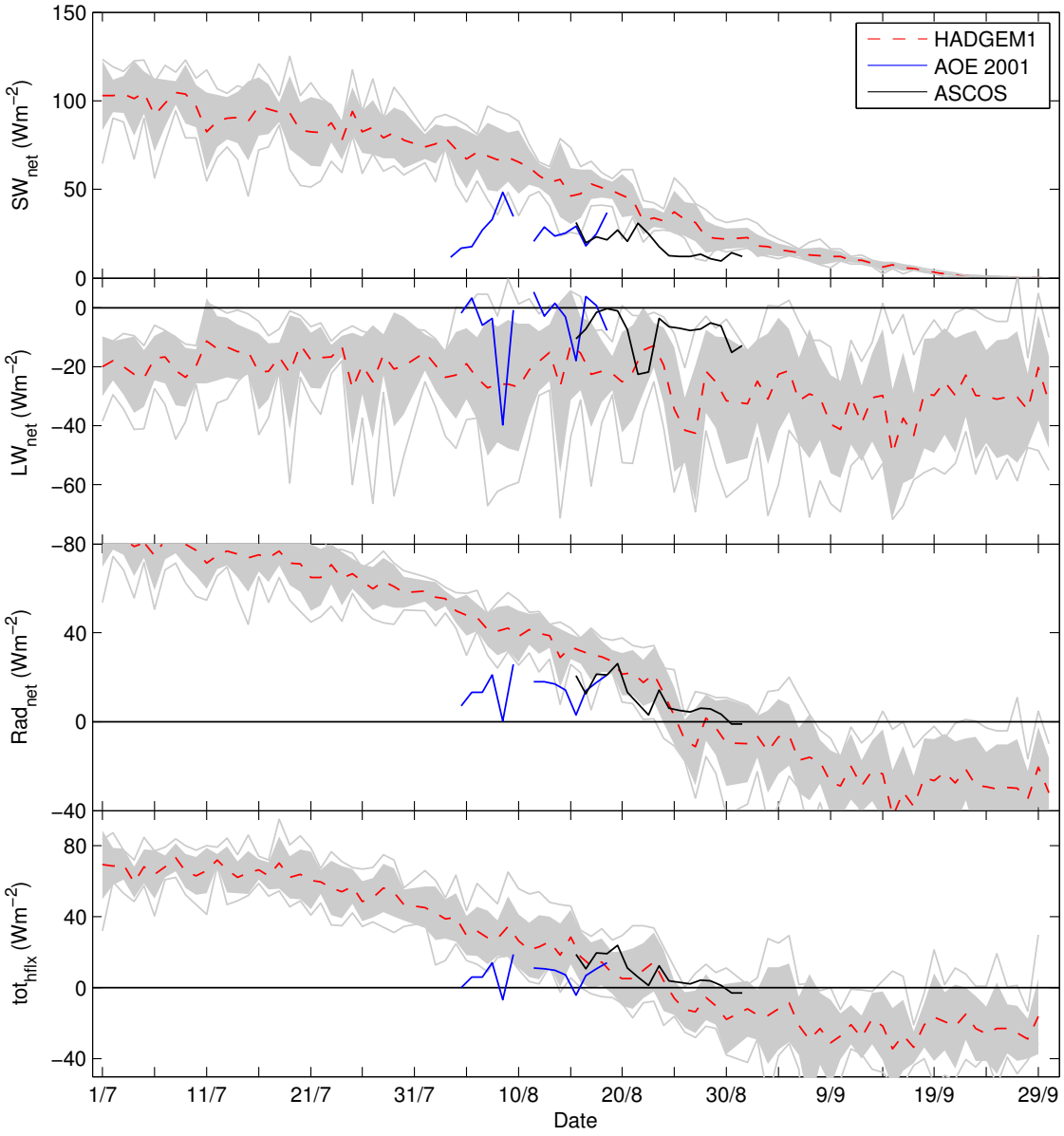

Figure 6.23: Same as Figure 6.20 but for the net radiation and total heat fluxes. A positive flux is defined as energy absorbed at the surface.

model, also in agreement with findings with the comparison with the NWP version. The total heat flux observations from ASCOS are however, generally within one standard deviation of the measurements and the total heat flux becomes negative at about the same time as the model.

It is difficult to assess how representative the measurements are of grid box means and thus how firm these conclusions can be. Since similar errors were found in the NWP version of the model, it is probable that the same applies to the climate version of the model. The effects of these errors in a climate simulation have the potential to be far larger than in the shorter term forecasts. This is because climate simulations run

unconstrained, whereas the operational NWP version is constrained by the assimilation of observations every 12 hours. Even though very few observations are made in the central Arctic, any that are made in the pan-Arctic region help to reduce systematic biases in the forecasts. In addition, the NWP version is an atmosphere-only model, in which ice fraction is prescribed daily from satellite observations. For this reason the overestimation of surface temperature and the total heat flux cannot cause a rapid loss of sea ice in the model. HadGEM1 however, is fully coupled to an ocean and sea ice model, in which sea ice can form, be transported and melt. Positive biases in the HadGEM's total surface heat flux that are suggested in this comparison have the potential to have a large effect on the surface energy budget of the region and the sea ice fraction, potentially causing a feedback similar to the ice-albedo feedback (Curry *et al.*, 1996). It is not clear from just 7 years of model data to what extent these errors could affect climate simulations in the future and a more detailed study, possibly using other observational data sets, is recommended.

Chapter 7

Conclusions and recommendations

7.1 Conclusions

The aim of this study was to use in-situ observations to gain an insight into surface exchange, the structure of the lower atmosphere and cloud formation over the central Arctic Ocean during the late summer/early freeze-up period. This knowledge can then be used to evaluate the performance of the Met Office Unified Model (MetUM) over the region, identify the parameterisations which cause the most significant errors and suggest improvements to them. Improvements to the model will help to improve climate predictions as well as seasonal and sub-seasonal mid-latitude weather forecasts.

The MetUM reproduced some aspects of the conditions observed during the AOE 2001 and ASCOS field campaigns reasonably well considering that relatively few observations are assimilated into the forecasts in this region. The 10 m wind speed, surface pressure and relative humidity and temperature away from the surface are generally reproduced with reasonable accuracy. Visual observations during ASCOS confirmed that the timing of synoptic scale fronts and the associated precipitation were also forecast well enough by the model for the forecasts to be of use during the ASCOS field campaign.

Detailed comparisons between model diagnostics and the observations did however, highlight a number of errors caused by specific model parameterisations. The MetUM, like many other models, was found to overestimate the magnitudes of the surface turbulent heat fluxes, especially the latent heat flux. This was found to be due to significant positive biases in the transfer coefficients. Most bulk flux parameterisation schemes are based on Monin-Obukhov similarity theory and the transfer coefficients are a function of the surface roughness and atmospheric stability. The roughness length for momentum, z_0 was found from the ASCOS observations to vary with the type of ice surface. The constant

value for z_0 used by the MetUM is too large for the ASCOS site, which partly explains the overestimation of the turbulent fluxes by the model. When z_0 was parameterised using the scheme based on observations from Antarctic sea ice (Andreas *et al.*, 2009), computed values of the momentum flux agreed well with the observations from the lower measurement levels. The errors in the sensible and latent heat fluxes were however, significantly overestimated when both the Andreas *et al.* (2009) parameterisation for the roughness lengths of temperature and humidity (z_t and z_q) and the assumption $z_t = z_q = z_0/10$ were used. The values for z_t and z_q that are used in the model unfortunately could not be evaluated with the ASCOS observations because there was too much variability in the computed values due to the relatively short data set.

The turbulence measurements were used to assess whether Monin-Obukhov similarity theory is valid under the observed conditions. Spectra and cospectra normalised using similarity theory were compared to the universal curves developed by Kaimal *et al.* (1972). The peaks in the curves from the upper measurement levels were found to be shifted to higher frequencies compared to the lower levels. In addition, in a comparison of the similarity function of momentum computed from observations at each measurement level, only the observations at the lowest level agreed well with the accepted form of the function. This shows that turbulent properties at the lower and upper levels are different and that at the upper levels a larger fraction of the total energy is associated with the smaller turbulent eddies. This can be explained by the depth of the surface layer. Estimates of observed boundary-layer depth were almost always less than 200 m, suggesting that surface-layer depth was less than 20 m and often only extended to a few metres above the surface. This indicates that Monin-Obukhov similarity theory was often not valid at the measurement heights above the 3.25 m level. The first model level in the MetUM is at 10 m for the wind speed diagnostic needed to compute the momentum flux and at 20 m for the temperature and humidity diagnostics needed to compute sensible and latent heat fluxes. These levels are almost always above the surface layer; similarity theory overestimates the intensity of the turbulence and thus the model overestimates the surface turbulent fluxes.

The second important error highlighted by the model evaluation involved the surface albedo parameterisation. Throughout the AOE 2001 observation period and for the first half of the ASCOS ice station the surface temperature and the near-surface air temperature were positively biased in the MetUM. This occurred even though air temperature above the first model level was reasonably accurate. The analysis shows that this was due to an important feedback of errors involving the surface radiative fluxes, surface albedo and surface temperature. Errors in cloud occurrence or radiative properties cause the amount of radiation that is absorbed at the surface to be overestimated. This

causes a positive bias in surface temperature and since the surface albedo is temperature-dependent, a negative bias in the albedo. This causes more radiation to be absorbed at the surface, creating a feedback loop that locks the albedo at its minimum of 0.5 and the ice surface temperature at 273.1 K. Air temperatures at the lowest model level are driven by the surface temperature and are therefore also overestimated for much of the observation period. The absorption of too much radiation at the surface has little effect on the sea ice in the NWP version of the model because it is represented as an isothermal slab, and ice fraction is not explicitly modelled, but is represented through the daily assimilation of satellite observations. This feedback could however, have consequences in the climate model since the atmospheric component is coupled to a sea ice model, which includes the transportation, formation and melting of sea ice.

The third significant error was the model's representation of cloud cover. For the AOE 2001 observation period the older version of the MetUM (model cycle G25) produced very few periods with a layer of low-level cloud. In contrast, the newer version (model cycle G42), which has significantly increased vertical resolution, produced a near-persistent layer of low-level cloud, apart from during periods of deeper clouds associated with the passage of synoptic scale fronts. The representation of these deeper clouds was shown to be reasonably accurate in both the timing of occurrence and their radiative properties. Errors in cloud occurrence and the associated surface radiative fluxes were larger during periods when a single layer of low-level cloud was observed. This is because the dynamical and microphysical properties of these clouds are very different to the marine stratocumulus clouds that occur at lower latitudes, on which the cloud parameterisations are based.

Detailed analysis of cloud formation in the operational NWP version of the MetUM showed that the cloud layer produced by the model during the ASCOS pre-conditioning period was too thin and too low. The cloud layer in unconstrained forecasts from the MetUM was however, able to evolve and become situated at altitudes similar to those observed. This suggests that there is a problem with the forecast and data assimilation cycle in the MetUM over the central Arctic region. The cloud layers in the operational forecasts are able to evolve within each 12 hour forecast but then seemed to be 'reset' back to a preferred state during the data assimilation or initialisation process. The cause of this is not obvious from the analysis and requires further investigation. The use of 7-day unconstrained forecasts showed that the model boundary layer was always too deep and most often too well-mixed. This confined the cloud layer to below boundary-layer top, explaining why it is often too low. Only when the cloud layer in the model became decoupled from the surface could it extend above boundary-layer top and show better agreement with the observations. When the vertical structure of the atmosphere was reasonably well represented (i.e. when boundary-layer type was 'decoupled stratocumulus

above a stable layer'), the cloud layer was reasonably well represented and boundary-layer depth was significantly reduced.

A number of sensitivity tests were performed using the MetUM to refine some of the conclusions made during the model evaluations. Firstly the model was run with the minimum albedo increased from 0.5 to 0.6. This decreased the amount of radiation absorbed at the surface and reduced the surface and near-surface air temperatures to produce better agreement with the observations. The second test involved reducing the value of z_0 from 3x10^{-3} m to 5x10^{-4} m, where $z_t = z_q = z_0/10$. The model produced values for the transfer coefficient for momentum that were very similar to those computed from the observations. There was also a small improvement in the modelled sensible and latent heat fluxes, although the magnitude of the modelled values remained much larger than the observations. The final sensitivity test involved running a version of the MetUM with 70 vertical levels, where the increase in resolution is in the lower atmosphere. This test produced significant improvements to boundary-layer depth. Improvements to the representation of the cloud layer also occurred because the increased resolution enabled the cloud to become decoupled from the surface more frequently.

A principle motivation for this study was to improve climate predictions of the Arctic region. The operational NWP version of the model is used as a method of ascribing errors in the physical parameterisation at the scale of individual weather systems. This would be extremely challenging in a climate model because errors in the large-scale circulation are not minimised through data assimilation. Since the physical parameterisations used in both the operational numerical weather prediction version of the MetUM and HadGEM1 are very similar, potential biases in climate simulations by HadGEM1 can be inferred from the evaluation of the operational NWP forecasts. The final section of the analysis compared data from HadGEM1 with the AOE 2001 and ASCOS observations. Although comparisons between a short data set and a climate model were difficult there are indications that the same errors caused by the albedo parameterisation and the bulk flux parameterisation scheme also exist in the climate version of the model. The consequences of this on climate predictions are uncertain from this analysis but warrants further investigation.

7.2 Recommendations

This study has highlighted a number of key errors in the Met Office Unified Model's representation of the central Arctic Ocean during the late summer and early freeze-up period. This section outlines improvements that could be implemented into the MetUM

reasonably easily and then suggests areas of further research that would lead to more significant improvements to the model.

7.2.1 Changes to the MetUM

- The value of z_0 used in the MetUM could be decreased to 5x10^{-4} m, at least during the summer months at latitudes with 80 to 100 % sea ice fraction. In reality the values of the roughness lengths are not constant in time or space over sea ice and therefore, a better solution would be to incorporate a parameterisation for z_0 that was developed from observations specifically for use over sea ice, such as that by Andreas *et al.* (2009).

- The minimum albedo in the temperature-dependent albedo parameterisation could be increased from 0.5 to between 0.6 and 0.7. This will reduce model bias in the surface radiation fluxes, surface temperature and near-surface air temperature. HadGEM1 incorporates a slightly different parameterisation to that in the NWP version of the MetUM that includes a snow depth dependency. This scheme could easily be implemented into the operational version of the MetUM. Prognostic schemes with a decay factor for the albedo of melting/ageing snow have been shown to perform better than temperature-dependent schemes. Incorporating a scheme such as this into the model would be beneficial. The ideal solution would be to implement a more sophisticated scheme that is based on observations, such as that by Bromwich *et al.* (2009), which has been shown to perform well in the Polar Weather Research and Forecasting (WRF) model.

- Increasing the vertical model resolution from 50 to 70 levels will reduce boundary-layer depth and help cloud layers to become decoupled from the surface. Adding one or more vertical levels between the surface and the first model level may also improve model performance. This level is more likely to be within the surface layer and increased resolution very close to the surface may help to produce a shallow boundary layer and improve the representation of low-level Arctic cloud layers.

- Creating a new boundary-layer type to represent summer Arctic low-level cloud is likely to improve the model's performance.

7.2.2 Suggestions for future research

- More detailed investigation into the problems highlighted in the forecast-assimilation cycle in the operational version of the MetUM. The operational forecasts could be improved by the assimilation of more in-situ observations. This would involve the

deployment of buoys or semi-permanent observation stations in the central Arctic region, which would be costly. This data could however, also be used for long term climate monitoring, which would make the expense more worthwhile.

- The results from this study suggest that Monin-Obukhov similarity theory is often not valid at heights of only a few metres above the surface under the conditions observed during AOE 2001 and ASCOS. This is one reason why the MetUM overestimates the turbulent surface fluxes and could be tested by performing a sensitivity test with a version of the MetUM with a lower first model level.

- The conclusions made about the validity of Monin-Obukhov similarity theory over the region could be reinforced by comparing the results of the spectral analysis with a similar analysis of the turbulence measurements made during the SHEBA experiment.

- A more detailed evaluation of the representation of cloud microphysical and radiative properties over the Arctic in the MetUM. There is a wealth of remote sensing, aerosol and meteorological data available from the ASCOS field campaign to allow this type of analysis. Simulations of Arctic clouds using the Met Office Large Eddy Model (LEM) would also be beneficial. This is being pursued as a PhD project by Thomas Pleavin at the University of Leeds.

- Further analysis of the climate version of the Met Office Unified Model. There is a need to assess in more detail whether the same errors found in the global NWP version in this study also occur in the climate version. A new version of the climate model (HadGEM3) is in development; it incorporates CICE, the Los Alamos sea ice model (Hunke & Lipscomb, 2004). This model includes a more sophisticated albedo scheme that is based on observations from the SHEBA experiment. It considers shortwave radiation in two spectral bands (visible and infra-red) and has an ice thickness, temperature and snow depth dependency. The SHEBA data set could be used along with the AOE 2001 and ASCOS observations to extend the evaluation of the climate model over more of the summer season and to provide contrasting observations at a different latitudes.

- A future expedition to the central Arctic for an extended period during the summer months is recommended. A longer, more extensive turbulence data set could be obtained, that includes latent heat measurements up to 30 m. The use of sonic anemometers with heated sensor heads is recommended to reduce the amount of data lost through icing problems. Adding a heat source to the Licor open path H_2O and CO_2 analyzer sensors could also be considered. This more extensive data set could then be used to calculate values of z_t and z_q, which the limited data set obtained during ASCOS could not provide.

- Model cycle G50, which has 70 vertical levels, became operational in November 2009. The Met Office should evaluate subsequent model developments such as this against the AOE 2001 and ASCOS data sets.

References

Alexander, M.A., Bhatt, U.S., Walsh, J.E., Timlin, M. & Miller, J.S. (2004). The atmospheric response to realistic Arctic sea ice anomalies in an AGCM during winter,. *Journal of Climate*, **17**, 890905.

Allan, R., Slingo, A., Milton, S. & Brooks, M. (2007). Evaluation of the Met Office global forecast model using geostationary earth radiation budget (GERB) data. *Quarterly Journal of the Royal Meteorological Society*, **133**, 1993–2010.

Anderson, D.E. (1987). Wind stress measurements over rough ice during the 1984 marginal ice zone experiment. *Journal of Geophysical Research*, **92**, 6933–6941.

Andreas, E.L. (1987). A theory for the scalar roughness and the scalar transfer coefficients over snow and sea ice. *Boundary-Layer Meteorology*, **38**, 159–184.

Andreas, E.L. & Claffey, K.J. (1995). Air-ice drag coefficients in the Western Weddell Sea: 1. Values deduced from profile measurements. *Journal of Geophysical Research*, **100**, 4821–4831.

Andreas, E.L. & Hicks, B.B. (2002). Comments of critical test of the validity of Monin-Obukhov similarity during convective conditions. *Journal of the Atmospheric Sciences*, **59**, 2605–2607.

Andreas, E.L., Tucker III, W.B. & Ackley, S.F. (1984). Atmospheric boundary-layer modification, drag coefficient, and surface heat flux in the Antarctic marginal ice zone. *Journal of Geophysical Research*, **89**, 649–661.

Andreas, E.L., Jordan, R. & Makshtas, A. (2005). Parameterizing turbulent exchange over sea ice: The Ice Station Weddell results. *Boundary-Layer Meteorology*, **114**, 439–460.

Andreas, E.L., Persson, P.O.G., Grachev, A.A., Jordan, R.E., Guest, P.S., Fairall, C.W., Horst, T.W. & Bao, J.W. (2009). *Announcing the SHEBA bulk turbulent flux algorithm*. 10th Conference on Polar Meteorology and Oceanography, American Meteorological Society, 18-21 May 2009, Madison, WI, USA.

Andreas, E.L., Persson, P.O.G., Jordan, R., Horst, T.W., Guest, P.S., Grachev, A.A. & Fairall, C.W. (2010). Parameterizing turbulent exchange over sea ice in winter. *Journal of Hydrometeorology*, **11**, 87–104.

Arrigo, K.R., van Dijken, G. & Pabi, S. (2008). Impact of a shrinking Arctic ice cover on marine primary production. *Geophysical Research Letters*, **35**, L19603, doi:10.1029/2008GL035028.

Arya, S.P.S. & Sundararajan, S. (1976). An assessment of proposed similarity theories for the atmospheric boundary layer. *Boundary-Layer Meteorology*, **10**, 149–166.

Arzel, O., Fichefet, T. & Goosse, H. (2006). Sea ice evolution over the 20th and 21st centuries as simulated by current AOGCMs. *Ocean Modelling*, **12**, 401–415.

Beesley, J.A., Bretherton, C.S., Jakob, C., Andreas, E., Intrieri, J.M. & Uttal, T.A. (2000). A comparison of cloud and boundary layer variables in the ECMWF forecast model with observations at Surface Heat Budget of the Arctic Ocean (SHEBA) ice camp. *Journal of Geophysical Research*, **105**, 12,337–12,349.

Beljaars, A.C.M. & Holtslag, A.A.M. (1991). Flux parameterization over land surfaces for atmospheric models. *Journal of Applied Meteorology*, **30**, 327–341.

Bhatt, U.S., Alexander, M.A., Deser, C., Walsh, J.E., Miller, J.S., Timlin, M.S., Scott, J.D. & Tomas, R.A. (2008). The atmospheric response to realistic reduced summer Arctic sea ice anomalies, in Arctic sea ice decline: Observations, projections, mechanisms, and implications. *Geophysical Monograph Series*, **180**.

Bigg, E. (1996). Ice forming nuclei in the high Arctic. *Tellus*, **48**, 223–233.

Birnbaum, G. & Lüpkes, C. (2002). A new parameterization of surface drag in the marginal sea ice zone. *Tellus*, **54A**, 107–123.

Bolton, D. (1980). The computation of equivalent potential temperature. *Monthly Weather Review*, **108**, 1046–1053.

Bromwich, D.H., Hines, K.M. & Bai, L. (2009). Development and testing of Polar Weather Research and Forecasting model: 2. Arctic Ocean. *Journal of Geophysical Research*, **114**, D08122, doi:10.1029/2008JD010300.

Brunke, M., Zhou, J., Zeng, X. & Andreas, E. (2006). An intercomparision of bulk aerodynamic algorithms used over sea ice with data from the Surface Heat Budget of the Arctic Ocean (SHEBA) experiment. *Journal of Geophysical Research*, **111**, C09001, doi:10.1029/2005JC002907.

Bryan, K. (1969). A numerical method for the study of the circulation of the world ocean. *Journal of Computational Physics*, **4**, 347–376.

Businger, J.A., Wyngaard, J.C., Izumi, Y. & Bradley, E.F. (1971). Flux-profile relationships in the atmospheric surface layer. *Journal of the Atmospheric Sciences*, **28**, 181–189.

Campbell Scientific Inc (2009). *Instruction manual: CSAT3 Three dimensional sonic anemometer*, Logan, Utah, USA.

Chapman, W.L. & Walsh, J.E. (2007). Simulations of Arctic temperature and pressure by global coupled models. *Journal of Climate*, **20**, 609–632.

Chen, B., Bromwich, D.H., Hines, K.M. & Pan, X. (1995). Simulations of the 1979-1988 polar climates by global models. *Annals of Glaciology*, **21**, 85–90.

Cogley, J.G. (1979). The albedo of water as a function of latitude. *Monthly Weather Review*, **107**, 775–781.

Comiso, J.C., Parkinson, C.L., Gersten, R. & Stock, L. (2008). Accelerated decline in the Arctic sea ice cover. *Geophysical Research Letters*, **35**, L01703, doi:10.1029/2007GL031972.

Comstock, K.K., Bretherton, C.S. & Yuter, S.E. (2005). Mesoscale variability and drizzle in southeast Pacific stratocumulus. *Journal of the Atmospheric Sciences*, **62**, 3792–3807.

Covert, D.S., Wiedensohler, A., Aalto, P.P., Heintzenberg, J., McMurry, P.H. & Leck, C. (1996). Aerosol number size distributions from 3 to 500nm diameter in the arctic marine boundary layer during summer and autumn. *Tellus*, **48B**, 197–212.

Cox, M.D. (1984). A primitive equation, three dimensional model of the ocean. Tech. rep., Ocean Group Tech, Rep. 1, GFDL, Princeton, NJ, USA, 143 pp.

Cox, P.M., Betts, R.A., Bunton, C.B., Essery, L.H., Rowntree, P.R. & Smith, J. (1999). The impact of new land surface physics on the GCM simulation of climate and climate sensitivity. *Climate Dynamics*, **15**, 183–203.

Cullen, M.J.P. & Davies, T. (1991). A conservative split-explicit integration scheme with fourth order horizontal advection. *Quarterly Journal of the Royal Meteorological Society*, **117**, 993–1002.

Curry, J., Rossow, W., Randall, D. & Schramm, J. (1996). Overview of Arctic cloud and radiation characteristics. *Journal of Climate*, **9**, 1731–1764.

Curry, J., Schramm, J., Perovich, D.K. & Pinto, J.O. (2001). Applications for SHEBA/FIRE data to evaluation of snow/ice albedo parameterizations. *Journal of Geophysical Research*, **106**, 15,345–15,355.

Curry, J.A. & Ebert, E.E. (1992). Annual cycle of radiation fluxes over the Arctic Ocean: Sensitivity to cloud optical properties. *Journal of Climate*, **5**, 1267–1280.

Curry, J.A. & Herman, G.F. (1985a). Infrared radiative properties of summertime Arctic stratus clouds. *Journal of Climate and Applied Meteorology*, **24**, 526–538.

Curry, J.A. & Herman, G.F. (1985b). Relationship between large-scale heat and moisture budgets and the occurrence of Arctic stratus clouds. *Monthly Weather Review*, **113**, 2234–2253.

Curry, J.A., Meyer, F.G., F., R.L., Brock, C.A. & Ebert, E.E. (1990). Occurrence and characteristics of lower tropospheric ice crystals in the Arctic. *International Journal of Climatology*, **10**, 749–764.

Curry, J.A., Pinto, J.O., Benner, T. & Tschudi, M. (1997). Evolution of the cloudy boundary layer during the autumnal freezing of the Beaufort Sea. *Journal of Geophysical Research*, **102**, 13,851–13,860.

Curry, J.A., Hobbs, P.V., King, M., Randall, D., Minnis, P., Isaac, G., Pinto, J.O., Uttal, T., Bucholtz, A., Cripe, D.G., Gerber, H., Fairall, C.W., Garrett, T., Hudson, J., Intrieri, J.M., Jakob, C., Jensen, T., Lawson, P., Marcotte, D., Nguyen, L., Pilewskie, P., Rangno, A., Rogers, D.C., Strawbridge, K.B., Valero, F.P.J., Williams, A.G. & Wylie, D.P. (2000). FIRE Arctic Clouds Experiment. *Bulletin of the American Meteorological Society*, **81**, 5–29.

Davies, T., Cullen, M.J.P., Malcolm, A.J., Mawson, M.H., Staniforth, A., White, A.A. & Wood, S. (2005). A new dynamical core for the Met Office's global and regional modelling of the atmosphere. *Quarterly Journal of the Royal Meteorological Society*, **131**, 1759–1782.

Deardorff, J.W. (1970). Convective velocity and temperature scales for the unstable planetary boundary layer and for Rayleigh convection. *Journal of the Atmospheric Sciences*, **27**, 1211–1213.

DeCosmo, J., Katsaros, K.B., Smith, S.D., Anderson, R.J., Oost, W.A., Bumke, K. & Chadwick, H. (1996). Air-sea exchange over water vapor and sensible heat: The humidity exchange over the sea (HEXOS) results. *Journal of Geophysical Research*, **101**, 12,001–12,016.

Deser, C. & Teng, H. (2008). Evolution of Arctic sea ice concentration trends and the role of atmospheric circulation forcing, 1979-2007. *Geophysical Research Letters*, **35**, L02504, doi:10.1029/2007GL032023.

Deser, C., Thomas, R.A. & Peng, A. (2007). The transient atmospheric circulation response to Northern Atlantic SST and sea ice anomalies. *Journal of Climate*, **20**, 4751 4767.

Duynkerke, P.G. & Coauthors (2004). Observations and numerical simulations of the diurnal cycle of the EUROCS stratocumulus case. *Quarterly Journal of the Royal Meteorological Society*, **130**, 3269–3296.

Dyer, A.J. (1974). A review of flux-profile relationships. *Boundary-Layer Meteorology*, **7**, 363–372.

Dyer, A.J. & Bradley, E.F. (1982). An alternative analysis of the flux-gradient relationships in the 1976 ITCE. *Boundary-Layer Meteorology*, **22**, 2–19.

Edwards, J.M. & Slingo, A. (1996). Studies with a flexible new radiation code. I: Choosing a configuration for a large-scale model. *Quarterly Journal of the Royal Meteorological Society*, **122**, 689–719.

Essery, R.L.H., Best, M.J. & Cox, P.M. (2001). MOSES 2.2 technical documentation. Tech. rep., Met Office, 14 August 2001.

Fairall, C.W., Bradley, E.F., Roger, D.P., Edson, J.B. & Young, G.S. (1996). Bulk parameterization of air-sea fluxes for tropical ocean-global atmospheric coupled-ocean atmospheric response experiment. *Journal Geophysical Research*, **101**, 3747–3764.

Finkelstein, P.L. & Sims, P.F. (2001). Sampling error in eddy correlation flux measurements. *Journal of Geophysical Research*, **106**, 3503–3509.

Fitzpatrick, M.F., Brandt, R.E. & Warren, S.G. (2004). Transmission of solar radiation by clouds over snow and ice surfaces: A parameterization in terms of optical depth, solar zenith angle, and surface albedo. *Journal of Climate*, **17**, 266–275.

Fletcher, N.H. (1962). *The physics of rainclouds*. Cambridge University Press, Cambridge, UK.

Francis, J.A., Chan, W., Leathers, D.J., Miller, J.R. & Veron, D.E. (2009). Winter Northern Hemisphere weather patterns remember summer Arctic sea-ice extent. *Geophysical Research Letters*, **36**, L07503, doi:10.1020/2009GL037274.

Friehe, C.A., Shaw, W.J., Rodger, D.P., Davidson, K.L., Large, W.G., Stage, S., Crescenti, G.H., Khalsa, J.S., Greenhut, G.K. & Li, F. (1991). Air-sea fluxes and surface layer turbulence around a sea surface temperature front. *Journal of Geophysical Research*, **96**, 8593–8609.

Garratt, J.R. (1992). *The atmospheric boundary layer*. Cambridge University Press, Cambridge, UK, 1st edn.

Gayet, J.F., Asano, S., Yamazaki, A., Uchiyama, A., Sinyuk, A., Jourdan, O. & Auriol, F. (2002). Two case studies of winter continental-type water and mixed-phase stratocumuli over the sea. 1. microphysical and optical properties. *Journal of Geophysical Research*, **107**, D21 4569, doi:10.1029/2001JD001106.

Glickman, T.S. (2000). *Glossary of Meteorology*. American Meteorological Society, Boston, USA.

Gorodetskaya, I.V., Tremblay, L.B., Liepert, B., Cane, M.A. & Cullather, R.I. (2008). The influence of cloud and surface properties on the Arctic Ocean short-wave radiation budget in coupled models. *Journal of Climate*, **21**, 866–882.

Grachev, A.A., Fairall, C.W., Persson, P.O.G., Andreas, E.L. & Guest, P.S. (2005). Stable boundary-layer scaling regimes: The SHEBA data. *Boundary-Layer Meteorology*, **116**, 201–235.

Grachev, A.A., Andreas, E.L., Fairall, C.W., Guest, P.S. & Persson, O.G. (2007). SHEBA flux-profile relationships in the stable atmospheric boundary layer. *Boundary-Layer Meteorology*, **124**, 315–463.

Graversen, R. (2006). Do changes in the midlatitude circulation have any impact on the Arctic surface air temperature trend? *Journal of Climate*, **19**, 5422–5438.

Guest, P.S. & Davidson, K.L. (1987). The effect of observed ice conditions on the drag coefficient in the summer East Greenland Sea marginal ice zone. *Journal of Geophysical Research*, **92**, 6943–6954.

Guest, P.S. & Davidson, K.L. (1991). The aerodynamic roughness of different types of sea ice. *Journal of Geophysical Research*, **96**, 4709–4721.

Gultepe, I., Isaac, G., Hudak, D., Nissen, R. & Strapp, J.W. (2000). Dynamical and microphysical characteristics of Arctic clouds during BASE. *Journal of Climate*, **13**, 1225–1254.

Harrington, J.Y. & Olssin, P.Q. (2001). A method for the parameterization of cloud optical properties in bulk and bin microphysical models. implications for Arctic cloudy boundary layers. *Atmospheric Research*, **57**, 51–80.

Harrison, E.F., Minnis, P., Barkstrom, B., Ramanathan, V., Cess, R. & Gibson, G. (1990). Seasonal variations of cloud radiative forcing derived from the Earth Radiation Budget Experiment. *Journal of Geophysical Research*, **95**, 18,687–18,703.

Harshvardhan, Davies, R., Randall, D. & Corsetti, T. (1987). A fast radiation parameterization for atmospheric circulation models. *Journal of Geophysical Research*, **92**, 1009–1060.

Haugen, D.A., Kaimal, J.C. & Bradley, E.F. (1971). An experimental strudy of reynolds stress and heat flux in the atmospheric surface layer. *Quarterly Journal of the Royal Meteorological Society*, **97**, 168–180.

Herman, G.F. & Curry, J.A. (1984). Observational and theoretical studies of solar radiation in Arctic stratus clouds. *Journal of Climate and Applied Meteorology*, **23**, 5–24.

Hicks, B.B. (1976). Wind profile relationships from 'Wangara' experiments. *Quarterly Journal of the Royal Meteorological Society*, **102**, 535–551.

Hill, M.K., Brooks, B.J., Norris, S.J., Smith, M.H. & Brooks, I.M. (2008). A compact lightweight aerosol spectrometer probe (CLASP). *Journal of Atmospheric and Oceanic Technology*, **25**, 1996–2006.

Hinzman, L.D.e.a. (2005). Evidence and implications of recent climate change in northern alaska and other arctic regions. *Climate Change*, **72**, 251 298, doi:10.1007/s10584–005–5352–2.

Hodur, R.M. (1997). The Naval Research Laboratory's Coupled Ocean/Atmosphere Mesoscale Prediction System (COAMPS). *Monthly Weather Review*, **125**, 1414–1430.

Holland, M.M. & Bitz, C.M. (2003). Polar amplification of climate change in coupled models. *Climate Dynamics*, **21**, 221–232.

Holland, M.M., Bitz, C.M. & Tremblay, L. (2006). Future abrupt reductions in the summer Arctic sea ice. *Geophysical Research Letters*, **22**, L23503, doi:10.1029/2006GL028024.

Holtslag, A.A.M. & De Bruin, H.A.R. (1988). Applied modeling of the nighttime surface energy balance over land. *Journal of Applied Meteorology*, **27**, 689–704.

Holtslag, A.A.M. & Duynkerke, P.G. (1998). *Clear and Cloudy Boundary Layers*. Proceedings of the colloquium 'Clear and Cloudy Boundary Layers', 26-29 August 1998, Amsterdam, The Netherlands.

Honda, M., Inoue, J. & Yamane, S. (2009). Influence of low Arctic sea-ice minima on anomalously cold Eurasian winters. *Geophysical Research Letters*, **36**, L08707, doi:10.1029/2008GL037079.

Horst, T.W. & Weil, J.C. (1992). Footprint estimation for scalar flux measurements in the atmospheric surface layer. *Boundary-Layer Meteorology*, **59**, 279–296.

Howell, J.F. & Sun, J. (1999). Surface-layer fluxes in stable conditions. *Boundary-Layer Meteorology*, **90**, 495–520.

Hunke, E.C. & Dukowicz, J.K. (1997). An alastix-viscous-plastic model for sea ice dynamics. *Journal of Physical Oceanography*, **27**, 1849–1867.

Hunke, E.C. & Lipscomb, W.H. (2004). The Los Alamos sea ice model, documentation and software. Tech. rep., Version 3.1, LA-CC-98-16. Los Alamos National Laboratory, Los Alamos, NM, 56 pp.

Ingram, W.J., Wilson, C.A. & Mitchell, J.F.B. (1989). Modeling climate change: An assessment of sea ice and surface albedo feedbacks. *Journal of Geophysical Research*, **94**, 8609–8622.

Inoue, J., Liu, J., Pinto, J.O. & Curry, J.A. (2006). Intercomparison of Arctic regional climate models: Modeling cloud and radiation for SHEBA in May 1998. *Journal of Climate*, **19**, 4167–4178.

Intrieri, J., Fairall, C.W., Shupe, M., Persson, P., Andreas, E., Guest, P. & Moritz, R. (2002). An annual cycle of Arctic surface cloud forcing at SHEBA. *Journal of Geophysical Research*, **107**, C19, 8039, doi:10.1029/2000JC000439.

Jiang, H. & Cotton, W.R. (2000). Cloud resolving simulations of mixed-phase Arctic stratus observed during BASE: Sensitivity to concentration of ice crystals and large-scale heat and moisture advection. *Journal of the Atmospheric Sciences*, **57**, 2105–2117.

Johns, T.C., Durman, C.F. & coauthors (2006). The new Hadley Centre Climate Model (HadGEM1): Evaluation of coupled simulations. *Journal of Climate*, **19**, 1327–1353.

Jorgenson, M.T., Shur, Y.L. & Pullman, E.R. (2006). Abrupt increase in permafrost degradation in Arctic Alaska. *Geophysical Research Letters*, **25**, L02503, doi:10.1029/2005GL024960.

Kaimal, J. & Finnigan, J. (1994). *Atmospheric Boundary Layer Flows. Their Structure and Measurement*. Oxford University Press, New York.

Kaimal, J.C. & Haugen, D.A. (1969). Some errors in the measurement of Reynolds stress. *Journal of Applied Meteorology*, **8**, 460–462.

Kaimal, J.C., Wyngaard, J.C., Izumi, Y.I. & Coté, O.R. (1972). Spectral characteristics of surface-layer turbulence. *Quarterly Journal of the Royal Meteorological Society*, **98**, 563–589.

Kay, J.E., L'Ecuyer, T., Gettelman, A., Stephens, G. & O'Dell, C. (2008). The contribution of cloud and radiation anomalies to the 2007 Arctic sea ice extent minimum. *Geophysical Research Letters*, **35**, L08503, doi:10.1029/2008GL033451.

Kessler, E. (1969). On the distribution and continuity of water substance in atmospheric circulations. *Meteorological Monogram*, **32**, 82–84.

Klein, S.A., McCoy, R.B. & coauthors (2009). Intercomparison of model simulations of mixed-phase clouds observed during the ARM Mixed-Phase Arctic Cloud Experiment. i: Single-layer cloud. *Quarterly Journal of the Royal Meteorological Society*, **135**, 979–1002.

Kolmogorov, A.N. (1941). The local structure of turbulence in incompressible viscous fluid for very lager Reynolds numbers. *Dokladt ANSSSR*, **30**, 301–304.

Koltzow, M. (2007). The effect of a new snow and sea ice albedo scheme on regional climate model simulations. *Journal of Geophysical Research*, **112**, D07110, doi:10.1029/2006JD007693.

Kwok, R. (2008). Summer sea ice motion from the 18 GHz channel of AMSR-E and the exchange of sea ice between the Pacific and Atlantic sectors. *Geophysical Research Letters*, **35**, L03504, doi:10.1029/2007GL032692.

Large, W.G. & Pond, S. (1982). Sensible and latent heat flux measurements over the ocean. *Journal of Physical Oceanography*, **12**, 464–482.

Lawrence, D.M., Slater, A.G., Tomas, R.A., Holland, M.M. & Deser, C. (2008). Accelerated Arctic land warming and permafrost degradation during rapid sea ice loss. *Geophysical Research Letters*, **35**, L11506, doi:10.1029/2008GL033985.

Leck, C., Bigg, E.K., Covert, D.S., Heintzenberg, J., Maenhaut, W., Nilsson, E.D. & Wiedensohler, A. (1996). Overview of the atmospheric research program during the International Arctic Ocean Expedition of 1991 (IAOE-91) and its scientific results. *Tellus*, **48B**, 136–155.

Leck, C., Nilsson, E., Bigg, E. & Bäcklin, L. (2001). Atmospheric program on the Arctic Ocean Expedition 1996 (AOE-96): An overview of scientific goals, experimental approach, and instruments. *Journal of Geophysical Research*, **106**, 32,051–32,067.

Leifer, I., de Leeuw, G. & Cohen, L.H. (2002). Optical measurement of bubbles: System design and application. *Journal of Atmospheric and Oceanic Technology*, **20**, 1317–1332.

Lin, Y.L., Farley, R.D. & Orville, H.D. (1983). Bulk parameterization of the snow field in a cloud model. *Journal of Climate and Applied Meteorology*, **22**, 1065–1092.

Lindsay, R.W., Zhang, J., Schweiger, A., Steele, M. & Stern, H. (2009). Arctic sea ice retreat in 2007 follows thinning trend. *Journal of Climate*, **22**, 165–176.

Lipscomb, W.H. (2001). Remapping the thickness distribution in sea ice models. *Journal of Geophysical Research*, **106**, 13,989 – 14,000.

Liu, J., Zhang, Z., Hu, Y., Chen, L., Dai, Y. & Ren, X. (2008). Assessment of surface air temperature over the Arctic Ocean in reanalysis and IPCC AR4 model simulations with IABP/POLES observations. *Journal of Geophysical Research*, **113**, D10105, doi:10.1029/2007JD009380.

Lock, A.P., Brown, A.R., Bush, M.R., Martin, G.M. & Smith, R.N.B. (2000). A new boundary layer mixing scheme. part i: Scheme description and single-column model tests. *Monthly Weather Review*, **128**, 3187–3199.

Lorenc, A.C., Ballard, S.P., Bell, R.S., Ingleby, N.B., Andrews, P.L.F., Barker, D.M., Bray, J.R., Clayton, A.M., Dalby, T.D., Dingmin, L., Payne, T.J. & Saunders, F.W. (2000). The Met Office global three-dimensional variational data assimilation scheme. *Quarterly Journal of the Royal Meteorological Society*, **126**, 2991–3012.

Louis, J.F. (1979). A parametric model of vertical eddy fluxes in the atmosphere. *Boundary-Layer Meteorology*, **17**, 187–202.

Mahrt, L. (1998). Stratified atmospheric boundary layers and breakdown of models. *Theoretical and Computational Fluid Dynamics*, **11**, 263–279.

Mahrt, L. (2007). The influence of nonstationarity on the turbulent flux-gradient relationship for stable stratification. *Boundary-Layer Meteorology*, **125**, 245–264.

Mahrt, L. & Vickers, D. (2006). Extremely weak mixing in stable conditions. *Boundary-Layer Meteorology*, **119**, 19–39.

Makshtas, A., Atkinson, D., Kulakov, M., S., S., Krishfield, R. & Proshutinsky, A. (2007). Atmospheric forcing validation for modeling the central Arctic. *Geophysical Research Letters*, **34**, L20706, doi:10.1029/2007GL031378.

Marshall, J.S. & Palmer, W.M. (1948). The distribution of raindrops with size. *Journal of Meteorology*, **5**, 165–166.

Martin, G.M., Ringer, M.A., Pope, V.D., Jones, A., Dearden, C. & Hinton, T.J. (2006). The physical properties of the atmosphere in the new Hadley Centre Global Environment Model, HadGEM1. Part I: Model description and global climatology. *Journal of Climate*, **19**, 1274–1301.

Maslanik, J.A., Fowler, A., Stroeve, J., Drobot, S., Zwally, J., Yi, D. & Emery, W. (2007). A younger, thinner Arctic ice cover: Increased potential for rapid, extensive sea-ice loss. *Geophysical Research Letters*, **34**, L24501, doi:10.1029/2007GL032043.

McGrath, R. (1989). Trajectory models and their use in the Irish Meteorological Service. In *Memorandum No. 112/89*, 12, Irish Meteorological Service, Dublin, Ireland.

McLaren, A.J., Banks, H.T., Durman, C.F., Gregory, J.M., Johns, T.C., Keen, A.B., Ridley, J.K., Roberts, M.J., Lipscomb, W.H., Connolley, W.M. & Laxon, S.W. (2006). Evaluation of the sea ice simulation in a new coupled atmosphere-ocean climate model (HadGEM1). *Journal of Geophysical Research*, **11**, C12014, doi:10.1029/2005JC003033.

Mellor, G.L. & Yamada, T. (1974). Development of a turbulence closure for geophysical problems. *Geophysics and Space Physics*, **20**, 851–875.

Monin, A.S. & Obukhov, A.M. (1954). Basic laws of turbulent mixing in the atmosphere near the ground. *Tr. Akad. Nauk SSSR, Geofiz. Inst.*, **151**, 163–187.

Monin, A.S. & Yaglom, A.M. (1971). *Statistical fluid mechanics*. MIT Press, vol. 1 edn.

Morrison, H. & Pinto, J.O. (2006). Intercomparison of bulk cloud microphysics schemes in mesoscale simulations of springtime Arctic mixed-phase stratiform clouds. *Monthly Weather Review*, **134**, 1880–1900.

Morrison, H., Shupe, M.D., Pinto, J.O. & Curry, J. (2005). Possible roles of ice nucleation mode and ice nuclei depletion in the extended lifetime of Arctic mixed-phase clouds. *Geophysical Research Letters*, **32**, L18801, doi:10.1029/2005GL023614.

Morrison, H., McCoy, R.B. & coauthors (2009). Intercomparison of model simulations of mixed-phase clouds observed during the ARM Mixed-Phase Arctic Cloud Experiment. i: Multilayer cloud. *Quarterly Journal of the Royal Meteorological Society*, **135**, 1003–1019.

Nghiem, S.V., Rigor, I.G., Perovich, D.K., Clemente-Colón, P. & Weatherly, J.W. (2007). Rapid reduction of Arctic perennial sea ice. *Geophysical Research Letters*, **34**, L19504, doi:10.1029/2007GL031138.

Nieuwstadt, F.T.M. (1984). The turbulent structure of the stable, nocturnal boundary layer. *Journal of the Atmospheric Sciences*, **41**, 2202–2216.

Nilsson, E. & Bigg, E. (1996). Influences on the formation and dissipation of high Arctic fogs during summer and autumn and their interactions with aerosol. *Tellus Series B - Chemical and Physical Meteorology*, **48**, 234–253.

Nilsson, E., Rannik, U. & Håkansson, M. (2001). Surface energy budget over the central Arctic Ocean during late summer and early freeze-up. *Journal of Geophysical Research*, **106**, 32,187–32,205.

NRL (2003). *COAMPS: Version 3 model description. General Theory and Equations*. Naval Research Laboratory, Marine Meteorology Division, Monterey, California, nrl/pu/7500–03-448 edn.

NSIDC (2009). *All about sea ice: Characteristics: Arctic vs. Antarctic*, National Snow and Ice Data Center, University of Colorado, Boulder, USA. http://nsidc.org/seaice/characteristics/difference.html.

Obukhov, A.M. (1946). Turbulence in an atmosphere with a non-uniform temperature. *Tr. Akad. Nauk SSSR. Inst. Teoret. Geofiz (Engl. transl. in Boundary-Layer Meteorology (1971), 2, 7-29)*.

Ortega-Farias, S.O., Cuenca, R.H. & M., E. (1996). Daytime variation of sensible heat flux estimated by the bulk aerodynamic method over a grass canopy. *Agricultural and Forest Meteorology*, **81**, 131–143.

Overland, J.E. (1985). Atmospheric boundary layer structure and drag coefficients over sea ice. *Journal of Geophysical Research*, **90**, 9029–9049.

Parkinson, C.L. & Cavalieri, D.J. (2008). Arctic sea ice variability and trend, 1979-2006. *Journal of Geophysical Research*, **113**.

Parkinson, C.L., Cavalieri, D.J., Gloerson, P., Zwally, H.J. & Comiso, J.C. (1999). Arctic sea ice extents, areas and trends. *Journal of Geophysical Research*, **104**, 20,837–20,856.

Pedersen, C.A. & Winther, J.G. (2005). Intercomparison and validation of snow albedo parameterization schemes in climate models. *Climate Dynamics*, **25**, 351–362.

Pedersen, C.A., Roeckner, E., Lüthje, M. & Winther, J.G. (2009). A new sea ice albedo scheme including melt ponds for ECHAM5 general circulation model. *Journal of Geophysical Research*, **114**, D08101, doi:10.1029/2008JD010440.

Perovich, D.K., Grenfell, T.C., Light, B. & Hobbs, P.V. (2002a). Seasonal evolution of the albedo of multiyear Arctic sea ice. *Journal of Geophysical Research*, **107**, C10, 8044, doi:10.1029/2000JC000438.

Perovich, D.K., Tucker III, W.B. & Ligett, K.A. (2002b). Aerial observations of the evolution of ice surface conditions during summer. *Journal of Geophysical Research*, **107**, C10, 8048, doi:10.1029/2000JC000449.

Perovich, D.K., Nghiem, S.V., Markus, t. & Schweiger, A. (2007). Seasonal evolution and interannual variability of the local solar energy absorbed by the arctic sea ice-ocean system. *Journal of Geophysical Research*, **112**, C03005, doi:10.1029/2006JC003558.

Persson, O.G., Bao, J.W. & Michelson, S. (2002a). *Mesoscale modeling of the Wintertime Boundary Layer Structure over th e Arctic Pack Ice*. 15th Symposium on Boundary Layers and Turbulence, American Meteorological Society, 15-19 June 2002, Wageningen, The Netherlands.

Persson, P., Fairall, C.W., Andreas, E., Guest, P. & Perovich, D. (2002b). Measurements near the atmospheric surface flux group tower at SHEBA: Near-surface conditions and surface energy budget. *Journal of Geophysical Research*, **107**, C10, 8045, doi:10.1029/2000JC000705.

Phillips, T.J., Potter, G.L., Williamson, D.L., Cederwall, R.T., Boyle, J.S., Fiorino, M., Hnilo, J.J., Olson, J.G., Xie, S. & Yio, J. (2004). Evaluating parameterizations in general circulation models. *Bulletin of the American Meteorological Society*, **85**, 1903–1915.

Pinto, J.O. (1998). Autumnal mixed-phase cloudy boundary-layers in the Arctic. *Journal of the Atmospheric Sciences*, **55**, 2016–2038.

Pope, V.D., Gallani, M.L., Rowntree, P.R. & Stratton, R.A. (2000). The impact of new physical parameterizations in the Hadley Centre climate model - HadAM3. *Climate Dynamics*, **16**, 123–146.

Prenni, A.J., Harrington, J.Y., Tjernström, M., DeMott, P.J., Avramov, A., Long, C.N., Kreidenweiss, S.M., Olsson, P.Q. & Verlinde, J. (2007). Can ice-nucleating aerosols affect arctic seasonal climate? *Bulletin of the American Meteorological Society*, **88**, 541–550.

Rawlins, F., Ballard, S.P., Bovis, K.J., Clayton, A.M., Li, D., Inverarity, G.W., Lorenc, A.C. & Payne, T.J. (2007). The Met Office global 4-dimensional variational data assimilation scheme. *Quarterly Journal of the Royal Meteorological Society*, **133**, 347–362.

Rigor, I.G. & Wallace, J.M. (2004). Variations in the age of Arctic sea-ice and summer sea-ice extent. *Geophysical Research Letters*, **31**, L09401, doi:10.1029/2004GL019492.

Rogers, R.R. & Yau, M.K. (1994). *A Short Course in Cloud Physics*. Elsevier Science Ltd, Oxford, UK, 3rd edn.

Rutledge, S.A. & Hobbs, P.V. (1983). The mesoscale and microscale structure and organization of clouds and precipitation in midlatitude cyclones, VIII: A model for the "seeder-feeder" process in warm-frontal rainbands. *Journal of the Atmospheric Sciences*, **40**, 1185–1206.

Sandvik, A., Biryulina, M., Kvamst, N.G., Stamnes, J.J. & Stamnes, K. (2007). Observed and simulated microphysical composition of Arctic clouds: Data properties and model validation. *Journal of Geophysical Research*, **112**, D05205, doi:10.1029/2006JD007351.

Schmid, H.P. (1994). Source areas for scalars and scalar fluxes. *Boundary-layer Meteorology*, **67**, 293–318.

Schotanus, P., Nieuwstadt, F.T.M. & De Bruin, H. (1983). Temperature measurements with a sonic anemometer and its application to heat and moisture fluxes. *Boundary-Layer Meteorology*, **26**, 81–93.

Schweiger, A.J., Zhang, J., Lindsay, R.W. & Steele, M. (2008). Did unusually sunny skies help drive the record sea ice minimum of 2007? *Geophysical Research Letters*, **35**, L10503, doi:10.1029/2008GL033463.

Sedlar, J. & Tjernström, M. (2009). Stratiform cloud - inversion characterization during the Arctic melt season. *Boundary-Layer Meteorology*, doi:10.1007/s10546–009–9407–1.

Semtner, A.J. (1976). A model for the thermodynamic growth of sea ice in numerical investigations of climate. *Journal of Physical Oceanography*, 379–389.

Serreze, M.C. & Francis, J. (2006). The Arctic amplification debate. *Climatic Change*, **76**, 241–264.

Serreze, M.C., Barrett, A.P., Slater, A.G., Steele, M., Zhang, J. & Trenberth, K.E. (2007). The large-scale energy budget of the Arctic. *Journal of Geophysical Research*, **112**, D11122, doi:10.1029/2006JD008230.

Shaw, R.H., Tavangar, J. & Ward, D.P. (1983). Structure of the Reynolds stress in a canopy layer. *Journal of Applied Meteorology*, **22**, 1922–1931.

Shimada, K., Kamoshida, T., Itoh, M., Nishino, S., Carmack, E., McLaughlin, F.A., Zimmermann, S. & Proshutinsky, A. (2006). Pacific Ocean inflow: Influence on catastrophic reduction of sea ice cover in the Arctic Ocean. *Geophysical Research Letters*, **33**, L08605, doi:10.1029/2005GL025624.

Shupe, M.D. (2007). A ground-based multiple remote-sensor cloud phase classifier. *Geophysical Research Letters*, **34**, L22809, doi:10.1029/2007GL031008.

Shupe, M.D. & Intrieri, J.M. (2004). Cloud radiative forcing of the Arctic surface: The influence of cloud properties, surface albedo, and solar zenith angle. *Journal of Climate*, **17**, 616–628.

Shupe, M.D., Uttal, T. & Matrosov, S.Y. (2005). Arctic cloud microphysics retrievals from surface-based remote sensors. *Journal of Applied Meteorology*, **44**, 1544–1562.

Shupe, M.D., Matrosov, S.Y. & Uttal, T. (2006). Arctic mixed-phase cloud properties derived from surface-based sensors at SHEBA. *Journal of the Atmospheric Sciences*, **63**, 697–711.

Slingo, A. (1989). A GCM parameterization for the shortwave radiation properties of water clouds. *Journal of the Atmospheric Sciences*, **46**, 1419–1427.

Slingo, A. & Wilderspin, R. (1986). Development of a revised long-wave radiation scheme for an atmospheric general circulation model. *Quarterly Journal of the Royal Meteorological Society*, **112**, 371–386.

Smeets, C.J.P.P. & van den Broeke, M.R. (2008). The parameterisation of scalar transfer over rough ice. *Boundary-Layer Meteorology*, **128**, 339–355.

Smith, R.N.B. (1990). A scheme for predicting layer clouds and their water content in a general circulation model. *Quarterly Journal of the Royal Meteorological Society*, **116**, 435–460.

Solomon, S., Qin, D., Manning, M., M., M., Averyt, K., Tignor, M.M.B., Miller, H.L. & Chen, Z., eds. (2007). *Climate Change 2007: The Physical Science Basis, IPCC*. Cambridge University Press, Cambridge, UK.

Sorbjan, Z. (1986). Local similarity of spectral and cospectral characteristics in the stable-continuous boundary layer. *Boundary-Layer Meteorology*, **35**, 257–275.

Staniforth, A., White, A., Wood, N., Thuburn, J., Zerroukat, M., Cordero, E. & Davies, T. (2006). Joy of UM 6.3 - model formulation. *Unified Model Documentation Paper*, **No. 15**.

Steele, M., Ermold, W. & Zhang, J. (2008). Arctic Ocean surface warming trends over the past 100 years. *Geophysical Research Letters*, **35**, L02614, doi:10.1029/2007GL031651.

Stevens, B., Beljaars, A., Bordoni, S., Halloway, C., Köhler, M., Krueger, S., Savic-Jovcic, V. & Zhang, Y. (2007). On the structure of the lower troposphere in the summertime stratocumulus regime of the Northeast Pacific. *Monthly Weather Review*, **135**, 985–1005.

Stimac, R. (2003). *Atmospheric stability*. [Accessed 14th January 2008], Eastern Illinois University, USA, http://www.ux1.eiu.edu/ jpstimac/1400/stability.html edn.

Stull, R. (1988). *An Introduction to Boundary Layer Meteorology*. Kluwer Academic Publishers, Dordrecht, 4th edn.

Stull, R. (2000). *Meteorology for Scientists and Engineers*. Brooks/Cole, California, USA, 2nd edn.

Sun, Z. & Shine, K.P. (1994). Studies of the radiative properties of ice and mixed-phase clouds. *Quarterly Journal of the Royal Meteorological Society*, **120**, 111–137.

Thorndike, A.S., Rothrock, D.A., Maykut, G.A. & Colony, R. (1975). The thickness distribution of sea ice. *Journal of Geophysical Research*, **80**, 4501–4513.

Tjernström, M. (2005). The summer Arctic boundary layer during the Arctic Ocean Experiment 2001 (AOE-2001). *Boundary-Layer Meteorology*, **117**, 5–36.

Tjernström, M. (2007). Is there a diurnal cycle in the summer cloud-capped Arctic boundary layer? *Journal of the Atmospheric Sciences*, **64**, 3970–3986.

Tjernström, M. & Rune, A. (2003). The turbulence structure of stratocumulus during the ASTEX first lagrangian experiment. *Quarterly Journal of the Royal Meteorological Society*, **124**, 1071–1100.

Tjernström, M., Leck, C., Persson, P., Jensen, M., Oncley, S. & Targino, A. (2004a). The summertime Arctic atmosphere. meteorological measurements during the Arctic Ocean Experiment 2001. *Bulletin of the American Meteorological Society*, **84**, 1305–1321.

Tjernström, M., Leck, C., Persson, P., Jensen, M.J., Oncley, S. & Targino, A. (2004b). Supplement - Experimental equipment. *Bulletin of the American Meteorological Society*, **84**, ES14–ES18.

Tjernström, M., Žagar, M., Svensson, G., Cassano, J., Pfeifer, S., Rinke, A., Wyser, K., Dethloff, K., Jones, C., Semmler, T. & Shaw, M. (2005). Modelling the Arctic boundary layer: An evaluation of six ARCMIP regional-scale models using data from the SHEBA project. *Boundary-Layer Meteorology*, **117**, 337–381.

Tjernström, M., Sedlar, J. & Shupe, M.D. (2008). How well do regional climate models reproduce radiation and clouds in the Arctic? *Journal of Applied Meteorology and Climatology*, **47**, 2405–2422.

Tsay, S.C. & Jayaweera, K. (1984). Physical characteristics of Arctic stratus clouds. *Journal of Climate and Applied Meteorology*, **23**, 584–596.

Uttal, T., Curry, J.A., McPhee, M.G., Perovich, D.K., Moritz, R.E., Maslanik, J.A., Guest, P.S., Stern, H.L., Moore, J.A., Turenne, R., Heiberg, A., Serreze, M.C., Wylie, D.P., Persson, O.G., Paulson, C.A., Halle, C., Morison, J.H., Wheeler, P.A., Makshtas, A., Welch, H., Shupe, M.D., Intrieri, J.M., Stamnes, K., Lindsey, R.W., Pinkel, R., Pegau, W.S., Stanton, T.P. & Grenfeld, T.C. (2002). Surface heat budget of the Arctic Ocean. *Bulletin of the American Meteorological Society*, **83**, 255–275.

van den Kroonenberg, A. & Bange, J. (2007). Turbulent flux calculation in the polar stable boundary layer: Multiresolution flux decomposition and wavelet analysis. *Journal of Geophysical Research*, **112**, D06112, doi:10.1029/2006JD007819.

van Dijk, A., Kohsiek, W. & de Bruin, H. (2003). Oxygen sensitivity of krypton and lyman-α hygrometers. *Journal of Atmospheric and Oceanic Technology*, **20**, 143–151.

van Dijk, A., Moene, A.F. & de Bruin, H. (2004). *The principles of surface flux physics: theory, practise and description of the ECPAK library*. Wageningen University, The Netherlands.

Vavrus, S. (2004). The impact of cloud feedbacks on arctic climate under greenhouse forcing. *Journal of Climate*, **17**, 603–615.

Verlinde, J., Harrington, J.Y., McFarquhar, G.M., Yannuzzi, V.T., Avramov, A., Greenberg, S., Johnson, N., Zhang, G., Poellot, M.R., Mather, J.H., Turner, D.D., Eloranta, E.W., Zak, B.D., Prenni, A.J., Daniel, J.S., Kok, G.L., Tobin, D.C., Holz, R., Sassen, K., Spangenberg,

D., Minnis, P., Tooman, T.P., Ivey, M.D., Richardson, S.J., Bahrmann, C.P., Shupe, M.D., DeMott, P.J., Heymsfield, A.J. & Schofield, R. (2007). The Mixed-Phase Arctic Cloud Experiment. *Bulletin of the American Meteorological Society*, **88**, 205–221.

Vickers, D. & Mahrt, L. (2003). The cospectral gap and turbulent flux calculations. *Journal of Atmospheric and Oceanic Technology*, **20**, 660–672.

Voronovich, V. & Kiely, G. (2007). On the gap in the spectra of surface-layer atmospheric turbulence. *Boundary-Layer Meteorology*, **122**, 67–83.

Walsh, J., Kattsov, V., Chapman, W., Govorkova, V. & Pavlova, T. (2002). Comparison of Arctic climate simulations by uncoupled and coupled global models. *Journal of Climate*, **15**, 1429–1446.

Walsh, J.E., Chapman, W.L. & Portis, D.H. (2009). Arctic cloud fraction and radiative fluxes in atmospheric reanalyses. *Journal of Climate*, **22**, 2316–2334.

Wang, J., Zhang, J., Watanabe, E., Ikeda, M., Mizobata, K., Walsh, J.E., X., B. & Wu, B. (2009). Is the dipole anomaly a major driver to record lows in Arctic summer sea ice extent? *Geophysical Research Letters*, **36**, L05706, doi:10.1029/2008GL036706.

Wang, Q. & Wang, S.P. (2004). Turbulent and thermodynamic structure of the autumnal Arctic boundary layer due to embedded clouds. *Boundary-Layer Meteorology*, **113**, 225–247.

Westwater, E.R., Han, Y., Shupe, M.D. & Matrosov, S.Y. (2001). Analysis of integrated cloud liquid and precipitable water vapour retrievals from microwave radiometers during SHEBA. *Journal of Geophysical Research*, **106**, 32,019–32,030.

Wilczak, J., Oncley, S. & Stage, S. (2001). Sonic anemometer tilt correction algorithms. *Boundary-Layer Meteorology*, **99**, 127–150.

Wilson, D.R. & Ballard, S.P. (1999). A microphysically based precipitation scheme for the U.K. Meteorological Office Unified Model. *Quarterly Journal of the Royal Meteorological Society*, **125**, 1607–1636.

Wilson, D.R., Bushell, A.C., Kerr-Munslow, A.M., Price, J.D. & Morcrette, C.J. (2008). PC2: A prognostic cloud fraction and condensation scheme. I: Scheme description. *Quarterly Journal of the Royal Meteorological Society*, **134**, 2093–2107.

Wyngaard, J.C. & Coté, O.R. (1972). Cospectral similarity in the atmospheric surface layer. *Quarterly Journal of the Royal Meteorological Society*, **98**, 590–603.

Yaglom, A.M. (1977). Comments on wind and temperature flux-profile relationships. *Boundary-Layer Meteorology*, **11**, 89–102.

Yamamoto, G. (1975). Generalization of the KEYPS formula in diabatic condition and related discussion on the critical Richardson number. *Journal of the Meteorological Society of Japan*, **53**, 189–195.

Yelland, M.J., Taylor, P.K., Consterdine, I.E. & Smith, M.H. (1994). The use of the inertial dissipation technique of shipboard wind stress determination. *Journal of Atmospheric and Oceanic Technology*, **11**, 1093–1108.

Zhang, T., Lindsay, R., Steele, M. & Schweiger, A. (2008). What drove the dramatic retreat of arctic sea ice during summer 2007? *Geophysical Research Letters*, **35**, L11505, doi:10.1029/2008GL034005.

Appendix A

Paper published in the Journal of Geophysical Research